Temperature Control of the Bacterial Flagellar Motor

Matthew A. B. Baker

A thesis submitted in partial fulfillment of
the requirements for the degree of
Doctor of Philosophy at the University of Oxford

Exeter College
University of Oxford
Trinity Term 2010

Abstract

Temperature Control of the Bacterial Flagellar Motor

Modern single-molecule biophysical experiments require high numerical aperture immersion-oil objectives in close contact with the sample. This thesis describes the design and construction of a temperature controller for a high numerical aperture microscope, and its use to investigate the temperature dependence of the speed and energetics of the sodium-driven chimeric bacterial flagellar motor of *E. coli*.

The temperature controller built for this thesis can control the temperature between 0 °C and 50 °C, and change the temperature up or down by 10 °C in 1 minute. It consists of an electronic Peltier heat pump cooled by water flow located directly around the nose of the objective. This novel temperature controller allowed rapid temperature change on a high resolution microscope enabling measurements of single molecules as they respond to a temperature change.

This controller was used first to investigate the characteristics of the motor at low temperature. This thesis presents torque speed curves at low temperature and low stator number to quantify the effect of cooling on motors at both large and small loads. Cooling has a greater effect on small loads, and the room-temperature characteristics of the torque speed curve remain at 5 °C.

Finally the measurement of the cellular membrane voltage (V_m) and its dependence on temperature is investigated. The mean membrane voltage dependence on temperature was measured using a published technique based upon a voltage sensitive fluorescent dye and was maintained at -120 – -130 mV between 5 °C and 40 °C. Subsequently the single cell membrane voltage was measured and tracked with temperature. This avoided the loss of detail due to averaging over many cells, and allowed quantification of single cell voltage decays that occurred when cells were kept at temperatures above 40 °C for around 5 minutes. These voltage decays coincided with motor stoppages over similar durations at similar temperatures observed by others, and so it is likely these high temperature stoppages are a voltage related temperature effect.

Declaration

The work in this thesis was undertaken at the University of Oxford; in the Clarendon Laboratory, Department of Physics. Work was performed from January 2006 to May 2010 under the supervision of Dr R. M. Berry. All the work in this thesis is my own unless stated and has not been submitted for a degree at this or any other university.

Publications

Matthew A B Baker and Richard M Berry (2009), "An Introduction to the physics of the bacterial flagellar motor: a nanoscale rotary electric motor", *Contemporary Physics*, 50, 617–632

Matthew A. B. Baker, Yuichi Inoue, Kuniaki Takeda, Akihiko Ishijima, & Richard M. Berry, (in final preparation) "Two methods of temperature control for single molecule measurements".

Acknowledgements

I would like to acknowledge the support and guidance of my supervisor, Dr Richard Berry. He is a true 'ideas-man', always providing useful approaches and creating new lines of enquiry. He also inspires me as an example of a highly successful scientist with a healthy work-life balance, something which is often times too rare.

I would like to thank the General Sir John Monash Award and the Life-Science Interface Doctoral Training Centre for funding my study these last few years.

I would also like to thank all my group colleagues past (Dr Yoshiyuki Sowa, Dr Teuta Pilizota, Dr Chien-Jung Lo, Dr Fan Bai, Dr Tom Bilyard, Dr Mark Leake, Matt Llewellyn-Jones and Petar Jurcevic) and present (Dr Bradley Steel, Dr Mostyn Brown, Dr Nicolas Delalez, Dr Richard Branch, Wei-Ming Ho, James Flewellyn, Claudio Silvestrin and Ashley Nord). In particular I would like to thank Dr Bradley Steel for multiple extremely vigorous readings of this thesis, his useful comments on experimental, analytical, and writing techniques. Bradley boosted my morale with his arrival by showing me how capable Australian scientists could be and I hope I can emulate his thoroughness one day. Richard Branch showed me how research and a thesis should be done - comfortably and with ease. Dr Chien-Jung Lo pioneered many of the techniques used in this thesis, and without his help, and his publications, none of this would have been possible. Dr Yoshiyuki Sowa is a phenomenal example of an experimentalist: thorough, meticulous, and successful. Dr Teuta Pilizota always gave useful advice in science and in life and work, as did Dr Tom Bilyard and Wei-Ming Ho. This wouldn't be much of a thesis without you all.

I would like to thank all colleagues and friends outside my group who have made my life and work more fun. Listing friends is perverse and likely to omit too many people.

I would like to thank the members of fencing club, in particular coach Tomek Walicki for all his expertise, psychologically and tactically, in fencing, win or lose, and in life.

I would like to thank the music.

I would like to thank my family for encouraging me to come and study here, and also for supporting me in all my endeavours, no matter how strange. Thanks to Dad for help with proof-reading.

I would like to thank Eleni for being silly, happy, grumpy, calm and helpful, at all the necessary times, and for believing in me more than I do myself.

Abbreviations

AC	alternating current
ADP	adenosine diphosphate
ATP	adenosine triphosphate
BFM	bacterial flagellar motor
cAMP	cyclic adenosine monophosphate
CCD	charge coupled device
CCCP	carbonyl cyanide m-chlorophenylhydrazone
CMOS	complementary metal-oxide-semiconductor
DC	direct current
EDTA	ethylenediaminetetraacetic acid
EMCCD	electron-multiplying charge-coupled device
GFP	Green Fluorescent Protein
IC	internal combustion
IMF	ion motive force
IPTG	isopropyl-β-D-thiogalactoside
LB	lysogeny broth
MP	melting point
NA	numerical aperture
NMB	7-nitrobenz-2-oxa-1,3-diazol-4-yl
P_i	phosphate
PMF	proton motive force
PMT	photon-multiplying tube
Q_{10}	temperature coefficient
QPD	quadrant photo-diode
SD	standard deviation
SEM	standard error of the mean
SMF	sodium motive force
TIRF	total internal fluorescence microscopy
TMR	tetramethylrhodamine
TMRM	tetramethyl rhodamine methyl ester
TB	terrific broth

crawling slithering along the edge of a straight razor

Contents

Chapter 1

Introduction

Movement is a signature of life and essential to movement is the ability to generate force. The bacterial flagellar motor is a rotary protein motor that produces the locomotive force with which bacteria swim. It is one of the oldest sources of motility, and one of the earliest wheels in existence. Nature has made little use of the wheel, due to the difficulties in maintaining rotating parts in constant use. However the bacterial flagellar motor is a nanowheel that is the fastest biomachine on the planet. It is capable of switching direction in milliseconds and determining whether it is swimming towards, or away, from nutrient in order to navigate its environment and improve the cell's situation. By examining this molecular motor using all available means, including investigating its temperature dependence and thus how its kinetics and energetics change with temperature, we can further our understanding of this remarkable biological machine.

1.1 Motility and Motor Proteins

Proteins are the main functional elements in molecular biology. They are large fluctuating molecules that perform a specific function based upon their structure, which depends in turn their sequence and on they way they are folded. Little is known about the details of how folding is controlled or directed and it is one of the central questions of biology (Alberts et al., 2002). Correctly folded proteins are typically only just stable and this marginal stability allows proteins to make transitions between several different meta-stable structures or conformations. These conformational changes underlie the mechanisms of most proteins, of which molecular motors are a particularly clear example.

Motor proteins, to manoeuvre their structures into strained positions, use chemical energy. If this conformational change generates mechanical force then it is known as a mechanochemical transition. Motor proteins use mechanochemical transitions to generate force and make things move. At the molecular level linear proteins such as kinesins are responsible for hauling components directionally inside a cell along a fixed track, carrying a cargo. There are many kinesins involved in intracellular transport, but one of the most well studied is kinesin-1. It exists as a dimer with two heads and a long entwined tail, and walks along microtubules in a hand-over-hand fashion in 8 nm steps (Svoboda et al., 1993).

When many motor proteins work in concert, macroscale motion can be generated. For example, the linear motor protein myosin is responsible for exerting a small force on an actin filament, and through many proteins acting together, myosin is the driving force behind muscle contraction. When an arm is lifted, billions of myosin proteins are pulling arrays of parallel actin filaments together, contracting the biceps muscle (Block, 1996; Geeves and Holmes, 1999; Haselgrove et al., 1976).

At the cellular level there are many cells that can move around their environment. One example is the sperm cell, which generates motion by the coordinated oscillation of linear motors that generates wave propagation in the tail (Riedel-Kruse et al., 2007). Another example is phagocytes, part of the immune system, which move by using linear motors to distort their structure and crawl along surfaces (Tauber, 2003). There are also examples of multicellular motion and cooperation in amoebic molds such as Dictyostelium. When faced with a lack of food Dictyostelium cells secrete cAMP as a chemotactic signal. This acts as a chemoattractant to which the cells respond by aggregating into multicellular slugs. If faced with further starvation, these slugs stand upright on end to form fruiting bodies, large mushroom-like structures with differentiated stalk cells and tip cells. This is an early demonstration of co-operativity where single cell organisms can co-ordinate their motion to benefit the aggregate at the expense of some individual cells (Dao et al., 2000).

Also at the cellular level, and the focus of this thesis, is the bacterial flagellar motor. Bacteria are able to swim because this motor rotates and drives a helical filament. This rotary motion is rare in biological systems and is unique as a mechanism for motility. Figure 1.1 shows these different examples of motor motility.

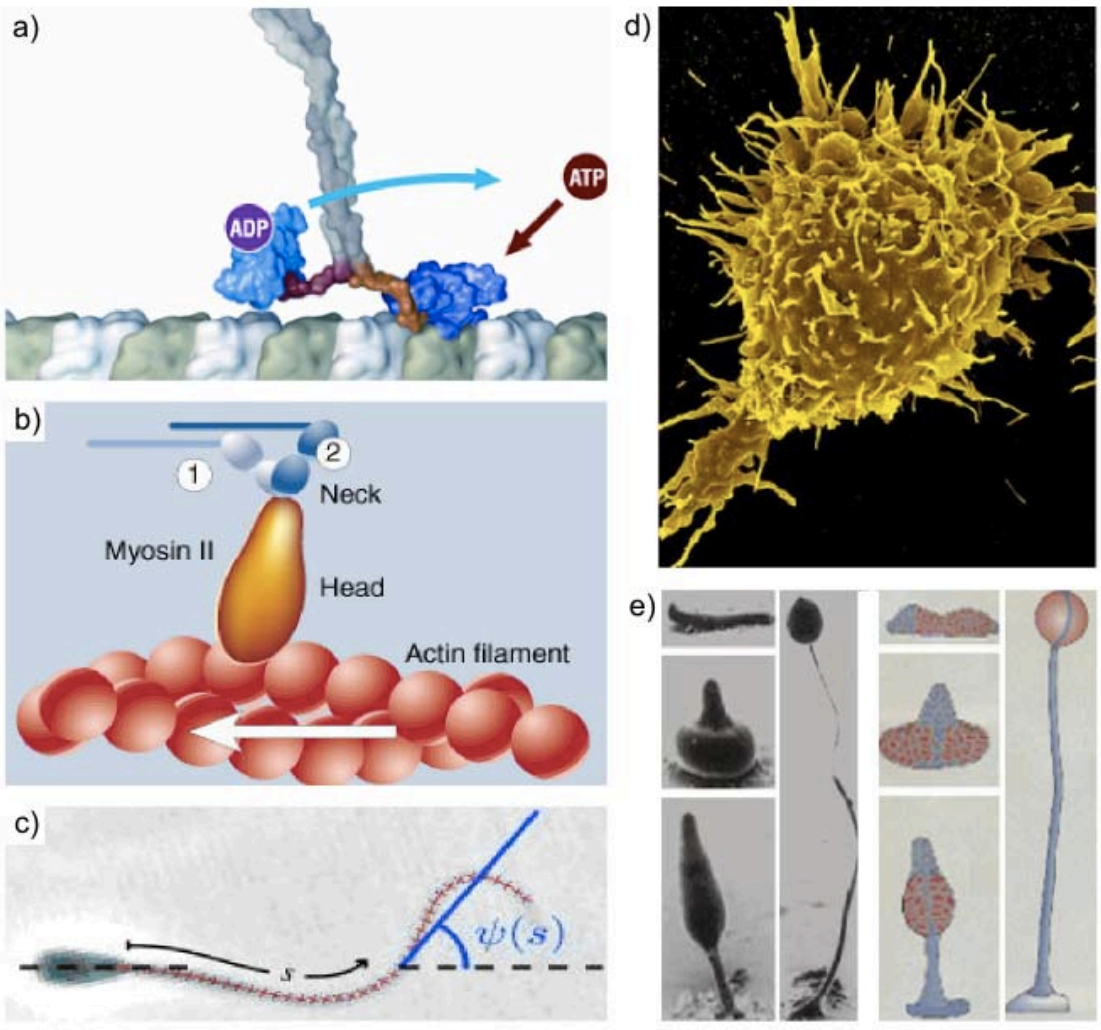

Figure 1.1: Di erent types of motility. left, top to bottom, and then right, top to bottom: a) kinesin moving along a microtubule. The dimer is entwined and the two heads walk along a microtubule in a hand-over-hand mechanism. Shown here is one state in the chemical cycle, where ATP is bound at the head attached to the track and ADP is released from the trailing head (Petsko and Ringe, 2004). b) Myosin II, one of the molecular motors responsible for muscle contraction, pulls an actin lament. In muscles, tail sections of Myosin II bundle to form the thick lament, and actin bundles to form the thin lament. The sliding of thick against thin l-aments, driven by Myosin II, is what causes muscle contraction (Cyranoski, 2000). c) Flagellar beating in sperm due to co-ordinated oscillation of dyneins acting on microtubules in the tail of sperm (Riedel-Kruse et al., 2007). d) A 30 m 25 m scanning electron microscope image of a phagocyte moving along (Rosenberger and Finlay, 2003). e) left: scanning electron microscope images of Dictyostelium aggregates forming fruiting bodies and raising o a surface. Right: blue shows prestalk cells and red prespore cells. When the single cells begin to starve they excrete a chemical signal, cAMP, and when this is detected cells aggregate to form slugs and subsequently fruiting bodies (Dao et al., 2000).

1.2 Biological Free-Energy - Petrol for Proteins

Molecular motors, by their nature, are directional and do work against a load. These directional processes occur in an environment dominated by fluctuation, and these motors operate at energies only marginally higher than the surrounding thermal bath. This is the central difference between macroscopic and molecular motors and these fluctuations are an essential component of the motor mechanism. Macroscopic ideas of atomic-scale components working as levers, cogs, wheels and pistons are useful to some extent, but do not convey the fact that these interactions are occurring in a fluctuating viscous environment, driven by energetic and entropic considerations. Movement in nanoscale motors is thus a stochastic and fluctuating process. Motion occurs by biasing this fluctuation in such a way that work is achieved.

Work is coupled to a free energy source, such as the hydrolysis of adenosine triphosphate (ATP), the so called energy currency of life. Kinesin and myosin are both examples of ATP-driven molecular motors which use the free energy released by hydrolysing ATP to power their mechanochemical transitions.

The change in Gibbs free energy of a reaction, ΔG, is a measure of whether the reaction will proceed or not. It is strictly defined for any process by the enthalpic change minus the temperature-weighted entropic change:

$$\Delta G = \Delta H - T\Delta S. \tag{1.1}$$

The Second Law of Thermodynamics dictates that the sum entropy production for a system must be greater than or equal to zero. Antientropic events, such as the thermal bath performing transitory work on a molecular motor causing a backstep, are possible over colloidal lengths and time scales, but overall the motor must move forwards (the direction for which $\Delta G < 0$) and the ratio of forwards to backwards steps is quantatively described by the Fluctuation Theorems (Sevick et al., 2008). Put simply, the total ΔG for a closed system must be negative for a process to occur, and molecular motors perform work by using the free energy produced by an associated chemical reaction to compensate for free energy consumed when mechanical work is done.

The BFM is atypical of molecular motors in that it is powered by an electrochemical rather than a purely chemical process, namely the transit of monovalent cations across the cell membrane. The free energy per unit charge crossing the membrane is called the ion motive force (IMF), and has units of Volts. The IMF arises from the active transport of protons across the membrane generating an electrochemical

potential which is maintained as part of the metabolic cycle (Alberts et al., 2002) (see Chapter 5, Section 5.1). The IMF has electrical and chemical components, and is defined by:

$$\mathrm{IMF} = \mathrm{V_m} + \frac{\mathrm{kT}}{\mathrm{q}} \ln\left(\frac{\mathrm{C_{in}}}{\mathrm{C_{out}}}\right), \tag{1.2}$$

where V_m is the voltage difference across the membrane (normally defined as negative inside), k is Boltzmanns constant, T the absolute temperature, q the ionic charge, and C_{in} and C_{out} the ion concentrations inside and outside the cell, respectively. The two parts of the IMF can be considered separately: as an enthalpic component, V_m, and an entropic component, $\Delta\mu/q = (kT/q)\ln(C_{\mathrm{in}}/C_{\mathrm{out}})$. The enthalpic component is the electrostatic energy gain that arises when an ion moves from outside the cell to inside the cell across the voltage drop located at the membrane. The entropic component is the chemical potential difference per unit charge due to the concentration difference across the membrane.

It is worth mentioning here that most living systems function only in aqueous solution at temperatures near room temperature[1]. Accordingly the free energy changes associated with the function of living systems are comparable to the thermal energy, kT. Thus it is convenient to introduce an appropriate energy scale based on units of kT_0, where T_0 is room temperature and kT_0 = 4 x 10$^-$21 J. In terms of mechanical work, this is equivalent to 4 pN nm. Under typical biological conditions, the hydrolysis of one molecule of ATP produces 20 kT_0 of free energy, and a single ion transit 6 kT_0.

1.3 The Importance of Temperature

Temperature is an important global variable in biophysics. Molecular motors operate at energies only marginally higher than the thermal bath, and the kinetics of the mechanochemical transitions where chemical energy is transduced into mechanical force depend on temperature. The entropic weighting in the Gibbs free energy, $\Delta G = \Delta H - T\Delta S$ changes with temperature[2], and thus T is an important control parameter to explore the energy landscapes that define a motor's mechanism (Baker and Berry, 2009). Temperature also affects kinetics as described by the Arrhenius equation: in biological systems the rate change over a 10°C increase in tempera-

[1]There are exceptions: antarctic fish survive and function at ∼2 °C, and thermophilic bacteria at ∼80 °C

[2]Note also ΔH is in general a weak function of T

ture (known as Q_{10}) typically ranges between 1 (temperature independence) and 3 (McNaught and Wilkinson, 1997; Hegarty, 1973).

The Arrhenius equation is an empirical relationship that relates the rate constant of a reaction, k, to the temperature:

$$k = Ae^{\ E_a\ kT} \tag{1.3}$$

where A is the pre-exponential factor, k is Boltzmann s constant and E_a is the *activation energy*. Under collision theory (Trautz, 1916), A represents the probability of the reactant molecules colliding with enough kinetic energy, and in the correct orientation, to break existing bonds and form the transition state, and E_a represents the minimum kinetic energy that reactants must have in order to form products when they collide. Figure 1.2 shows a standard Arrhenius plot.

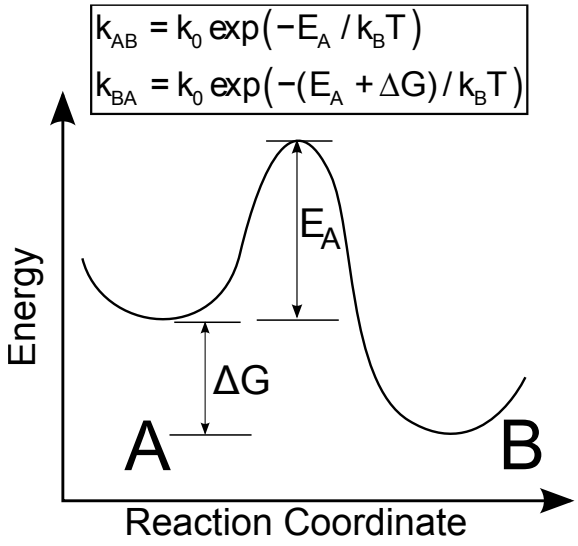

Figure 1.2: Arrhenius plot for a reaction between two states, A and B. Transitions from one state to another can be characterized by a reaction co-ordinate, an abstraction of the multiple pathways that the system can follow between any two states. The reactants pass through a transition state at the peak of the potential energy, and then form the products at state B. The potential energy di erence between the transition state, and the reactants, is known as the activation energy, E_a, and can be calculated empirically by performing multiple rate measurements at di erent temperatures. The di erence in free energy between the reactants and the products is the Gibbs free energy of the reaction, G, and determines whether the reaction will occur spontaneously. The rates for the forwards and reverse reactions, k_{AB} and k_{BA}, follow the Arrhenius equation.

Transition state theory is an alternative Arrhenius-like theory relating the rate

constant of a reaction to the enthalpy and entropy of activation. The principle of transition state theory is that there exists a transition state, the potential energy peak between the reactants and products, which is in quasi-equilibrium with the reactants (Atkins and de Paula, 2002). Using statistical thermodynamics it is possible to calculate an equilibrium constant for the quasi-equilibrium between the reactants and the transition state, and relate this to the Gibbs energy of activation (see Atkins and de Paula (2002) for a full derivation). The result is the Eyring-Polanyi equation (Eyring, 1935):

$$k = \frac{k_{\mathrm{B}}T}{h}\exp\left(-\frac{\Delta G^{\ddagger}}{RT}\right) \tag{1.4}$$

$$= \left(\frac{k_{\mathrm{B}}T}{h}\right)\exp\left(\frac{\Delta S^{\ddagger}}{R}\right)\exp\left(-\frac{\Delta H^{\ddagger}}{RT}\right) \tag{1.5}$$

where k is again the rate constant of the reaction, $\Delta G^{\ddagger}$ is the Gibbs energy of activation, $\Delta H^{\ddagger}$ is the enthalpy of activation, $\Delta S^{\ddagger}$ is the entropy of activation, and h is Planck's constant. In this reaction $\Delta H^{\ddagger}$ corresponds to the energy that must be gained for the reaction to reach the transition state and to subsequently form the products. The magnitude of $\Delta H^{\ddagger}$ determines the rate of reaction, and the Eyring-Polanyi Equation determines the dependence of the rate constant on temperature. By measuring reaction rates at different temperatures it is possible to calculate the enthalpy and entropy of activation for a reaction.

Controlling the temperature of high resolution single molecule experiments offers new experimental approaches to the study of molecular motors: of the kinesins, myosins, and dyneins discussed in the subsequent Section 1.4 as well as the BFM which is the topic of this thesis and discussed in Sections 1.5–1.5.5. Cooling a sample can slow the kinetics and allows the resolution of individual force and torque generating steps, as well as investigating the change in the size, duration, and dwell times of these steps. This information can be used to characterise the thermodynamics and kinetics of the mechanochemical transition that is the core of a motor's mechanism of action. Due to a current absence of temperature controllers for high resolution microscopes, many of these types of experiments have not yet been performed.

Temperature control for biological applications ideally requires fast temperature change across a small range of temperatures. Temperature controlled single molecule measurements allow us to probe the temperature dependence of individual reaction kinetics and the energetics of the reaction pathways along which the molecule operates. The importance of temperature control, what has been done previously, and

the design and implementation of the temperature controller used in this thesis are covered in detail in Chapter 3

1.4 Molecular Motors

1.4.1 Kinesin, Dynein and Myosin: Linear Motors

Early studies on motor proteins focused on the linear motors, so called because they moved along linear tracks such as actin filaments in the case of myosin and microtubules in the case of kinesin and dynein. Pioneering single molecule studies on these motors investigated how various strains of these motors differed (Guilford et al., 1997; Block, 1996; Gibbons, 1963; Vale et al., 1985). Discrete steps were observed (Veigel et al., 1999; Svoboda et al., 1993; Hirakawa et al., 2000) and exploring stepping under different conditions was the favoured approach to understand the properties of the mechanochemical transition and how these motors responded to force acting with or against the direction of motion.

The three motor types share some common attributes. All have a *head* which binds to the track, a *neck linker* which links and amplifies the motion of the head to the *stalk*, and a *tail* which binds to a cargo (or in multimeric motors, is entwined with a paired tail) (Howard, 2001). All three motors are powered by ATP hydrolysis, and generate force by conformational change in the head region, or motor domain. This is the part of the protein closest to the track, where binding to ATP and the track occurs[3]. Force is generated in dyneins by the swing of the linker domain, in kinesins by the docking and undocking of a flexible linker, and in myosins by a lever arm swinging as a rigid structure in a power stroke (Houdusse and Carter, 2009). The head is typically highly conserved within motor species (Case et al., 2000). The structures of all three motors are different, however, and they have different functional roles within the cell. Structures of the three linear motors are shown in Figure 1.3.

Kinesins

Kinesins were the last family of cytoskeletal motors to be discovered, but the first for which discrete stepping data was observed. Vale et al. (1985) discovered a novel force generating protein, kinesin, involved in intra-cellular motility, which up until then

[3]Dynein is unique in that the site of ATP hydrolysis is located away from the microtubule binding site

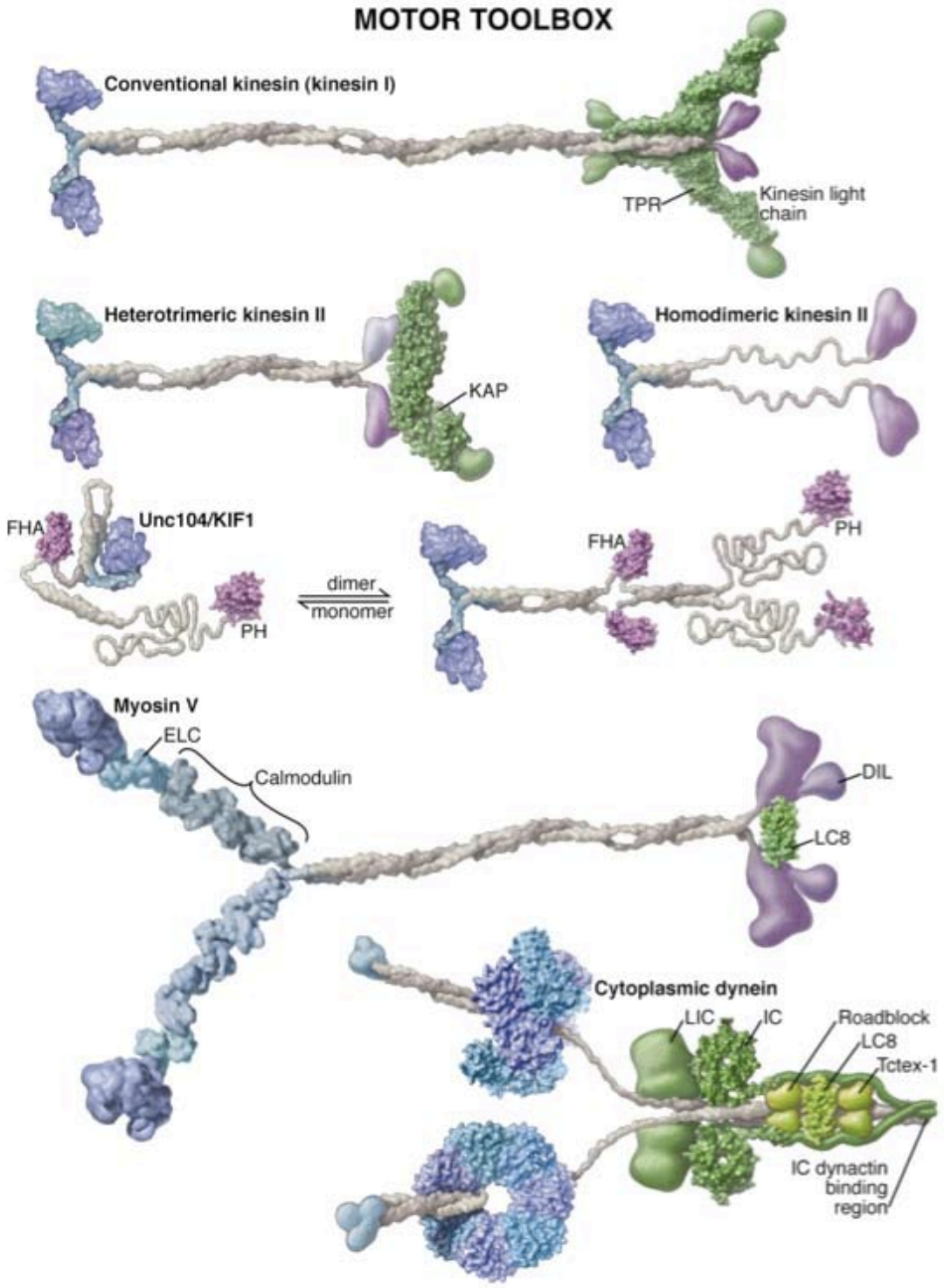

Figure 1.3: Structural schematic of Kinesins, Myosin V, and cytoplasmic dynein. From Vale (2003)

was not well understood. There are 41 kinesin-like proteins divided into subgroups of a family tree. The entire kinesin supertree has a conserved domain in the catalytic head, and the subgroups are separated by the conserved elements of the neck linker (Case et al., 2000). All use the energy from ATP hydrolysis and interact with microtubules, which are semi-rigid, hollow, structures within the cell that form the backbone structure of a cell known as the cytoskeleton (Alberts et al., 2002). Microtubules are biopolymers made of a heterodimer of the proteins α-tubulin and β-tubulin, each 55 kDa in size. Typically one end is attached to the centrosome, a microtubule organising centre, and the other end is close to the cell membrane. Microtubules grow faster at one end (the plus-end, with an exposed β-unit) than the other (the minus-end, with an exposed α-unit), and most kinesins move towards the plus-end, although some, like Ncd, are minus-end directed. The movement and coordination of the microtubules in forming the mitotic spindle which drives mitosis is one of the most important functions of kinesins. Some kinesins have a high duty-ratio, which means they spend large amounts of time in contact with the track (processive motion), and the addition of further motors when transporting a large cargo will not increase the speed at which the cargo moves along the track. Others have a low duty ratio, which means that they are non-processive and can cooperate to increase the speed at which a cargo is transported. Most motor proteins are to some extent a combination of both processive and co-operative types.

There are 14 known classes of kinesin used to transport different types of cargo, such as organelles, mitochondria, lysosomes, and mRNA complexes. Kinesin has a heavy chain (KHC) and a light chain (LHC), which correspond to the head (where ATP binds, and microtubules bind) and a tail. Kinesin most commonly exists as an entwined dimer. The sequence of the head (N-terminal in all plus-directed kinesins and C-terminal in all minus-directed kinesins) is conserved among most kinesins. Next is the neck linker which attaches the head to the tail, and can transfer force from the head to the tail and its attached cargo. The neck linker undergoes nucleotide dependent conformational change and is an amplifier for the motion generated in the conserved catalytic head (Case et al., 2000).

Distinct 8-nm steps were first resolved for kinesin in 1993 by Svoboda et al. (1993). They were looking for steps occurring over an average 'sliding distance' in which ATP hydrolysis and movement were tightly coupled. The occurrence of stepping and the distribution of steps and the dwell times of steps placed "constraints on possible mechanisms of movement". One of the reasons kinesin was more suited to early stepping experiments is that it could be made to move more slowly by

increasing the load (applying more force using optical tweezers). This enabled better time averaging of the position of the motor. Svoboda et al. (1993) measured stepping on length scales of nanometres on time scales of milliseconds. In comparison, the BFM steps through angles of 14° (60 nm of the circumference of a 0.5 μm bead) in approximately half a millisecond. Carter and Cross (2005) subsequently showed that kinesin can, in fact, step backwards under high loads.

Kinesin is involved in mitosis and the assembly of the mitotic spindle (Knight, 2009). Kinesin-5 family members exist as tetrameric motors with two motor domains at each end of a central stalk (Kashina et al., 1996). This allows the motor to cross-link two microtubules and slide them relative to each other. A particular Kinesin-5, Eg5, crosslinks microtubules, essential for moving microtubules within the cell and assembling the mitotic spindle which separates the chromosomes (Kapitein et al., 2005, 2008).

Recently interest has developed in studying the co-operativity of kinesin and how this affects the discrete steps in the movement of a microtubule. Leduc et al. (2007) showed that a single kinesin-1, with its tail attached to a surface and its head attached to a microtubule, would move the microtubule in 8-nm steps, but when an additional kinesin-1 motor attached to the microtubule, it would step in 4-nm steps. This is analogous to the situation in the BFM, where there are multiple stators acting on the rotor, but verifying this requires measuring steps in motors powered by multiple stators, which is beyond current resolution. How motors respond to force feedback when driving a cargo co-operatively, and more generally how bidirectional traffic of multiple motors is regulated, are intriguing issues which are still mostly unsolved (Vale, 2003).

Some temperature-related work has been performed on kinesin. Collins and Vallee (1987) explored the role of temperature in kinesin stability and showed that taxol-restrained microtubule dynamics were strongly dependent on temperature and Kawaguchi and Ishiwata (2000) showed that the velocity and processivity of single kinesin molecules was strongly dependent on temperature in an Arrhenius manner, but that force generation of kinesin was independent of temperature. Kawaguchi and Ishiwata (2000) also showed that the efficiency of mechanochemical conversion was not strongly affected by temperature, and thus that the force generation was attributable to the conformational changes within the kinesin-microtubule complex. They inferred that velocity is determined by the rate of ATPase activity, which is temperature dependent.

Dyneins

Dyneins are a family of large minus-directed microtubule motors that are unrelated to kinesins and can move cargoes extremely rapidly (up to 14 μm/s). They drive the beating of cellular cilia, or sperm flagella, to provide propulsion. They exist as heterodimers or heterotrimers, are not restricted to acting on a single microtubule, and their mass is 10 times larger than that of kinesin (Vallee et al., 2004). This size and the difficulty of expressing mutants have made research into dyneins difficult. The conserved motor domain has been modelled on the basis of sequence analysis and electron microscopy but an atomic level structure is not known (Houdusse and Carter, 2009). Despite these difficulties dynein was the first force generating microtubule ATPase to be discovered (Gibbons, 1963).

Dyneins contain 1-3 heavy chains each with a molecular mass of 500 kDa. Each heavy chain consists of a donut-shaped head with two long structures known as the stalk. Dyneins fall into two major classes: axonemal dyneins from cilia and flagella in eukaryotes, and cytoplasmic dyneins. Axonemal dyneins are localised around doublet microtubules in axonemes and form projections called dynein arms which are groups of several dyneins. These dynein arms, called inner and outer arm dyneins on the basis of their location, are responsible for the coordinated beating of cilia and flagella, for example, in the swimming motility of sperm (Riedel-Kruse et al., 2007).

Dynein force-generation is not completely understood. It has been proposed that the swing of the N-terminal linker between the tail and donut shaped head, between primed and unprimed states, provides the force driving dynein along a microtubule (Houdusse and Carter, 2009). One remarkable feature is the presence of oscillations at high frequency that drive beating motility. Single molecule studies show that dynein can generate forces of 2 pN at 70 Hz. The mechanism by which this oscillation is co-ordinated, through stress and strain on damping and elastic elements, is one of the outstanding questions in dynein research (Oiwa and Kojima, 2009).

Some temperature related work has been performed on Dynein. The rate of ATPase activity has been investigated in antarctic fish (*Notothenia coriiceps* with a body temperature $\sim$2 °C) and has been observed to increase from 0 °C to 19 °C, but decrease upon further heating (King et al., 1997). Temperature sensitive mutants have also been explored in *C. elegans* that lost function with $\pm$10 °C changes in temperature. Dynein is the largest and most complex of the cytoskeleton motors and its mechanism is the least understood.

Myosins

Myosins are motors that exert force on an actin filament. Myosins have three main functional regions: 1) the motor region, that binds ATP, binds the actin filament, and produces the force, 2) the regulatory region, that has up to six light chains and works as a lever arm to amplify and reverse the action of the motor, and 3) the tail region that binds to cargos (Knight, 2009). The structure of the myosin head is shown in Figure 1.4, from structural work on scallop myosin S1 (Houdusse et al., 2000)

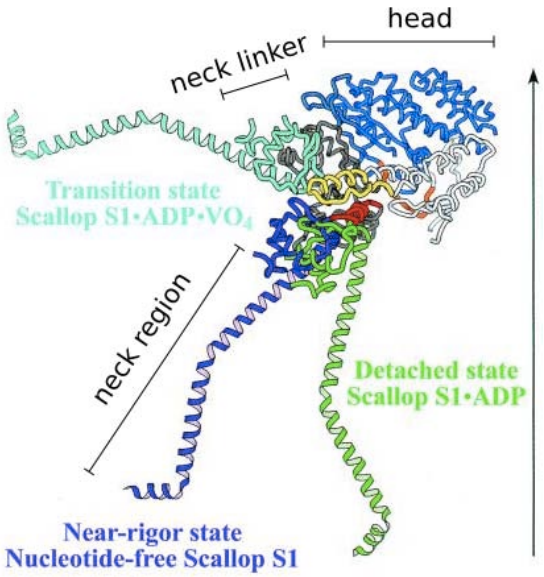

Figure 1.4: Structure of Myosin II head with three states of action superimposed, the detached state (dark green), the near-rigor state (blue) and the transition state (light green). Nucleotide binding at the head induces a conformational change which is amplified in the regulatory region and passed on to the neck region which acts as a rigid lever arm. The arrow indicates the direction of the actin filament relative to the head. Adapted from Houdusse et al. (2000).

Conventional myosin, Myosin II, is directly linked to muscle function and thus has a rich history of investigation. Electron microscopy of muscle tissue in the 1960s showed myosin crossbridges acting on actin filaments (Huxley and Simmons, 1971). This was soon after coupled to the enzymatic cycle by looking at the ATPase activity of myosins by Lymn and Taylor (1971), who proposed that tightly bound actomyosin complexes dissociated when ATP was bound, and that release of hydrolysis products accompanied the timing of the power stroke.

The structure of the myosin head contains a catalytic core that is responsible for ATP hydrolysis and actin binding, and attached to this core is the so-called convertor domain. This acts as a hinge for a rigid component of the head, known as the lever arm, to swing relative to the catalytic core and generate force (Vale and Milligan, 2000). Since myosin is bound to actin only briefly, and only during this force generating cycle, it is highly non-processive and cannot move continously along the actin track (Vale and Milligan, 2000). Myosin II moves quite differently to kinesin in that it swings a large rigid structure to step ∼10 nm while kinesin has a small conformational change in the head that generates force, assisted by binding of the alternate head in the dimer to the next section of the track in a highly processive mechanism. This behaviour matches their functions since kinesin is primarily used to transport a single cargo, whereas Myosin II is used in large aggregates to create large forces where the individual myosins must not impede the action of each other.

Single molecule measurements of force and step size in Myosin II are difficult because the forces involved are small and the binding is intermittent (Knight, 2009). Force measurement has been accomplished by using a three-bead assay where an actin filament is suspended from two optical traps (see Section 1.7.1 for a discussion of this technique) and lowered onto a third bead covered in a low concentration of Myosin II. When the myosin binds to the filament the displacement of the actin filament can be measured by one of the traps bound to the filament. Care must be taken to use weak traps so that the stiffness of the apparatus is much less than the stiffness of the actomyosin complex, allowing the displacement of the filament to be detected (Knight, 2009). Figure 1.5 shows two types of 3 bead dumb-bell assays. Single molecule force measurements were first successfully executed by Finer et al. (1994), who observed average step sizes of 11 nm. Shortly afterwards, Molloy et al. (1995) used a similar technique to refine this estimate of step size to ∼4 nm, and to define the *working distance* as the difference in mean position of the actin filament when free and when bound to myosin. Steffen et al. (2001) were able to map the location of myosin binding sites along the actin filament and found that the binding sites were close to the 36 nm helix repeat distance, and that myosin operated with a working stroke of 5.4–6.3 nm (Smith et al., 2001a). By adding high frequency oscillations to one of the optical traps, Veigel et al. (1999) observed that Myosin I moved in two distinct steps of 6 nm and 5.5 nm, but they were unable to resolve this in the faster Myosin II. Capitanio et al. (2006) later resolved these two independent events, the first 3.4-5.2 nm and the second ∼1.0-1.3 nm. The working stroke size depends on the type of myosin: skeletal muscle Myosin II has a working stroke

of ∼5 nm which can be increased or decreased by lengthening or shortening the regulatory region, as demonstrated by Ruff et al. (2001) who genetically engineered amplifier domains in the neck linker to probe the importance of linker length on step size.

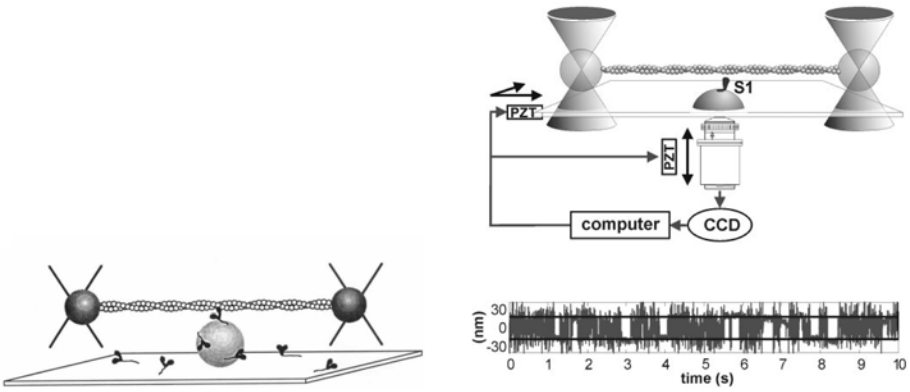

(a) (b)

Figure 1.5: Two schematics of the Myosin II 3 bead dumb-bell assay. a) The original experiment from Finer et al. (1994) showing suspended actin filament and surface-bound bead coated in dilute myosin. b) The dumb-bell assay from Steffen et al. (2001) showing piezocontrolled feedback of the trap position and the vertical z-position of the stage to minimize drift. The image from the CCD is used to determine the bead position and focus and send a voltage to the piezostages (PZT on diagram). An example trace is also shown (lower) indicating reduction in brownian noise when myosin binds to track. For full discussion of optical trapping see Section 1.7.1. From Finer et al. (1994); Steffen et al. (2001).

There are also other significantly different myosins, for example non-muscle myosins, such as Myosin V, and a minus-directed myosin, Myosin VI (Knight, 2009). Myosin V is a two headed highly processive motor that transports vesicles and organelles inside the cell. Much single molecule work has been done on Myosin V precisely because it is processive. It produces steps with a working distance of 25 nm in two steps, one of 20 nm and one of 5 nm as shown in Figure 1.6 (Veigel et al., 2001). Myosin V has preferred binding positions every 36 nm along the actin filament and Veigel et al. (2001) propose that the motor makes 36 nm steps that are a combination of the 25 nm working head stroke and an 11 nm diffusive movement that is thermally driven. Myosin V is a dimer with two processive heads which are each bound to the filament $> 70\%$ of the time, in contrast to the head of Myosin II which is bound $\sim 5\%$ of the time (Knight, 2009).

Myosin VI is involved in intracellular transport and is the only consistently

minus-directed myosin. This reverse action was thought to be due to a 53-amino acid insert into the convertor domain that links the neck to the head (Knight, 2009), but it was shown subsequently that the motor core domain, not an insert, determined directionality. This was demonstrated by interchanging the Myosin V head onto Myosin VI and observing polarity change, thus showing that polarity depended on neither the large insert nor the converter region (Homma et al., 2001).

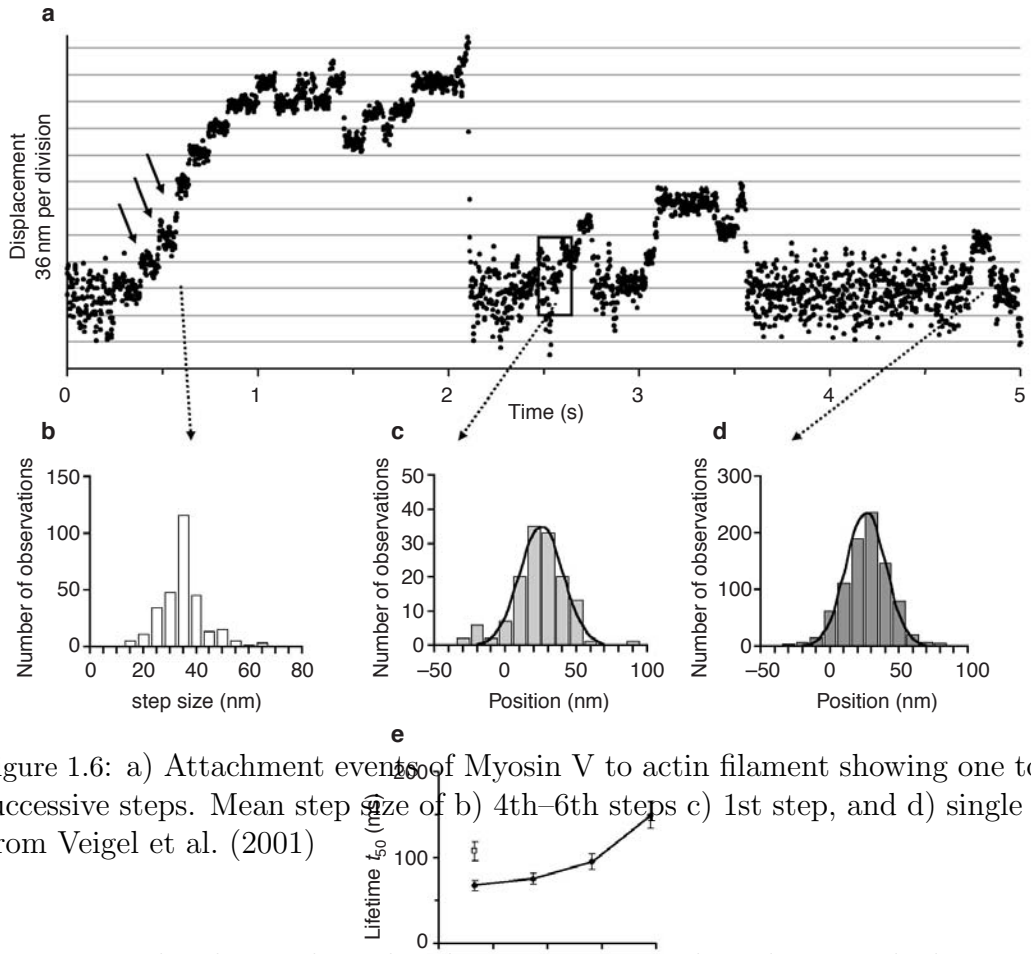

Figure 1.6: a) Attachment events of Myosin V to actin filament showing one to nine successive steps. Mean step size of b) 4th–6th steps c) 1st step, and d) single steps. From Veigel et al. (2001)

Figure 3 **Single-molecule mechanical interactions measured for TPMV.** **a**, Attachment events with one to nine successive steps ('staircases') were observed (100 μM ATP). **b**, Mean step size of the second to fourth steps in the staircases; mean ± s.e.m. 34.5 ± 0.6 nm, $n = 302$, 3000 μM ATP. **c**, Amplitude of the first step in the staircases; mean ± s.e.m. 26.2 ± 2.3 nm, $n = 142$, 100 μM ATP. **d**, Amplitude of single step displacements; mean ± s.d. 25.0 ± 0.6 nm, $n = 885$, 5 μM ATP. **e**, Force-dependent lifetime of steps. Filled diamonds show dwell times during staircases; $n = 125$, 127, 107 and 86 for external forces of 0.5, 1.2, 1.9 and 2.7 pN, respectively. The open square shows the dwell time of single interactions of TPMV with actin $n = 885$, average force of 0.77 pN.

We found that the amplitude of such single isolated events and also the first step in a 'staircase' produced by TPMV (Fig. 3c, d) were similar to the isolated interactions produced by MVS1. We conclude that the working stroke of both MVS1 and TPMV is 21–25 nm, whereas the average step size produced by the processive interaction of TPMV is 34–36 nm (Fig. 3b)[3]. We believe that the slightly smaller working stroke measured for MVS1 (21 nm) than the stroke size measured for TPMV (25 nm) is most probably based on slight differences in binding of the two different molecules to the nitrocellulose surface.

Actin scanning experiment. To explore this result further, we used

Myosins that have adapted to low temperatures have been studied in antarctic fish. Johnston et al. (1975) found that myosins from *Notothenia rosii* were more likely to aggregate and denature at high temperature, and proposed structural differences that enable myosins in these fish to maintain high levels of activity at low temperature. Hwang et al. (1990) discovered that acclimatising carp to low (10 °C) or high (30 °C) temperature for 5 weeks changed the activity of dorsal myosins; that is, that the myosins were acclimatised to temperature conditions. Piazzesi et al. (2003) investigated the temperature effects on step size and force generation in frog skeletal myosin II and found that force generation increased with heating but that step-size was unchanged. Decostre et al. (2005) also found that the force

during processive interactions. Finally, we measured changes in stiffness produced by TPMV interacting with actin. [illegible] actin filament (Fig. 5A). To do this we applied a rapid sinusoidal oscillation to one of the beads holding the actin filament and monitored pickup of this signal at the other bead. We found a brief decrease in stiffness from ~0.35 to ~0.18 pN nm^{-1} immediately preceding many of the transitions between step levels. At low load (<1 pN), the dwell time at reduced stiffness was ~18 ms, although at high load (>2 pN) intervals of reduced stiffness increased to hundreds of milliseconds. We interpret intervals of high stiffness to be those in which both heads are bound and the brief intervals of low stiffness to be those

generation increased when the temperature was increased from 2 °C to 17 °C. They concluded from the fact that working stroke energies were higher at higher temperatures that high temperatures increased the probability of the first transition in the myosin head. Temperature effects on myosins and muscles have been investigated more closely than effects on kinesin and dynein due to the range of temperatures at which muscles need to operate. For a good review of the effects of temperature on muscle crossbridges, focussing on the dependence of force on temperature, see Woledge et al. (2009).

1.4.2 Rotary Molecular Motors

Helical Motors

Many molecular motors operate along DNA to replicate, repair and package the genome and are thus helical in their motion. These motors, called helicases, rotate around the track of DNA as opposed to walking along it, and thus are classed rotary motors (Doering et al., 1995). They derive energy from nucleotide hydrolysis but the mechanism by which this energy is transduced into force is unknown.

In bacteriophages, the ultimate purpose of assembly is to inject a viral package into a preformed protein shell called the procapsid. Approximately 100 kilobases are injected into the capsid head by molcular motor ϕ29 at a velocity of more than 1μm/s (Lee et al., 2009). This work is highly entropically unfavourable as the DNA is extremely compact inside the capsid head (Lee et al., 2009). The packing is driven by ATP hydrolysis and one molecule of ATP is hydrolysed to pack two base pairs. The motor is 30 nm in diameter, uses 6 copies of an ATP-binding packaging RNA (pRNA) to gear the motor, and is one of the strongest molecular motors in terms of the force generated ($\sim$57 pN) (Smith et al., 2001b). Unique to ϕ29 is the presence of pRNA that participates in DNA translocation. The pRNA binds ATP and enhances the ATPase activity of gp16: six pRNA from ϕ29 form a hexamer ring. DNA translocation is geared by pRNA in a sequential fashion as demonstrated by complete blockage of packaging when a single pRNA is replaced. (Lee et al., 2009). Recently the sequential nature of ϕ29 packing was confirmed using optical tweezers to study packing in 10 base pair increments (Aathavan et al., 2009). The 10-bp increments are composed of four 2.5-bp steps which indicate a novel co-ordination mechanism between components. The scalability of the pRNA macromolecular structure and the strong tendency of the individual pRNA to form dimers, trimers and hexamers has generated interest in research towards biomimetic

motors for gene delivery based upon $\phi 29$ (Lee et al., 2009).

Helical motors are essentially a cross between rotary and linear motors. They walk linearly along a track which happens to be helical, causing them to rotate, but they contain rotary parts and exert torques. Bacteriophages share other features with the BFM, for example the SecIII pathway used for export and assembly, discussed in Section 1.5.1.

F_OF_1 ATPase

There are very few purely rotary motors in biology and two of these are present in F_OF_1 ATPase, also known as ATP synthase. It is responsible for the synthesis of ATP, the energy currency of life, and every day produces ∼65 kg of ATP in an average human. F_OF_1-ATPase is highly conserved during evolution, with greater than 60% of the amino acids of the catalytic β-subunit conserved between bacteria and mammals (Yoshida et al., 2001). F_O is membrane-bound and F_1 resides in the cytoplasm. F_O is a rotary motor that is powered by the proton gradient across the membrane, and this rotation is coupled to a central shaft, known as the γ unit, which in turn rotates inside F_1 in order to synthesise ATP from ADP and phosphate, while F_1 is held by a peripheral stalk. The establishment of a proton gradient (Figure 1.7) is one of the end products of the metabolic cycle, discussed in detail in Chapter 5 Section 5.1.1, and is used to drive ATP synthesis. Alternatively, ATP can by hydrolysed to counterrotate the γ unit, which in turn causes rotation within F_O and pumps protons across the membrane. In bacterial ATPase, F_1 is a water soluble protein of ∼380 kDa which consists of $\alpha_3\beta_3\gamma\delta\epsilon$ subunits, where $\alpha_3\beta_3$ are located in a hexameric ring around the γ shaft. ATP synthesis and hydrolysis occur in the $\alpha\beta$ units, with 3 binding sites in the hexameric ring, and the γ subunit is the shaft which rotates. The δ subunit makes up part of the peripheral stalk, necessary in order to prevent rotation of $\alpha_3\beta_3$ during hydrolysis relative to F_O (Noumi et al., 1992), and the ϵ subunit inhibits ATP hydrolysis (Klionsky et al., 1984). F_O consists of ab_2c_{9-15} subunits. The c subunits are located in a ring connected to the end of the γ stalk and the protein gradient drives rotation of the ring of c subunits and thus the γ subunit. The structure of bovine F_1-ATPase was first resolved by Abrahams et al. (1994), for which Walker received the Nobel Prize in 1997. The structure of F_OF_1-ATPase is shown in Figure 1.8.

Direct observation of the rotation of F_1 was demonstrated by Noji et al. (1997), whose presentation of this work at the American Biophysical Society Meeting prompted spontaneous applause. Noji et al. (1997) used a fluorescent actin filament attached

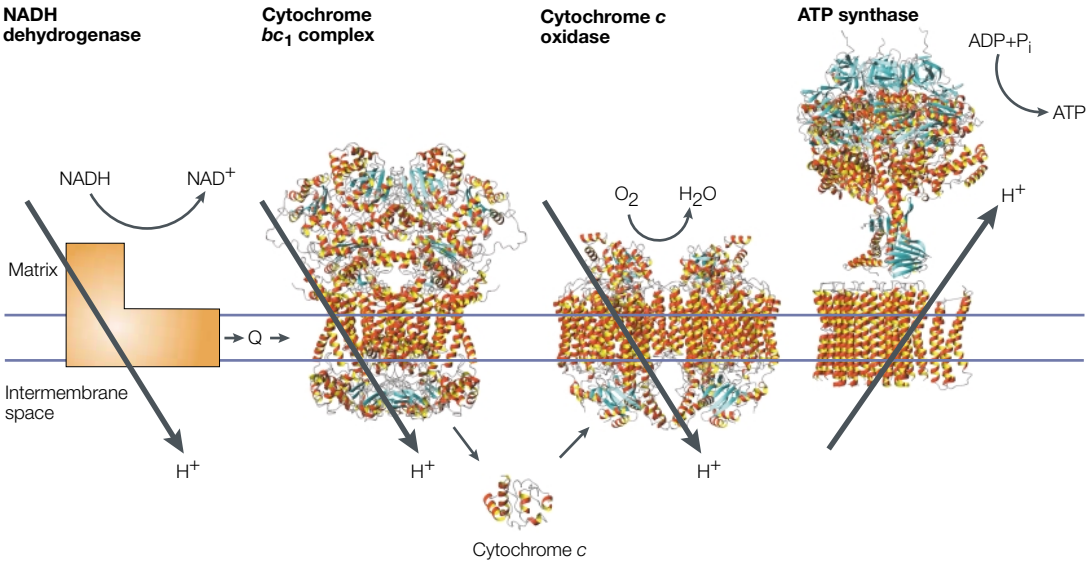

Figure 1 | **The respiratory chain and ATP synthase.** Electrons are transferred from NADH dehydrogenase to cytochrome *c* oxidase by coenzyme Q (Q), cytochrome bc_1 complex and cytochrome *c*. The established proton gradient that powers mitochondrial membrane drives the proton flow in ATP synthase that accompanies ATP synthesis. Structures are taken from: cytochrome bc_1 complex[4], cytochrome *c* oxidase[5], the F_1 part of ATP synthase[6], and the F_o part of ATP synthase[7].

Figure 1.7: The end result of the metabolic cycle is a proton gradient that powers F_O rotation. Electrons are transferred from NADH dehydrogenase to cytochrome c oxidase by coenzyme Q, cytochrome bc1 complex and cytochrome c. Structure and Figure taken from Yoshida et al. (2001)

Structure of F_1

In the initial crystal structure of the $(\alpha\beta)_3\gamma$-portion of native bovine mitochondrial F_1 (termed the 'native' structure)[6], three α-subunits and three β-subunits are

equivalents in the native structure. The β-subunit equivalent to β_E takes a 'half-closed' (C′) conformation (FIG. 3d), and retains Mg-ADP and sulphate (a mimic of phosphate) at the catalytic site. In the C′-form β, the car-

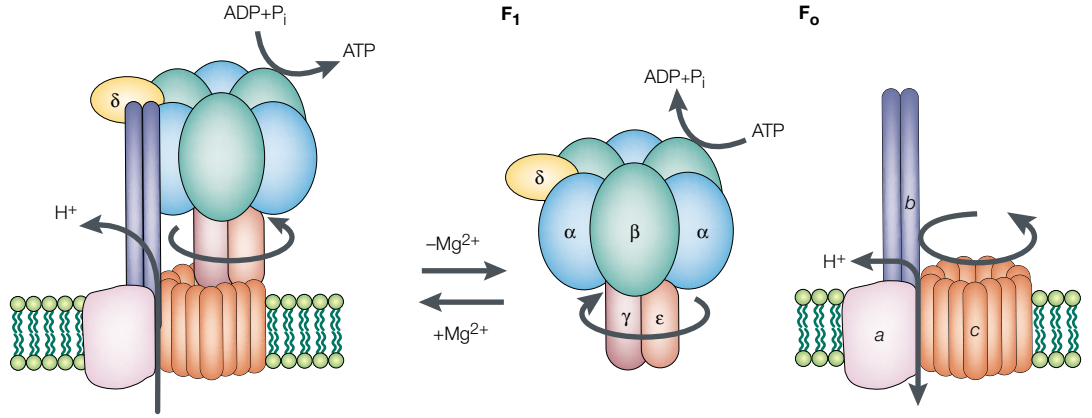

Figure 2 | **Structure of ATP synthase.** The bacterial ATP synthase is illustrated as the simplest version of ATP synthases. It is composed of about seven protein subunits and contains F_1 and a hydrophobic transmembrane portion, F_o (REFS 6,7). Mg^{2+} at low concentrations of salt allows the F_1 part to be extracted in water, leaving the F_o portion in the membrane. F_o and F_1 can, however, reassemble into the intact ATP synthase by adding back Mg^{2+} (REFS 61,73,74). This reversible separation of F_o and F_1 has proved invaluable in studying the mechanism and function of the $F_o F_1$ type of ATP synthases (which is considered a reverse reaction of ATP synthesis). The subunit structures of ATP synthases are well conserved during evolution, but there are some variations among sources. The simplest is bacterial ATP synthase, in which F_1 contains five kinds of subunits with a stoichiometry $\alpha_3\beta_3\gamma_1\delta_1\varepsilon_1$, and F_o contains three kinds of membrane subunits with stoichiometry $a_1b_2c_{10-14}$. The numbers of transmembrane helices are five (F *a*), one (F *b*) and two (F *c*). Chloroplast ATP synthase has the same subunit composition except that two kinds of $F_o b$ homologue exist. Mitochondrial ATP synthase has at least six kinds of additional accessory subunits. Confusing subunit nomenclature exists for historical reasons (for example, mitochondrial δ corresponds to bacterial ε, and the mitochondrial subunit named OSCP corresponds to bacterial δ), but in this review we use the names of subunits according to the bacterial enzyme. The catalytic sites for ATP hydrolysis are located on the β-subunits of F_1, but residues of the α-subunits also contribute. The α-subunits contain a non-catalytic nucleotide-binding site, the function of which is not yet fully understood. The central stalk is made of the γ- and ε-subunits, and the side stalk from the $F_1\delta$- and $F_o b_2$-subunits.

Figure 1.8: Bacterial ATP synthase as $F_o F_1$ (left), F_1 separately (middle) and F_o separately (right). As $F_o F_1$ the energy gained from ion transit from outside the membrane (bottom) to inside the membrane (top) drives the rotation of the c_{10-14} ring and thus the central γ unit, which drives ATP synthesis in the upper $\alpha_3\beta_3$. Removal of Mg^{2+} allows F_1 to detach from F_o, leaving F_o in the membrane. F_1 on its own can hydrolyse ATP to rotate the γ-subunit. F_o on its own will rotate the c-subunit ring. F_o has five transmembrane helices in *a*, one in *b* and two in each *c* subunit. From (Yoshida et al., 2001).

'the two β-strands (one before the P-LOOP and the other before the switch II loop), which leads to the outward (opening) movement of the whole carboxy-terminal domain of β. This movement produces the C′ form, and subsequent loss of ADP/P_i from the catalytic site sets the

and colleagues[9] have proposed a model by which concerted transitions — the closing of β_E driven by ATP binding and the opening of β_{DP} driven by ATP hydrolysis — induce the 120° rotation of the γ-subunit. A similar model was postulated previously by Ren and

to the γ subunit to image the rotation directly. Stepping was observed by Yasuda et al. (2001) who observed steps of 120° broken into two substeps of 80° and 40°, with ATP binding driving the larger step. They achieved higher resolution of the rotation by using the signal from 40 nm gold beads attached to the γ subunit and a dark-field microscope. A schematic of their experiment is shown in Figure 1.9. Similar high resolution dark-field microscopy experiments have been applied to the flagellar motor (Yuan and Berg, 2008), and have been recently developed in our group in Oxford.

Itoh et al. (2004) rotated a magnetic bead attached to the γ subunit in the synthesis direction to show that the rotation of the γ subunit drove ATP synthesis. This demonstrated that a torque at one location on a chemical protein could drive a chemical reaction at another point.

Full-speed rotation with 40-nm beads

Bead rotation was imaged by laser dark-field microscopy[12] (Fig. 1c),

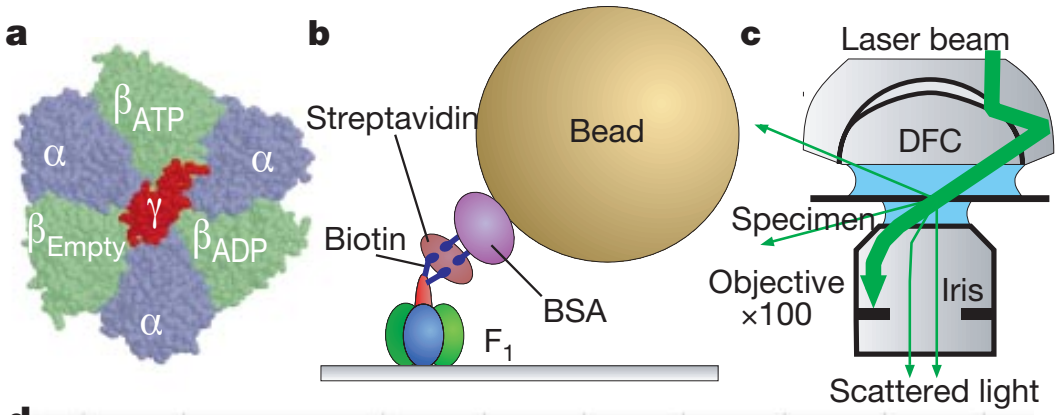

Figure 1.9: Schematic showing the dark field method that enabled Yasuda et al. (2001) to observe the rotation of F_1 at high resolution. a) Top view structure of F_1. b) 60nm gold bead linked to γ subunit by a streptavidin biotin linker. c) Laser illumination is blocked by an iris in the back focal plane of the objective and scattered light from the gold bead is observed in the image plane. From Yasuda et al. (2001).

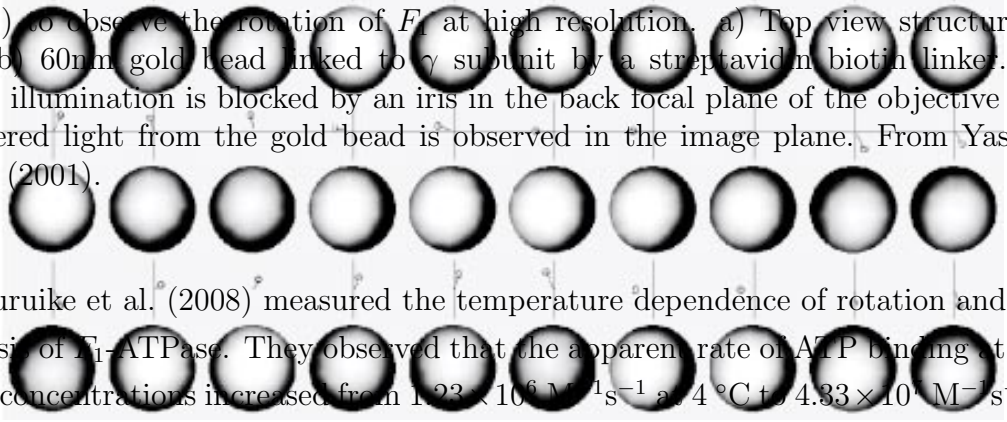

Furuike et al. (2008) measured the temperature dependence of rotation and hydrolysis of F_1-ATPase. They observed that the apparent rate of ATP binding at low ATP concentrations increased from 1.23×10^{6} $M^{-1}s^{-1}$ at 4 °C to 4.33×10^{7} $M^{-1}s^{-1}$ at 40 °C, while the torque remained constant at around 40 pN·nm across the temperature range. They observed that F_1 generally rotated faster at higher temperatures and hypothesised that this was a temperature effect acting primarily upon the ADP release step. They observed a particularly steep temperature dependence at temper-

Figure 1 Observation of F_1 rotation. ***a***, Atomic structure[7] of F_1-ATPase viewed from the F_o side (top in **b**). **b**, Side view of the observation system. The 40-nm bead gave a large enough optical signal that warranted a submillisecond resolution; but the bead was small enough not to impede the rotation. **c**, Laser dark-field microscopy for observation of gold beads. Only light scattered by the beads exited the objective and was detected. DFC, dark-field condenser. **d**, Sequential images of a rotating bead at 2 mM ATP. Images are trimmed in circles (diameter 370 nm) to aid identification of the bead position; centroid positions are shown above the images at ×3 magnification. The interval between images is 0.5 ms.

atures <10 °C, from which they inferred the appearance of a different rate-limiting process at those temperatures, since at high temperatures ADP release is not rate limiting. This was confirmed by the observation of pauses at the 0° position, differing from the room temperature observation of pausing in the 80° position due to ATP hydrolysis at room temperature. Comparisons between the temperature controller of Furuike et al. (2008) and the Peltier collar designed in this thesis are mentioned in Section 3.10.

The Bacterial Flagellar Motor

The other biological rotary motor, and the only rotary motor used for motility, is the Bacterial Flagellar Motor (BFM). This is the focus of this thesis. First the structure and function of the BFM is covered (Section 1.5) then the environment of bacteria is introduced to familiarise the reader with some of the oddities of the micron-scale world (Section 1.6), and lastly some of the experimental techniques used in this thesis, and in the study of molecular motors in general, are discussed (Section 1.7).

1.5 The Bacterial Flagellar Motor

The Bacterial Flagellar Motor (BFM) is a self assembled protein complex 50 nm in diameter embedded in the bacterial cell envelope, which is capable of rotating at speeds up to 100,000 rpm, five times as fast as a modern Formula one engine. BFMs from several species have been studied, and all are broadly similar. In this thesis we will refer to the motor of *Escherichia coli* (*E. coli*) unless otherwise stated, as this is the most studied and best understood example, and the focus of this thesis. As mentioned previously, the motor is powered by ions crossing the cell membrane, driven by electrical and chemical potential differences, and uses this energy to rotate either clockwise or counterclockwise, switching in response to the environmental signals. Motor rotation is coupled to helical flagellar filaments through the hook, a helical protein polymer which acts as a universal joint. When filaments are rotated counterclockwise (CCW, looking down the filament towards the cell) they form bundles which propel the swimming cell. When they are rotated in the opposite direction (CW), one or more filaments splay from the bundle initiating a tumble, which is a random re-orientation of the cell. Tumbles are suppressed when a cell detects that the concentration of attractant molecules in its environment is increasing, thus prolonging episodes when the cell is swimming to where nutrient concentrations are

greater. In this way cells can execute a biased random walk that moves them towards regions of increased nutrient concentration, a process known as chemotaxis. Much has been learned about chemotaxis but it is not the focus of this thesis (Berg, 2003; Sourjik, 2004; Hazelbauer et al., 2008; Bai et al., 2010).

1.5.1 Structure, Assembly and Architecture

The structure of the flagellar motor was determined by a combination of cryo-electron microscopy and X-ray diffraction. Some parts, such as the rotor, have well elucidated structures, but others, such as the stators, have yet to be successfully crystallized (Thomas et al., 2006). By using these imaging techniques, in combination with genetic and biochemical methods which target certain protein interactions and their location in the motor, structural information can be gathered.

The BFM is composed of 45 different proteins and aggregates of these proteins make up larger structures, such as rods and rings. The BFM is a meso-scale structure where clusters of proteins work together to form large macromolecules to do a fixed task. These aggregates, such as the rings of the BFM, assemble in a piecewise fashion, and in a fixed sequence, using guided self assembly mechanisms. The basal body of the motor assembles first. This consists of 4 rings and a rod which acts as a driveshaft to the filament and is the core of the motor - a set of rings embedded in the cell envelope. The outermost of these, the L ring, is embedded in the lipopolysaccharide membrane and the next ring, the P ring, is embedded in the peptidoglycan layer. These protect the rotating parts of the motor from interference with the cell membrane, but it is not known whether they rotate inside the membrane or whether the rod rotates inside the ring. One ring, the so-called C ring, constitutes the rotor of the motor. It consists of the proteins FliG, FliM and FliN. The structure of the BFM is shown in Figure 1.10

Stators are dynamic and straddle the cell membrane acting on the rotor to produce torque (Sowa and Berry, 2008). In wild-type *E. coli* the stators are MotA and MotB which are driven by a proton powersource. In other strains, such as salt water *Vibrio alginolyticus* the stators are the proteins PomA and PomB and the power source is sodium ions. Wild-type *E. coli* also contains two proteins, MotX and MotY, whose exact function is not known but it is hypothesized that they stabilize the rotation. Stators are embedded in the cell wall in stoichiometric groups of $MotA_4MotB_2$ which comprise a single stator unit.

Mechanisms of assembly are probed primarily by looking at mutants and suppressions of particular proteins and observing the resulting structure. If a certain

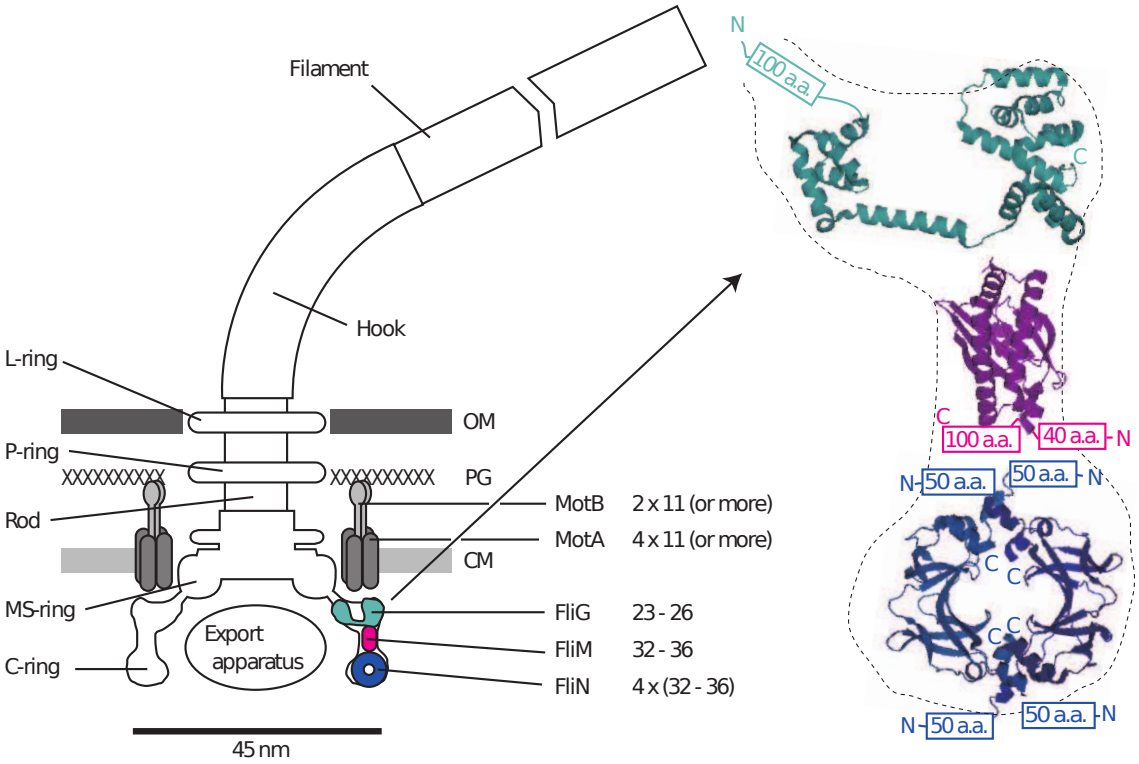

Figure 1.10: Schematic side-view of the BFM with the proposed location and copy number of proteins involved in torque generation. The basal body consisting of the C-ring, MS-ring, rod, P-ring and L-ring, assembles first, followed by the hook and filament proteins. The stators are dynamic and each has the stoichiometry $MotA_2MotB_4$. Right: detail of the proposed location and orientation of the three C-ring proteins. X-ray crystal structures of truncated rotor proteins, FliG (Cyan), FliM (Magenta) and FliN (Blue), are shown docked into the C-ring structure. N- and C-termini and unresolved amino acids are indicated. Figure reproduced from Sowa and Berry (2008).

protein is knocked out, and the assembly of the BFM reaches a certain stage, then it is determined that that protein assembles at that point in the overall assembly pathway. Likewise, the structure of the BFM can be observed when certain proteins are modified to determine their effect on the export process.

First to assemble is the cytoplasmic MS ring Macnab (2003). This is named MS since it was previously thought to be two rings - membrane and supermembranous (Sowa and Berry, 2008). The constituent prokaryotic cytoplasmic membrane proteins are inserted into the membrane by the Sec pathway, a group of proteins that are dedicated to inserting proteins inside the membrane. Once embedded, the MS ring acts as the mounting plate for the rotor and switch, and connects to the entire axial structure. This MS ring houses the export structure responsible for exporting the filament and hook proteins, and this export structure is the second element of the structure to assemble, beneath the MS ring.

Next to assemble is the motor and switch. The C ring constitutes the rotor and the switch complex, and is mounted under the MS ring. FliG probably assembles first, as it is anchored to the MS ring, and then FliM and FliN in an unknown order. It is thought that the assembly of the C ring is a simple self-assembly process. The C ring is most probably the site of torque generation, and the location of the stator-rotor interaction. It consists of the proteins FliG, FliM and FliN which are critical in stator/rotor interactions.

The remaining proteins which constitute the rod, hook, and filament are exported by the specific type III export apparatus of the BFM (Macnab, 2003; Kojima and Blair, 2004). Type III signifies three things. First, that the export uses a well-defined structure, which for the BFM happens also to be a vital component of the motility (hook, basal-body and filament). Secondly, that proteins are transported to the tips via hollow interior (the tubular inside of the hook and filament) and thirdly that proteins are added distally by diffusion down the central channel. This was formerly used as evidence by proponents of intelligent design as it was considered a unique assembly mechanism (Young and Edis, 2004). However elements of this export apparatus were found to be highly similar to the export apparatus in the needle complexes used in virulence secretion factors (Winstanley and Hart, 2001).

The type III export apparatus is composed of 6 integral membrane proteins, FlhA, FlhB, FliO, FliQ and FliR, and three soluble general components, FliH, FliI, and FliJ. A description of their function is too lengthy for here but a more detailed discussion is contained in the review of Macnab (2003).

The first protein exported by the type III apparatus is FliE. FliE is used in the

export of later proteins and its location is probably the distal face of the MS ring. This provides a junction between the 26-fold symmetry of the MS ring, and the later helical symmetry of 5.5-units per turn. Next assembled are the axial proteins: first the rod proteins, FlgB, FlgC, FlgF and FlgG, followed by FlgJ, a rod protein which can bind to the other rod proteins as a cap but also uses its murimadase activity to digest the peptidoglycan layer and allow the nascent rod to penetrate it. The rod is metastable and no structures including a partial rod have been detected (Macnab, 2003).

Next comes the hook, in an analogous fashion. The hook-cap, FlgD, displaces the rod cap, and the hook proteins diffuse out through the rod and being assembling the hook (Macnab, 2003). It is remarkable that the hook retains its precise length: 55nm. In terms of function it is clear why the hook has a fixed length but how this is monitored is unknown. It is known that FliK and FlhB are involved, as suppression of those proteins produces long polyhooks and no filament.

The hook is a highly flexible protein composed of 120 copies of the protein FlgE. This allows many filaments to rotate together in a bundle in the peritrichous species of bacteria. The hook is responsible for transmitting torque to the filament and can be compressed and extended. It is a tubular structure composed of 11 protofilaments (Samatey et al., 2004). In operational state the subunits are contracted on the the cell-side and extended on the opposite side. This flexibility of the hook is made possible by the apparent ease with which FlgE subunits can slide alongside each other and the flexibility to rotate relative to each other. These are verified by Molecular Dynamics simulations of FlgE proteins which show many stable sub-states occurring when two subunits slide alongside each other.

After the hook is assembled, the cap is discarded and is replaced by three junction proteins that begin to assemble the filament on the end of the hook (Macnab, 2003). The first two are hook associated proteins that stay in place and define the border of the hook and the filament. The third protein, known as the filament cap, moves outward as flagellin proteins are assembled underneath. Filament assembly begins after the junction proteins are in place and is the major undertaking of the entire assembly process. There is no length control on filament size and so a filament may contain as many as 20,000 subunits of the protein flagellin. There is a large deal of complexity in the cap, a ring-shaped pentameric structure with a flat top. It is suspected that the cap is involved in aiding the assembly of the flagellin into the helical structure. There is a large space underneath the cap which accommodates different vertical positions of flagellin subunits. It is thought that each flagellin

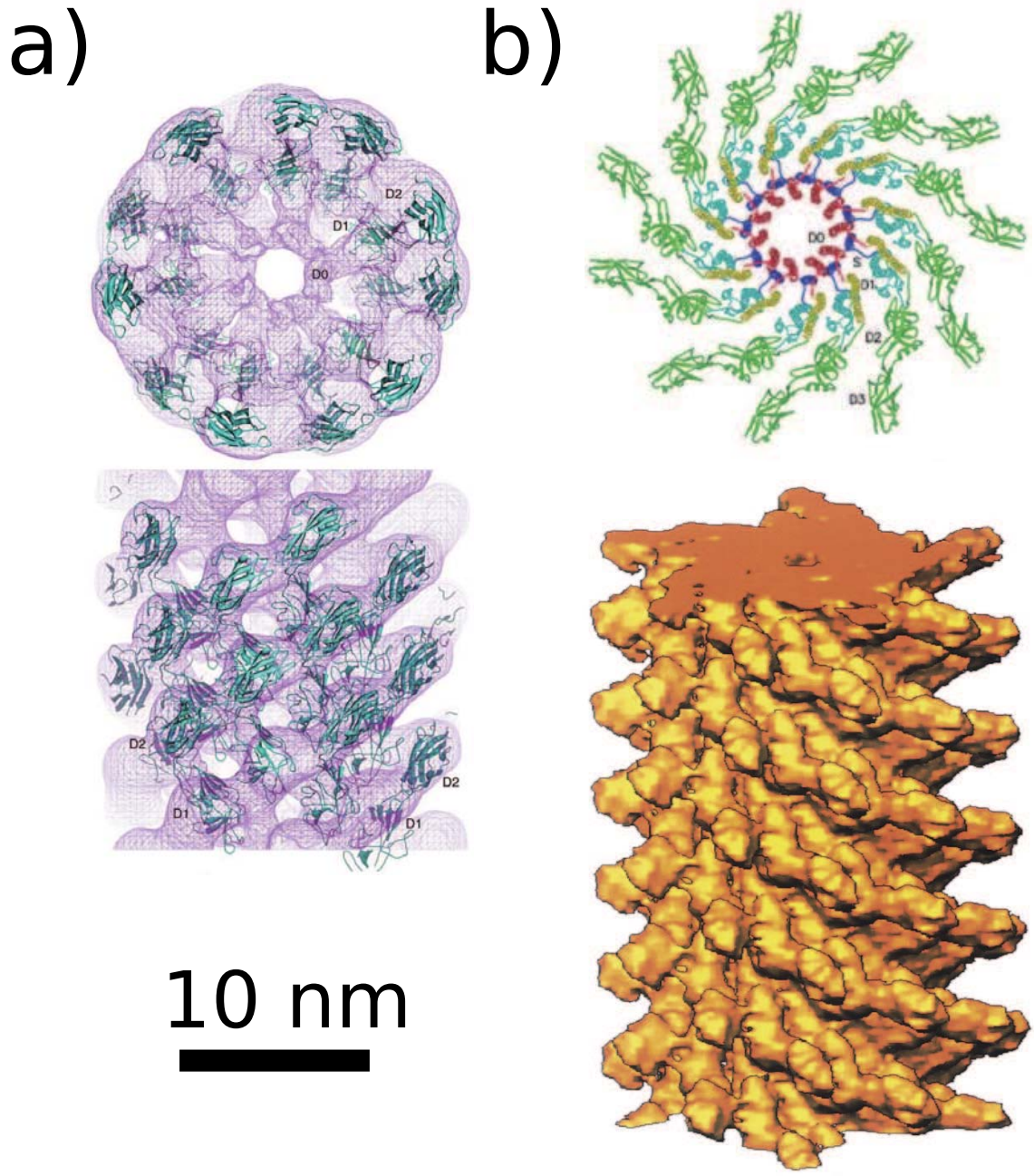

Figure 1.11: Structure of hook (a) and filament (b) revealed by X-ray crystallography and electron microscopy. Scale bar shows 10 nm. Figure adapted from Sowa and Berry (2008), from research by Samatey et al. (2004); Yonekura et al. (2003).

subunit folds into its monomer here and forms quaternary interactions with the adjacent monomers, then the cap rotates and the next flagellin unit assembles in the adjacent helix position. The structure of the hook and the filament are shown in Figure 1.11.

By considering the structure of the subunit flagellin some functional information can be inferred. The filament is a helical assembly of flagellin. Its tubular structure is formed by 11 proto-filaments per roughly two-turns of helix. These proto-filaments occur in 2 distinct conformations, L-type (long) and R-type (short) (Yonekura et al., 2003). When the filament is entirely composed of L-type, the filament is straight with left handed symmetry. Similarly when the filament is entirely composed of R-type, the filament is straight, with right handed symmetry (Samatey et al., 2001). When a mixture of both conformers is present the coil forms a helical filament (Figure 1.12). The filament subunit structure changes during a switch, where the sudden torsional strain can change the handedness of the filament, which results in the splay of the filaments and the subsequent tumble trajectory. Because of this conformational change inside the filament, the switching of a single motor is enough to cause a filament to leave a bundle causing a tumble in the bacterium.

What about the stators? It is important to note that the stators are dynamic and can bind onto and release from the motor (Leake et al., 2006). Stators can arrive in the membrane during formation of the C ring but they are highly labile. Motors can rotate stably with up to 11 stators (Reid et al., 2006), with each additional stator offering an incremental speed increase. Stators operate in a high-duty ratio, which means most stators are attached to the motor while it is functioning (Ryu et al., 2000). The absence of an atomic-level crystal structure makes it difficult to locate accurately a torque generating site. Studies using biochemical cross-linking and site-specific mutagenesis have identified some likely regions for activity. Mot/PomA have 4 alpha-helices spanning the membrane and Mot/PomB have 1. The cytoplasmic end of MotA contains 2 charged residues that interact with 5 charged residues on the C-terminal of rotor subunit FliG (Zhou et al., 1998). No single mutation of any of these residues destroys torque generation. Reversing the charge on both proteins results in compensation, which implies there is an electrostatic interaction at the interface of these 7 residues (Sowa and Berry, 2008).

1.5.2 Speed and Torque during Rotation

Finding the relationship between torque and speed is a means to quantify the mechanochemical cycle of any motor. In the case of the BFM the load on the

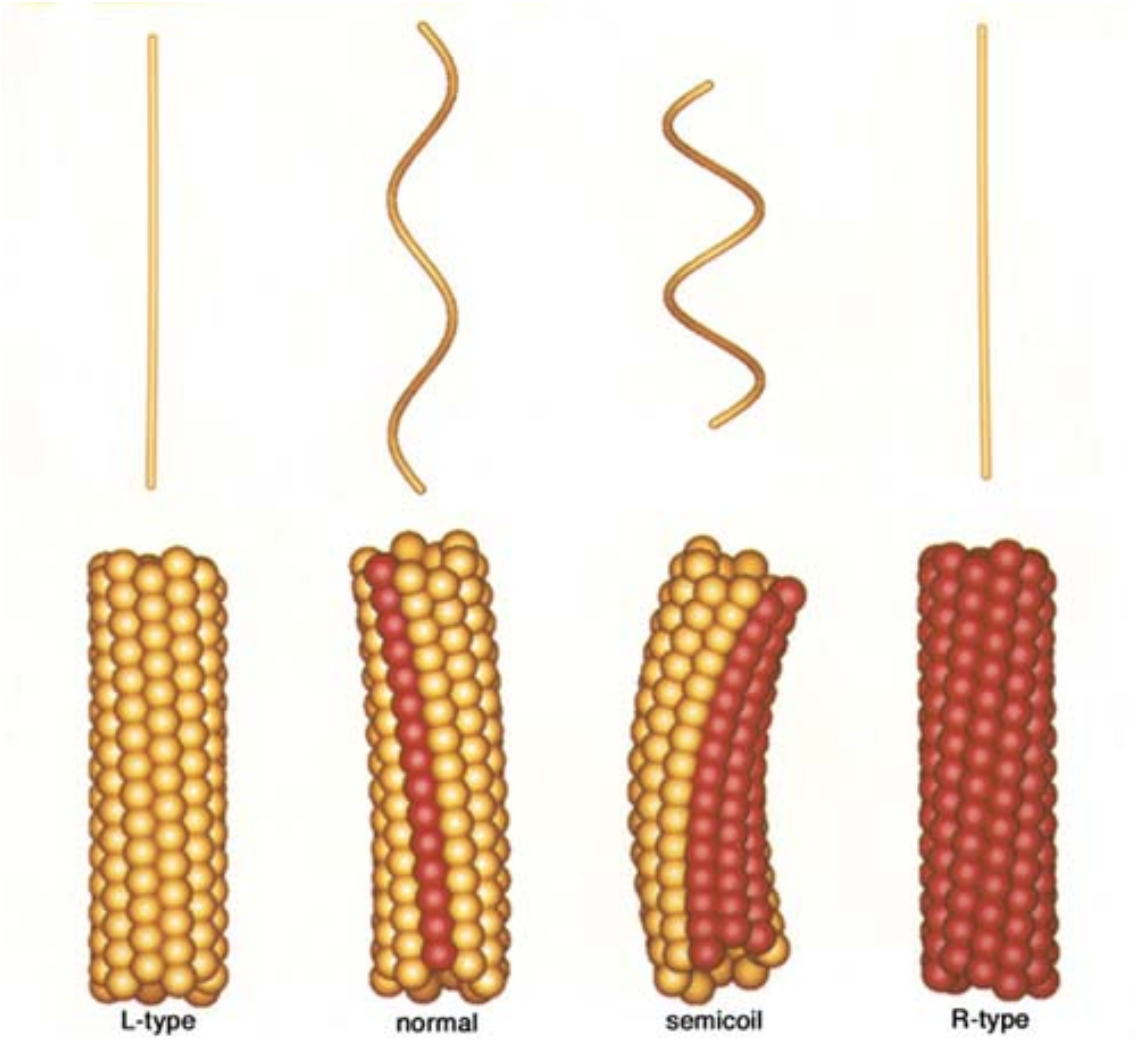

Figure 1.12: Symmetry of proto-filament structure. When all 11 proto filaments in a full turn of the flagellar helix are in the L- (long) conformation, the filament is straight, and L-type. When all 11 proto-filaments are in the R- (short) conformation, the filament is straight and R-type. When it is a mix of both L- and R- proto-filaments, then is is coiled. Figure taken from Namba and Vonderviszt (1997).

motor can be adjusted by changing the size of the bead used as the marker. Larger beads have larger drag coefficients and result in the motor rotating more slowly but driving a larger load, that is, operating with greater torque for any given speed. The drag coefficient can also be changed by varying the viscosity of the medium while observing the same bead and motor (Chen and Berg, 2000a). Torque-speed curves obtained for wild-type and chimeric motors in *E. coli* using these methods as well as electrorotation are summarized in Figure 1.13.

What can be ascertained by looking at this relationship? First the maximum speed of the motor may be determined, which is the zero-torque speed. Also the stall torque, which is the y-intercept in Figure 1.13, may be determined. The other key features of the torque-speed curve are the plateau at low speed and the steeper linear regime at high speed. Where these two regimes intersect is known as the knee of the torque-speed curve. The continuity of the plateau regime on either side of stall shows that there is no irreversible step in the mechanochemical cycle. If such a step did exist, the torque would be expected to increase sharply before the motor could be forced backwards (Berry and Berg, 1999). The plateau is a region of constant torque at high load where the motor is rate limited by the mechanical relaxation of the bead. After the knee, the torque decreases linearly to zero as the motor moves faster. At low loads the motor is rate limited by kinetic rate-constants in the mechanochemical cycle, for example the arrival, binding or transit of ions. Evidence for this is shown by the large effect of temperature and isotope substitution on the speeds at low load, compared with the small effect of these changes at high load (Chen and Berg, 2000a; Berg and Turner, 1993). At high and low loads the speed varies linearly with the proton motive force (PMF) (Gabel and Berg, 2003). Torque and speed and the characteristics of torque-speed curves are discussed further in Section 4.1. The torque speed curves for the BFM at low temperature and low stator number were measured and are discussed in Section 4.4.4.

1.5.3 Models of Torque Generation

Any model that hopes to explain the torque generating mechanism of the BFM has to be able to reproduce the observed torque-speed relation. Two models are outlined: a fully kinetic model from Berry and Berg (1999), and a reaction-diffusion model from Xing et al. (2006). Berry and Berg used a minimal 3 state kinetic model. Each step in the cycle is assigned a chemical free energy change, U_i, and also rotation of the rotor through some angle ω_i. If ϕ is the angle moved in one cycle and β_i is the fraction moved in step i, the motor performs work $W_i = \phi_i\Gamma = \beta_i\Gamma\phi$ in step i,

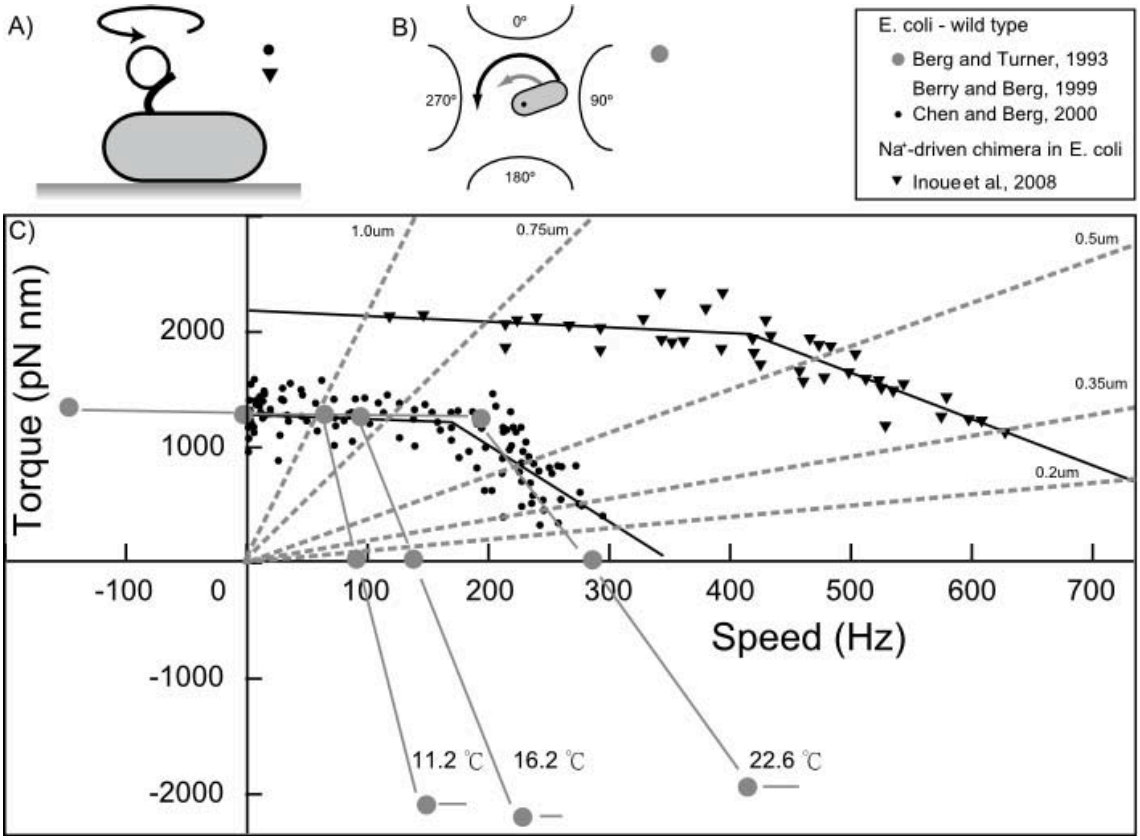

Figure 1.13: Torque-speed curves for the proton powered wild-type *E. coli* and for Na^+-driven chimera at full induction (maximum number of stators). A-B) Methods of measuring torque-speed relations. A) Beads attached to agella. The size of the bead can be changed to vary the load and thus the torque of the motor. Load lines for 6 di erent sizes of beads are shown on the plot as dashed grey lines, for beads from 2.0 m to 0.35 m. B) Electrorotation of tethered cells - microelectrodes generate a MHz rotating electric eld at the cell which applies an external torque (black arrow) that adds to the motor torque (grey arrow). In this way the torque speed relation can be explored for motors forced to rotate in reverse. C) Torque-speed relationships for agellar motors using di erent methods. The *E. coli* wild type torques are shown by black circles, the Na^+-driven chimera by black triangles, and the electrorotation torque-speed measurements are shown using grey circles. Figure from Baker and Berry (2009), using data from Sowa and Berry (2008).

where, Γ is the torque. The sum of all U_i must be equal to nq·PMF, where n is the number of protons transiting the membrane, q is the charge of a single proton, and PMF is the proton-motive force. Similarly to β_i, a second set of parameters, α_i, are defined as the fractions of the free energy from proton transit that are dissipated as heat, or used to do work, in step i, so that $U_i = \alpha_i nq$·PMF . A third parameter for each step, k_i, determines the absolute rate of each step, and rate constants are given by

$$k_{fi} = k_i \exp(\frac{U_i - W_i}{2kT}) \quad (1.6)$$

$$k_{bi} = k_i \exp(\frac{-(U_i - W_i)}{2kT}) \quad (1.7)$$

for the forwards and reverse rates of step i respectively. These expressions assume for simplicity that U_i and W_i each affect the forward and reverse rate constants symmetrically. With torque and PMF specified, solution of the coupled linear ordinary differential equations for the occupancy probabilities of each kinetic state, assuming steady state, gives the flux around the mechanochemical cycle and thus also the rotation speed. A brief exploration of the parameter space of this model is shown in Figure 1.14.

Some of the assumptions in this model are no longer valid. It assumes that either one or two protons are translocated in each mechanochemical cycle, that there are 8 stators, and each stator completes 120 cycles per revolution. Current understanding is that there are up to 11 stators (Reid et al., 2006), with each probably completing 26 cycles per revolution. However changing these values does not affect the models prediction of the shape of the torque-speed relationship. The advantage of kinetic models such as these is that they are simple and therefore fast to compute, allowing automated searching of a multi-dimensional parameter space to find good fits to the experimental data. Despite their lack of mechanical detail, kinetic models substantially constrain possible models of the motor mechanism.

Xing et al. (2006) proposed a reaction-diffusion model which was designed to ensure that motor rotation and ion transport are tightly coupled. Figure 1.15 shows energy profiles (potentials of mean force versus rotor-stator angle) for 2 states of a single model stator. Transitions between state 1 (solid lines) and state 2 (dashed lines) are coupled to the motor binding two ions from outside the cell, and are possible only at angles corresponding to the upper shaded area. Ion transit is completed by release of the two ions into the cell, which in turn is possible only at the angles indicated by the middle shaded area. The lowest shaded area shows the start of

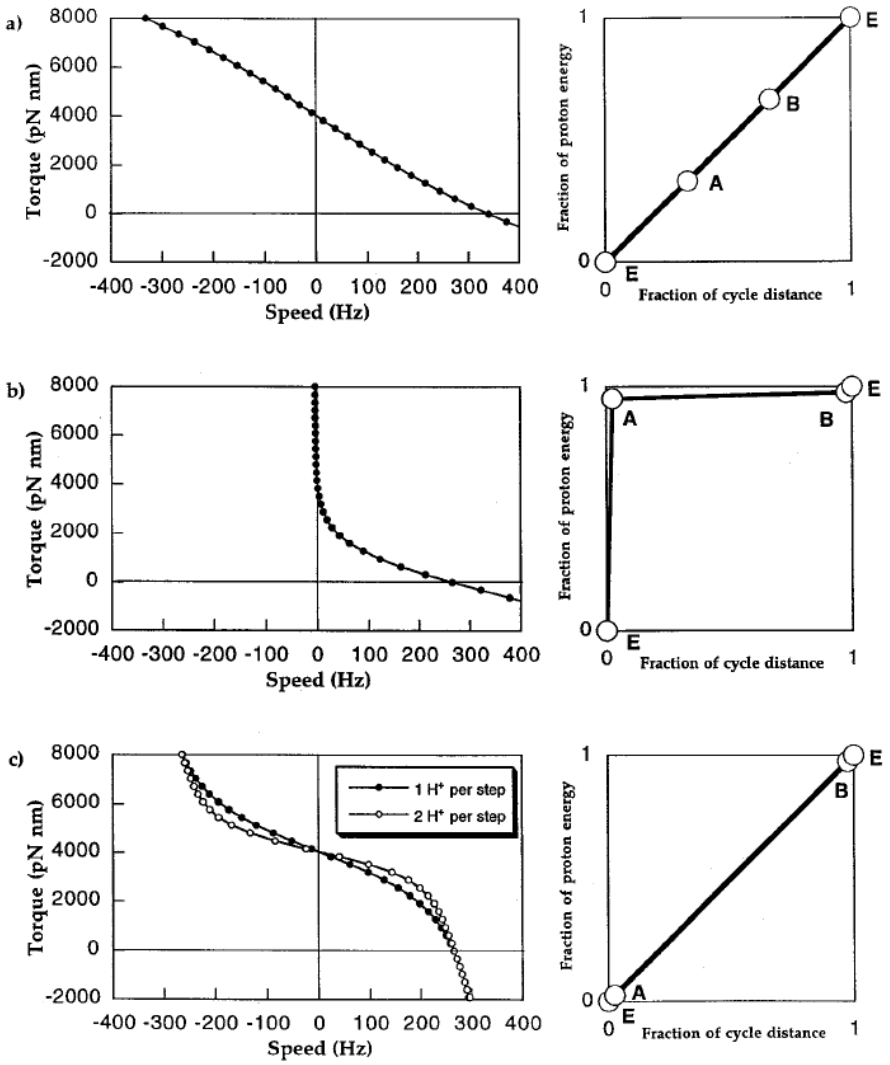

Figure 1.14: The torque-speed relationship for the kinetic model described in the text from Berry and Berg (1999). The right-hand panels are a graphical representation of the parameter sets, showing the degree to which each step of the cycle dissipates the available free energy and results in motor rotation. (a) The torque speed relation when all three steps in the cycle are equivalent, with parameters: $\alpha_1 = \alpha_2 = \alpha_3 = \beta_1 = \beta_2 = \beta_3 = 1/3$, $k_1 = k_2 = k_3 = 6 \times 10^4\ s^{-1}$. (b) The dissipation of proton free energy, and the rotation occur in nearly entirely separate steps, with parameters: $\alpha_1 = \beta_2 = 0.95, \alpha_2 = \alpha_3 = \beta_1 = \beta_3 = 0.025$, $k_1 = k_2 = k_3 = 105\ s^{-1}$. (c) If the dissipation of the proton free energy and the rotation of the rotor happen in a single step the torque-speed relation predicted by the model looks qualitatively similar to the experimentally observed torque-speed curve. Parameters: $\alpha_2 = \beta_2 = 0.95, \alpha_1 = \alpha_3 = \beta_1 = \beta_3 = 0.025$, $k_1 = k_2 = k_3 = 105\ s^{-1}$ (closed circles); $k_1 = k_2 = k_3 = 4.2 \times 104\ s^{-1}$(open circles). From Berry and Berg (1999).

the next cycle of the motor. The linear sections of the energy profiles are chosen to produce constant torque in the plateau region. The peaks in the profiles were found to be necessary to prevent slipping, for example when the system moves over the top of a tooth in a single potential, leading to rotation un-coupled from the chemical state transition. The coupling to two ions at a time was introduced to ensure that enough free energy is available in a single step of 1/26 of a revolution to generate the measured torque of the motor at low speeds. This point is discussed in more detail in Section 1.5.5. Otherwise, the 2-state kinetic cycle and the potentials were chosen to be as simple as possible, reflecting the limited structural and kinetic data available to constrain the model. The angle θ of the rotor relative to a single stator obeys the Langevin equation (Langevin, 1905):

$$\zeta_M \frac{\mathrm{d}\theta}{\mathrm{d}t} = -\frac{\partial}{\partial\theta} V_M(\theta, s) - \kappa(\theta - \theta_L) + [2k_B T \zeta_M]^{1/2} f_M(t) \tag{1.8}$$

where ζ_M is the drag coefficient of the rotor, V_M is the energy potential of mean force along the minimum energy path described as a function of θ, s is a binary variable describing the state of the stator, κ is the spring constant of the link to the bead and θ_L is the angle of the bead. The last term is the stochastic Brownian force acting on the stator, where $f_M(t)$ is uncorrelated white noise. The slope of V_M determines the force profile the stator exerts on the rotor. Motors with multiple stators are modeled by replacing V_M with a potential which is the sum of the potentials from all stators. A similar Langevin equation describes the motion of the bead, but without the V_M term (Xing et al., 2006).

Numerical analysis and simulations of this model confirmed that for a motor dragging a large load, there is a time scale separation between the motor and the load dynamics, in addition to the a priori assumed time scale separation between the motion of the rotor and the chemical transition time. The soft linker allows the motor to work against an approximately constant conservative torque. For large loads, this torque slows the rotor to the point where chemical transitions are almost certain to occur before the rotor has moved beyond the low-angle part of the allowed transition zone in Figure 1.15, where the torque is constant. This produces the plateau region of the torque-speed curve. By contrast, for small loads the bead relaxes much faster and there is a significant probability that the rotor will reach the minimum of an energy profile before a chemical transition takes the system to the next state. Since the average torque at the minimum is zero, this produces steeply decreasing motor torque as the load is decreased and the speed

approaches the zero-load speed. The success of this model consists in explaining the experimentally observed sharp transition between these two regimes at the knee, as shown in Figure 1.16.

Xing et. al. revisited this model in 2009 (Bai et al., 2009). They added compliant springs linking the stators to the cell wall, to explain the most recent results from Yuan and Berg (2008). The original model predicted that the zero-load speed would actually decrease with increasing number of stators, as co-ordinated transitions in all stators were required for the rotor to rotate. Yuan and Berg (2008) found a lack of dependence of zero-torque speed on stator number, which implies that competing stators do not impede each others' interaction with the rotor. Stator springs allow each stator to step independently, storing energy in stretching its own spring, rather than requiring the rotor-stator angles of all stators to change in synchrony. The stator-spring model can also reproduce the experimentally observed stepping behaviour, and was used to predict dwell time distributions between steps as well as a variety of possible dependences of stepping patterns upon the number and relative anchorage points of separate stators.

1.5.4 Energetics

The wild-type BFMs of *E. coli* and many other species are powered by H^+ ions (protons) (Sowa and Berry, 2008). Several other species, including the marine bacterium *V. alginolyticus*, have BFMs powered by Na^+ ions (Yorimitsu and Homma, 2001). The stator proteins in the Na^+-driven motor of *V. alginolyticus* are called PomA and PomB, and are structurally similar to MotA and MotB from *E. coli*. Based on this similarity, a chimeric fusion protein known as PotB, combining parts of PomB and MotB, was made by Asai et al. (2003), and combined with PomA to make a Na+ driven chimeric motor that works in E. Coli. The sodium-motive force (SMF) of *E. coli* can be changed without drastically affecting cell function, unlike the protonmotive force (PMF) which is closely regulated and linked to pH. Extremes of pH change the charge state of ionizable groups on the surface of proteins, and therefore usually have severe effects on protein folding and function. Controlling the SMF in cells with chimeric motors has allowed the dependence of the BFM on each component of the IMF to be explored. In order to control the SMF for experiments on the chimeric motor, fluorescence microscopy methods were developed to measure either the internal sodium concentration or the membrane voltage in single, live, E. coli cells (Lo et al., 2007). Lo et al. (2007) found the following dependence of membrane voltage and the sodium chemical potential in cells with chimeric motors,

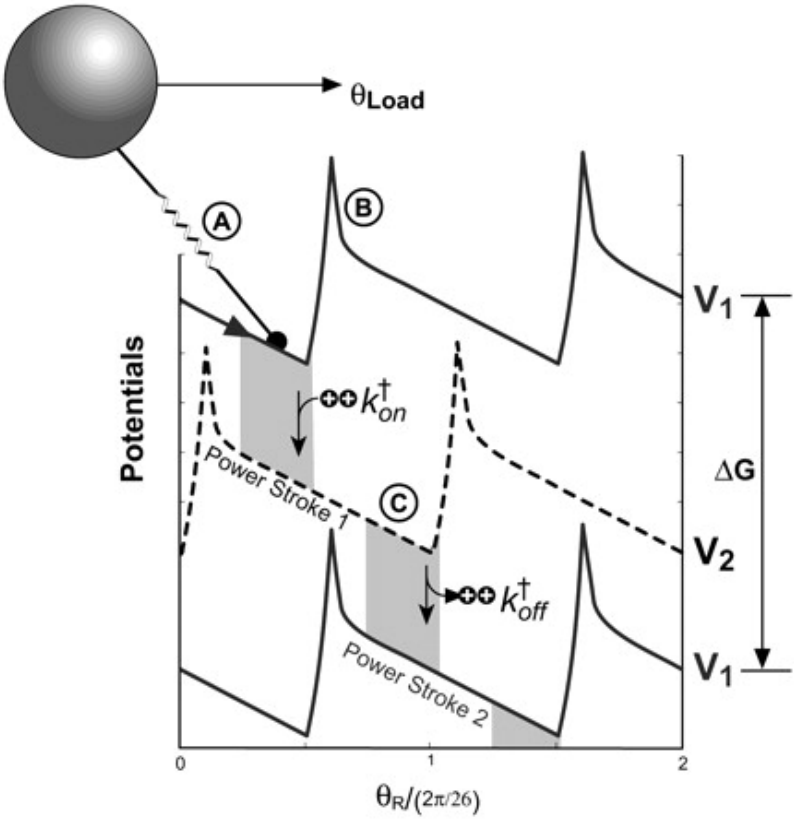

Figure 1.15: The Brownian Dynamics model of Xing et al. (2006). The energy potentials in each of 2 chemical states of a single stator are modelled as identical periodic piecewise linear functions o set by half a period. The 26-fold periodicity re ects the structure of the FliG ring in the rotor and the observation of 26 steps per revolution. Each transition between the two potentials initiates a power stroke, which is modelled as a constant torque. The soft linker between the rotor and the load is indicated by the spring, A. The sharp peaks in the potential labelled B prevent thermal uctuations from causing back-steps that are uncoupled from the chemical transitions, thus ensuring tight coupling between rotation and proton ux. Each motor cycle transports two ions from periplasm to cytoplasm, which decreases the free energy of the system by $2q$ PMF and advances the rotor by 2χ 26. The (shaded) transition regions specify the positions where the transitions between the potentials can take place. Figure reproduced from Baker and Berry (2009).

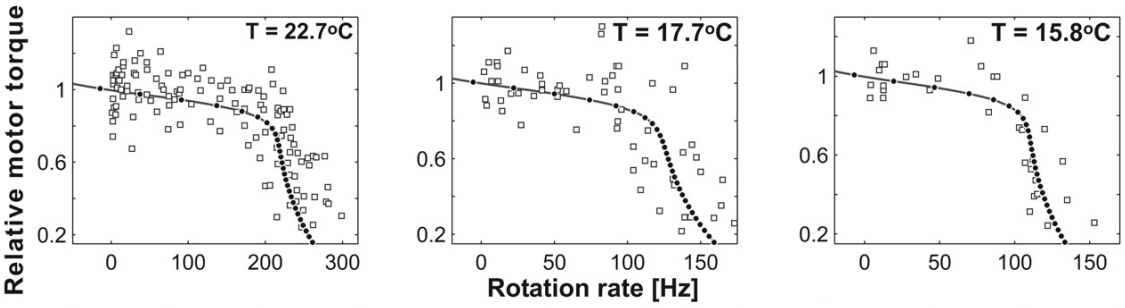

Figure 1.16: Figure 10. Comparison of model predictions from Xing et al. (2006) (dots and lines) with experimental data (squares), for torque speed curves at di erent temperatures. Figure reproduced from Baker and Berry (2009).

according to the pH and $[Na^+]$ of the surrounding solution:

$$V_m(\text{mV}^{\ 1}) \qquad 57 \quad 28\ \text{pH} \tag{1.9}$$

$$q(\text{mV}^{\ 1}) \qquad 5 + 5\ \text{pH} \quad 47 \log_{10}[Na^+] \tag{1.10}$$

where pH and $[Na^+]$ are the pH and sodium concentration in mM of the medium surrounding the cell respectively. Thus to a reasonable approximation the membrane voltage depends on pH, but not $[Na^+]$, and the chemical potential depends on $[Na^+]$ but not on pH. This allows independent control of the two components of SMF. The chimeric motor rotated stably for all combinations of pH between 5 and 7 (corresponding to Vm between -80 mV and -140 mV) and $[Na^+]$ between 1 and 85 mM (corresponding to q between +30 mV and -50 mV). Membrane voltage and its dependence on temperature will be discussed further in Chapter 5.

1.5.5 Stepping

Molecular motors operate on periodic tracks and with periodic chemical cycles. The consumption of a discrete number of fuel molecules per cycle, and the repetition of a track unit implies that at some fundamental level there are discrete mechanical steps where torque or force generation occurs. This quantized movement can be used to obtain a more detailed picture of the motor mechanism. For example, kinesin was rst observed to step by Svoboda et al. (1993). This was the rst observation of discretised molecular motion and they saw 8 nm steps corresponding to the 8 nm ϕ- -tubulin structural repeat of the microtubule track. Further experiments con rmed that each step uses one molecule of ATP (Schnitzer et al., 2000). Rotational motion of F1-ATPase was rst observed by Noji et al. (1997). The 3-fold symmetry of the

track, with three pairs of α and β subunits arranged in a hexagon, was reflected by the presence of 3 steps per revolution. This was followed Yasuda et al. (2001) discovering substeps within this rotation of 80° and 40°. From an analysis of these substeps and adjusting the ATP concentration they were able to determine which substeps corresponded to which parts of the chemical cycle. The 80° substep was driven by ATP binding and the 40° substep by release of hydrolysis products.

For the BFM, the ∼26-fold periodicity of the FliG ring in the rotor (Thomas et al., 2006) implies a discrete torque generating step at the heart of motor function. The first evidence for a stepping mechanism was found by Samuel and Berg (1995). They performed a fluctuation analysis which observed a quadratic relationship between the mean and variance of rotation speeds, a predicted result for any mechanism involving a Poisson stepper with exponentially distributed dwell times. In a further analysis of variance and speed they predicted 50 steps per revolution per stator (Samuel and Berg, 1996).

Due to the high speed rotation of the BFM under standard biological conditions only recently has sufficient experimental resolution been available to observe stepping in the BFM. The smoothing of the signal by the hook means that the intervals between steps must be larger that the relaxation time of the bead if steps are to be seen. The drag coefficient can be reduced as discussed earlier by using smaller beads, but this leads to faster rotation, and thus requires greater time resolution. The spring constant of the hook has been measured by Block et al. (1989) to be ∼400 pN nm rad^{-2} and the subsequent damping of the bead motion is equal to the viscous drag on the bead divided by the spring constant of the hook. Effectively this means that for 0.5 μm beads the rotation speed needs to be less than 12 Hz for the steps to be observable using the back focal plane interferometry technique, and standard bead assay, described in Section 2.3.

Sowa et al. (2005) first observed steps in the BFM. Sodium driven chimeric motors in *E. coli* were kept at low stator number by controlling the amount of stator protein made in the cells, and the SMF was reduced so that the speed of the motor was kept below 10 Hz, enabling discrete steps to be observed as shown in Figure 1.17. The steps were measured using two different methods. The first method was using a laser focused on a 500 nm polystyrene particle attached to a truncated filament as in the standard bead assay (see Section 1.7). In this case, the SMF was reduced by lowering the external sodium concentration to 0.1 mM, although at the time the relationship between SMF and sodium concentration was not known. The second method was using high-speed video of 200 nm fluorescent

beads attached to rotating truncated filaments. In this case, cells were illuminated with a high-intensity mercury arc lamp at 475 nm-bandpass, which was thought to reduce the membrane voltage, and thus the SMF, by unspecified mechanisms of photodamage.

Both methods showed 26 steps per revolution, and a corresponding step size of 13.8°, in agreement with the periodicity of the ring of FliG in the rotor. If steps of 13.8° are the smallest unit of movement in the BFM then using energy balance it should be possible to calculate the number of ion transits that correspond to a step. The stall torque for the chimera sets an upper bound to the step size per single ion transit. Under standard conditions ($[Na^+]_{ex}$ = 85 mM and pH 7) SMF is -150 mV and the average torque per stator unit is 150 pNnm to rotate a 1 μm bead (Lo et al., 2007). From this the upper bound to step size can be calculated to be 10° per step, or 36 ions per revolution. This corresponds to the 35-fold symmetry of the C ring, but implies that each step at high load, if tightly coupled, requires more than one ion transit, but less than two. The problem of dividing 38 ions into 26 steps, while retaining tight coupling, requires new models and further measurements of the energy in different conditions. Two possibilities are immediately apparent: either the motor is tight coupled and the stall-torque estimation is incorrect, or rotation is not tightly coupled to proton translocation and the model of Xing et al. (2006), with 2 ions per step, must be altered to include slipping. Additional drastic possibilities, such as that the mechanochemical cycle and the observed steps are not equivalent would also explain this, but this would require several elastic links between the site of torque generation and another site with a 26-fold interaction that produces the observed steps (Baker and Berry, 2009).

The original motivation for exploring temperature control and the cooling of the BFM was to slow rotation to aid step measurement and analysis. In order to do this it was first necessary to characterise the kinetic and energetic response of the motor with temperature, as has been done in this thesis. The steps measured by Sowa et al. (2005) were measured in under-energised motors or in light damaged motors, because fully energised motors rotated too quickly to discern individual steps. Thus cooling was proposed as one mechanism to slow rotation in order to measure steps, but have the motor operating at full energisation, and with multiple stators driving rotation. Currently our group has developed a new dark field microscope, not discussed here, that is capable of measuring low loads (40 nm gold beads) stepping in fully energised motors rotating at 100 Hz. However multiple stator motors are still beyond our current step resolution, so temperature control, specifically cooling,

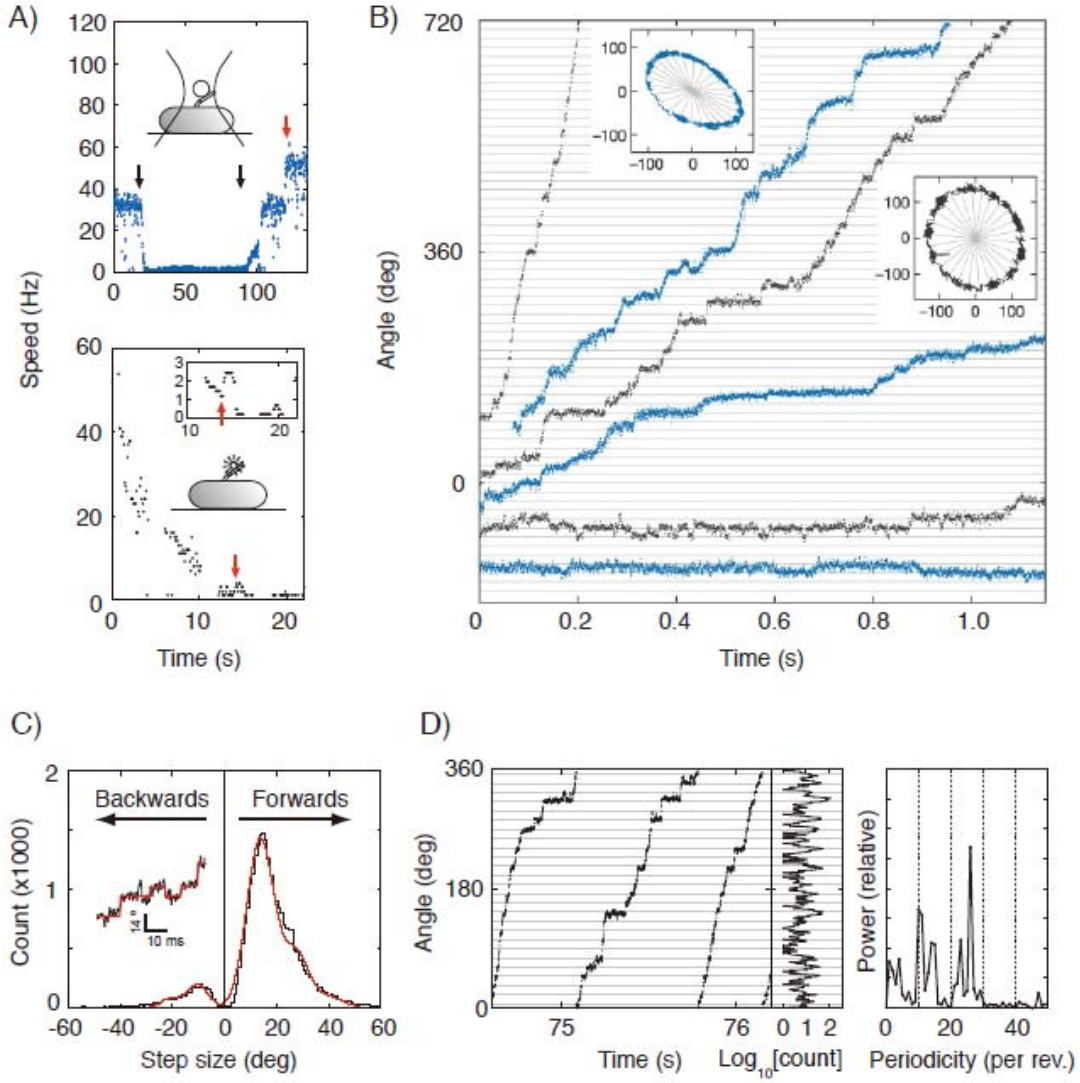

Figure 1.17: Figure 11. Steps in slow flagellar rotation. A) Reducing SMF and motor speed of a chimeric Na^+-driven flagellar motor in E. coli; upper: by lowering external sodium concentration (5 mM to 0.1 mM and back, black arrows) and lower: by photodamage. The speed doublings marked by red arrows indicate a change from one to two stators. B) Stepping rotation of flagellar motors with a range of average speeds depending on different SMF. Insets show the positions of beads attached to flagellar filaments, scales in nanometres. Horizontal and radial lines indicate 1/26 rev. C) Step size distribution (black) with multiple Gaussian fit (red). The peak of forwards steps is 13.7°C, indicating 26 steps per revolution. An example of steps identified by a step-finding algorithm is shown (inset). D) Plot of angle against time during three revolutions, a histogram of dwell angles for the same revolutions and the power spectrum of that histogram. The peak at 26 per revolution corresponds to a step size of 13.8°, and shows that the motor stops at the same angles on successive revolutions. Speeds shown in black were measured using optical interferometry, those in blue using high-speed fluorescence microscopy (insets in A). Figure taken from Sowa et al. (2005) and caption reproduced from Baker and Berry (2009).

may make multiple stator step measurements accessible.

1.6 Bacteria: *E. coli* and its Environment

1.6.1 Bacteria as swimmers - Low Reynolds Number

The swimming environment faced by a bacterium is significantly different that of common experience. A bacterium is small, and thus the viscous forces felt by a swimming bacterium are large in comparison to the inertial forces acting on it. One characteristic which defines the comparative strength of viscous and inertial forces is the Reynolds Number (Reynolds, 1883).

$$R = \frac{av\rho}{\eta} = \frac{av}{\nu}, \tag{1.11}$$

where a is the characteristic length, the radius for a sphere or approximately spherical bacterium, v is the velocity of the solution relative to the particle, ρ is the density of the surrounding solution, η is the dynamic viscosity and ν is the kinematic viscosity, where $\nu = \eta/\rho$.

When the viscous forces dominate, the Reynolds number is small, and when the inertial forces dominate, the Reynolds number is large. Bacteria encounter a vastly different swimming environment than that which we are accustomed to, due to the small size of a in comparison to a human swimmer, or most fish. A man swimming in the ocean has a Reynolds number of 10^4, whereas a micron size bacterium has a Reynolds number of 10^{-4}. If you are at the beach, and stop swimming suddenly, inertial forces dominate and you will coast to a stop over a bodylength or so. A cell swimming at 30 μm/s on the other hand is completely dominated by viscous forces, and will coast to a stop in a distance of 0.01 nm (a fraction of a hydrogen atom) over 0.6 μs (Purcell, 1977).

Because the viscous forces dominate over these length scales, traditional notions of how to swim also do not apply. If you were in a rowboat, and stuck your oars underwater and moved them slowly in one direction, while underwater, and then fast in the opposite direction, also underwater, eventually you would move away from your fast stroke, although not very efficiently (a coach at this point might advise you to lift your oars out of the water in between strokes). However if you were in a micron-size rowboat, and tried the same, you would not move anywhere at all. At low Reynolds number fixed reciprocal motion does not generate propulsion. This is because the slowness or fastness of your stroke, in fact any time dependence, is

not relevant. What is instead necessary is a change in shape over a non-reciprocal path. Consider the Navier Stokes equation (for an incompressible fluid) (Stokes, 1842, 1847):

$$-\nabla p + \eta \nabla^2 \mathbf{v} = \rho \frac{\partial \mathbf{v}}{\partial t} + \rho(\mathbf{v} \cdot \nabla)\mathbf{v} \tag{1.12}$$

where η is the viscosity, p the pressure, $\mathbf{v}$, the velocity and ρ the density of the fluid.

Consider an l^3 parcel of fluid flowing past a spherical obstruction, of radius r. The velocity, $\mathbf{v}$, must change direction in time $\Delta t \approx r/v$ in order to flow around the sphere, and this change in velocity, $\partial \mathbf{v}/\partial t \approx v^2/r$. (Nelson, 2004). Similarly, $(\mathbf{v} \cdot \nabla)\mathbf{v} \approx v^2/r$, since $\nabla \mathbf{v} \approx v/r$. Multiplying both sides of the equation by $r^2/\eta v$ yields:

$$-\nabla p \frac{r^2}{\eta v} + \frac{r^2}{v}\nabla^2 v \approx \frac{r^2}{\eta v}\left(\frac{\rho v^2}{r} + \frac{\rho v^2}{r}\right) = \frac{2\rho v r}{\eta} = \mathrm{Re} \approx 0 \tag{1.13}$$

when Re is very small. Thus the inertial terms are irrelevant, and so is any history with regard to propulsion. The only factor that determines how fast you are moving is how hard you are pushing at that exact moment.

In a time-invariant low Reynolds number environment, what kind of swimmer actually *can* swim? Any motion that is periodic, but is not strictly reciprocating, that is, it operates around a cycle in which the forwards and the reverse motion are distinguishable, will swim at low Reynolds number. The simplest example of this is a 'Swiss army knife' swimmer, which has two hinges, as shown in Figure 1.18, which shows a single rower, with a hinged oar, that can proceed along its path in such a way as to separate forwards and reverse action, and swim.

The extended analogy of this two-hinge oar is a flexible oar, with a near-infinite number of hinges. If the microscopic rower had a flexible oar, so that it could bend in one direction on one stroke, and the opposite direction on the way back, then the reciprocal symmetry would be broken and the rower could propel himself in one direction. This flexible oar is similar to how sperm swim, by oscillating their tails through co-ordinated dynein contractions, and is also similar to ciliary propulsion in cells (Riedel-Kruse et al., 2007; Nelson, 2004).

Bacteria propel themselves at low Reynolds number by rotating a helical corkscrew about its axis. This is a periodic motion that is non-reciprocal, where all the x,y components cancel due to the axial symmetry of the helix, and the net propulsion is along the helix axis, away from the filament. Additionally there is a counter rotation of the body of the cell. The filament is not exactly a rigid helical coil in *E.*

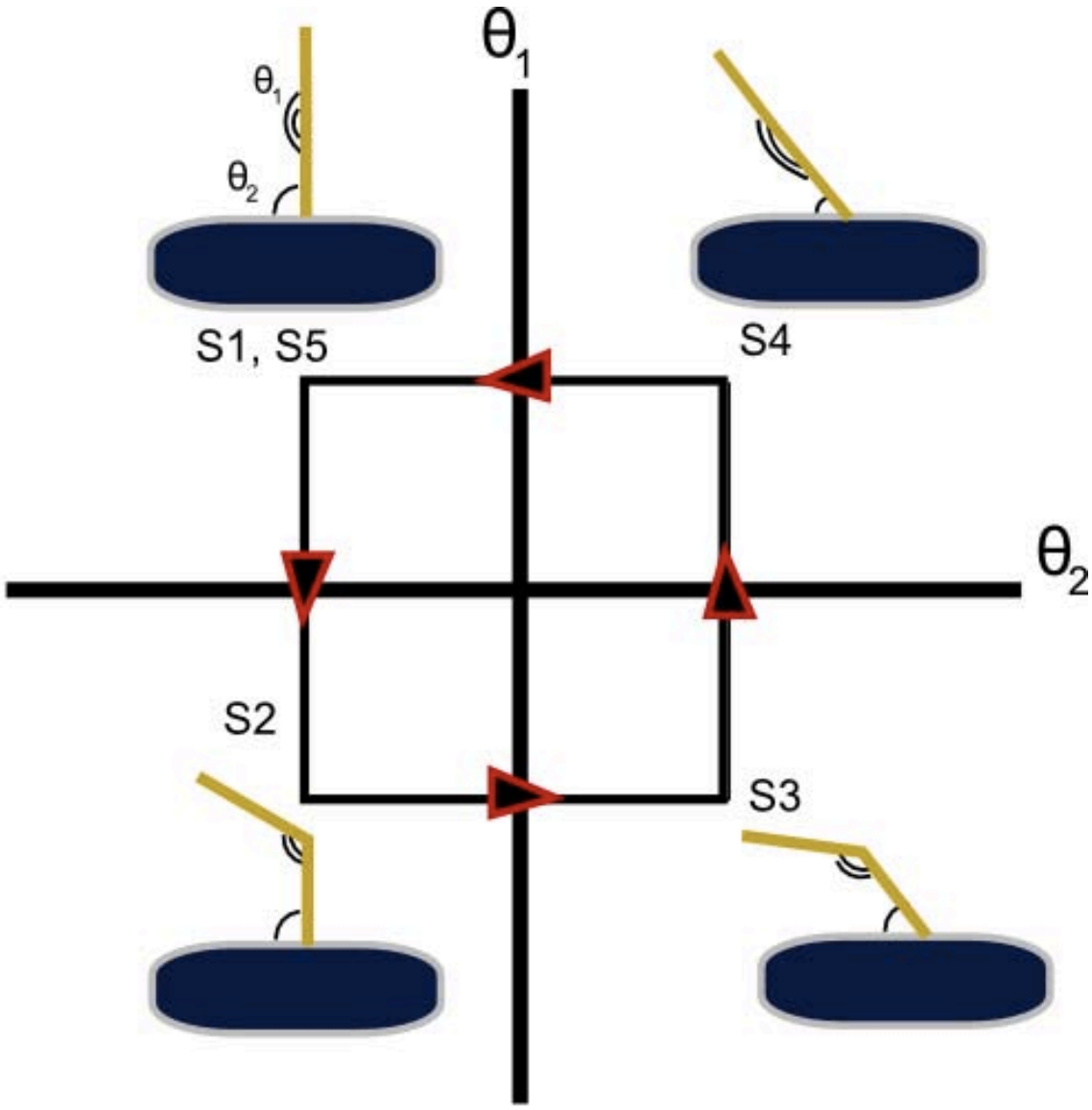

Figure 1.18: The Swiss army knife swimmer. The swimmer starts in S_1, with the both hinges pointing straight out of the body of the swimmer, that is, $\tau_1 = \chi\ 2$ and $\tau_2 = \chi\ 4$. The rst hinge then bends so that $\tau_1 < \chi\ 2$, and the swimmer is in state S_2. Subsequently hinge 2 moves so that $\tau_2 < \chi\ 4$, taking the swimmer to S_3, then hinge 1 straightens so that $\tau_1 = \chi\ 2$, S_4, then nally hinge 2 straightens so that $\tau_2 = \chi\ 2$ and the swimmer is in $S_5 = S_1$. It is evident that moving in reverse is distinguishable from operating forwards, and this is enough to cause non reciprocal periodic motion which can propel the swimmer at low Reynolds number.

coli, it is in fact a peritrichous bundle of many filaments but the effective propulsion is the same. This has been shown by considering large-scale helices spinning in a viscous solution of oil, and tracking the viscous flow around the helix bundle (Kim et al., 2004). Experimental verification of the translational and angular momentum during flagellar rotation has been performed using optical traps (see Section 1.7.1. Chattopadhyay et al. (2006) measured the force necessary to hold a bacterium in a trap and thus determine the propulsion matrix relating the translational and angular momentum of the flagellar to the torques and forces propelling the bacterium using an optical trap at the tail of the cell (closest to the filament) and the nose of the cell (furthest from the filament). This is depicted in Figure 1.19.

1.6.2 Diffusion

Bacteria bias their motion to move towards regions of higher nutrient concentration. In a low Reynolds regime it is not easy to change your environment, as you drag it along with you when you swim. Transport in this regime is measured against diffusion. In order for bacteria to benefit from swimming they must outrun diffusion to a region of higher nutrient concentration. Bacteria can swim in a straight line for only a few seconds, before Brownian motion re-orients them randomly. A typical nutrient molecule has a diffusion coefficient of $\sim$400 μm^{2}s^{-1} which means that diffusion will carry nutrients $\sim$ 70 μm in 2 s. Typical swimming speeds are in the range 40-60 μm s^{-1} so swimming driven by the flagellar motor does indeed help, but only just. Bacteria stay swimming straight as long as they are moving up a concentration gradient of nutrient. When the chemotactic signalling pathway indicates that this is no longer true, a switch is induced in the motor which causes a tumble, or a random reorientation of the cell. The distribution of durations of runs and tumbles in live swimming cells are discussed in Min et al. (2009) and an allosteric model for switching is discussed thoroughly in Bai et al. (2010).

1.6.3 Bacteria and Humans

The popular notion of bacteria evokes illness and disease. There do exist enterotoxic and pathogenic types of bacteria but human contact with bacteria is not always detrimental to our health. There are roughly ten times more bacterial cells on the surface of and inside the human body than there are human cells (Eckburg et al., 2005). From birth we are assisted by facultative anaerobic bacteria like *E. coli* which we can obtain from our mother's faeces, or from skin contact with our parents and

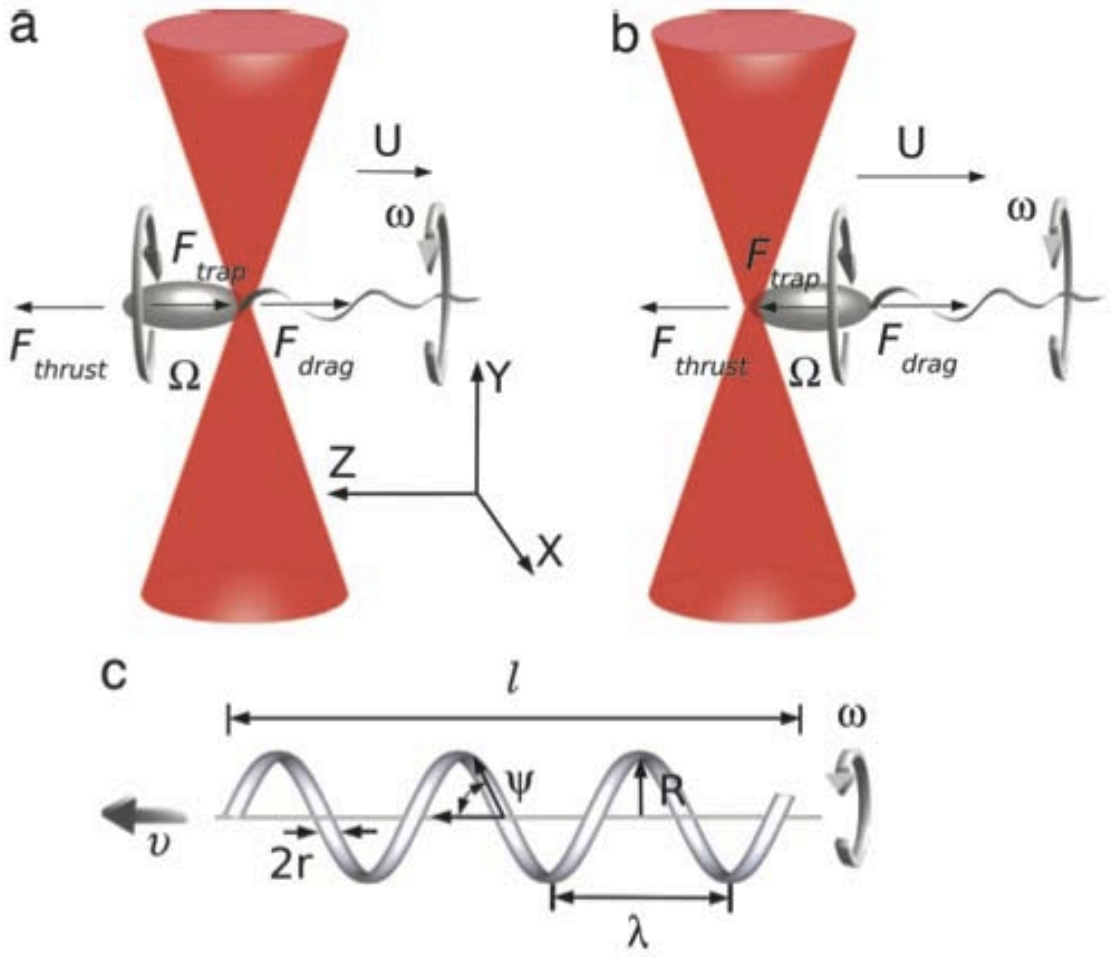

Figure 1.19: Figure showing the experimental model of Chattopadhyay et al. (2006). Bacterium trapped at tail (a) and nose (b), showing the di ering rotational directions of the body ( ) and the lament ( ). The thrust, F_{thrust} and the drag, F_{drag} can be measured by the optical trap and the change in these measurements with respect to the controlled ow of solution, U, can be used to determine the propulsive e ciency. c) Schematic of the left-handed helical propellor of the bacterial lament. The helix has radius R, pitch and length l, and the lament has radius r. The helix rotates around its axis with angular frequency and the resulting propulsive force is to the left, v. From Chattopadhyay et al. (2006).

nurses. Within 1 month the intestinal flora are well established and by the age of 2 years the intestinal flora is similar to that of an adult. Bacteria have a significant role in the gut, where they break down potential carcinogens and contribute to immunity by training the immune system to respond only to pathogens. This in turn favours the bacteria as it promotes the survival of *E. coli* (Eckburg et al., 2005).

Some strains of bacteria are indeed toxic. In the case of *E. coli* one particular strain, O157:H7 is an enterotoxic strain of *E. coli* with an inherited shigella-like toxin which causes haemhorragic diarrhoea leading to death. In the last year in the UK alone there were 2 separate instances of serious O157:H7 infection resulting in renal failure and unconsciousness but not death. The first case was caused by lack of food hygiene in the town of Llay near Wrexham in Wales, and the second by animal contact with a pig at a touch farm in South England (Melkle, 2009; Gammell, 2009).

1.7 Microscopy Techniques for Single Molecule Nanometry

To understand the mechanism of the Bacterial Flagellar Motor (BFM) we need to measure its motion. We want to use information about the torque and speed of the motor to reconstruct attributes such as energy profiles and state transitions so that we may examine the underlying torque-generating mechanism. To do this we need to be able to measure with high precision the position of and torque applied to the rotor. This is an example of single molecule biophysics. Although the BFM contains hundreds of thousands of atoms, the label single molecule is still applied to experimental measurements of single BFMs; partly because the experimental and theoretical techniques are the same as those used on smaller molecular motors, and partly because the atomic precision of protein structures distinguishes even a large protein complex like the BFM from objects made of bulk materials, in which the exact position of individual atoms is neither specified nor important.

How can the rotation of a single BFM be measured? The main techniques for imaging objects on the nanometre length-scale, electron microscopy and X-ray crystallography, both require dead samples, so neither is appropriate for live recording of any molecular motor. Atomic Force Microscopy (AFM) is promising, but molecular motor studies to date using AFM have been limited to purified motors isolated on flat surfaces, and it may be a long time, if ever, before AFM develops to the point where it can be used to monitor the BFM in live cells. This leaves light microscopy. The motor itself is too small to observe in visible light, and so a visible marker

must be attached to a part of the motor that rotates. The earliest demonstration of BFM rotation was achieved using tethered cells by Silverman and Simon (1974). In order to control for possible rotation caused by other motors on the cell, non-motile cells with no filaments (*hag* deletion) and with long polyhooks (*FlaE* deletion) were fixed to a glass microscope coverslip using polyhook antibodies and these cells were observed to rotate around the fixed tethers. This demonstrated that the motion of the BFM was rotational, not oscillatory. The marker attached to the rotor in this case was the micron sized cell body of *E. coli* itself, easily observable with video microscopy. In the standard modern version of this experiment, known as a bead assay, a polystyrene bead is attached to a truncated filament of a cell body fixed to the surface of a coverslip. The bead can be varied in size and each size has a well-defined viscous drag-coefficient. The rotation of the marker can be detected by many methods. The most straightforward is to image it using dark-field or bright-field microscopy with a fast camera, and track its rotation in recorded video. Subsequently software can be used to track the motion of the bead. The Rayleigh criterion (or other similar criteria) for optical resolution is not relevant here since we are trying to determine the position of the image of a single object, not to resolve the separation of two separate objects. By fitting the image to a 2-D Gaussian or other empirical function, offsets in the centre of this function can be determined with arbitrary accuracy, depending only on the number of photons collected to form the image (which in turn determines the precision of the fit). The slower and brighter the object being tracked, the greater the position sensitivity. For example, single fluorescent molecules are typically tracked with frame rates on the order of 1 s^{-1} and corresponding spatial precision of $\sim$1 nm. Brighter objects can be tracked with more temporal and spatial resolution, and a trade-off always exists between faster frame rates and better spatial resolution in each frame. A less computationally intensive method, and the standard method used in this thesis, is to detect the rotation of the bead by using an optical trap, invented by Ashkin et al. (1986).

1.7.1 Optical Trapping

An optical trap uses light with a Gaussian intensity profile passing through a bead of higher refractive index than its surroundings to form an harmonic potential and exert force on the bead. Rather than using a strong laser and an optical trap to exert and measure force, a weak laser is focused on the bead for position detection. Any small change in the position of the bead is measured by an associated intensity

shift of the laser light in the back focal plane by a quadrant photodiode, which is a set of four photodiodes arranged in a quadrant to track two-dimensional movements. A schematic of the apparatus used in this thesis is shown in Figure 1.20.

The invention of optical trapping allowed researchers to probe piconewton forces across nanometres. This made it possible to perform single molecule measurements on molecular motors at energies around their level of operation. Spatial resolution of bead displacement is limited by the width of the beam waist in the specimen plane which is related to the wavelength of the laser light or, for an overfilled objective, the aperture of the objective. For small beads of diameter d, and for displacements much smaller than the laser focus, the response of the quadrant photo-diode (QPD) was experimentally verified to be proportional to $(d/\omega_0)^3$ by Gittes and Schmidt (1998). In the case of the experiments in this thesis this allows measurement of beads from as small as 200 nm up to as large as 2000 nm using a 633 nm HeNe laser and a 1064 nm Nd:YAG laser with a 100× immersion-oil objective with NA 1.30. By altering the size of the bead, the drag can be reduced and thus the performance of the BFM under different torque regimes can be explored.

Observations of the motor are limited by the use of a comparatively large marker (BFM diameter is 40 nm in comparison with a 500 nm bead). For a motor rotating a large bead there is a time scale separation between the motor and the load. This separation of timing scales yields very high Stokes efficiency, a thermodynamic measure of how efficiently a molecular motor, operating in viscous environment, can utilize free energy to drive its load (Wang and Oster, 2002; Bustamante et al., 2001). A thermodynamic efficiency of 100% is approached as the motor rotates infinitesimally slowly (ie reversibly). A large bead and a soft linker satisfies this criterion, even at speeds up to 100 Hz, because the bead motion is much slower than the internal dynamics of the motor. The elastic linker of the hook is soft enough to allow the rotor to fluctuate over several steps before the load moves noticeably and similarly work done to stretch the linker can be returned to the motor before it is dissipated by moving the load. Thus the hook effectively smooths the discrete stepped motion of the rotor. At high speed and low load, the tension between the load and motor relaxes faster, and the motor works against a smaller elastic load. This smoothing decreases along with the load, and so small loads allow us to look more closely at the rotor's motion. The change in response time for different size loads is shown in Figure 1.21.

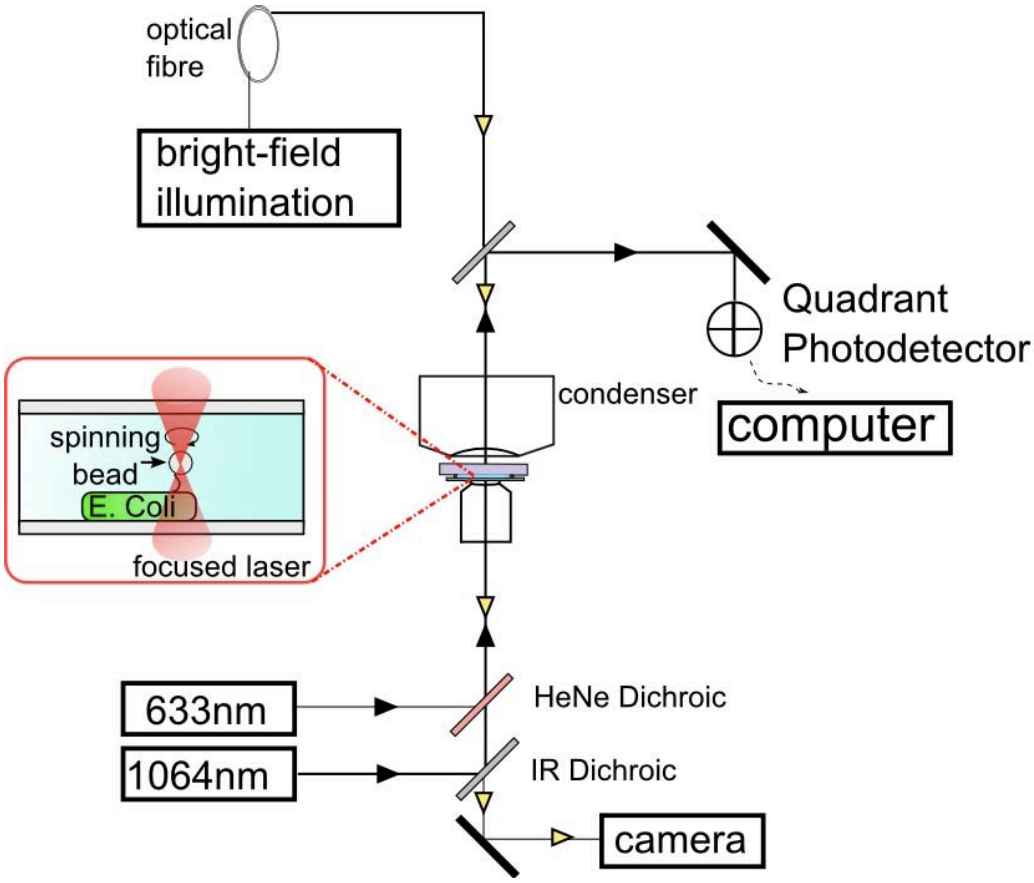

Figure 1.20: Schematic of a dual optical trap apparatus applied to a bead assay. The polystyrene bead is attached to a lament stub of an *E. coli* cell xed to the surface of a coverslip by owing a solution of beads over a surface covered in cell bodies. The excess beads are washed out and the slide is sealed and placed on a microscope. The spinning beads can be seen on a camera which images the image plane, and their position can be resolved to high precision by looking at the change in scattering with displacement in x-direction and y-direction measured by a quadrant photodiode in the back focal plane. This microscope has two optical traps so that lasers of di erent wavelengths can be used to track beads of di erent sizes, and, for experiments involving stage feedback, tracking a bead xed to the surface to counter drift. A more detailed schematic of the optical trap used in this thesis is shown in Figure 2.3.

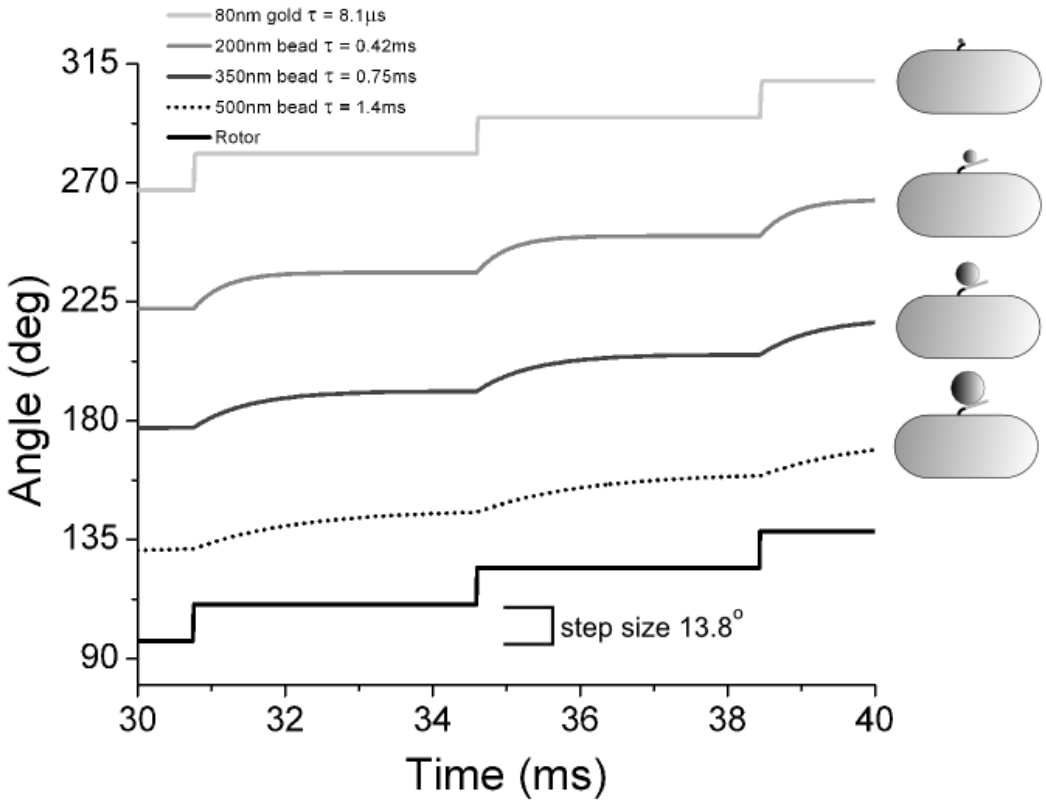

Figure 1.21: Di erence in response time for di erent size loads. Four di erent loads are shown (top to bottom); 80 nm gold beads attached directly onto the hook, 200 nm, 350 nm, and 500 nm polystyrene beads attached to truncated laments. The data is derived from known hook-sti ness and drag co-e cient for each size bead. The trace in black at the bottom of the gure is the stepping motion of the rotor, and the traces above are the response curves of the marker, each o set by 45 for clarity. The response is smoothed due to the soft linker of the hook and depends on the size of the load. The rotor step is 13.8 as observed by Sowa et al. (2005) and the motor is spinning at 10Hz. Reproduced from Baker and Berry (2009).

1.7.2 Force Measurement

Optical traps can measure a bead's position within 10 nanometres, but they are also very useful for measuring and applying forces. A force feedback trap uses a feedback loop to maintain a trap at a fixed distance from a motor, thus observing the motor as it operates under a constant load. The position of the stage relative to the trap and the motor is determined using a marker fixed to the coverslip, such as a fluorescent protein. The position of the trap with respect to the bead is controlled using a feedback circuit that maintains the position of the fluorescent marker. Finer et al. (1994) built the first feedback trap to measure stepping on myosin using a three bead assay: an assay where the actin filament itself is suspended over a myosin motor fixed on the surface of a bead that is fixed to the surface of the coverslip. In this way the position of the filament with respect to the motor can be held. Rief et al. (2000) used a force clamp to measure the stepping of myosin under constant load. They marked the stage position using a fluorescently labelled biotinylated actin filament on an avidin coated coverslip, and adjusted the position of the stage to hold the trap in place. Schematics of both were shown earlier in Figure 1.5.

Rotational analogues to the linear force feedback trap can be considered but are more difficult to realise in practice due to the difficulties of applying torque to a sample. Pilizota et al. (2007) built a programmable optical angle clamp using acousto-optical deflectors (AODs) to manoeuvre the position of the trap while also controlling the stage position. Using this they were able to apply a torque to a bead pair attached to F_1-ATPase. The bead pair was necessary, as opposed to a single bead, in order to counter the free rotation about the universal joint of the hook. This angle clamp could be used to probe stall torques of F_1 and BFM rotation under load. A schematic of the angle clamp used by Pilizota et al. (2007) is shown in Figure 1.22

Torque can also be exerted directly using magnetic or electrical fields. Electrorotation, exerting a torque on a bead with an oscillating electrical field, was used to study the BFM by Berg and Turner (1993). This technique was used to further characterise the torque-speed curve of the BFM across a range of torques, including reverse rotation (Berry and Berg, 1996, 1997, 1999; Saxl, 2007). Similarly a magnetic field can be used to exert torque on magnetic beads. Magnets have been used for in vivo measurements of cytoplasm and rheology since the 1950s (Crick and Hughes, 1950), but micromanipulation of magnetic beads was introduced by Amblard et al. (1996) who demonstrated two dimensional translation and rotation of 3 μm diamagnetic beads with piconewton forces and femtonewton-metre torques. Improvements

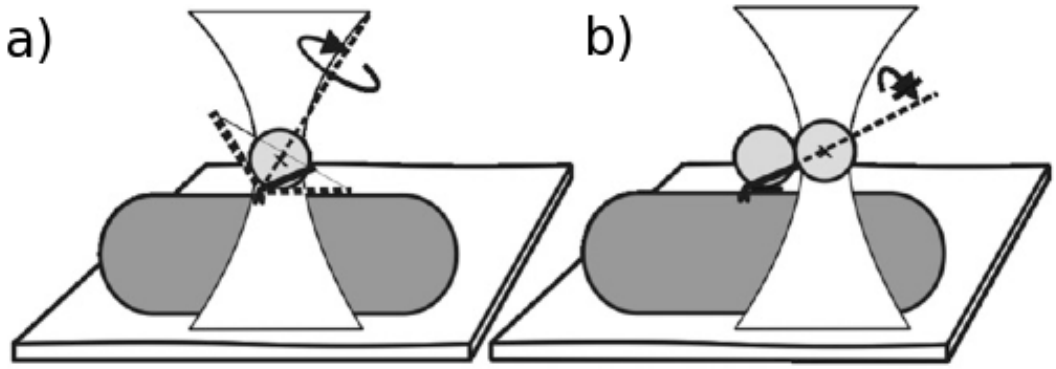

Figure 1.22: a) Single bead experiment on the bacterial agellar motor. Bead centre is marked with a cross and the bead rotation axis is indicated with a dashed line and curved arrow. The bead can rotate even when held xed, due to the universal joint properties of the hook. b)) Bead-pair experiment on bacterial agellar motor. Black bars signify that the rotation of the bead pair around its axis is blocked by the interaction between the inner bead and the cell surface, with the outer bead held by the trap. Motor can be stalled by holding the bead pair xed with the trapping laser. From Pilizota et al. (2007).

in eld uniformity using coils (Gauthier-Manuel and Garnier, 1997) and systems of electromagnets (Gosse and Croquette, 2002) has allowed manipulation of magnetic beads in three dimensions at 10 m/s. Electrorotation and magnetic tweezer schematics are shown in Figure 1.23.

1.7.3 Fluorescence

Fluorescence is the emission of a photon that occurs when an electron in an excited singlet state returns to the ground state. This typically occurs in $\gg 10^{-8}$ s (Lakowicz, 2006). The rapid nature of uorescence is what makes it useful as a biological probe: many cycles of excitation and emission occur in a single exposure of 10ms.

Fluorophores typically emit at longer wavelengths than excitation wavelengths (Stokes law: Stokes (1852)). This is because uorophores rapidly decay (in a few picoseconds) to the lowest vibrational energy level in the excited state, S_1, before undergoing emission. This is also why the same emission spectrum is usually observed regardless of excitation wavelength (Kasha s rule: Kasha (1950)). Both of these features are summarised in a *Jablonski Diagram*, a diagram showing the comparative energy levels in excited and ground states, shown in Fig. 1.24.

Most uorescent molecules are aromatic, for example the rhodamine dye family, of which tetra-methyl-rhodamine is a member, and which is the uorescent dye used

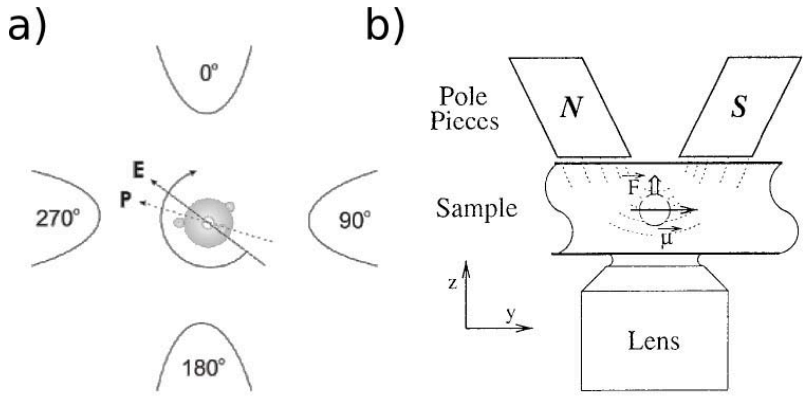

Figure 1.23: Schematics of (a) electrorotation and (b) magnetic tweezers. a) Electrodes are symmetrically arranged around the bead and a sinusoidal voltage is applied with each χ 2 out of phase. The electric eld thus rotates and exerts a torque on the polarisation vector of the particle. From Saxl (2007). b) Pole pieces produce a horizontal magnetic eld in the middle of the sample. The magnetic moment, , of the bead aligns with the eld lines and the vertical magnetic eld gradient exerts a force, **F**, that raises the super-paramagnetic object. With more poles in di erent spatial combinations motion in x, y, and z can be achieved. From Gosse and Croquette (2002)

in this thesis, has electrons delocalised over 4 aromatic rings. The structure of ve common membrane potential probes are shown in Figure 1.25.

Bleaching

Photobleaching occurs when a uorophore loses its ability to uoresce permanently due to photon-induced chemical damage from overexposure. When in the excited state a molecule can interact with its environment and undergo chemical reactions that alter its structure. In particular, the excited triplet state (where the spin of the electrons is unpaired, that is, the total electron spin quantum number is 1) has a longer lifetime than the singlet state, and thus there is more time in which the uorophore can react with reactive molecules in its environment. The average number of excitation and emission cycles for a uorophore depends heavily on the structure of the uorophore and its local environment.

Bleaching causes a signi cant loss of emission intensity and can a ect the signal or image catastrophically. When making measurements based upon intensity, photobleaching must be avoided by using short exposures with lasers of a suitable power. Photobleaching is inevitable as every uorophore has a nite number of emission and excitation cycles available to it, but the rate of bleaching can be controlled by

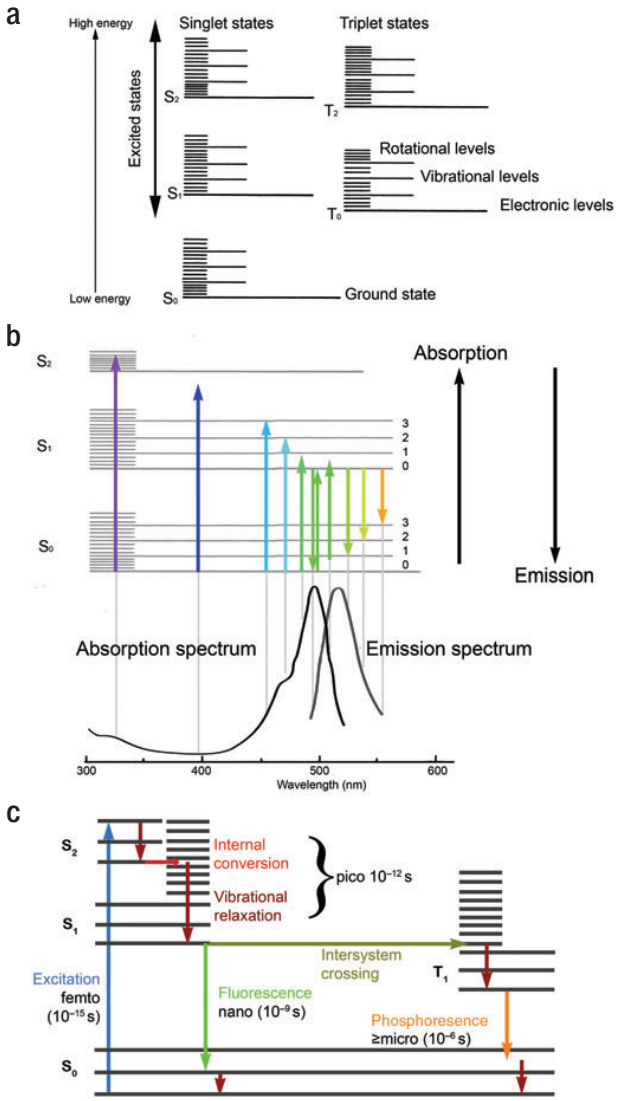

Figure 1.24: Fundamentals of uorescence. a) Jablonski diagram displaying the energy states of a molecule. Molecules that do not absorb energy are con ned to the ground state (S_0). b) The spectral characteristics related to absorption and emission of energy by a molecule are related to the size of the energy steps needed to bring a molecule from one energy level to another. The absorption and emission spectra of the common uorophore uorescein isothiocyanate (FITC) are shown below a Jablonski diagram. Each vertical gray line aligns the spectra with the energy of the absorbed (arrows pointing up) or emitted (arrows pointing down) photons. The arrows are colored to represent the wavelength of the photons. For example, the purple arrow to the left represents the energy of an ultraviolet photon that can cause the molecule to transition from the ground state to the second singlet excited state. The orange arrow on the right represents the lowest energy photon that can be emitted by this molecule as it drops back from the lowest energy state of S_1 to a high vibrational state of S_0. c) The time scales of the various steps in uorescence excitation and emission and phosphorescence take. Excitation is very rapid, of order femtoseconds, relaxation takes picoseconds, and uorescence emission occurs over nanoseconds. From Lichtman and Conchello (2005)

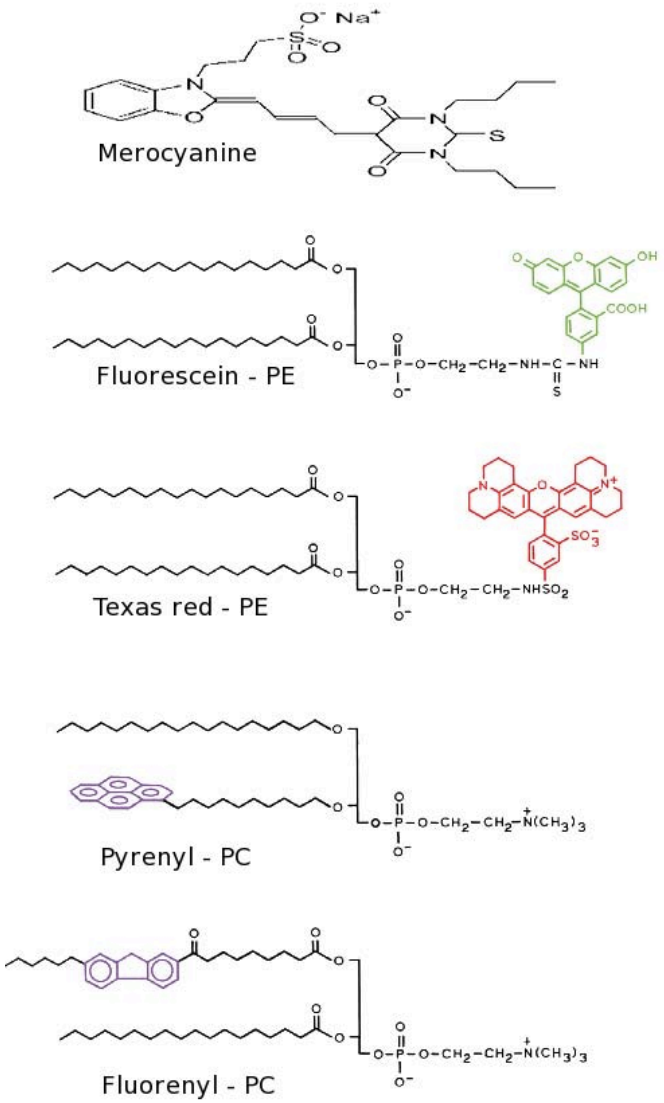

Figure 1.25: Figure showing ve membrane potential probes. At the top is Merocyanine, the rst dye used to probe membrane potentials, and then uorescein, texas - red, a rhodamine dye similar to the TMRM dye used in this thesis, pyrenyl and uorenyl. PC represents phosphatidylcholine and PE represents phosphatidylethanolamine. Adapted from Lakowicz (2006).

using neutral density filters and shutter controlled exposures.

A certain class of experiments focus on fluorescence recovery after photobleaching (FRAP). These experiments deliberately bleach sections of a sample in order to measure the recovery in fluorescence as new fluorophores diffuse into the focus of the microscope, thus demonstrating turnover. In the case of the BFM FRAP experiments have been used to demonstrate turnover in the stator units, and FliM (Leake et al., 2006).

1.7.4 Fluorescence Microscopy

Fluorescence microscopes are built to focus light of the specific excitatory wavelength into a sample and detect the fluorescence of the sample by a light sensitive camera. In order to accomplish this these microscopes require 1) a method of specifying the wavelength of the illumination path, 2) a method of selecting the wavelength of the emission path (and blocking scatter from the illumination path) and 3) a detection method for the emission light. The remaining features exist only to improve the signal from the emission and reduce any noise contained in the excitation path.

The light source can be a lamp of some type (for example an arc, incandescent xenon or mercury lamp), an LED (Landgraf, 2004), or a laser that emits at a known wavelength (the most common wavelengths are 532 nm (green) and 633 nm (red)). The excitation and emission paths typically contain thin-film filters that have a narrow band pass to control precisely the wavelength of light. Custom filters can be obtained to almost any specification but for common fluorophores there exist standard filters for purchase and microscope construction. Elements such as dichroic beam splitters can serve a dual purpose in reflecting excitation wavelengths towards the excitation path but allowing the emission wavelength to pass. An example schematic of the most simple epifluorescence microscope is shown in Figure 1.26

Detection can be performed by individual photon counters such as a photon-multiplying tube (PMT) or by a charge coupled device (CCD) such as in a high-end camera. In fluorescence microscopy imaging is usually performed by CCD or complementary metal-oxide-semiconductor (CMOS) devices in high sensitivity cameras. For a review of these and other solid-state imaging techniques refer to Aikens et al. (1989).

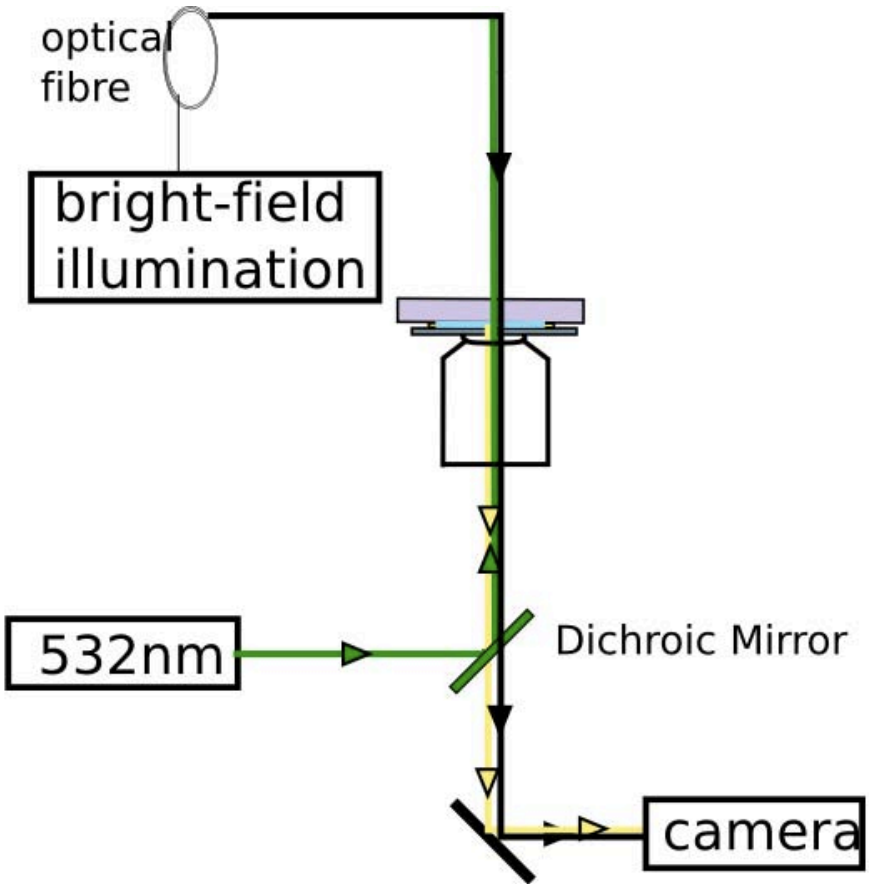

Figure 1.26: Simple schematic demonstrating an epi uorescence microscope and properties of a dichroic mirror. Excitation path consists of a 532nm laser and a dichroic mirror that re ects light of wavelength 532 nm, up into the objective and through the sample. Fluorophores in the sample are excited by this 532 nm light and then emit in yellow light at 568 nm which is scattered back through the objective and passes through the dichroic to be re ected onto the camera. This setup mirrors closely a Cy3 lter set with a 570 nm dichroic, a 530-560 nm excitation lter and a 573-648 nm emission barrier.

1.7.5 Single-Molecule Detection

Fluorescence microscopy is in wide spread use today for myriad applications such as cellular imaging, live animal confocal microscopy and also for single molecule detection (Michalet et al., 2003). Single-molecule methods allow detection of individual states and avoid ensemble averaging. For example, the time course of an enzymatic reaction or the structural change in a macromolecule may be directly observed using single molecule detection, whereas these would be lost in an ensemble averaged measurement. Single molecule methods arose from the development of bright fluorophores and methods to restrict sample illumination volumes to a small size. One method is to use confocal microscopy where a pinhole between the light source and the sample, and between the sample and the detector removes flare fluorescence from the out-of-focus regions close to the focus (Amos and White, 2003; Cox, 2002). Another popular method is to use total-internal-reflection fluorescence (TIRF) microscopy to restrict the volume of illumination to an evanescent field close to the surface of the coverslip. For this angles of incidence are used such that the excitation light is totally internally reflected and thus the illumination region is sub-wavelength in depth into the sample, ideal for illuminating single molecules immobilised on the surface (Lakowicz, 2006). For further reading regarding TIRF microscopy see Nikon (2010). Figure 1.27 demonstrates schematically the optics of confocal and TIRF microscopes.

In Chapter 5 an epifluorescence microscope is used to image a voltage sensitive dye to measure the response of membrane voltage to temperature. These are ensemble fluorescence measurements. The microscope used for these measurements is described in Section 2.2 and a further discussion of fluorescence methods and analysis is undertaken in Sections 5.4–5.7.

1.8 Summary

The essential concepts concerning molecular motors such as mechanochemical transitions, biological free energy and the importance of temperature, as well as an introduction to the structure and function of the linear and rotary motors have been given. Also the structure, function, and environment of the bacterial flagellar motor, and some of the high resolution techniques with which the BFM can be studied have been introduced. In the following chapters the research performed during this thesis will be outlined. For this thesis I designed and built a novel temperature controller capable of changing the temperature up or down by 20 °C in 2 minutes

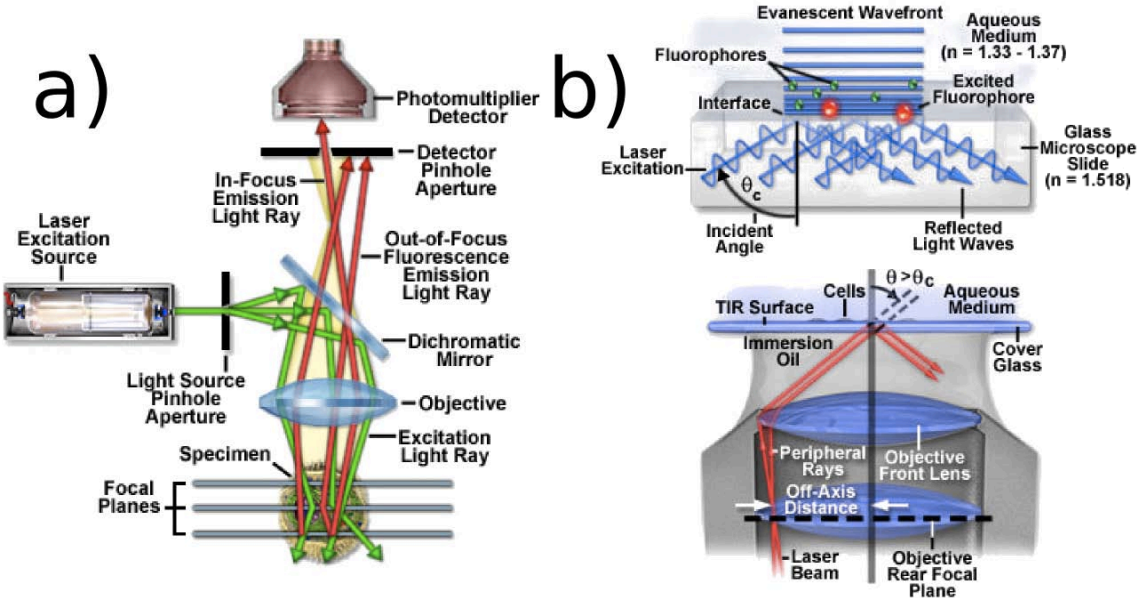

Figure 1.27: Schematics of two types of uorescence microscopes. a) Confocal microscope. Pinhole apertures immediately after the emission source (here a laser) and before the detector (here a photomultiplier detector) ensure that only a thin layer around the focus is imaged at the detector. b) TIR Fluorescence. Top shows optical schematic showing totally internally re ected rays an evanescent eld penetrating nanometres into the sample and bottom shows how TIR is achieved in objective based TIRF. A laser is focussed su ciently o -axis in the back focal plane so as to have an incident angle on the sample that totally internally re ects. All images taken from Nikon (2010).

(Chapter 3). I used this temperature controller to observe the dependence of speed and torque on temperature (Chapter 4), and of cellular membrane voltage on temperature (Chapter 5). Chapter 2 details the experimental methods used in this thesis, focussing on the microscopy and cell preparations used to obtain the data shown in the later chapters. Chapter 3 will discuss the methodology behind temperature control, the design of the controller, and the evaluation of its performance. Chapter 4 will introduce torque and speed as a measure of motor performance and discuss the operation of the BFM at low temperatures, including measuring the low stator number torque-speed curves at 5 °C at 10 °C and looking at the torque-speed curves of the chimeric Na^+ powered BFM as a function of temperature. Chapter 5 will discuss how the membrane voltage, the end product of metabolism, can be measured and how it changes as a function of temperature. This will include the decay in voltage of chimeric motors at temperatures above 40 °C. The final chapter, Chapter 6 will discuss future work arising from this body of work and the conclusions that can be drawn from it.

Chapter 2

Methods and Materials

This section describes the design considerations, materials and methods for the experiments carried out in this thesis. The first section describes the temperature controller built for use in this thesis, and discussed further in Chapter 3. Next the microscopes used to make the single molecule measurements are discussed: first the optical trap used for speed and torque measurements at low temperature (Chapter 4), and secondly the fluorescent microscope used to make measurements of the membrane voltage (Chapter 5). The third section contains information about the cell strains and biochemical preparations used in both experiments.

2.1 Temperature Control

2.1.1 Heating and Cooling the Objective

The objective collar consists of 2 copper rings (64 mm in diameter) that sandwich a ring-shaped Peltier device (PE-032-14-15RH, Supercool, Sweden). The top section of the collar fits directly over the nose of the objective with its outer case removed. (Plan Fluor, 100x, N.A. = 1.30, Oil, Nikon). The collar is coated with thermal grease and tightened around the nose to ensure full thermal contact (thermal conductivity $\sim$0.63 W/mK, from Rabin and Podbilewicz (2000)). The annular Peltier is 55 mm in diameter along the bottom face, 44 mm in diameter across the top face which actively controls the temperature, and has a hole with internal diameter of 28 mm. The Peltier is attached short-face up to the the underside of the top copper ring, and then the bottom ring completes the stack, but is not in contact with the objective.

The active side of the Peltier is thus in thermal contact with the objective, and the bottom, water-regulated copper ring offsets the temperature induced on the large face of the Peltier. The active side of the Peltier can be used to heat or cool the objective, while the bottom ring circulates water either to cool the hot-side of the Peltier, when the collar is being used to cool the objective, or to heat the cold-side of the Peltier when the collar is being used to heat the objective. Water is driven by siphon flow (∼500 mL/min) under gravity to decouple the noise of the pump (MC-450, Micro-Jet, UK) from the microscope and stage. Air is initially cleared from the system using only the pump, and the fluid circuit is then broken underneath the water at the higher reservoir. Constant flow rate is achieved by using a consistent reservoir height, and the pump is used at an equal flow rate to maintain the volume of water at the higher reservoir. Water at room temperature and ice water at 0 °C are used as coolant for the Peltier when heating or cooling respectively. The apparatus is shown in Fig. 2.1.

2.1.2 Temperature Measurement with the Peltier Collar

The temperature is measured at two points: at the top of the collar (T_c) using a thermistor (TS136-170, Oven Industries, US) embedded in the top plate of the collar, and at the focus of the sample (T_s) using a wax of known melting point. The wax technique from Berg and Turner (1993) was adapted and a range of waxes with melting points from 5.5 °C to 49.5 °C were used. For temperatures above room temperature, the surface of a coverslip is coated in sonicated micron size particles of wax, which appear smooth and spherical when liquid, or jagged and polygonal when solid, indicating sample temperature on the surface. For temperatures below room temperature, the phase change of a liquid micron sized droplet to a solid micron-size particle is less noticable. Instead the entire chamber is filled with wax, taking care to use waxes with a thermal conductivity similar to that of water, and the phase transition is noted directly above the marked surface of the coverslip (tendrils of a crystalline structure can be seen as the wax solidifies in the chamber). As the wax in the chamber melts, starting with the top layers above the microscope focus, the image becomes more and more transparent until the final layer, in contact with the coverslip and in focus, melts to a transparent liquid, during which the individual tendrils can be seen to melt.

Six waxes with different melting points were used to calibrate the relationship between the thermocouple and the inside of the coverslip: tetradecane (C_{14}: MP 5.5 °C), cyclohexane (cyclic C_6: MP 7.0 °C), pentadecane (C_{15}: MP 9.8 °C), hex-

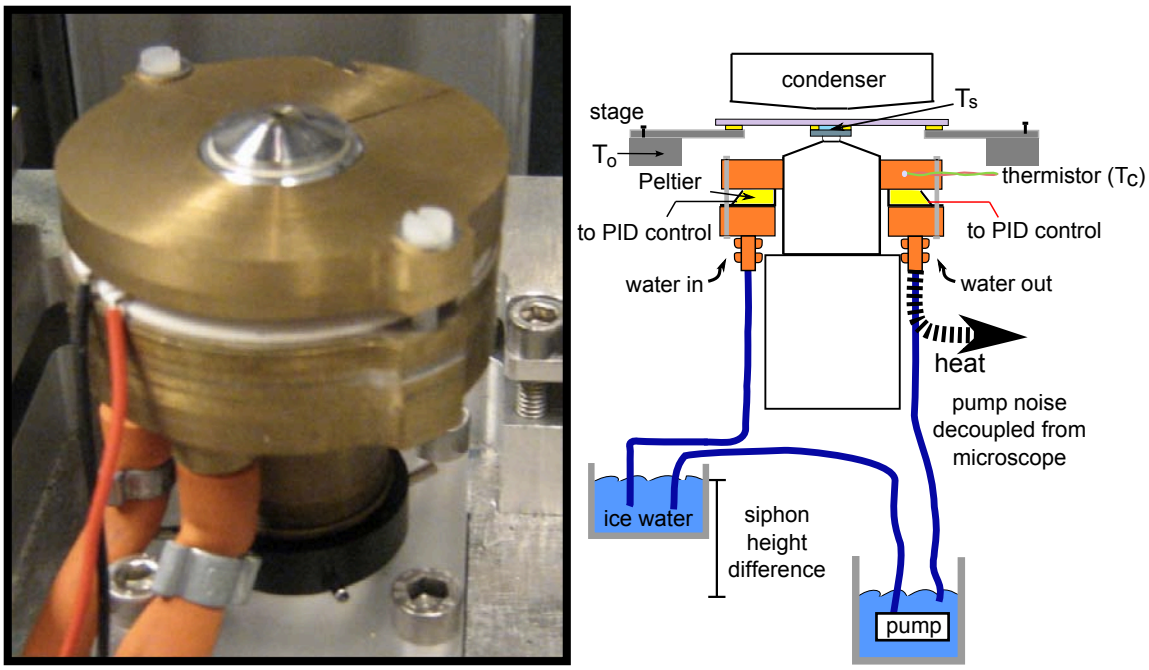

(a) (b)

Figure 2.1: The Peltier collar. a) Image of the collar attached to the objective in place on the microscope. b) Schematic of the system, showing the location of the thermistor used to measure temperature of the collar. In this example, the Peltier-collar is used to cool the objective, so the Peltier acts to pump heat out of the objective. This hot side of the Peltier is then cooled by owing water. The ow of water is maintained by a head of pressure, and this head is maintained by an aquarium pump uncoupled from the microscope to reduce noise. The collar temperature is related to the sample temperature by a calibration curve that is discussed in Section 3.9.2. Coolant owing through the bottom half of the collar is either water at room temperature, or an ice/water mixture depending on the temperature range needed.

adecane (C_{16}: MP 18.0 C), eicosane (C_{20}: MP 36.7 C) and tetracosane (C_{24}: MP 49.5 C) (Acros Organics, UK). An additional calibration point is the equivalence of the sample and collar at room temperature in the absence of temperature control ($T_s = T_c = 22$ C).

To correlate the temperature of the sample with the measured collar temperature the set point is cycled above and below an estimated melting point with increasingly smaller oscillations to determine accurately the correlated melting point. For example, for the tetradecane wax, with a melting point of 5.5 C, the wax was rst observed to solidify near 2 C, and so the set point was set to 0 C, then up to 4 C, then down to 1 C, and the temperature was oscillated around this hypothesised melting point in smaller intervals until the melting point was determined to be 2.4

0.2 °C, as judged by a steady state where the crystalline structure of the wax is neither growing nor shrinking. As the set point temperature approaches the correlated melting point the temperature response of the sample, that is, the phase change response of the wax, becomes very rapid, responding in $\sim 2s$ to a small temperature variation ($\pm$ 0.2 °C). For the initial temperature ramps, the phase change response lags the temperature controller by $\sim$ 50 s. For the sonicated particles at temperatures higher than room temperature the procedure is the same except rather than looking for a steady state where a layer of the wax is both melted and solidified, the correlated melting point is judged by the collar temperature lying closest to the phase transition, for example, the correlated melting point of tetracosane is 52.8 $\pm$ 0.1 °C where an increase of 0.1 °C results in a phase transition to liquid, and returning to XXX °C results in the return phase transition to a solid. The final correlation relation (Figure 3.5) is displayed and discussed in Section 3.9.2.

2.1.3 Feedback for the Peltier Collar

Power is supplied to the Peltier device from a PID Temperature Controller (5C7-195, Oven Industries, US), at a maximum of 4.0A and 6.5V. The unit measures the temperature at the collar using a thermistor (TS136-170, Oven Industries, US), and moderates the current supplied to the Peltier with a tuned PID response to drive temperature change quickly while minimising oscillation. PID tuning is performed manually following the Ziegler-Nichols algorithm (Ziegler and Nichols, 1993), as described in Section 3.5.

2.2 Fluorescent Microscope

The multiple illumination-path fluorescent microscope used in this thesis was custom built by Dr M.C. Leake and Dr R. M. Berry in 2004. The microscope contains illumination paths for 532 nm, 473 nm and 440 nm laser light, and can be used for epi-fluorescence, total-internal reflection (TIRF), and photo-bleaching recovery measurements (Plank et al., 2009; Leake et al., 2006). In this thesis I use epi-fluorescence and 532 nm illumination to image the tetramethylrhodaminemethyl ester (TMRM) dye inside the cell (Sections 5.8–5.9.5).

2.2.1 The Microscope

The fluorescence microscope (Figure 2.2) is an inverted custom built microscope. For the objective, a Plan Fluor 100×/1.30 oil objective (Nikon, UK) was used. The outer casing was removed in order for the temperature controller to be fitted to the nose of the objective, as discussed in Section 2.1. The sample was attached to a slide holder which was then screwed into a 3 axis piezoelectric nanostage (controller: E-509.C3 and E-503, stage: PI-517.3CL, Physik Instrumente, Germany). The main stage and housing, on which the piezoelectric stage rested and into which the objective was secured, was custom built from aluminium in the Oxford Physics workshop. An additional section was removed to make space for the temperature controller and water flow pipes.

A tungsten halogen lamp (LHS-H100P-1, Nikon, UK) was used for low-intensity bright-field illumination which was focused into the sample using a long working distance condenser (LWD 0.52, Nikon, UK). This bright-field image was recorded on a small CCD camera (LCL-902-HS, Watec, US) and displayed on a black and white monitor (SSM-175-CE, Sony, UK).

Fluorescence excitation for the TMRM dye at 532 nm was provided by a fan cooled Diode Pumped Solid State Laser (LCMT111-20, Laser2000, Northants, UK), via a dichroic mirror (530 nm long pass). The total illuminated area was 600 μm^2 and the illumination intensity at the sample was $\sim$7 W/cm^2 ($\pm$5%) for TMRM. Fluorescence emission was passed through a 580 nm long pass emission filter and a 532 nm notch rejection filter.

Exposure time was moderated using electronic shutters (SC10, Thorlabs, UK) which could be operated manually or automatically when a signal was sent using a National Instruments LabVIEW .vi and block (BNC2110, National Instruments, UK). Typical exposure times were 10–30 ms. Images (128×128 pixels, $\sim$6 μm×6 μm) were acquired using a Peltier and water cooled, back-thinned electron-multiplying charge-coupled-device (EMCCD) camera (iXon DV860-BI, Andor Technology).

For the membrane voltage measurements the laser intensity entering the objective was measured and adjusted to $\sim$40 μW (corresponding to 200 μW leaving immediately prior to the TIRF lens). The illumination was adjusted such that the illumination pattern was uniform and centred using either a dense sample of 200 μm fluorescent beads, or a dye filled slide.

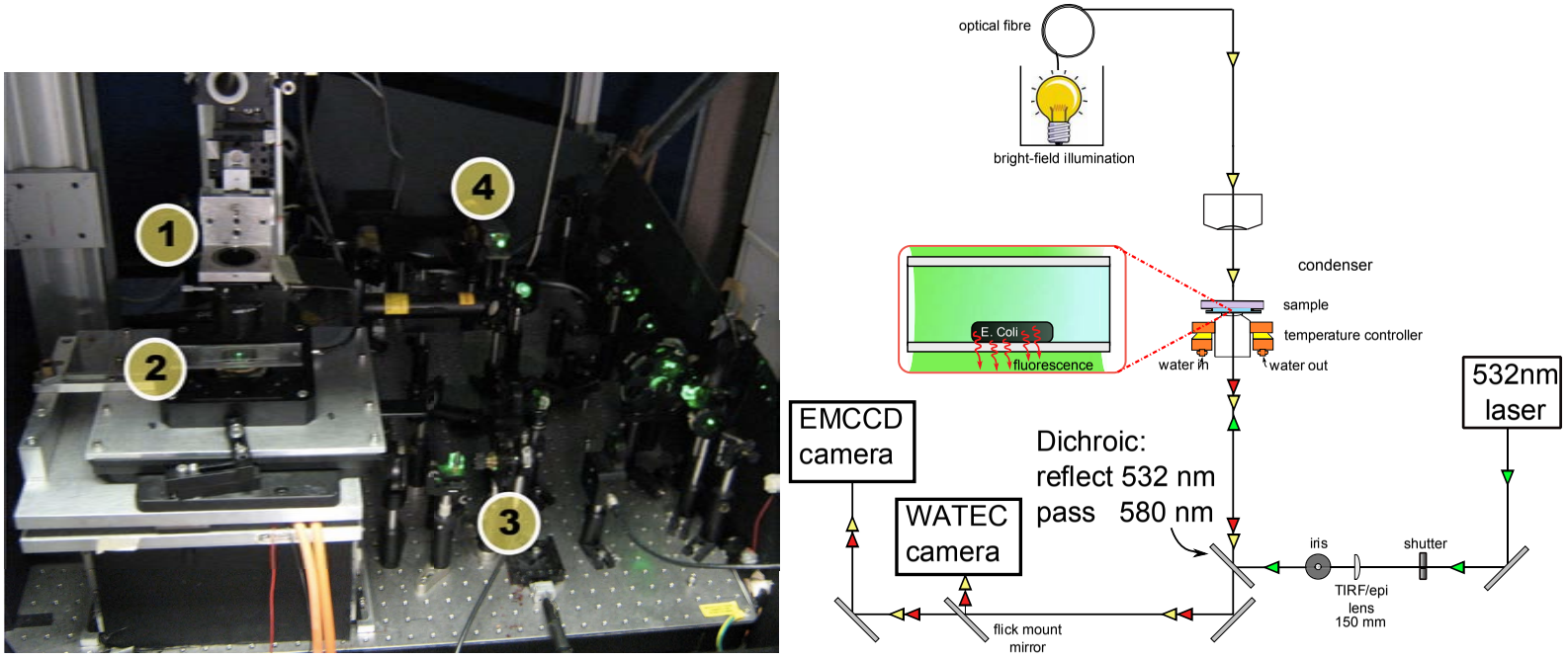

(a) (b)

Figure 2.2: Fluorescence microscope used in this thesis. a) Labelled photograph of the microscope: (1) long working distance condenser focussing bright eld illumination on sample, (2) piezoelectric nanopositioning stage with acrylic slide holder resting on top of objective with brass Peltier collar temperature controller, (3) TIRF adjustment lens and eld iris, (4) 532 nm laser. b) Full schematic of the uorescence microscope. Laser illumination is brought in from the right side, re ected onto the objective and through the sample with a 580 nm long pass dichroic. Excitation light (red arrow in inset) passes through this dichroic and is measured at the EMCCD camera. Additionally there is a second low resolution camera in the camera path, which can be enabled by placing a ick mounted mounted mirror in the camera path. The Watec camera is used for bright eld imaging, with illumination introduced through a multimode bre and long working distance condenser.

2.2.2 Fluorimetry

The excitation and emission peaks of the tetramethylrhodamine methyl ester dye (TMRM), and the emission dependence with temperature, were measured using a variable temperature fluorescence spectrophotometer (Cary Eclipse, Varian, Australia). Emission and excitation peaks were scanned with photon multiplying tube set to low amplification, and with a slit width of 5 nm with an averaging time of 0.1 s. Temperature dependence of the fluorescence of the TMRM dye between 10 °C and 45 °C was measured with a 5 nm slit width and an averaging time of 0.5 s, with an excitation wavelength of 532 nm and an emission wavelength of 580 nm, and the temperature being adjusted at a rate of 2 °C / minute. For temperatures between 5 °C and 10 °C, the slit width and emission and excitation wavelengths were the same, but the temperature was adjusted at a rate of 0.1 °C / minute.

2.2.3 Image Acquisition and Analysis

Images from the EMCDD camera were recorded in .sif format and imported into MATLAB for further analysis. The details of image analysis, the conversion of pixel intensity into an associated fluorescence, dye concentration, and voltage, will be discussed in detail in Chapter 5, Sections 5.6–5.7.

2.3 The Optical Trap

An optical trap can be used to apply force on a particle, or hold it in position, or also to measure the position of a particle to within 10 nm. The history and theory of optical trapping was discussed previously in Section 1.7.1. For the experiments in this thesis an optical trap custom built by Dr A. Rowe and Dr R. M. Berry was used. This trap was realigned and augmented, by myself and Dr B. C. Steel, with the addition of a Helium-Neon (HeNe) laser. This yielded two laser paths (1064 nm and 633 nm). The 633 nm laser provided better position resolution of the smallest beads (0.2 μm in diameter), but caused cellular damage at an increased rate in comparison with the 1064 nm laser. Thus, the infra-red laser was used for large beads, and long time measurements, such as IPTG resurrections, and the HeNe laser was used when measuring the speed of the 0.2 μm beads.

2.3.1 The Microscope

The objective was the same as used in Section 2.2, a Plan Fluor 100×/1.30 oil objective (Nikon, UK). This was mounted on an inverted microscope on an aluminium stage designed by Dr R. M. Berry and built at Imperial College, London. The sample was affixed with double sided sellotape to a custom built acrylic slide holder, and then placed on a piezeoelectric nanostage (controller: E-509.C3 and E-503, stage: PI-517.3CL, Physik Instrumente, Germany) mounted into the aluminium stage.

This objective was overfilled in the back aperture by laser light from either path, and the focussed beam in the image plane formed the optical trap. The 1064 nm illumination was provided by a diode-pumped solid state laser (1 W, L04-1000S-1064, Elforlight, Northants, UK), and the 633 nm illumination by a Helium-Neon laser (10 mW, 25-LHP-111-230, Melles Griot, UK). Both lasers were attenuated by a $\lambda/2$ waveplate and polarizer to give adjustable laser intensity in the sample plane. The 633 nm laser was passed through a beam expander to ensure the back aperture of the objective was overfilled.

The transmitted beam was collimated by a condenser lens (Oil 1.4, Nikon, UK), with a 300 mm plano-convex lens glued onto the back and reflected by a 1064 nm reflecting (and partially 633 nm reflecting) dichroic to fill the surface of a quadrant photo-diode (Pin-SPOT 9DMI, UDT Sensors, CA, USA). The photo-current from each quadrant was amplified using a custom-built current-to-voltage amplifier (Rowe, 2005) and this was subsequently sampled at variable rates (∼5 kHz) using a National Instruments hardware block (BNC2110, National Instruments, UK).

Tungsten-halogen illumination (C-LP, Nikon, Japan) was filtered to remove high energy short wavelength light, and introduced into the condenser via a multi-mode fibre. Illumination passed through a field iris 300 mm behind the condenser, and the 1064 nm reflecting dichroic mirror. The iris edge was used as a reference marker to ensure the condenser was at the correct distance from the sample. Figure 2.3 shows a photograph and schematic of the optical trap used in this thesis.

2.3.2 Signal Analysis

The method used to interpret the voltage signal from the QPD, that is, the conversion photodiode voltage into X,Y-position, and subsequently into speed and torque is discussed in detail in Section 4.3.3. In summary, a discrete Fourier transform is used to identify speed from the position trace of a rotating bead.

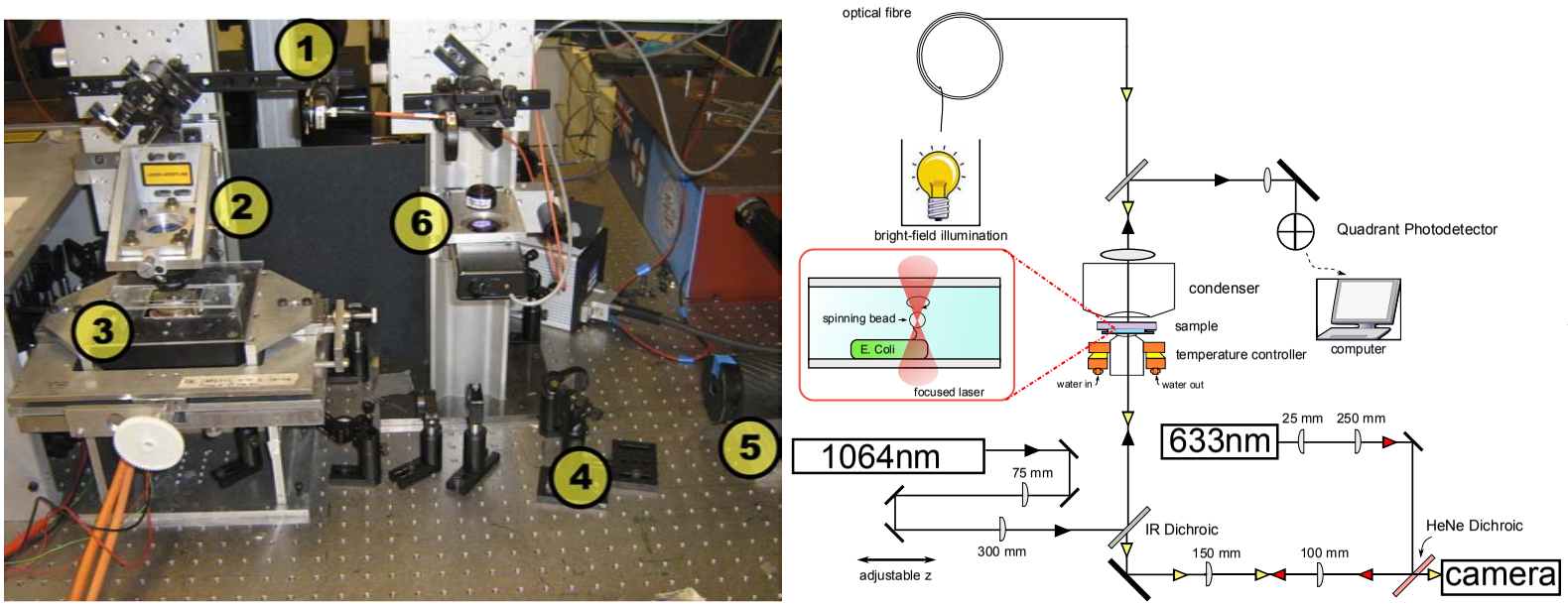

(a) (b)

Figure 2.3: Optical trap used in this thesis. a) Labelled photograph of the optical trap: (1) bright eld illumination introduced by multimode optical bre, (2) condenser mount containing Oil 1.4 condenser, (3) Piezoelectric stage, acryllic plastic slide holder and copper temperature control collar on objective, (4) HeNe dichroic to introduce HeNe optical trap, (5) camera used for bright eld imaging (6) quadrant photodiode with IR or HeNe pass notch lter to remove unwanted room light. The 1064 nm laser path is out of view, to the left of the stage. b) Full schematic of the optical traps used for bead assay experiments (Section 2.4.3). Infra-red laser light is introduced from the left side, with rail mounted mirrors allowing for adjustment of the position of the depth of laser focus. HeNe laser light is introduced from the right side, in the same optical pathway as the camera. Laser light is focussed in the speciment plane by a 100 1.3 N.A. objective, and transmitted light is re-collimated by the condenser and accompanying lens and projected on the a QPD used as a position detector.

2.4 Biochemistry and Sample Preparations

2.4.1 Bacterial Strains

The chimeric strain was originally prepared by Asai et al. (2003) to explore the ion selectivity of the bacterial flagellar motor (BFM). In this thesis I use the YS34 strain which was originally prepared by Dr Y Sowa and brought to our laboratory in Oxford in 2003 (Lo, 2007). The YS34 strain has the following genotype: *ΔcheY, fliC::Tn10, ΔpilA, ΔmotAmotB*, and was derived from strain RP4979 (Scharf et al., 1998; Sowa et al., 2005). *ΔcheY* indicates that the motor is non-switching, as it is *cheY* deleted, and *cheY* is a key component in the chemotactic signalling network. *fliC::Tn10* indicates that the transposon Tn10 has been inserted into the *fliC* gene, rendering filament expression inactive (Kuwajima, 1988; Ryu et al., 2000). *ΔpilA* indicates that the pili of *E. coli* are deleted, and *ΔmotAmotB* indicates that the stators are deleted from the genotype and phenotype.

The cells were transformed with plasmids pYS11 and pYS13. Plasmid pYS11 ($fliC^{st}$, ampicillin resistance) expresses the filament as 'sticky filament', which promotes hydrophobic interaction with the polystyrene beads and removes the need for anti-filament antibody coating (Scharf et al., 1998). Plasmid pYS13 (*pomApotB*, isopropyl-β-D-thiogalactoside (IPTG) inducible, chloramphenicol resistant) expresses PomAPotB chimeric (Na^+ powered) stator proteins which are inducible by varying the concentration of IPTG during growth (Asai et al., 2003).

2.4.2 Cell Growth and Preparation

Experimental cultures were grown from frozen (-80 °C) stocks for 5 h at 30 °C in 5 ml of T-broth (1% Bacto tryptone Difco/85 mM sodium chloride) containing the appropriate antibiotics. Inducer, IPTG, was present at low concentrations (5–10 μM) for speed measurements, and at high concentration (20 μM) for V_m measurements. Optical density was then measured to check that cells were in mid-log phase (OD600 $\sim$ 0.6) using a spectrometer (UVmini-1240, Shimadzu, Japan). Cells (1 μL from grown stock) were collected in syringes and pumped 60× through 26 G needles in order to truncate the filament (known as 'shearing'). Cells were then isolated using centrifugation (3 iterations at 7000 rpm for 2 minutes), and concentrated 3× by resuspension in motility buffer (10 mM potassium phosphate, 0.1 mM ethylene diamine tetraacetic acid (EDTA), and 85 mM NaCl at pH 7.0).

2.4.3 Sample Preparations

For measurements which required no medium exchange after preparation, for example the standard bead assay (Section 2.4.3), the IPTG resurrection (Section 2.4.3), and the fluorescence measurements without the addition of CCCP (Section 2.4.3), simple tunnel slides were used. For experiments requiring medium exchange, such as the fluorescence experiments involving the subsequent addition of CCCP (Section 2.4.3), custom-built flow cells were used. Schematics of both are shown in Figure 2.4.

Tunnel slides are assembled by placing two strips of double sided sellotape ∼30×10×0.1 mm along the centre of a microscope slide with a small space between them. A 22×22×0.1 mm coverslip is then placed on top of the two sections of sellotape and a tunnel is formed between the coverslip and slide and sellotape, ∼15 μL in volume. Flow slides are assembled similarly, except that a slide is prepared with two holes drilled through it with diamond tip drill bits (bits; DIAMA, UK, drill: Dremel, US) and with two sections of tubing inserted through and glued to the slide using epoxy resin. A single piece of sellotape is then placed over the holes and tubes, and an interior section of the piece is cut out. A 22×40×0.1 mm coverslip is then placed on the sellotape to create a sealed chamber of air that is accessible only through the two sections of tubing. Fluid can be inserted, or exchanged, in this chamber, by flowing fluid from a pipette directly into a 10 μL pipette tip that is fixed inside one of the tubes. Care must be taken during fluid exchange not to introduce air bubbles into the flow cell which would interfere with cellular function and imaging.

Glass Cleaning

Glass coverslips were cleaned by immersion in a saturated solution of KOH/EtOH for 3 hours at 30 °C. Cleaning removed autofluorescent dirt that might affect fluorescence measurements. After 3 hours the coverslips were rinsed three times with water and stored in water at room temperature. These coverslips were subsequently used for a month before they were discarded and the cleaning process was repeated.

Bead Assay

Tunnel slides were treated with a 0.1% solution of polylysine to coat the coverslip glass to aid cell adhesion. The slides were then washed with 200 μL of motility buffer (10 mM potassium phosphate, 0.1 mM ethylene diamine tetraacetic acid

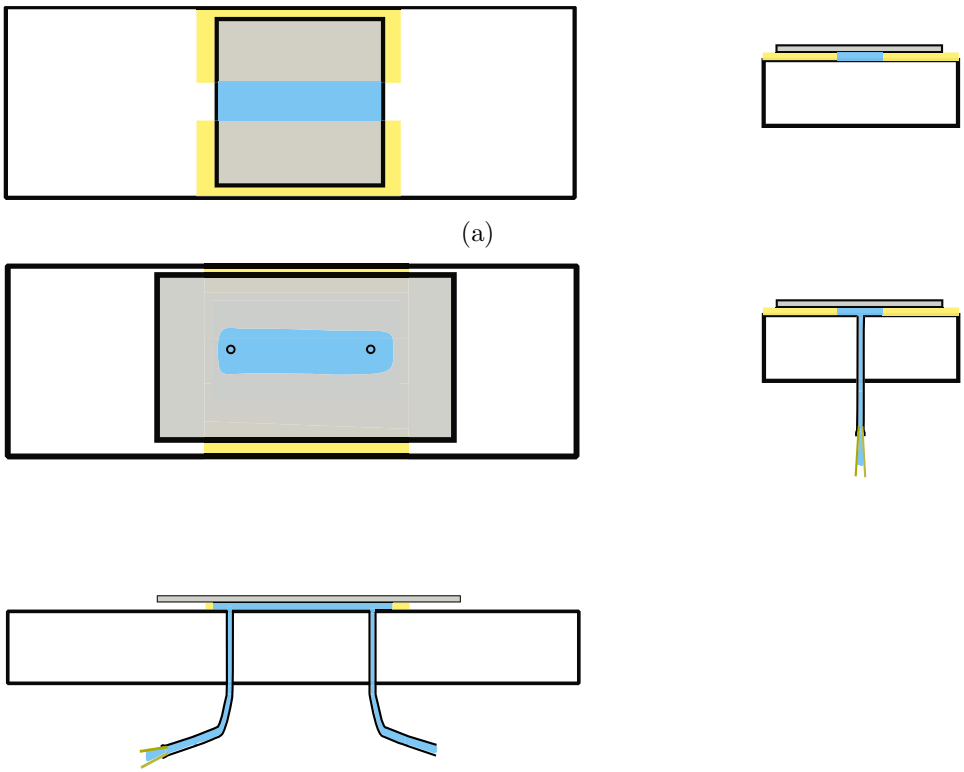

(a)

(b)

Figure 2.4: Schematics of slides used in this thesis. a) To scale (1:1) diagrams of top and front views of a tunnel slide, with front and side views magni ed 10 in the z axis. Tunnel slide consists of a sandwich of a 22 22 0.15 mm coverslip (grey), two pieces of 0.1 mm thickness sellotape (yellow), and a 76 26 1 mm microscope slide (clear). The tunnel is formed between the coverslip and the slide and the two pieces of coverslip. Fluid is injected in one side of the tunnel, and wicked away at the other end (blue). b) To scale (1:1) top, front and side views of a simple ow slide, with front and side views magni ed 10 in the z-axis. The tubing shown on the ow slide is not to scale. The ow cell consists of a sandwich of 22 40 0.15 mm coverslip (grey), one piece of 0.1 mm thickness sellotape (yellow) with a section removed in the middle, and a 76 26 1 mm microscope slide (clear). The slide has two 1 mm holes drilled through the surface using diamond tip drill bits and two 1 mm outer diameter pipes inserted into these holes and secured with epoxy. The slide is then assembled with the holes over the chamber, creating a ow chamber where the uid can be exchanged using ow into one of the pipes. A 10 L pipette tip is inserted in the end of one of the tubes (dark yellow) and uid is owed into this pipe by inserting a larger full pipette into this tip (with a 100 L tip), and carefully delivering the volume without allowing air into the chamber.

(EDTA), and 85 mM NaCl at pH 7.0). Cells (∼10 μL at ∼ OD600 1.0) were then inserted into the tunnel slide using a pipette along the edge of the coverslip/slide interface, using tissue (Kimwipes, Kimberly-Clark, UK) to wick moisture from the other end of the tunnel slide. Cells were left to incubate onto the coverslip surface for 10 minutes, then the slide was washed with 200 μL of motility buffer to remove cells from solution, while leaving the cells adhered to the surface. Beads (1.0 μm, 0.75 μm, 0.50 μm, 0.35 μm or 0.20 μm; Polysciences, US) were diluted (0.05% - 1.4% wt. solid/water) and inserted into the tunnel slide. The beads were left for 10 minutes to adhere to the sticky filament, or the surface, and then the solution was washed with 200 μL of motility buffer. Finally the tunnel slides were sealed at each end using nail varnish. The varnish seal did not allow oxygen exchange and so sealed samples were discarded after a maximum of two hours to prevent decreasing oxygen conditions reducing motility.

IPTG Resurrection

For the IPTG resurrection experiments, slides and cells were prepared as per the standard bead assay (Section 2.4.3). After the beads have adhered to the filament, and excess beads have been washed out with motility buffer, a second wash is performed with 100 μL of IPTG resurrection buffer (1 mM IPTG, 10 mM potassium phosphate, 0.1 mM EDTA, and 85 mM NaCl at pH 7.0, in 20% tryptone broth (TB)). The IPTG resurrection buffer contains an excess of IPTG, the inducer that induces chimeric stator protein expression, and also tryptone broth (TB) in order to provide the cells with the essential amino acids for cell growth. After the IPTG resurrection buffer is flowed in, the slide is sealed with nail varnish and taken to the microscope. A cell is selected within 5 minutes and within approximately 10 minutes (at 22 °C) chimeric stators start to be expressed and discrete speed jumps can be observed on a monitored cell (Section 4.4.2).

Membrane Voltage Measurements

Cells were grown and 1.5 μL of cells were taken and isolated using centrifugation as per Section 2.4.2 (3 iterations at 7000 rpm for 2 minutes). These cells were then resuspended in 1 mL of 100× ethylene diamine tetraaceticacid (EDTA) solution (85mM NaCl, 10mM KP_i, and 10mM EDTA at pH 7) and left to incubate for 10 minutes. This high EDTA buffer permeabilizes this membrane to allow rapid transit and equilibration of the TMR dye across the membrane. The cells are then again centrifuged (2 iterations at 7000 rpm for 2 minutes) and washed in motility buffer

((10 mM potassium phosphate, 0.1 mM ethylene diamine tetraacetic acid (EDTA), and 85 mM NaCl at pH 7.0) to remove the high EDTA buffer. A tunnel slide is then prepared, washed with polylysine, and injected with cells and left to incubate for 10 minutes, as per Section 2.4.3. For the final wash 0.3 μM TMR dye is injected into the tunnel slide. Slides are then placed on the microscope and illuminated with 532 nm light and measured as per Section 2.2.

Membrane Voltage Measurements with Added CCCP

For voltage measurements requiring the addition of CCCP, to measure C_{bound}, the cells and sample were prepared as per Section 2.4.3, using a flow slide instead of a tunnel slide. TMRM dye at a concentration of 0.3 μM is injected as previously, and cell fluorescence measurements are recorded for approximately 30 minutes. While the slide is on the microscope, at a target temperature, 100 μL of a solution containing 100 μM CCCP and 0.3 μM TMRM in motility buffer is flowed into the flow cell using the technique detailed in Section 2.4.3.

2.4.4 Cell Plates and Growth

Cells were prepared as for a bead assay detailed in Chapter 2, Section 2.4.3. These cells were then normalised to a concentration equivalent to absorbance OD600 = 0.60. Cells were then distributed into 4 aliquots of 100 μL in eppendorf tubes and 3 of these tubes were placed in a water bath at 45 °C. After 5, 10 and 20 minutes respectively these tubes were removed and placed at room temperature. The aliquots were then sequentially diluted to 2×10^{-6} of their original concentration, smeared across LB agar plates, and incubated at 30 °C for 18 hours. Images of plates are recorded using a photography system for gels (G:Box Chemie-XT16 Gel Documentation System, Syngene, UK) and then counted manually.

Chapter 3

Temperature Control

3.1 Introduction

Temperature is a global variable that affects life in many ways and most life has adapted to live within a limited range of temperatures. Temperature change does not only influence the thermotactic signals and responses of an organism, but it also bears a direct effect on the energetics and kinetics of underlying cellular processes. Controlling the temperature of a system allows researchers to investigate how biophysical processes change with temperature. The need for increased resolution has meant that immersion-oil objectives are now standard in the microscopes used for biophysical measurements. This allows for temperature control via the objective rather than via the stage, and in fact for a sample to be cooled sufficiently either the objective must be cooled or the stage cooling component of a temperature controller must be placed as close as possible to the sample. Objective temperature control is desirable because it does not require significant alterations to the stage and an existing microscope can be used. In this thesis a novel immersion-oil microscope temperature control method was developed based on a ring-shaped Peltier device in contact with the objective. This chapter demonstrates the efficacy of the system by showing its temperature-related performance and its application to biophysics by cooling and slowing the rotational speed of the BFM.

3.2 Temperature Control in Biophysics

A temperature controller must perform two functions: 1) measuring and 2) altering the sample temperature. A feedback system to drive the measured temperature towards the setpoint can also be included. Temperature control solutions can satisfy these requirements in myriad ways, combining different measurement and cooling techniques depending on the required application and the thermal circuit formed by the microscope.

3.3 Measuring the Sample Temperature

3.3.1 Thermometers, Thermistors, and Thermocouples

The earliest method of measuring temperature was to use the temperature dependent expansion of a gas to draw a liquid up a column in a device known as a thermoscope. This was built and sketched by Galileo in 1594 and later converted into a thermometer, with scale markings, by Fludd in 1638 (McGee, 1988). Gas expansion is still used in some building thermometers, as are bimetallic thermostats in air-conditioning units, but most laboratory thermometers use liquid expansion up a scaled column of glass. These are generally not small enough for use in a microscope sample, nor easy to record over time.

Electronic temperature sensors allow easy logging of temperature. Early electronic temperature sensors used thermo-resistive devices. There are two types of thermo-resistive sensors: Resistance Temperature Detectors (RTD) which use platinum wire wound into a coil, whose resistance scales linearly with temperature, and thermistors, which have a large change in resistance over a small change in temperature, either in the positive (PTC) or negative (NTC) direction. Thermistors use semiconductors in the place of the metallic RTD. Most applications use RTD temperature sensors which can operate between -200 °C and 850 °C and have maximum accuracy of ± 0.15 °C at 0 °C.

A cheaper option than an RTD thermo-resistive sensor is the thermocouple, a junction between two different metals that produces a voltage that is dependent upon its temperature. When two different metals are joined together, a small voltage is generated at this junction. If two such junctions are created and held at different temperatures, then the voltage across the circuit will change proportionally with the temperature difference. This is known as the Thomson effect (Thomson, 1854). By holding one junction at a fixed temperature the temperature at the second, sensing

junction can be deduced from the voltage generated. This is known as the Seebeck effect, the inverse of the Peltier effect (Bridgman, 1924; Callen, 1948).

Thermocouples can be constructed with many different combinations of metals dependent on the temperature range of the desired application. For biophysical applications K (chromel-alumel) and T (copper-constantan) type thermocouples are the most suitable. K-type thermocouples are common general purpose thermocouples that operate between -200 °C to +1350 °C with an accuracy of ±1.5 °C. T-type thermocouples operate between -200 °C to +400^{o}C with an accuracy of ±0.5 °C (Croarkin et al., 1993). In industrial applications the reference junction is usually replaced by an integrated circuit called a cold junction compensator which produces a voltage equal to the thermocouple voltage between 0 °C and room temperature. Thermocouples are a cheap, widely used temperature sensor for industrial applications.

3.3.2 Microscopic Temperature Probes

Sometimes a situation requires a very small temperature probe, such as within a cell. Fluorimetric techniques have been developed to deal with this by using fluorescent dyes that can respond to temperature. Chapman et al. (1995) used 7-nitrobenz-2-oxa-1,3-diazol-4-yl (NBD) and 6-dodeca-noyl-2-dimethylamino-naphthalene (laurdan) as fluorescent probes. The decay rate of NBD increases in response to temperature and so fluctuations in intensity and fluorescence lifetimes can be correlated with cell temperature. NBD can be used to measure the temperature to within 2 °C, while laurdan has finer control, 0.1-1 °C, but over a smaller range. More recently Ross et al. (2001) used temperature sensitive dyes to measure temperature between room temperature and 90 °C with a precision of 0.03 - 3.5 °C and with spatial and temporal resolution of 1 μm and 33 ms respectively.

A less accurate, but significantly less elaborate, micron sized thermometer uses wax droplets on the surface of a glass coverslip. The solid-liquid phase change of a wax with known melting point can be observed and used to measure the temperature on the surface. Berg and Turner (1993) used droplets of butyl ester of stearic acid with a melting point of 27.5 °C to measure the temperature at the microscope focus. The advantage of this system is that it is cheap and easy to implement as it only requires the microscope to image the phase change. The disadvantage is that impurities may cause the melting point to differ from the literature value, and with small droplets of some waxes it may be hard to distinguish the liquid and the solid phases.

3.4 Altering the Sample Temperature

Heat is a waste product of any electrical system and so heating requires simply flowing current through a suitably arranged resistance wire, as in a toaster or a hair dryer. Removing heat from a system is more difficult and requires placing a cold object in thermal contact with the system, such as flowing water or some type of heat sink.

An exhaustive history of temperature control is difficult due to the wide variety of applications used to explore temperature dependence. Primitive heating techniques sprang into existence shortly after the microscope became widespread. Mast (1903) made a simple stage heater by putting a bottle of hot or cold water on the stage immediately prior to swift measurements. Francis and Smith (1916) built pipes into a large microscope slide and flowed hot fluid from a flask on an adjacent heating mantle. Shortly afterwards microscope ovens and incubators were available to purchase in the early 20th century as Dox and Roark Jr (1917) adapted a commercially available electrically heated incubator to form a heating stage for their microscope and insulated it with asbestos. Krog and Simmet (1954) built a stage based temperature controller that could heat or cool using flow from hot and cold mains tap supplies. Krog and Simmet were able to moderate the temperature between 7 °C and 30 °C by controlling the rate of flow from the two taps. Around the same time Pijper (1955) built a similar heating and cooling device on a microscope stage and subsequently (Pijper et al., 1956) used this to probe the structure of the bacterial flagellar filament at different temperatures - the first example of a bacterial flagellar experiment using temperature control. One method of temperature control is to, of course, control the temperature of the entire room. Tilney and Porter (1967) were early in using a microscope inside a 4 °C cold room to observe microtubules in heliozoa. Figure 3.1 shows early temperature controllers.

3.4.1 Electronic cooling - Peltier Heat Pumps

Electronic cooling arose after the development of semi-conductor technology and Peltier heat pumps. The Peltier effect, discovered by Jean Charles Anathase Peltier in 1834, arises when voltage is applied across a paired junction of two different metals, generating heat at one junction and cooling the other (Callen, 1948; Gurevich and Logvinov, 2005). A Peltier plate is an arrangement of semiconductors, P-type and N-type junctions, connected electrically in series but thermally in parallel. When DC current flows around the circuit, the electrons in the N-type material

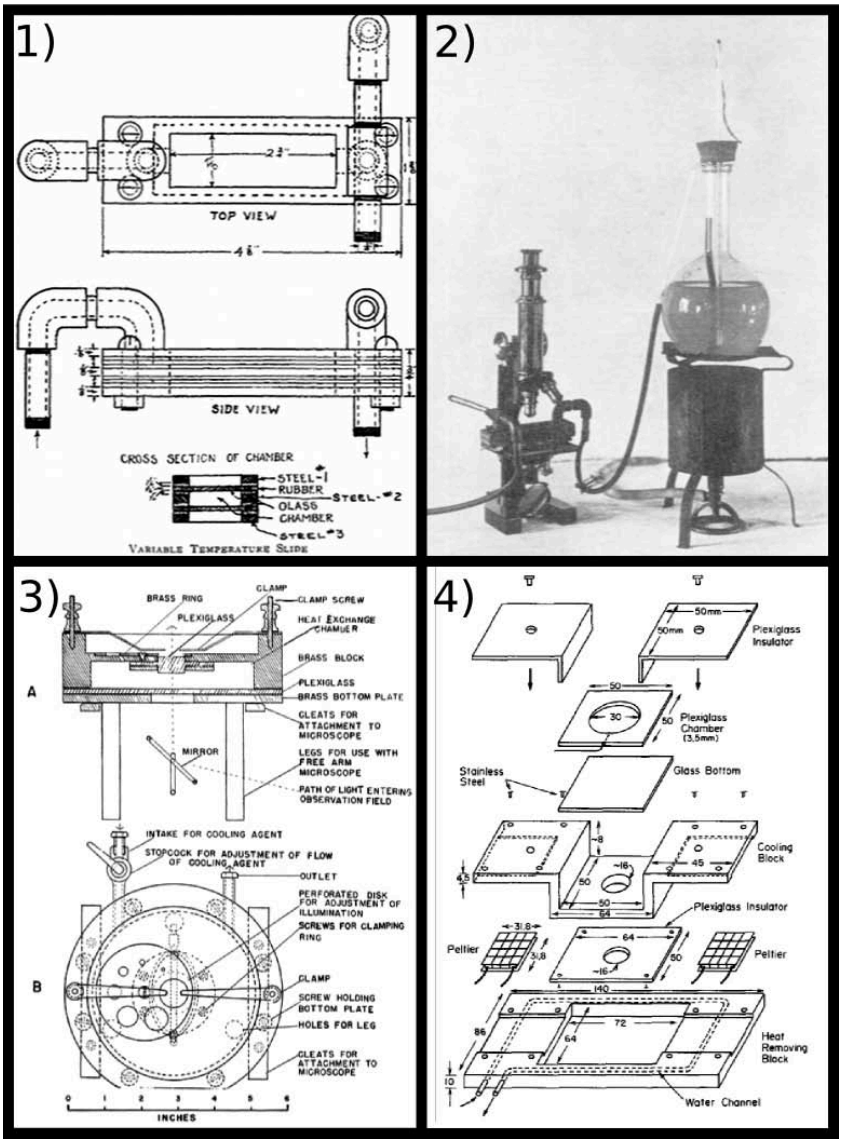

Figure 3.1: Figure showing selection of historical temperature controllers. 1) and 2) The slide based uid ow temperature controller from Francis and Smith (1916). 1) Shows the schematic of the slide mounted on the microscope and 2) shows the microscope slide mounted on the microscope, next to the heating mantle with hot uid. 3) Schematic for the stage based temperature controller of Krog and Simmet (1954) showing A) side view and B) top view. Water from mains supply ows through the chamber marked heat exchange chamber and can be either hot or cold. 4) Schematic of the Peltier based stage temperature controller of Chabala et al. (1985). Peltiers cool the stage on which the slide is mounted, and a water circuit cools the hot side of the Peltier.

ow towards the positive terminal, and the holes in the P-type material ow towards the negative terminal, causing heat to ow away from one side of the Peltier. This is shown in Figure 3.2. Temperature controlled microscopes using Peltier heat pumps were designed in the 1980s by Chabala et al. (1985). A stage based Peltier temperature controller was used to study temperature dependence of BFM rotation (Berg and Turner, 1993; Turner et al., 1996). Berg and Turner used a water-cooled Peltier to cool the stage and measure the temperature near the plates using two thermistors in a method from Khan and Berg (1983).

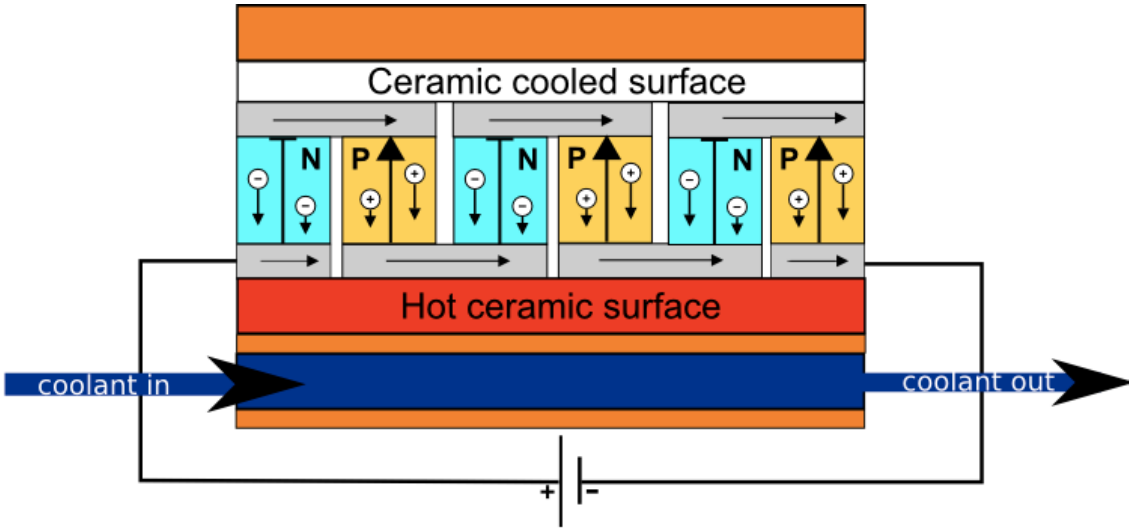

Figure 3.2: Schematic of a Peltier plate showing P-type and N-type junctions connected electronically in series but thermally in parallel. At an N-type junction electrons move towards the positive terminal, and likewise, at a P-type junction holes move towards the negative terminal, and both are located at the bottom of the plate with clockwise owing DC current. The top-side of the junctions, in close thermal contact with a ceramic plate, are cooled, and the bottom-side of the junctions, also in contact with a separate ceramic plate, are heated. When the Peltier collar temperature controller is operated in cooling mode the top of the plate is attached to a copper collar that cools the objective and the heat from the bottom plate is removed by a owing water coolant system. When the Peltier collar is operated with current owing the opposite direction, the owing water heats the cold bottom side, and the top side heats the objective and thus the sample.

When current ows through a circuit composed of two di erent semiconductors, heat will be absorbed at one junction and produced at the other depending on the direction and the magnitude of the current (the Peltier e ect (Callen, 1948)). The quantity of the heat pumped, Q, per unit time t, is proportional to the current, I:

$$P_p = \frac{Q}{t} = \quad I = S \quad T \quad I \tag{3.1}$$

where Π is the Peltier coefficient, S is the Seebeck coefficient, and T the absolute temperature.

Since an electric current is flowing in an homogeneous conductor in the direction of the temperature gradient, $\frac{dT}{dx}$, heat will be absorbed or produced depending on the material (Thomson effect), according to:

$$P_T = \tau \cdot I \cdot \frac{dT}{dx} \tag{3.2}$$

where τ is the Thomson coefficient. The direction of the heat flow depends on the sign of the Thomson coefficient, the direction of the current, and the direction of the temperature gradient.

Also the Joule heating from the electrical circuit must be considered, as well as thermal conduction of heat from the hot side to the cold side of the Peltier. With a current I, flowing in an isothermal conductor of resistivity R, we have:

$$P_J = R \cdot I^2 \tag{3.3}$$

and from heat conduction we have:

$$P_C = \kappa \frac{A}{d}(T_h - T_c), \tag{3.4}$$

where κ is the thermal conductivity, A the cross sectional area of the Peltier, and d the thickness of the Peltier plate.

The full equation describing the amount of heat that is removed on the cold side of the plate is (PHYWE, 2008):

$$P_{cool} = -[ST_C I \pm \frac{\tau I \Delta T}{2d} + \frac{1}{2} I^2 R - \frac{\kappa \cdot A \cdot \Delta T}{d}] \tag{3.5}$$

with contributions from the Peltier effect, the Thomson effect, the Joule effect and heat conduction respectively, and a negative sign because heat is absorbed on the cold-side. Likewise the heat produced on the hot side of the plate is:

$$P_{heat} = ST_C I \pm \frac{\tau I \Delta T}{2d} + \frac{1}{2} I^2 R - \frac{\kappa \cdot A \cdot \Delta T}{d}, \tag{3.6}$$

and the power supplied to the Peltier is:

$$P_{el} = SI\Delta T + \frac{\tau I \Delta T}{d} + I^2 R. \tag{3.7}$$

If the heat capacity of a system on either side of the plate is known, P_{cool} and P_{heat} can be approximated by considering the rate of change of temperature in the linear section of the curve, near ambient temperature, from:

$$P_{cool} = \frac{C_{total} \cdot \Delta T_C}{\Delta t}. \tag{3.8}$$

Temperature controlled microscopes using Peltier heat pumps were designed in the 1980s by Chabala et al. (1985). A schematic of the Peltier stage of Chabala et al. (1985) is shown in Figure 3.1. Khan and Berg (1983) used thermistors in early biophysics temperature experiments on ATPase in *Streptococcus*. This temperature measurement formed the foundation of the later temperature control experiments on the BFM performed by Turner et al. (1996) who used a water-cooled Peltier to cool the stage.

3.5 Feedback and Process Control

Traditional feedback circuits operate using proportional, integrative, and differential feedback (PID), to drive a system from a measured temperature to a set point temperature. The difference between the measured temperature and the set point is known as the error. Proportional feedback responds to the error at the current moment in time, integrative feedback responds to the sum of recent errors, and differential feedback responds to the rate of change of the error. Proportional feedback responds directly to the current error but scales it by a constant, K_p. Using only proportional feedback will result in an offset at a steady-state away from the set-point, but in most applications proportional feedback provides the bulk contribution to the tuning. Integrative feedback scales the feedback in a manner proportional to the integrated error over time. Using integrative feedback with proportional feedback moves a system more quickly towards the setpoint and removes the offset, but can introduce oscillations around the setpoint. Lastly, differential feedback scales the feedback proportional to the derivative of the error with respect to time, or the rate of change of the error. This is used to correct the oscillation and overshoot caused by the integrative term, however the derivative term is very sensitive and if the noise is high it can cause a process to become unstable. PID feedback calculates the total error based on a linear sum of proportional, integrative and differential errors. In equations:

$$P_{\text{out}} = K_p\, e(t) \tag{3.9}$$

$$I_{\text{out}} = K_i \int_0^t e(\tau)\, d\tau \tag{3.10}$$

$$D_{\text{out}} = K_d \frac{de}{dt}, (t) \tag{3.11}$$

where P_{out}, I_{out}, and D_{out} are the proportional, integrative and derivative contributions to the output respectively, and K_p, K_i, and K_d are the gains associated with each respectively. The three errors can be combined to form the final output, u(t):

$$\text{u(t)} = K_p e(t) + K_i \int_0^t e(\tau)\, d\tau + K_d \frac{de}{dt}(t) \tag{3.12}$$

For more information on PID systems and process control, including autotune algorithms, see Lipták (1995); Astrom and Murray (2008).

Various combinations of PID feedback, whether solely P, PI, or full PID feedback can be used depending on the application and most modern PID implementations can be autotuned using algorithms to optimise the constants K_p, K_i, and K_d. The standard autotune algorithm is Ziegler-Nichols which increases the gain on the proportional feedback, K_p until it reaches a critical value, K_C, at which the measured value oscillates around the set point with a constant amplitude. The period of this oscillation, T_C, together with K_C, is then used to set the values for K_p, K_i and K_d according to Table 3.1 (Ziegler and Nichols, 1993; Lipták, 1995).

Table 3.1: Ziegler-Nichols algorithm output after calculating K_C and T_C.

Control Type	K_p	K_i	K_d
P	$0.5K_C$	-	-
I	$0.45K_C$	$1.2K_p/T_C$	
D	$0.5K_C$	$2K_p/T_C$	$K_pT_C/8$

The first PID feedback I used to control the Peltier collar controller was a software implementation based upon the PID Toolkit component of NI LabVIEW 8.5. This PID feedback loop was autotuned using a Ziegler-Nichols algorithm on demand. Subsequently, this controller was replaced with an Oven Industries hardware controller (5C7-195, Oven Industries, US, see Section 2.1), which was tuned using a manual implementation of the Ziegler-Nichols algorithm to achieve minimum os-

cillation and rapid response times. The Oven Industries unit has three parameters: proportional bandwidth, integral gain and derivative gain. The proportional bandwidth was first set to 0.1 °C, which drove the unit at full power until the measured temperature is within 0.1 °C of the setpoint. Then the integral gain was increased slowly from zero to minimise oscillation around the set point, and finally the derivative gain was increased from zero slowly until the speed of the temperature change was maximised without introducing new oscillations.

3.6 Temperature Control and High Resolution Microscopy

The drive towards increased resolution involving high NA objectives and optical traps to measure position across nanometer scales has meant that immersion-oil objectives are now standard in the high resolution microscopes used for biophysical measurements. If there is good thermal contact between an objective and a sample then to cool a sample sufficiently either the objective must be cooled or the cooling component of a temperature controller must be in as good, or better, thermal contact with the sample as the sample is with the objective. Equally, the proximity of the objective to the sample renders the objective a perfect site for cooling. Heating and cooling the objective, however, comes at the possible cost of degradation or even destruction of the optics.

3.6.1 Stage Cooling

Stage cooling has been used with non-immersion oil objectives for many years (Berg and Turner, 1993; Turner et al., 1996) but stage cooling in tandem with a 100× immersion objective has not. Our collaborators Dr Yuichi Inoue and Dr Akihiko Ishijima developed a fluid chip method that uses a microfluidic device to heat and cool a microscope sample using a highly portable custom chip in the place of a microscope slide. It can be used to make high and low temperature measurements on a wide variety of microscopes without making changes to the microscope, however the temperature range is limited and the proximity of the objective prevents cooling below 6°C. The chip is ideal for making multiple measurements at an approximately fixed temperature, but is less suited for making measurements at a range of temperatures since that would require altering the fluid reservoir temperature or flow rate. Precise control ±1°C is difficult to achieve due to varied heat loss from the

tubing connecting the reservoir to the chip. Also, it is di cult to maintain constant temperatures at high and low extremes due to heat change at the reservoir, and the chip itself may be easily broken if roughly handled. These disadvantages are o set, however, by the low cost (only glass slides, tubing and bottles are required), fast response, and ease of implementation. A schematic of this temperature controller is shown in Figure 3.3.

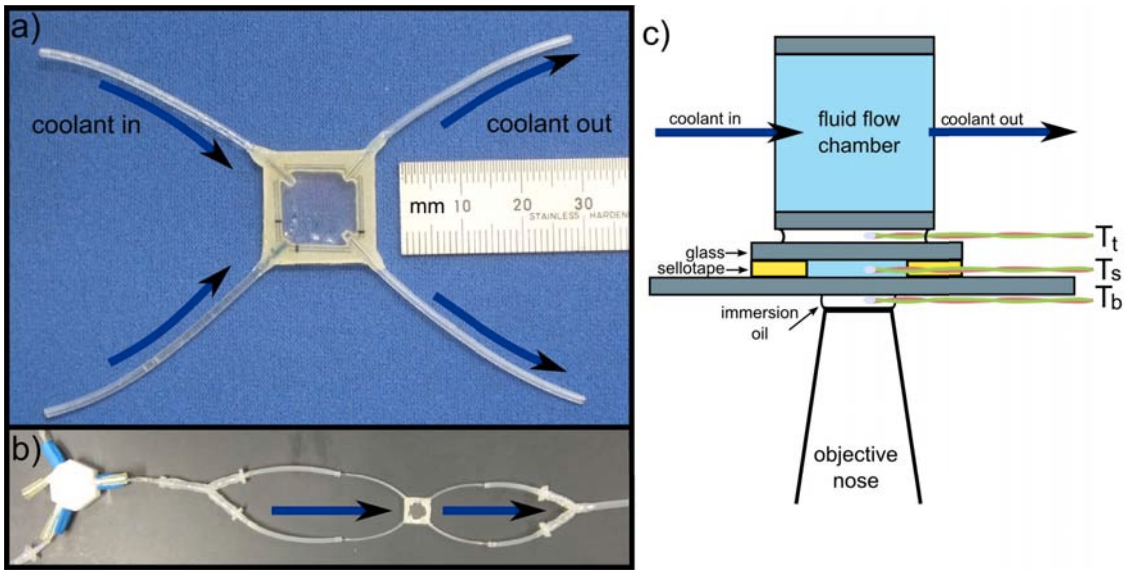

Figure 3.3: a)Top view of the uid ow cooling chip. The uid is pumped across chip from left side to right side. b) Fluid ow chip and switching gate. A switching gate switches ow from reservoirs of hot (70 C) or cold (-20 C) water, and uid is split into two channels using Y-type connectors to make cooling more homogeneous across the chip. The chip cools or heats the sample by placing a large volume of water in close thermal contact to the sample. c) Scale schematic of the uid chip temperature controller with 20:1 vertical:horizontal expansion. The three locations at which temperature was measured are indicated by the thermocouples (top: T_t; sample: T_s; bottom T_b). Two of these are measured simultaneously to determine sample temperature as shown in Figure 3.6. Schematic drawn by the author, photographs of apparatus taken by Dr Yuichi Inoue.

This thesis will not outline the methods and performance of the uid chip, however it will include original analysis of the calibration and thermal circuit for the uid chip controller (Section 3.9.3). This is useful to compare the properties of stage based temperature controllers with the objective based temperature controller constructed for this thesis, and to propose construction guidelines for each type of temperature controller.

3.6.2 Objective Cooling

Objective cooling was first suggested by Lambert and Bajer (1977). They used low rate water flow (80 mL/min) in a cooling coil around a low NA objective to investigate arrest of chromosome movement at low temperature. More recent temperature controllers have explored high NA objective cooling more closely. Rabin and Podbilewicz (2000) built a custom heat exchanger for the objective and used water flow to cool both the stage and objective to observe the temperature dependence of elongation of *C. elegans*. Mao et al. (2005) and used a pair of water cooled collars on two 60× water immersion objectives sandwiching the sample to observe the folding and unfolding of DNA at different temperatures. Thermal currents were reduced by using a sandwich of two cooling elements to eliminate first order temperature gradients at the sample. They measured the heat stress felt by the objective in terms of focus drift, which they recorded as ≈ 20 μm movement for every 10 °C temperature change. This required the realignment of the optics each time a new temperature was set rendering it difficult to take biophysical measurements during temperature transients. Mao et al. (2005) considered Peltier plates too large for use in objective cooling but newly available commercial Peltiers led Komarova et al. (2009) to use a Peltier-driven collar attached to the nose of a microscope objective. They used the Peltier device to maintain the temperature at 25 °C while observing microtubule dynamics, but not to cool the sample below room temperature. Furuike et al. (2008) used two water cooled objectives to control the temperature between 4 °C and 50 °C to study the kinetics of F_1-ATP-ase.

For this thesis I designed and built a rapid (± 20 ^{o}C in 200 s) microscope temperature controller using a high magnification objective. The method uses a water-cooled ring-shaped Peltier mounted on an objective collar, with a thermocouple temperature sensor mounted in this collar and calibrated to the sample using known melting points of waxes. This method has a PID feedback circuit controlling the Peltier current in response to the sensor temperature. The collar must be made to fit a specific objective, and can actively heat or cool to any desired temperature within range (0 ^{o}C - 50 ^{o}C). The calibration, response and efficacy of the controller is demonstrated in this Chapter.

3.7 Temperature Control and the Bacterial Flagellar Motor

The first temperature experiments on bacterial flagella were performed by Pijper et al. (1956). Pijper (1955) built a heating and cooling device on a microscope stage similar to the setup of Krog and Simmet (1954), and Pijper et al. (1956) used this temperature controller to probe the wavelength of the helix of the flagella of bacteria at different temperatures.

The first efforts to apply temperature control specifically to the motor were by Berg and Turner (1993). Berg and Turner explored how the mechanics of the motor, specifically the torque speed relationship, changed with temperature in the wild-type BFM. They used a microscope equipped with a calibrated temperature controller that cooled both the objective and the stage, using a water-cooled Peltier element and two thermistors from Khan and Berg (1983), one near the Peltier element in the control feedback circuit and the other next to the slide. A separate temperature calibration was performed using a smaller thermistor at the tethering site, with silicon oil substituted for the tethering buffer. Temperatures set with the control feedback circuit stabilized within 1 min. These measurements were taken using a 40× objective not in contact with the sample as they were observing rotation speeds and directions of tethered cells ≈ 1 μm in size. Their results are discussed in Section 4.2.2.

3.8 Methods

Materials and methods are detailed in full in Section 2.1, with a schematic and photograph of the device. The design drawings of the Peltier collar itself are included in Appendix A.

3.9 Results

3.9.1 Prototype Temperature Controllers

Stage based temperature control was explored when designing the temperature controller used in this thesis. A custom built stage was made with two water-cooled Peltier elements cooling the aluminium stage on which the microscope slide and sample rested. This avenue proved fruitless however as the close proximity of the

room temperature objective to the focus meant that in order to cool below 10 °C the stage had to be cooled below -5 °C, introducing complications due to condensation, which froze as ice, and large thermal currents. Figure 3.4 shows the temperature relationship between stage and slide temperature using a prototype stage cooling device. The temperature in the back of the slide was measured using a K-type thermocouple with digital thermometer (206-3722, RS, UK) through a hole drilled in the back of the sample slide. This had a large variation depending on the depth of the probe, and was a misestimate of the sample temperature as it only measured the slide temperature and not the coverslip in contact with the objective. Using waxes, as described in Section 2.1.2, it was not possible to solidify pentadecane (melting point 5.5 °C) even when the stage was cooled to -15 °C, which indicates that the thermistor-slide measurement was not accurate, and that stage-only cooling would not be suitable for cooling a BFM on a surface bound cell to 5 °C.

Objective temperature control was first attempted using water circulating through a collar (Objective Collar, 150303, Intracel, UK) resting around the objective. Fluid was cooled using a custom heat exchanger built from Peltier plates and computer overclocking components (Thermaltake, USA). The temperature was found to be highly dependent on the distance of the heat exchange block (fluid to Peltier interface) from the objective, and the insulation of the piping. Response times were too slow: ∼10 minutes for a 20 °C temperature change. Annular Peltier plates later moved from being available only for custom Peltier designs to the general market, and so I chose to use one to build the Peltier collar already described in Section 2.1. The properties and temperature response of this collar are described in the following Sections 3.9.2–3.9.5.

3.9.2 Calibration of the Sample Temperature

The linear relation between the temperature of the collar and the sample is shown in Figure 3.5, using the method described in Section 2.1.2. During biophysical measurements only the temperature of the collar (T_c) is used to estimate sample temperature (T_s). The linear fit of the collar temperature to the sample temperature is used to calculate the relationship:

$$T_s = (0.843 \pm 0.016) \times T_c + (3.8 \pm 0.5)\ ^\circ\mathrm{C}. \tag{3.13}$$

Similarly, for the fluid chip the relationships between three temperatures are shown in Figure 3.6 (T_s, measured with a thermocouple in the sample; T_t, measured

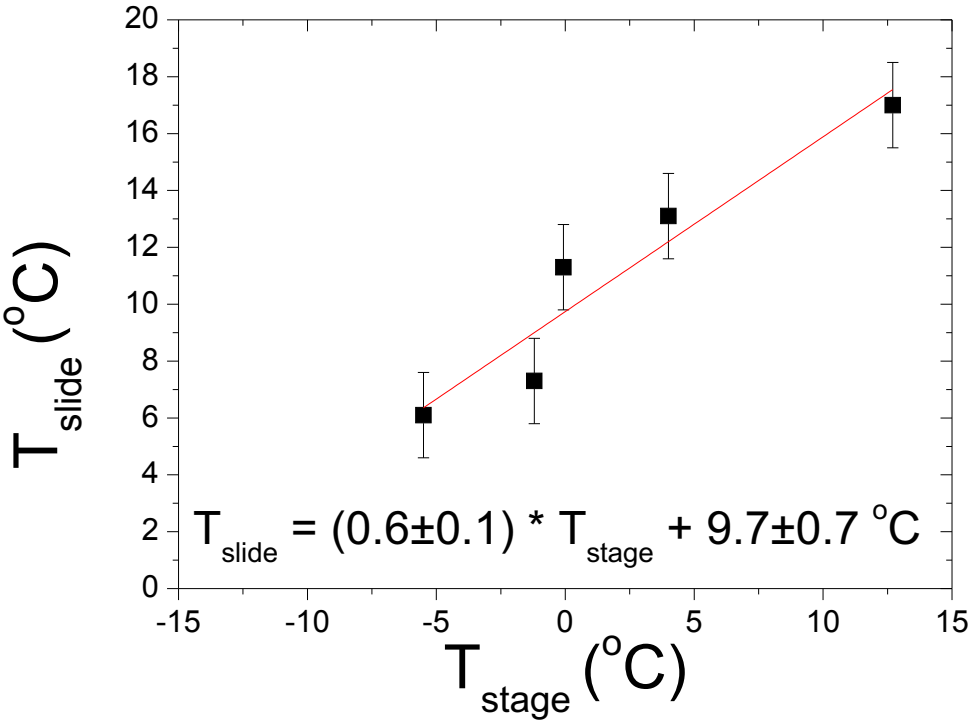

Figure 3.4: Temperature relation (black squares) between back of slide and stage when cooling the aluminium stage and slide holder with two Peltier plates. A hole was drilled in the back of the slide so that a thermistor probe could be placed in the back to approximate the sample temperature for a variety of stage temperatures. Linear fit is shown in red. The slide temperature was offset from the stage temperature by 10 °C (linear fit intercept), which implies that in order to cool the slide to 5 °C the stage would have to be at ∼-7.7 °C. Wax measurements indicated that the temperature on the coverslip, which was warmer than the measured slide temperature, was not cooled to 5.5 °C even when the stage was cooled to -15 °C.

between the chip and the sample; and T_{b}, measured between the objective and the sample). During biophysical measurements only the temperature measured at the site above the sample (T_{t}) is used to estimate the sample temperature from the calibrated relation derived from the linear fits:

$$T_{\mathrm{s}} = (0.743 \pm 0.006) \times T_t + (6.7 \pm 0.2)\ ^{\circ}\mathrm{C} \quad (3.14)$$

$$T_{\mathrm{b}} = (0.378 \pm 0.006) \times T_t + (13.9 \pm 0.2)\ ^{\circ}\mathrm{C} \quad (3.15)$$

The lower limit of sample temperature using coolant at -20 °C was 6 °C, but the typical temperature induced was 6-10 °C. In practice T_{s} varied ±1 °C between different runs at the same nominal flow rate restricting the ease with which the fluid

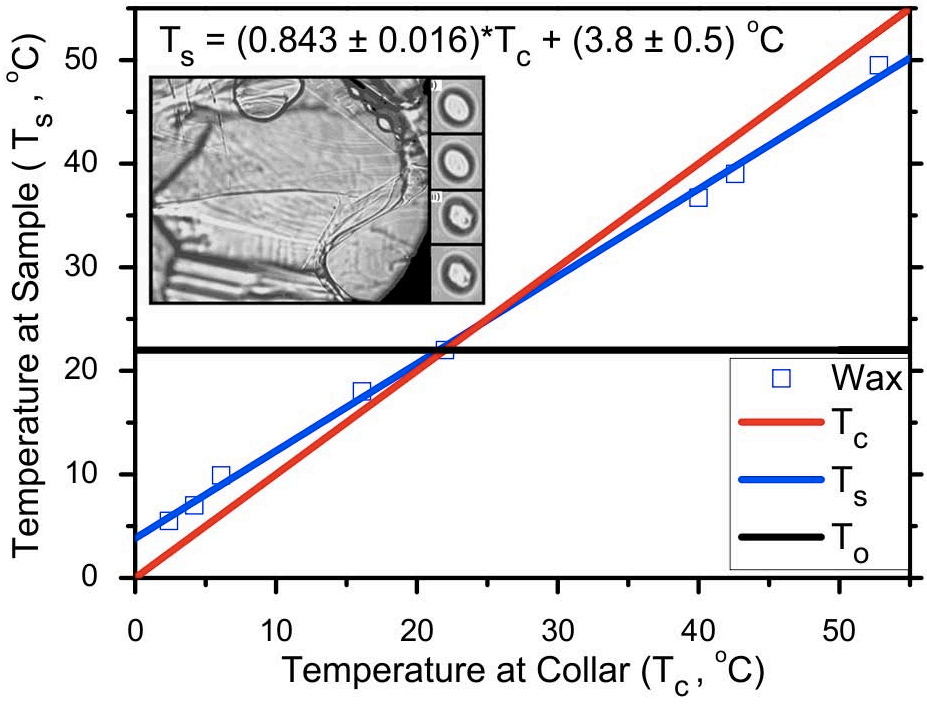

Figure 3.5: Linear relationship between the temperature as measured on the coverslip using of known melting point, and measured on the collar using a thermistor. An additional point is included at steady-state room temperature ($T_0 = 22$ C) where the two temperatures are equal. The inset shows a chamber entirely full of wax during a phase transition from solid to liquid, and also i) two spherical droplets in the liquid phase, ii) two jagged crystals in the solid phase. Temperatures at the collar and at the sample were measured with a precision of 0.1-0.2 C, and the error for the melting points of the waxes are 0.1 C thus error bars are too small to be displayed.

chip can be set to a speci c sample temperature.

3.9.3 Analysis of the Thermal Circuit

This method works by pumping heat into or out of the sample through the objective underneath the sample. Heat ows obey a linear relationship analagous to Ohm s Law for electrical currents, $Q = T R$, where Q is the rate of heat ow through an element with thermal resistance R spanning a temperature di erence T. This relationship can be used to calculate the relative thermal resistances of di erent components of each system. Figure 3.7 displays a schematic and thermal circuit diagram for both systems.

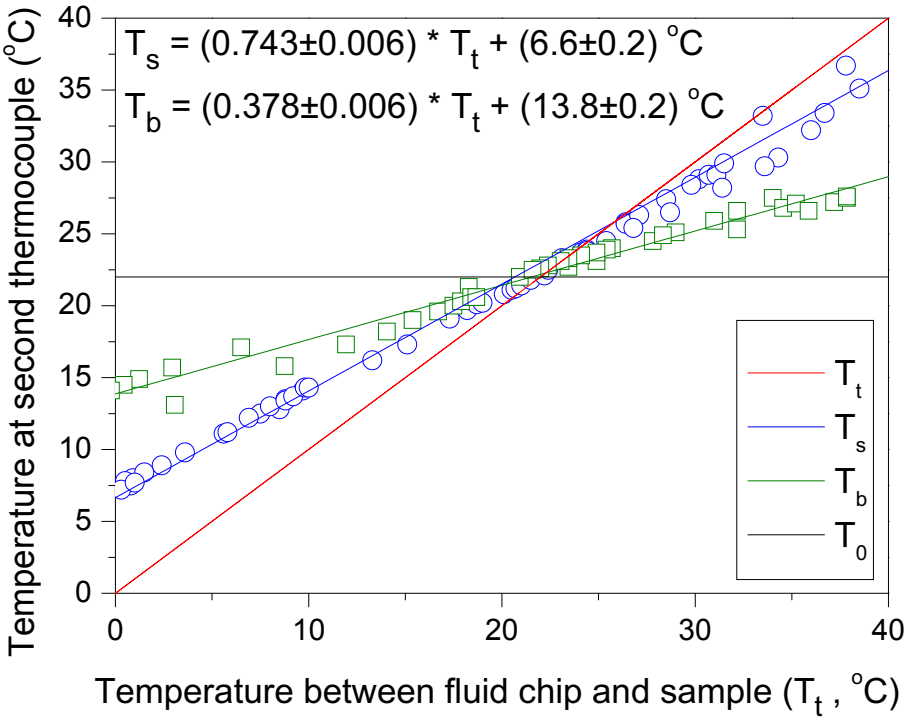

Figure 3.6: Linear temperature relations between the three sites used to measure temperature for the chip temperature controller. The temperature was measured simultaneously by thermocouples at two out of three locations: T_t, between the chip and the sample (red), T_s, inside the sample (blue), and T_b between the sample and the objective (green). Steady-state room temperature at 22 °C is shown in black. Temperatures from the thermocouple were measured with a precision of ± 0.1 °C and so error bars are not displayed here.

In the case of the Peltier collar method, the effectiveness of the system requires that the objective is in closer thermal contact with the sample than the sample is with the stage and surrounds ($R_\mathrm{s} \gtrsim R_\mathrm{o}$). With the surrounds at T_0 we may write:

$$T_\mathrm{s} = T_\mathrm{o} + \frac{R_\mathrm{s}}{R_\mathrm{s} + R_\mathrm{o}}(T_\mathrm{c} - T_0) = T_0 + \alpha(T_\mathrm{c} - T_0) \tag{3.16}$$

following from a direct analogy to an electrical potential divider, where $\alpha = R_\mathrm{s}/(R_\mathrm{s} + R_\mathrm{o})$. A linear fit to the blue line in Figure 3.5 gives $\alpha = \frac{dT_\mathrm{s}}{dT_\mathrm{c}} = (0.843 \pm 0.016)$, indicating that $R_\mathrm{s}/R_\mathrm{o} = \alpha/(1-\alpha) = 5.37 \pm 0.14$.

In the case of the fluid chip, the efficacy of the system is dependent on the thermal contact between the chip and the sample relative to that between the sample and the objective plus stage as shown in Figure 3.7 ($R_\mathrm{os} \gtrsim R_1$). Similarly to Eq. 3.16,

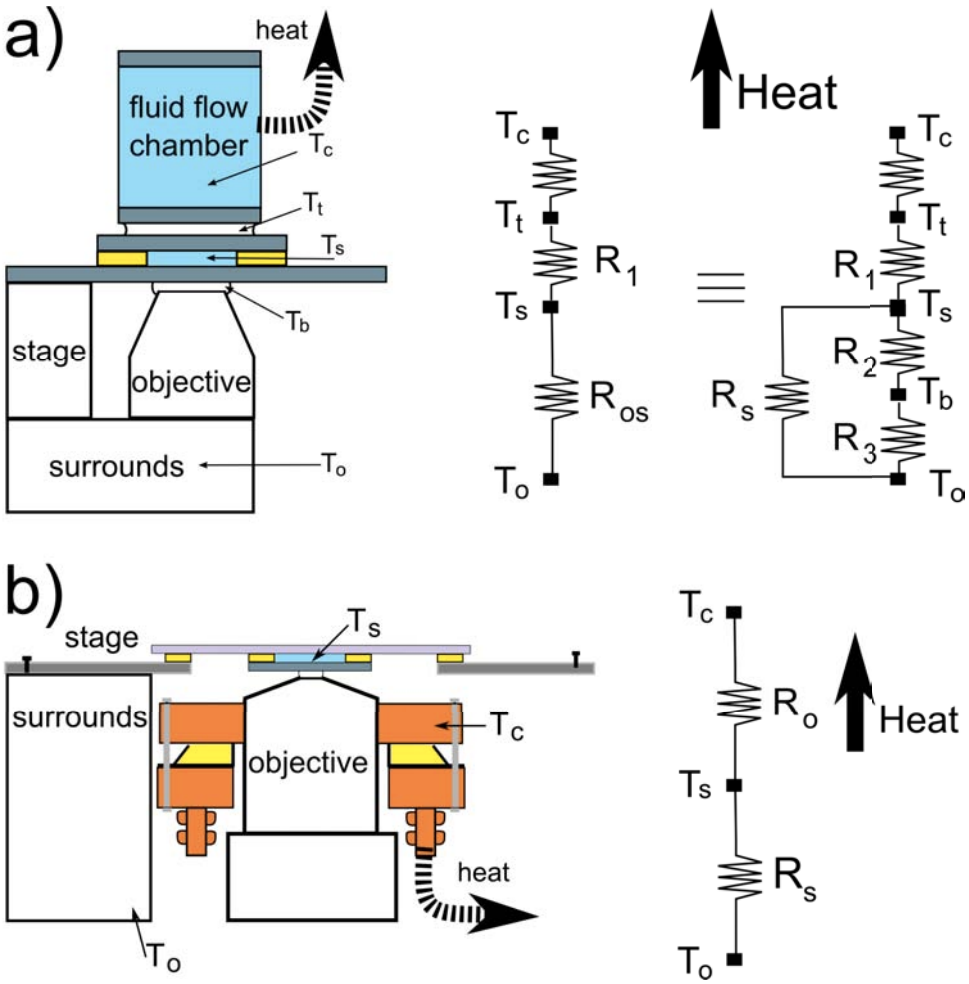

Figure 3.7: a) Left) schematic of the uid chip controller operating in cooling mode. Heat ows into the sample from the surrounds (T_0) through the stage and objective, which are in thermal contact with the sample. Heat ows out of the system through the cooling chip. The 5 locations shown in the circuit diagram are indicated. Middle) Thermal circuit diagram for the uid chip temperature controller. R_{os} $R_1 = 2\ 89$ $0\ 03$ is calculated as shown in the text. Right) The full circuit diagram including all measurement sites.
b) Left) Schematic for the Peltier collar temperature controller in cooling mode. Heat ows into the sample from the surrounds (T_0) through the stage, which is in thermal contact with the surrounds. Heat ows out of the system through the Peltier device located in the collar, which acts as a heat pump pumping heat out of the system. Right) Thermal circuit for the Peltier collar. R_s $R_o = 5\ 37$ $0\ 14$ is calculated as detailed in the text.

we may write:

$$T_s = T_0 + \frac{R_{os}}{R_1 + R_{os}}(T_t - T_0) = T_0 + \alpha(T_t - T_0) \tag{3.17}$$

which, using a linear fit to the blue line in Figure 3.6, gives $\alpha = \frac{dT_s}{dT_t} = 0.743 \pm 0.016$ and subsequently $R_{os}/R_1 = \alpha/(1-\alpha) = 2.89 \pm 0.03$.

Measurement of T_b (Figures 3.3 and 3.6) allows analysis of the thermal circuit of the fluid-flow chip if we assume that $R_s \gg (R_2 + R_3)$. Similarly to Equations 3.16 and 3.17 we may write:

$$\begin{aligned} T_s &= T_b + \frac{R_1}{R_1 + R_2}(T_t - T_b) = T_b + \alpha(T_t - T_b) && (3.18)\\ &= T_b(1-\alpha) + T_t\alpha. && (3.19) \end{aligned}$$

Since $T_b = m_1 T_t + b_1$, where $m_1 = (0.378 \pm 0.006)$ and $b_1 = (13.9 \pm 0.2)$ °C, and $T_s = m_2 T_t + b_2$, where $m_2 = (0.743 \pm 0.006)$ and $b_2 = (6.7 \pm 0.2)$ °C (from linear fits in Fig 3.6), we have:

$$\begin{aligned} \frac{dT_s}{dT_t} = m_2 &= m_1(1-\alpha) + \alpha && (3.20)\\ \Rightarrow \alpha &= 0.587 \pm 0.010 && (3.21) \end{aligned}$$

which gives $R_1/R_2 = \alpha/(1-\alpha) = 1.42 \pm 0.02$. Note that T_b differs substantially from T_0 (22 °C) indicating considerable heat flow through the objective in the fluid chip method. Also the large difference between T_t and the input temperature of the coolant (either 70 °C or -20 °C) indicates temperature gradients in the coolant fluids which depend on flow rate, tubing insulation, and distance from the reservoir.

3.9.4 The Time Response of the Peltier Collar Temperature Controller

The time responses of the Peltier collar for cycles between room temperature (22 °C) and 2 °C or 40 °C are shown in Figure 3.8a. One to two minutes were required to change the temperature by 20 °C to or from room temperature, depending on the duration of the previous change and the history of the temperature changes. The measurements shown in Figure 3.8b show time taken to drive the system away from a steady state room temperature equilibrium of 22 °C. If the system is kept at 40 °C for long times before performing temperature cycles starting at 22 °C then the response

times change. For a system kept at 40 °C for over 10 minutes, which is then returned to 22 °C and used to measure full cycles from 22 °C up to 40 °C and from 40 °C down to 22 °C, the response times were 46 s and 93 s respectively. This can be compared with 99 s and 71 s respectively for a system kept in long term equilibrium at room temperature. This is because heat is retained in the system (microscope, objective and stage) when it is maintained away from room temperature for a length of time. The change in response time for cooling from 22 °C to 2 °C and heating from 2 °C to 22 °C were similar on the 40 °C pre-equilibrated microscope and the room temperature pre-equilibrated microscope. Figure 3.9 shows the temperature response of the Peltier collar for a system that has been kept at 40 °C for 15 minutes prior to temperature change.

Initially the Peltier collar input voltage was controlled by a LabVIEW software PID circuit, with voltage amplified by a custom built DC amplifier which could drive a maximum of 2.6 A and 2.7 V. The response times for this system are slower, $\sim 1.5\times$, leading to the adoption of a dedicated Oven Industries power supply with PID circuitry built in. The response times for the LabVIEW system are shown in Figure 3.10.

3.9.5 Noise of the Temperature Controller

Position detection noise profiles were measured for surface immobilised beads with the Peltier and coolant flow on, and with both the Peltier and flow off. One second of position data was split into 10 fragments of 0.1 s. The power spectrum was calculated over all these fragments and averaged to produce a smoothed power spectrum from 10 Hz to 500 Hz. The power spectrum, both averaged over 10 fragments and the entire power spectrum of the full 1 s trace, between 10 Hz and 500 Hz, is shown in Figure 3.11. The averaged noise profile over the full frequency range permitted by the sampling rate (1 Hz to 50000 Hz) is shown in Figure 3.12, as log-log and linear-log plots. The temperature controller does not add significantly to the noise of the system, with noise levels below 0.01 $nm^2\ Hz^{-1}$ at frequencies between 10 and 500 Hz, and below 0.0001 $nm^2\ Hz^{-1}$ for frequencies between 500 and 50000 Hz). The spikes at high frequency (>20 kHz) are independent of the temperature controller and arise from high frequency variations in the mean intensity of the bead signal.

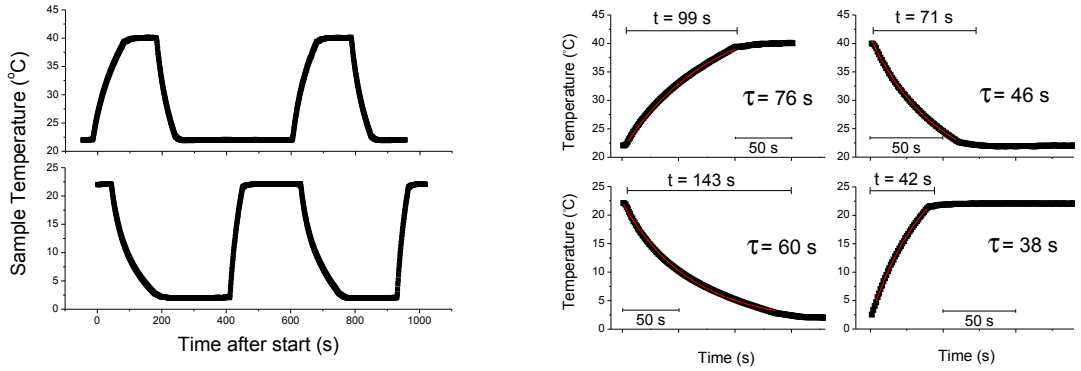

(a) (b)

Figure 3.8: (a) Cycling of collar temperature from room temperature (22 °C) to 40 °C and then from room temperature to 2 °C, using Peltier-driven collar, powered by Oven Industries PID Controller (maximum output 4.0 A, 6.5 V). (b) Closer detail of heating and cooling with exponential fits and durations for temperature response. Exponential fits are taken when the Peltier is being driven at maximum power, and represent the time constant for the exponential curve describing the long term equilibrium temperature when the Peltier is run at full power. In practice, the PID controller reduces the power as the set point is approached, and so the duration of the change is also indicated as a measure of the controller's performance. Durations are measured as time taken to complete 95% of the temperature change. All measurements are taken with the microscope at equilibrium at 22 °C and then driven to 40 °C or 2 °C respectively, and then driven back to room temperature at 22 °C.

3.10 Discussion

The recent advent of cheap commercially available ring-shaped Peltier plates means that Peltier cooling of objectives is a suitable approach for microscope cooling. Mao et al. (2005) showed the advantages of objective cooling systems, namely a fast heat exchange between sample and objective, a wide range of accessible temperatures, and, when using a sandwich of two objectives, high temperature uniformity throughout the sample. My work extends objective temperature control with rapid electronically moderated PID feedback. I have demonstrated its function over a range of temperatures, in contrast with Komarova et al. (2009) who used Peltier control only to stabilize a sample at 25°C. The Peltier controller is capable of heating or cooling by 20 °C in approximately 2 minutes, down to a minimum temperature of -1.6 °C with ice water flowing, and could reach colder temperatures with a salt/ice or antifreeze coolant. Extreme heating and cooling is in practice limited by the strength of the objective to withstand large temperature stresses (Leake, 2001). In compar-

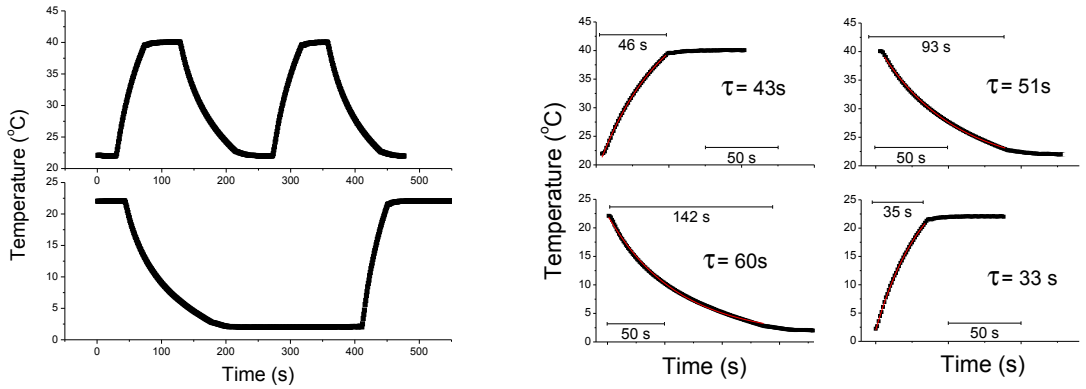

(a) (b)

Figure 3.9: (a) Cycling of collar temperature from room temperature (22 °C) to 40 °C and then from room temperature to 2 °C, using Peltier-driven collar, powered by Oven Industries PID Controller (maximum output 4.0 A, 6.5 V), for a microscope that has been maintained at 40 °C for 15 minutes prior to these measurements. (b) Closer detail of heating and cooling with exponential fits and durations for temperature response. Exponential fits are taken when the Peltier is being driven at maximum power, and represent the time constant for the exponential curve describing the long term equilibrium temperature when the Peltier is run at full power. The duration of the change is also indicated as a measure of the controllers performance. Durations are measured as time taken to complete 95% of the temperature change. In a pre-heated system like this, response from 40 °C to 22 °C takes 22 s longer, and while heating from 22 °C to 40 °C is 53 s quicker. Cooling from 22 °C to 2 °C and heating from 2 °C to 22 °C takes a similar amount of time as in the microscope equilibrated at room temperature.

ison the controller of Mao et al. (2005) requires 20 minutes to reach equilibrium at a new temperature, to a minimum of 4.5 °C. Additionally the temperature is measured using a wax technique adapted from Berg and Turner (1993), instead of a thermocouple, which gives more accurate calibration of the temperature of the microscopic sample itself. Mao et al. (2005) achieved high homogeneity of temperature (±0.1 °C throughout 2 mm × 2 mm) due to using a sandwich of two objectives, one in place of a condenser, thus controlling the temperature from the top and bottom simultaneously. This would be possible as an extension for my system if chamber homogeneity was desired, using a second Peltier collar operating on an objective over the sample, or using a stage cooling apparatus, such as the fluid chip, in tandem. The collar method has z-directional drift, observed as a focus-drift at the sample, of ≈5 μm/°C in comparison with ≈2 μm/°C for Mao et al. (2005). Thermal expansion and contraction in z also slightly affects x,y-directional drift (≈0.1 μm/°C) due to the stage and slide not being perfectly level with respect to the microscope objective.

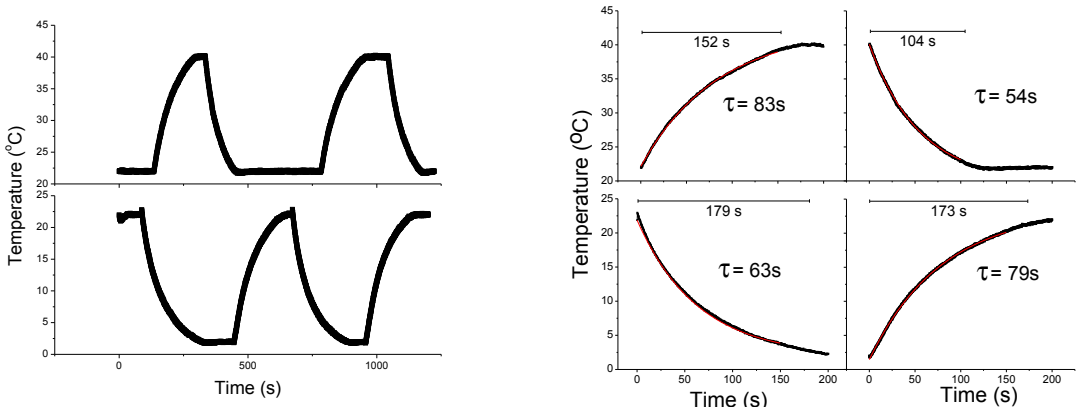

(a) (b)

Figure 3.10: Cycling (a) and temperature response (b) of collar temperature from room temperature (22 °C) to 40 °C and then from room temperature to 2 °C, using PID feedback controlled from LabVIEW software and a DC amplifier (maximum output 2.6 A and 2.7 V). Exponential fits are taken when the Peltier is being driven at maximum power, and represent the time constant for the exponential curve describing the long term equilibrium temperature when the Peltier is run at full power. Durations were measured as time taken to complete 95% of the temperature change. Heating and cooling times are significantly slower than using the Oven Industries controller: heating 22–40 °C took 53 s longer, and cooling 22–2 °C took 36 s longer.

Focus was adjusted manually to account for drift using the piezostage controller for continuous recording during temperature transients. Automatic tracking could easily be implemented, for example, by using a second laser to track the position of a bead on the surface of the coverslip, if this were desired. Lastly the Peltier plate used in this thesis can maintain a heat difference across the plate of $\Delta T_{\max} = 74$ °C with a maximum power of 35 W. Future improvements in Peltier technology should provide higher power Peltiers in myriad shapes for custom temperature control solutions over a range of temperatures.

In the objective controller the thermal resistance between the sample and the environment was shown to be $\sim 5\times$ greater than that between the sample and the objective. For a fluid chip stage-based temperature controller it was shown that the thermal contact between the sample and the chip is at most $\sim 3\times$ greater than that between the sample and the objective. These observations may serve as guidelines for temperature controller construction. If a stage-based heat pump cannot be constructed so that $R_{\mathrm{os}}/R_1 < R_{\mathrm{s}}/R_o$ then it will not prove effective, as the objective is a large heat source or sink in proximity to the sample.

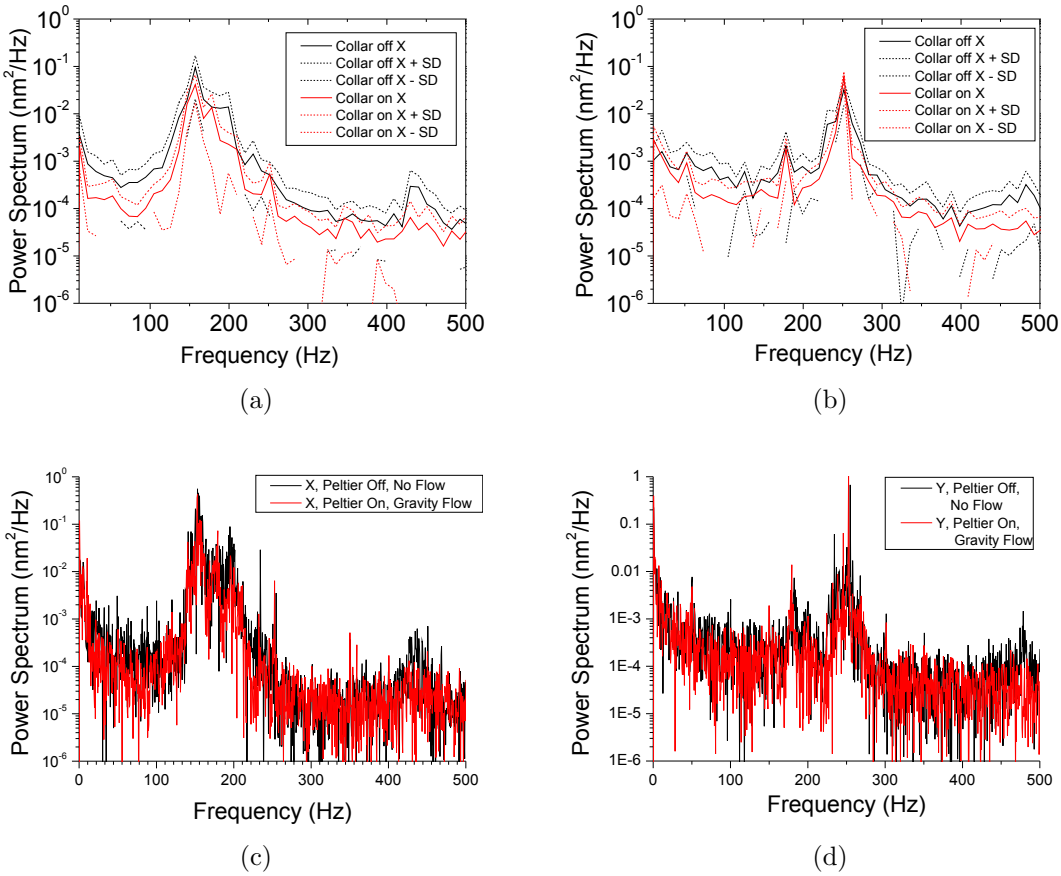

Figure 3.11: Position detection measured at quadrant photo-diode (QPD) for noise profile power spectrum of the x-position (a,c) and y-position (b,d) of a surface bound bead with Peltier and gravity flow on (red), and off (black) for the Peltier Collar controller. Data is sampled at a rate of 105 kHz, and the mean power spectrum is calculated over ten concurrent recordings of 0.1 s each (a, b), and over a full 1 s recording (b,d). Data is shown from 10 Hz up to 500 Hz. Dashed lines (a,b) show the upper and lower error bounds (± SD) on each noise trace calculated from the standard deviation over all 10 measurements.

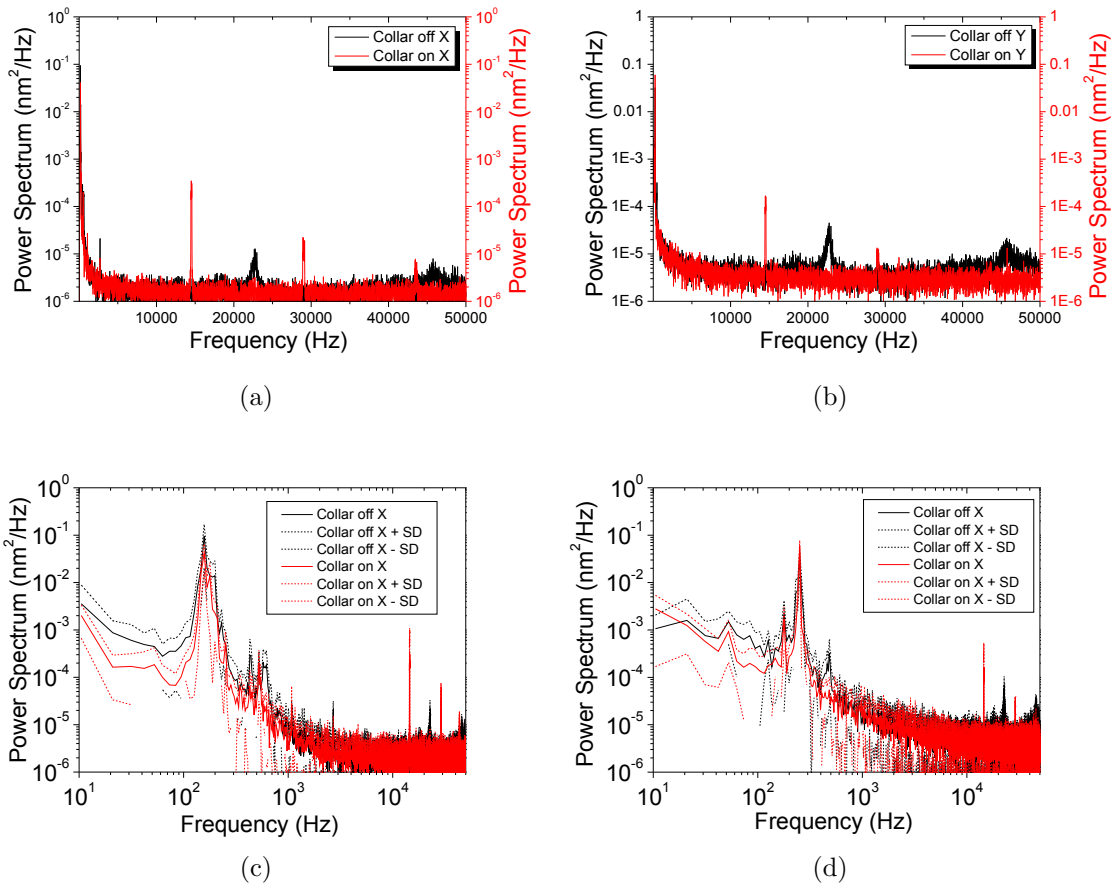

Figure 3.12: Noise profile for the Peltier collar temperature controller. Power spectrum of the x-position (a,c) and y-position (b,d) is calculated from position detected by QPD. Noise profile is with Peltier and gravity flow on (controller on: red), and Peltier and flow off (controller off: black) for the Peltier Collar controller. (c,d) Log-log plots of power spectra. Data is sampled at a rate of 105 kHz, and the mean power spectrum is calculated over ten concurrent recordings of 0.1 s each. Data is shown for full range of 10 Hz to 50000 Hz. Dashed lines show the upper and lower error bounds (± SD) on each noise trace calculated from the standard deviation over all 10 measurements.

3.11 Conclusions

Temperature control consists fundamentally of pumping heat into or out of a sample while measuring the temperature response. In this Chapter the Peltier collar temperature controller was introduced, capable of controlling the temperature up or down from room temperature by 20 °C in under 2 minutes, driven by a Peltier heat pump located around the objective. The relative thermal resistance between the sample and the objective, and the sample and surrounds, was calculated as $R_s/R_o = 5.37$. In the subsequent chapters this temperature controller will be used to cool and heat the flagellar motor and observe the effect on torque, speed, and voltage, including transient effects during a temperature change. The next chapter discusses the reduction in speed and torque when the flagellar motor is cooled.

Chapter 4

The Dependency of Torque and Speed on Temperature

From the perspective of the engineer or automechanic the bacterial flagellar motor (BFM) is remarkable: That a device only 40 nm in diameter is capable of rotating at up to 60000 rpm and exerting torques of 5000 pNnm is difficult to comprehend. By comparison a modern Formula 1 engine only rotates at 21000 rpm and exerts torques of 270 Nm. Of course, the BFM is not rotating in air, or turning the driveshaft of a vehicle, it is rotating in the membrane, in an environment rife with fluctuation. Consideration of the mechanical aspects of the motor, such as the speed and torque produced, and how these vary over the motor's range of operation, are fundamental characteristics of any motor.

This chapter discusses the experiments performed using my custom built temperature controller to probe the temperature dependence of the rotation of the bacterial flagellar motor. In particular I investigate the effects of cooling on torque and speed to produce torque-speed curves at low stator number and low temperature (Section 4.4.4). The decrease in the stability of BFM rotation at low temperature interfered with the recording of these measurements and so a new technique was developed to measure the single stator speeds at low temperature involving tracking a motor down from room temperature to the colder temperatures (Section 4.3.2). This instability, and possible causes, is discussed in Section 4.4.1 and finally hysteresis effects at low temperatures are discussed (Section 4.4.6).

4.1 Torque

Torque is the rotational analogue of force. It is defined in terms of the force exerted at the end of a lever to apply a rotational drive, such as a spanner tightening a nut.

Torque, $\boldsymbol{\tau}$, can be defined as:

$$\boldsymbol{\tau} = \mathbf{r} \times \mathbf{F}, \tag{4.1}$$

where $\mathbf{r}$ is the position vector of the particle relative to the axis around which torque is applied, and $\mathbf{F}$ is the force acting on the particle. Subsequently the work, W, can be defined as:

$$W = \int_{\theta_1}^{\theta_2} \tau \, \mathrm{d}\theta, \tag{4.2}$$

where a torque acts through a rotational angle θ_1 and θ_2. The power is the work per unit time:

$$P = \boldsymbol{\tau} \cdot \boldsymbol{\omega}, \tag{4.3}$$

where ω is the angular speed.

The torque speed curve is a plot that represents the torque output from the motor at different speeds. When the motor is stalled, or stationary, then this corresponds to the so called *stall torque*, τ_s. This is frequently a maximum torque as all the power from the motor is going into torque, and none into rotation.

Finding the relationship between torque and speed is a means to quantify the cycle of any motor. A motor's basic function is to turn electrical or chemical energy into mechanical work, and motors are used everywhere in everyday life - in air conditioners, cars, trains, watches - in almost any modern electrical device. The simplest motor is the direct current (DC) motor. This device works by supplying direct current to a coil, inducing a magnetic field which interacts with fixed magnets to drive the rotation of the rotor. A simple schematic of a DC motor, and the torque-speed curve of a DC motor is shown in Figure 4.1

The torque speed relation for most DC motors is very well approximated by a linear relation. This is because the torque and speed of a DC motor are dependent only on the current supplied to the rotating solenoid, known as the armature, of the motor. Torque is proportional to the speed, and the maximum torque and the maximum speed are shown by the y-intercept and the x-intercept of the torque-speed curve respectively. A simple engine with no gearing, such as a non-geared steam locomotive engine with pistons directly connected to its wheels, also has a linear torque-speed relation, where the maximum torque is also the zero-speed torque.

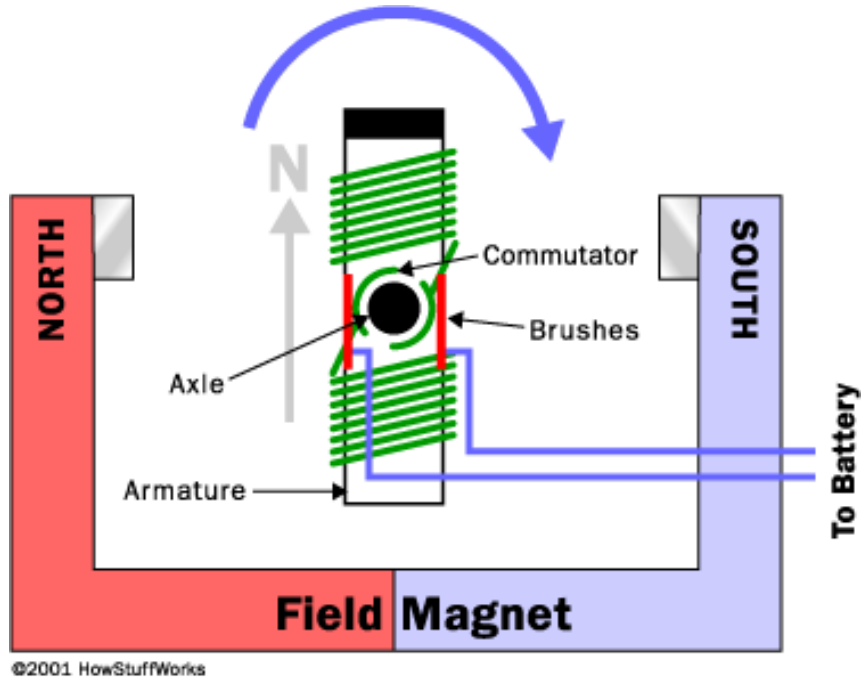

(a)

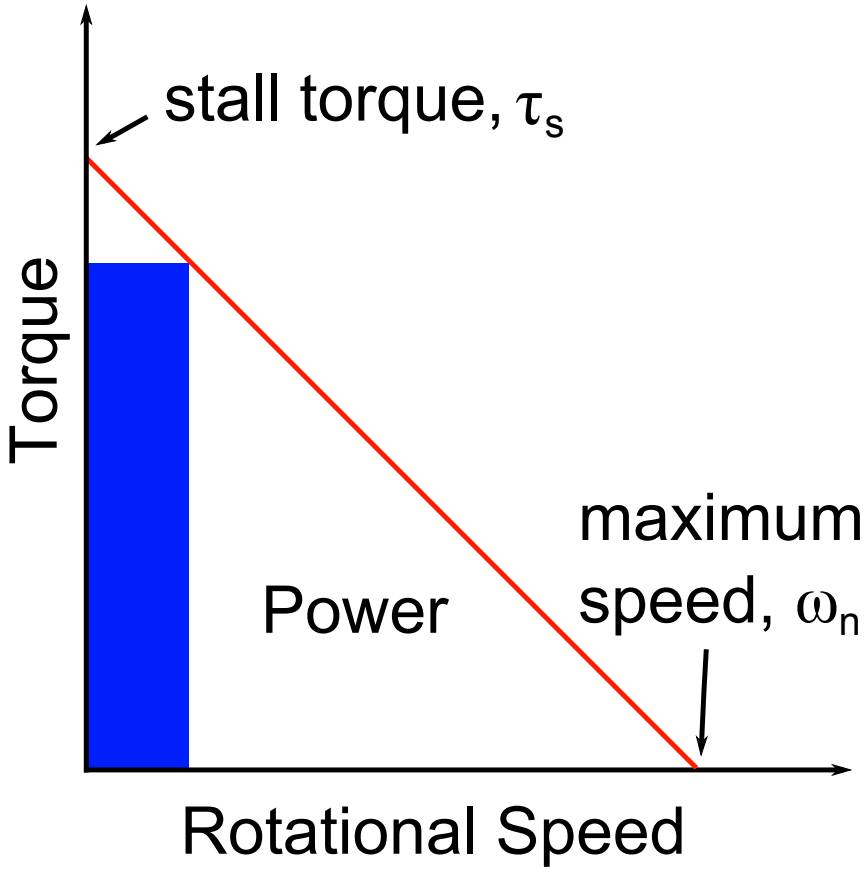

(b)

Figure 4.1: (a) Figure showing schematic of components of a brushed DC motor. Figure from Marshall (2000) (b) Ideal torque speed relation for a DC motor under constant input voltage.

A more complex motor, and a common industrial motor, is the alternating current (AC) induction motor. In an AC induction motor, instead of the current being directly supplied to the rotor, for example via the brushes shown in Figure 4.1, the current in the rotor is induced by the changing magnetic field from a polyphase supply (usually 3-phase) (Say, 1958). The upper limit of the speed of these motors is defined by the maximum speed of rotation of the magnetic field, N_s, called the *synchronous speed*. When the rotor is spinning at this speed there is no difference between the rotor speed and the rotating magnetic field, and so there is no torque. In practice the rotor spins more slowly than this due to friction and other losses, and this speed difference between the rotor and the magnetic field is called slip and is measured as a percentage of N_s. Depending on the construction of an induction motor, the torque-speed curve is shaped differently dependent on such traits as the starting torque or full load speed. Figure 4.2 shows an example of an induction motor with its torque-speed relation for the most common type of motor.

Another example of a motor is the internal combustion (IC) engine. IC motors differ from AC and DC motors because they do not work at zero speed and typically use a clutch to ease the load onto the motor. In the case of the DC motor, at zero speed there is still magnetic attraction that is creating a torque, and in the AC motor, there is magnetic attraction to the rotating magnetic field, but in an IC motor the bang stroke of the piston would break the engine if it was attached to a big enough load that the engine didn't turn (ie, a stall torque). Car enthusiasts measure 'dynos', or torque-relations of their engines and compare the torque output of the engine across a range of motor speeds (in rpm). These can be further compared with a dyno measurement at a different location of the car (for example the driveshaft) in order to find a suitable target for enhancement. Formula 1 cars have much higher speeds, slightly lower torques and overall higher powers than ordinary cars. Figure 4.3 shows an IC motor and the dyno for a car engine.

4.2 Torque in Biophysics

The bacterial flagellar motor, along with F_0 and F_1, is one of three rotary molecular motors, and so when considering the BFM we are naturally interested in torque, speed, and power. Examining torque and speed and angular displacement of a rotary motor is directly analogous to examining the forces and displacements involved in the linear motion of kinesins or myosins. Practically however, making measurements of torque can be much more difficult.

(a)

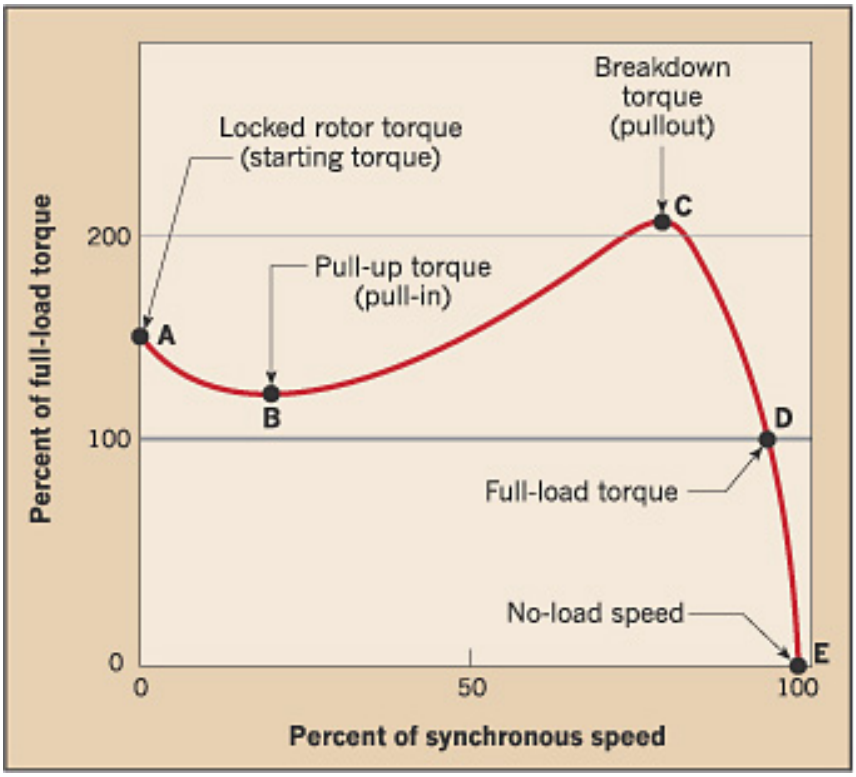

(b)

Figure 4.2: (a) Figure showing schematic of an induction motor. The three coils in the stator produce a rotating magnetic field when polyphase alternating current is cycled through them. This magnetic field exerts a torque on the inner rotor, causing rotation. Figure from Wikipedia (2010b) (b) Torque speed curve for a typical induction motor. When starting the motor (y-intercept) the magnetic field is rotating much faster than the stationary rotor, so the slip is 100% and the current drawn is high. As the rotor starts to rotate the torque output dips as the rotor speeds up relative to the magnetic field, then it peaks at a maximum, known as the *breakdown torque* and then drops off rapidly to the full load speed (x-intercept). Figure from Cowern (2004).

(a)

(b)

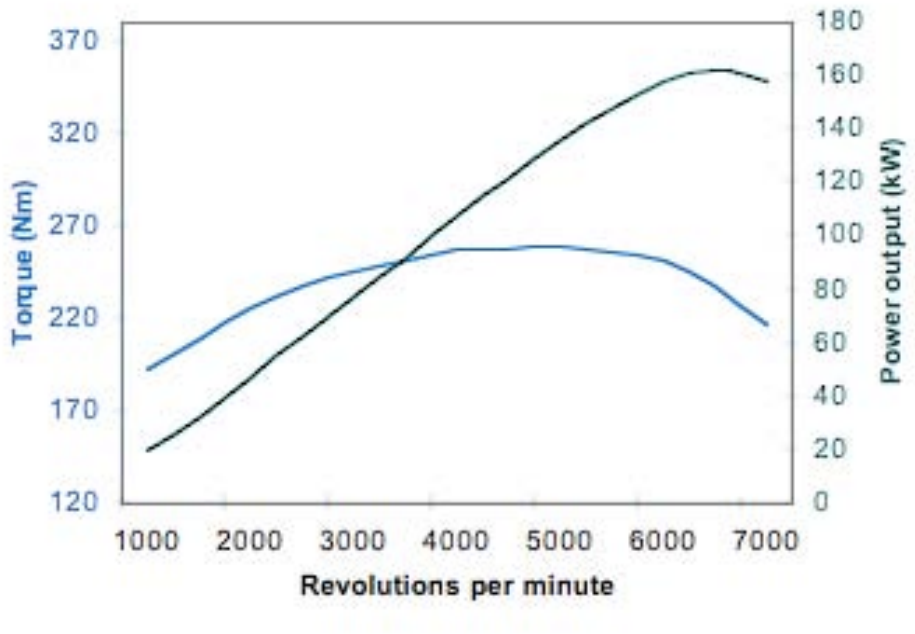

(c)

Figure 4.3: Examples of internal combustion motor. a) L20b Nissan engine (produced 1975-1985) with twin 45 mm Webers with 34 mm chokes, 60 mm Ram tubes and S2 Bluebird Electronic Ignition (horsepower estimate ≫100kW at the ywheel). b) Powering a 1972 Datsun 1600 into a left-hand turn at Appliance Installations Stages 2009 Rally, ACT, Australia. c) Dyno for Porsche boxster, showing the torque-speed relation between 1000 and 7000 rpm, with the power, the speed multiplied by the torque. ((a-b) from personal correspondence with Nic Herrald (driver), (c) adapted from Wikipedia (2010a)).

4.2.1 Torque-Speed Relation of F_1-ATPase

Torque-speed relations are also used to characterise the performance of F_1-ATPase, since it is a rotary motor. Typically instead of plotting torque against speed, in F_1-ATPase research speed is plotted against drag. This is analogous, since torque is simply the speed multiplied by the drag. A plot of speed against drag, for varied load sizes, is shown in Figure 4.4. Note that this is a log-log plot, and that the torque-speed plot for F_1-ATPase is in fact a near linear relation, similar to the DC motor in Figure 4.1. The asymptote close to the abscissa corresponds to the maximum speed. As the load becomes vanishingly small, the speed approaches a maximum. On a torque-speed plot this would correspond to the ordinate intercept. At the other end of the plot, as the drag becomes larger, the rotation speed will drop, until it falls below resolution (in Figure 4.4 this limit is 0.1 Hz). For F_1-ATPase for loads smaller than a 40 nm diameter gold particle, the speed is the full speed of the F_1 motor, which, at 2 mM ATP and 23 °C, is 134 Hz (Yasuda et al., 2001). Maximal rotation rate for loads smaller than a 40 nm diameter gold bead depend only upon the ATP concentration (Yasuda et al., 2001).

4.2.2 Torque-Speed Relation of the BFM

The properties of the torque-speed curve in the BFM are discussed at length in Section 1.5.2. Additionally, potential models of torque generation are covered in Section 1.5.3. The main features of the torque-speed curve in the BFM, summarised here, are the plateau regime, where torque is approximately constant, up to a *knee*, where the torque-speed relationship decreases linearly to zero torque at the maximum speed. In the sodium chimera that is the focus of this thesis, the stall torque is $\sim$ 2000 pNnm, and the maximum speed is $\sim$ 900 Hz. The torque speed relationship of the sodium powered chimera is shown in Figure 4.5

The variation of torque speed curves of the BFM with temperature has been tested between 16 °C and 23 °C using electrorotation of tethered cells. Figure 4.6 shows existing measurements of torque and speed vs temperature for these measurements (Chen and Berg, 2000b). With cooling there is a general tendency for a leftward shift in the location of the knee, and a steepening of gradient for the linearly decreasing regime of the torque speed curve. Recently Yuan and Berg (2008) added more low load points to the torque speed curve for the wild type BFM using 40 nm gold beads and a dark field microscopy system, but this has as yet not been performed on the chimeric BFM.

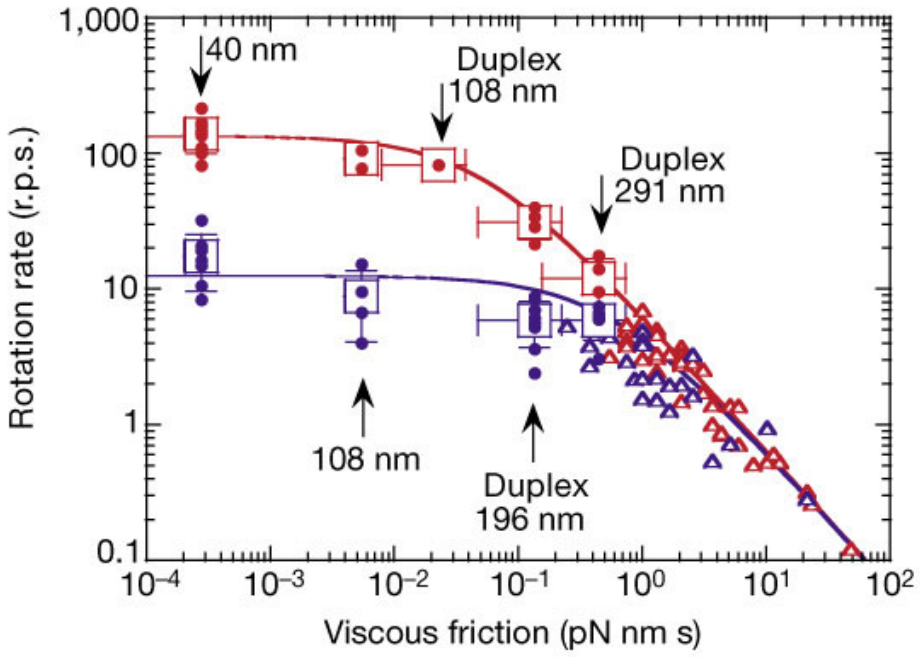

Figure 4.4: Speed vs drag in a log-log plot for F_1-ATPase. For viscous friction less than 10^{-1} pN nm s the speed is constant. ATP at 2 mM and 2 μM is indicated by red and blue colours respectively. Squares represent the average over at least 20 measurements of different sized loads attached to the γ subunit (40 nm gold bead or 108, 196 or 291 nm polystyrene beads). Triangles represent actin filaments attached to the γ subunit, to characterise the curve at high drag. Lines show expected fit for motor producing a linear torque-speed relation. Figure from Yasuda et al. (2001).

4.2. To

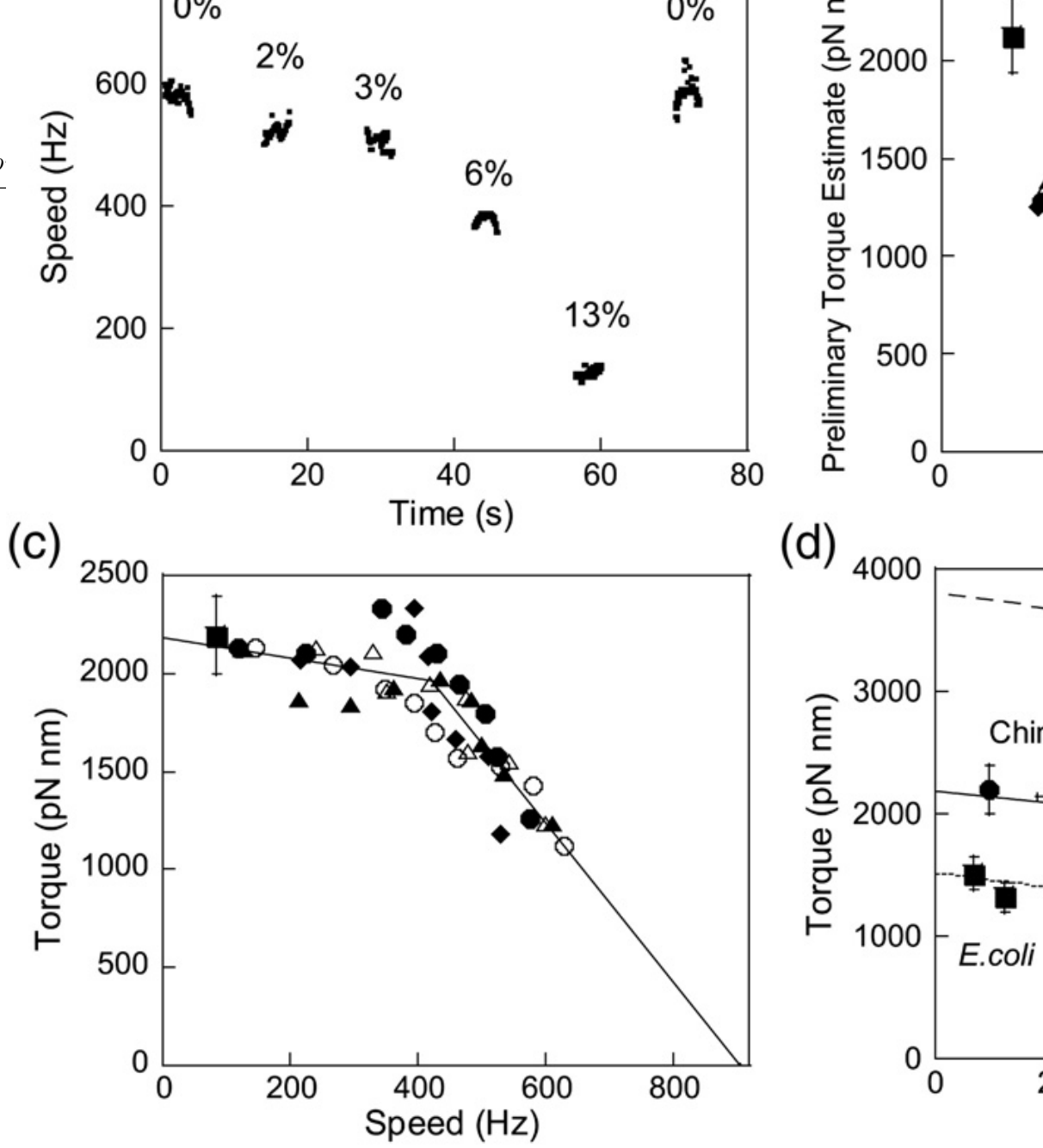

Figure 4.5: Torque versus speed, for the sodium powered chimera, using the filament stub correction discussed in section 4.3.3 (black square: 13 measurements from 1 bead using a 0.36-µm (diameter) bead in media containing 0.35 mM NaCl and varying viscosity). The torque-speed curve was fitted by two straight lines with an intersection at 421 Hz, representing the location of the knee. Figure from Inoue et al. (2008).

Fig. 1. Torque–speed relationships with fully induced stators. (a) Speed measured using a 0.36-µm (diameter) bead in media containing 0–13% (w/v) torque estimates *versus* speed, neglecting the contribution of filament drag (squares, mean±SD) and 5 individual 0.36-µm beads in 0%, 2%, 3%, 4%, 5%, each bead). (c) Corrected torque *versus* speed, using the method describe coefficient without Ficoll was estimated as 0.80±0.20 pN nm s/rad (mean±SD) straight lines with an intersection at 421 Hz. (d) Comparison of the torque motors, estimated using four different bead sizes without Ficoll. Measured motors (circles) and the H^+-driven *E. coli* motor (squares), using the average fil Continuous line: the fitted line for the chimeric motor in (c). Dotted line: publi the zero-speed torque is similar to the torque with 1-µm beads. Dashed lin *V. alginolyticus* motors.[9] Beads (10–18) of each size were measured for each m

(=8.18×10^{-3} Pa s) are viscosities at 0% and 13% Ficoll, and ω_1 and ω_2 are speeds measured with 1-µm beads without Ficoll and 0.36-µm beads with 13% Ficoll, respectively. Rearranging Eq. (1) gives

following pr
torque–speed
torque of ~2
~910 Hz and

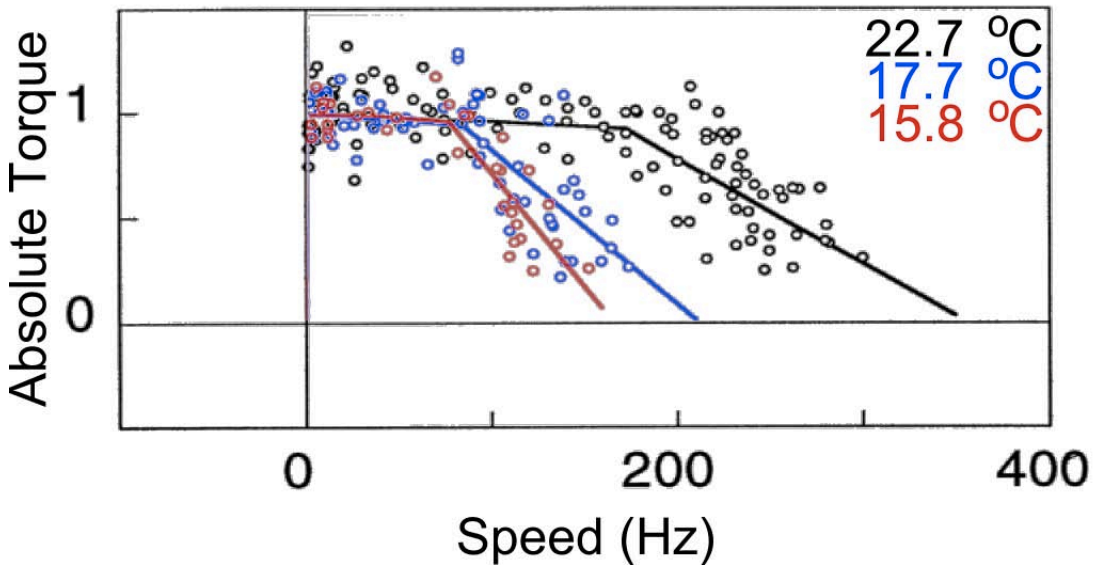

(a)

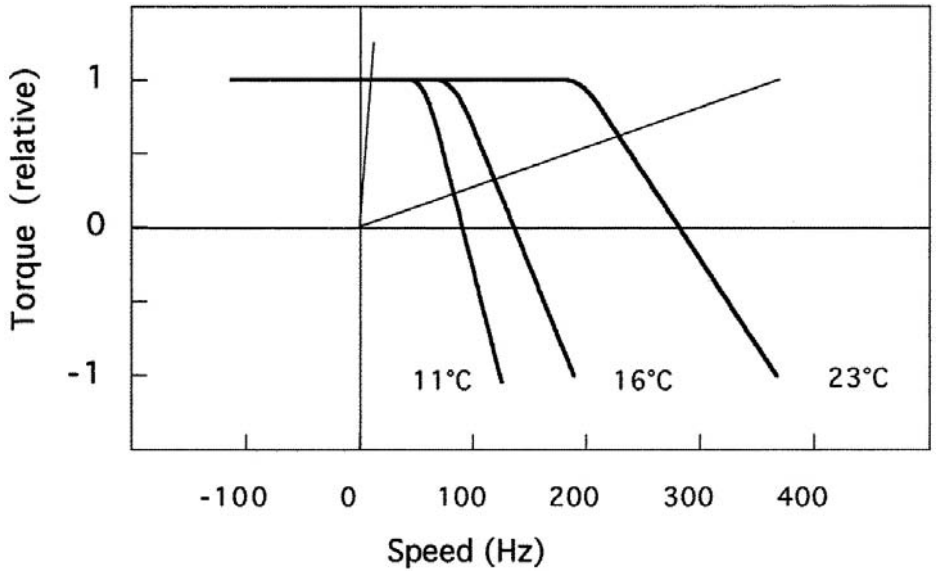

(b)

Figure 4.6: (a) Relative torque measurements at 22.7 C (30 cells), 17.7 C (14 cells) and 15.8 C (11 cells). Load was varied using Ficoll to increase viscosity and either 0.25 or 0.36 m beads. Adapted from Chen and Berg (2000b) (b) Relative torque measurements at 22.6 C (27 cells), 16.2 C (33 cells) and 11.2 C (17 cells). Load varied using electrorotation data from Berg and Turner (1993). Straight lines intersecting origin show load lines for 1.0 m (left) and 0.35 m beads. Data for fully induced wild-type *E. coli* with Figure from Berg (2003).

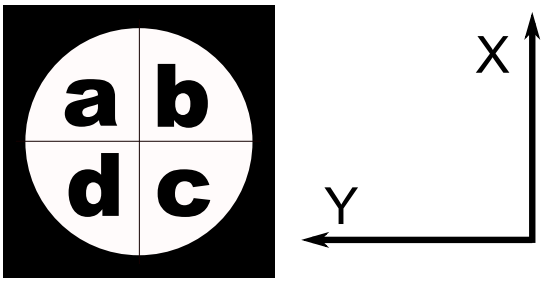

Figure 4.7: A 3:1 schematic of the quadrant photo-diode (QPD) used in this thesis. By convention panels of the QPD are labelled clockwise. The diameter of the QPD window is 10.01 mm, and the dimensions of the square enclosure are 11.99 mm. The X and Y position values are calculated from summing a, b, c and d appropriately, and dividing by the total intensity, as shown in Equation 4.5. Measurements from Osioptoelectronics (2007).

4.3 Methods

Cell and biochemical preparations were as described in Sections 2.4.2–2.4.3, including a full discussion of conditions for cell growth, preparation of tunnel slides, motility buffer, and IPTG resurrection solutions.

The mechanism of back-focal plane interferometry and optical trapping techniques were detailed in Section 1.7.1. Additionally, the materials and methods used in the optical trapping and position detection microscope were listed in Section 2.3. In summary, a weak laser is focussed on a bead acting as a marker attached to the BFM and any change in the position of this particle is detected as the change in scattered light in the back focal plane by a quadrant photodiode (QPD).

4.3.1 Measuring the Speed of the BFM from the QPD Signal

The 4-channel voltage output from each quadrant of the QPD (Figure 4.7)is recorded by software at a chosen sampling rate (5000 Hz). The signal from each of these four channels, a, b, c, and d, can be combined to calculate the x-position and y-position respectively:

$$X = \frac{(a+b)-(c+d)}{a+b+c+d} \tag{4.4}$$

$$Y = \frac{(a+d)-(b+c)}{a+b+c+d} \tag{4.5}$$

This two-channel signal, for the x and y positions of the marker attached to the BFM indicates the position of the bead relative to the centre of the optical trap. Because the BFM is a rotary motor, the path traced out by this bead is either circular or elliptical depending on the orientation of the cell. This means the x-position and y-position are sinusoidal, and a natural transform to convert this position data into a rotational speed is to take a windowed Fourier transform over the position signal and use this to calculate the *power spectrum*. The power spectrum is the square of the discrete Fourier transform of the position signal. It yields a plot of the power of the signal for each given frequency bin, from the minimum detectable frequency, defined by the window size, to the maximum frequency, defined by the sampling rate. The discrete Fourier transform, F_n, and power spectrum, Φ_ω, can be calculated from:

$$F_n = \frac{1}{\sqrt{2\pi}} \sum_{n=-\infty}^{\infty} f_n e^{-i\omega n} \tag{4.6}$$

$$\Phi(\omega) = \left| \frac{1}{\sqrt{2\pi}} \sum_{n=-\infty}^{\infty} f_n e^{-i\omega n} \right|^2 = \frac{F_n(\omega) F_n^*(\omega)}{2\pi} \tag{4.7}$$

A full description of Fourier series analysis and derivation of Equations 4.6–4.7 will not be given here but for a good description see Walnut (2004).

The frequency of the largest peak in the complex power spectrum is used to calculate the speed of rotation over a given window. This acts as a filter, removing transient speeds and calculating the most stable rotation speed during the window. Figure 4.8 shows a raw X,Y signal from the QPD, its complex power spectrum, and the associated calculated speed.

Raw speed vs time traces are produced using a complex power spectrum and fast Fourier transform in LabVIEW. These raw traces are then filtered to remove all stops (moments with speed less than a defined lower limit, usually 1 Hz) and processed using a 50 point median filter in MATLAB, to reduce the signal noise and noise due to fluctuation in the environment surrounding the cell.

4.3.2 Identifying Stator Number

Rotation of the BFM is driven by up to 11 stators, as discussed in Section 1.5.1. The arrival and departure of these stators can be observed by discrete jumps or drops in the speed plotted in a speed vs time trace. If a histogram is calculated for the recording of a single cell over a long duration, or over multiple recordings of many cells, then discrete peaks should be visible in the histogram corresponding to

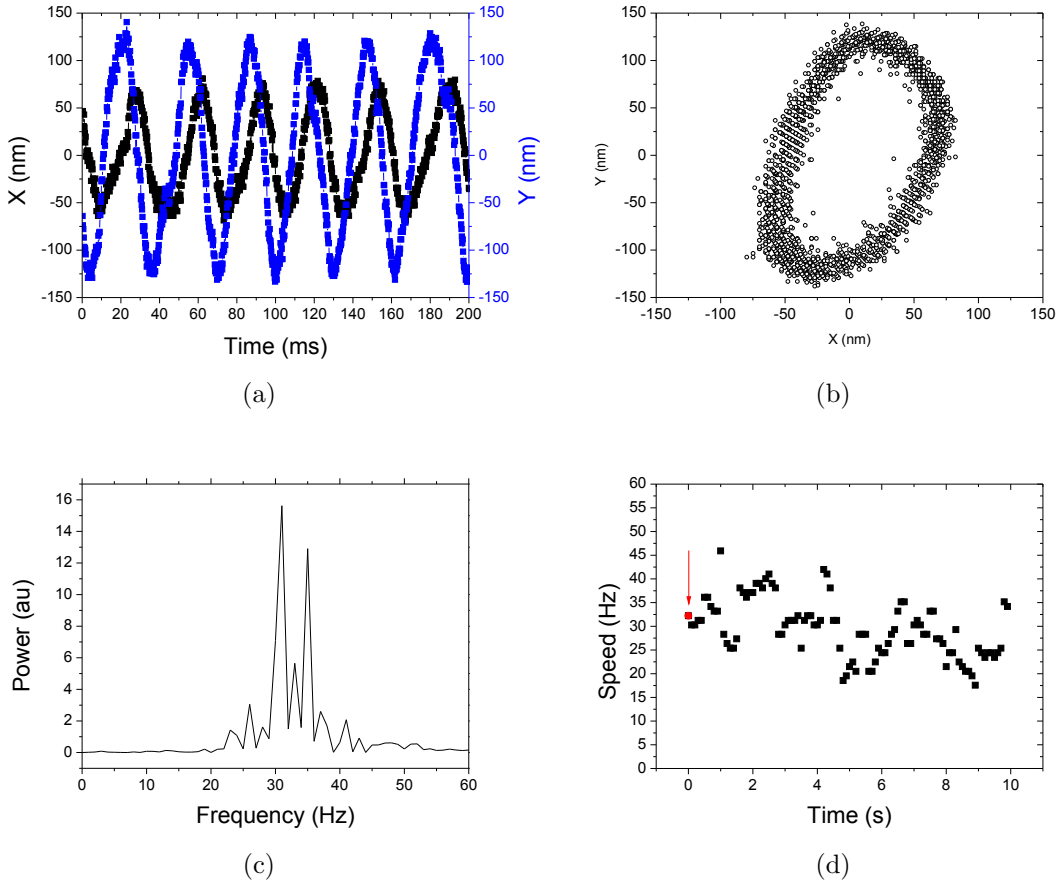

Figure 4.8: BFM rotational measurement. a) X and Y signals from the QPD sampled at 5000 Hz plotted against time. b) X vs Y plot of QPD signal showing the elliptical trace of the marker bead attached to a rotating BFM filament. c) Power spectrum of same trace showing maximum peak at 32 Hz corresponding to the rotational frequency. Taking only the maximum peak acts filters the transient speeds yielding more stable speed vs time plots. d) Speed vs time. Data point from the trace shown in (a,b,c) is shown in red and with arrow. To calculate the speed the Fourier transform of the X-Y signal is calculated over a window of length 1 s, and the maximum peak is selected as the rotational frequency for this window. The entire window is then progressed 0.1 s and the calculation is repeated. This speed vs time trace corresponds to 10 s of data, that is 99 moving window calculations, equivalent to that shown in parts (a-c) of this Figure. Data taken using the microscope describe in Section 2.3 and the method described in Section 4.3.

	1st	2nd	3rd	Saturated	$\Delta\overline{\omega}$	Ratio
1.0 μm	8.8 ± 1.1	16.2 ± 1.7	23.3 ± 2.8	92.5 ± 3.7	8.3	11.14
0.75 μm	15.8 ± 2.8	35.8 ± 2.7	52.5 ± 5.5	174 ± 7	17	10.23
0.50 μm	41 ± 7	76 ± 7	122 ± 10	402 ± 21	40	10.05
0.35 μm	73 ± 10	153 ± 21	233 ± 11	601 ± 30	75	8.01
0.20 μm	111 ± 16	213 ± 21		678 ± 41	109	6.22

Table 4.1: Speed (Hz) per level for the first three levels of the chimeric BFM. Lo (2007) measured 30 cells at room temperature for 10 s each and calculated speed histograms. Cells were measured at low induction (6 μM IPTG) and full induction (25 μM IPTG). Gaussians were fitted to the peaks in the histogram to determine the speed and error at each level. The number of stators present in fully induced motors was calculated by dividing the saturated speed by the average speed per stator, $\Delta\overline{\omega}_{22^{\circ}C}$. These are the literature values used for comparison and stator identification in this thesis. Data from Lo (2007).

individual stator speeds.

In this thesis multiple peak Gaussian fits are applied to the individual peaks of speed histograms to determine the mean speed and error per discrete speed level. These values can then be compared with literature values for stator speeds at room temperature in the chimera (Lo, 2007; Reid et al., 2006). Single stators are typically identified either from jumps from two stators to one stator that correspond to a halving in speed, or from stationary motors that begin rotating. Subsequent stator identification is based upon multiples of this single stator number. Table 4.1 shows the literature values for stator numbers at various load sizes, used in this thesis as a guideline for stator number allocation (Lo, 2007), and Figure 4.9 shows an example trace of a 0.5 μm bead attached to the BFM.

4.3.3 Measuring Torque

Once the stator speeds are known for different loads, the torque can be calculated using the radius of the bead, the eccentricity of its orbit and the viscosity of the medium.

The drag equation for a sphere in a viscous solution (Stokes, 1842) is defined by:

$$F_d = 8\pi\eta r_b^3 + 6\pi\eta r_b r_r^2 + \eta g_b \tag{4.8}$$

where r_b is the radius of the bead, r_r is the radius of its orbit around the motor, η is the viscosity of the solution, which varies with temperature as discussed in Section 4.3.4, and g_b is the filament stub correction. Values for r_r were taken from

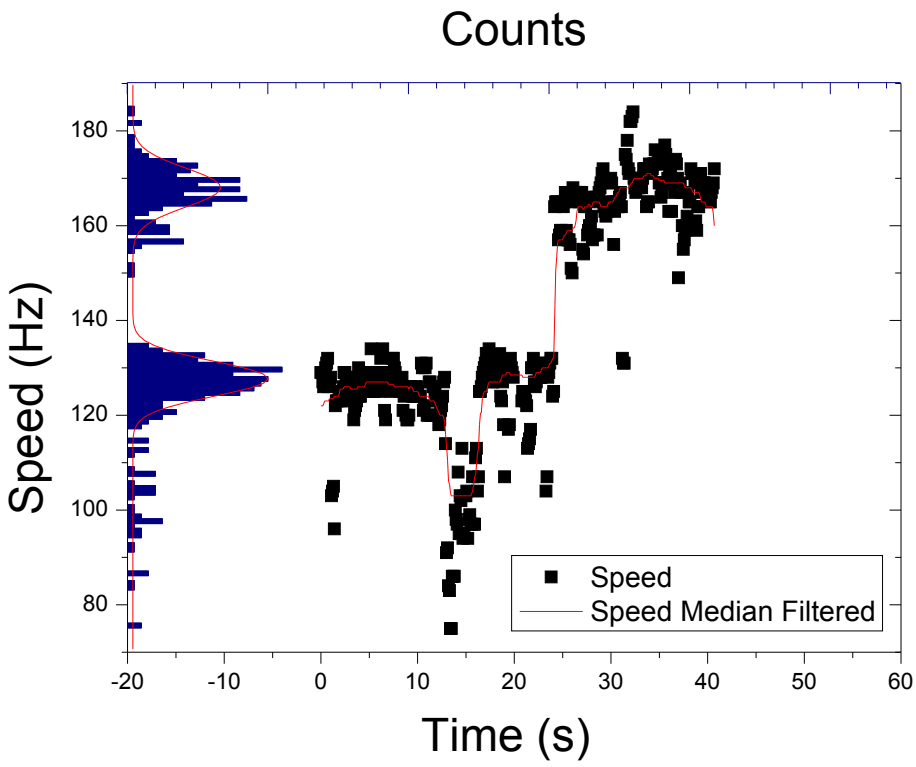

Figure 4.9: Speed vs time (black) with histogram of speeds against Y-axis (blue) at 22 °C. Raw speed vs time for a 0.5 μm bead attached to a rotating BFM is shown by black squares, with red trace indicating a 50 point median filter over the speed. This cell is initially powered by 3 stators, dropping to two stators briefly at 10 s – 15 s then jumping up to four stators at ∼25 s. The histogram shown plotted against the Y-axis shows two clear peaks for the three and four stators respectively, with Gaussian fits indicating, for this cell, that the 3-stator speed is 127 ± 7 Hz, and the 4-stator speed is 167 ± 8 Hz.

Lo (2007): for bead sizes of 1.0, and 0.75 μm r_r = 200 nm, for 0.50 μm beads r_r = 150 nm, for 0.35 μm beads r_r = 140 nm, and for 0.20 μm beads r_r = 130 nm. The literature values from Lo (2007) were used for r_b as those values were calculated using averages over many cells (100+), and over all bead sizes. This has the weakness that the size of orbit is not directly correlated for each bead and cell, but care is taken to ensure that the beads rotate directly above the cell, and in cases where the orbit was measured, it deviated from the literature value by less than 5%. The filament stub, the section of the filament which remains when the filaments are truncated and to which the bead is attached, adds extra drag. Filament stub correction accounts for this extra drag and this was measured previously by Inoue et al. (2008) who compared plateau torques, measured at low speeds, of 1.0 μm beads in water with 0.35 μm beads in 13% Ficoll. Inoue et al. (2008) calculated that $g_b = 1.29 \pm 0.32 \times 10^8$ nm^3, and this is the value used in this thesis.

4.3.4 Viscosity and Temperature

Viscosity in liquids tends to be independent of pressure and decreases with an increase in temperature. To a first order approximation there is an exponential relationship between viscosity and temperature that can be fitted by the Vogel Equation (Gmehling, 2010):

$$\eta = \exp(A + \frac{B}{C + T}), \tag{4.9}$$

where A, B, and C are parameters and T is the temperature in K. A plot of the dynamic viscosity of water over the temperature range 0 °C – 100 °C is shown in Figure 4.10. The viscosity is calculated independently for each temperature and used in Equation 4.8 to calculate the torque.

4.4 Results

Determining the average speed per stator for different loads is necessary to build a torque speed curve for a distinct numbers of stators. There are multiple methods for determining stator speeds. The standard method is to measure the speed of multiple cells, plot a histogram of all speeds, and use Gaussian fits to the individual peaks on the histogram. Another method is to perform an inducer resurrection, where cells are grown at a low concentration of inducer and subsequently washed in a solution with a high concentration of inducer, causing the expression of additional stator proteins (Reid et al., 2006). As these stators are produced by the cell, the

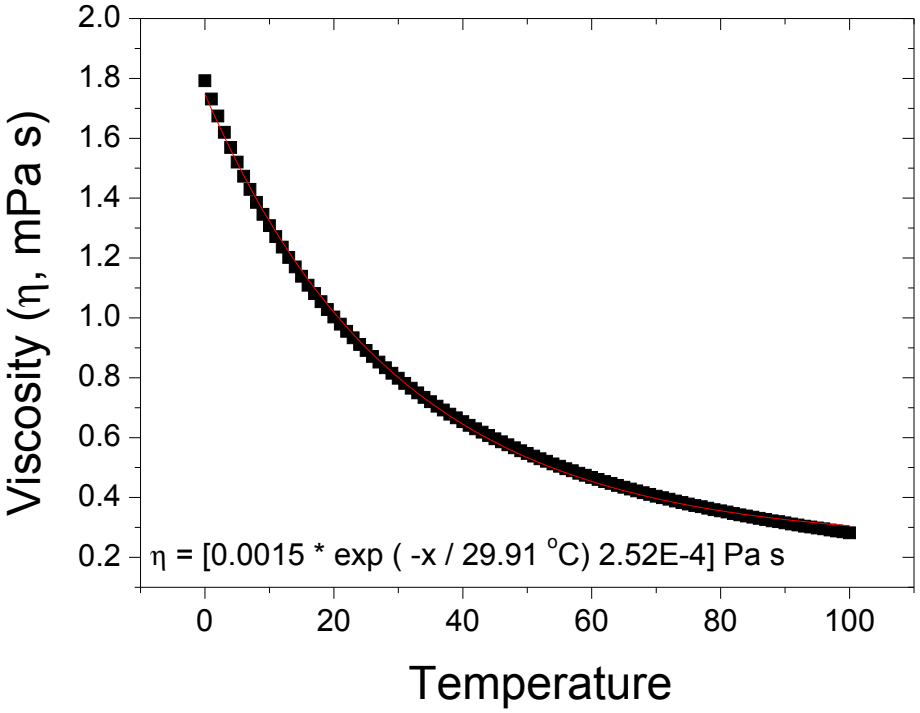

Figure 4.10: Dynamic viscosity of water in mPa s between 0 °C – 100 °C. Red line indicates exponential fit where $\eta = 0.0015 \exp(-T/29.91\ ^\circ\mathrm{C}) + 2.52 \times 10^{-4}$ Pa s. Data from Gmehling (2010).

speed increases in discrete jumps. A third method is to remove the sodium motive force (SMF) by flowing in a solution of 0 mM [Na^+], which causes the stators to release from the motor, stopping rotation. As sodium is flowed back in, the stators bind to the membrane and act on the motor increasing the speed in discreet steps (Rowe, 2005).

Peak finding on speed histograms was used as a first approach. At low temperature it was difficult to resolve individual peaks due to motor instability, and low resolution to discern separate low speeds. Secondly, the inducer resurrection technique was tried, using IPTG as the inducer. Inducer resurrections were successfully performed at 22 °C and 16 °C, but at 5 °C they were not successful due to stator expression being too slow at this temperature. Finally a method was developed (Section 4.4.1) where single motors were tracked during cooling from room temperature down to low temperatures to confirm the number of stators present while recording rotational speed at low temperatures.

4.4.1 Histograms of Low Temperature Speed

Speeds were measured for ∼30 cells at low induction (8 μM IPTG (Reid et al., 2006)) with two different loads (0.50 μm and 0.35 μm beads), at two different temperatures (22 °C and 5 °C), at full energisation (85 mM [Na^+], pH 7), and at low energisation (5 mM [Na^+], pH 6). Measurements were taken at a sampling rate of 5000 Hz, and speeds were calculated with a running window Fourier transform with a window size of 5000 points, or 1 s. Subsequently data were filtered to remove all speeds below 1 Hz in order not to count stops and time spent at zero speed when calculating histograms.

Since rotational speed is discrete, multiple peaks were apparent, and it was possible to identify dominant single or double stator peaks at room temperature. At low temperature however, it was more difficult to identify these peaks due to an increase in variation in motor speed, putatively due to instability of rotation at low temperature. Additionally, since speeds were calculated over a window size of 1 s, the minimum speed resolution was 1 Hz. At greater window sizes, the low speed resolution improves, but short duration variation within a window can be averaged out, as only the maximum of the power spectrum is used to calculate speed. Figure 4.11 shows histograms of fully energised BFM rotation at 22 °C and 5 °C

At low SMF and low temperature stator peaks become even more difficult to discern. Low SMF is useful for slowing the motor further. The first observation of

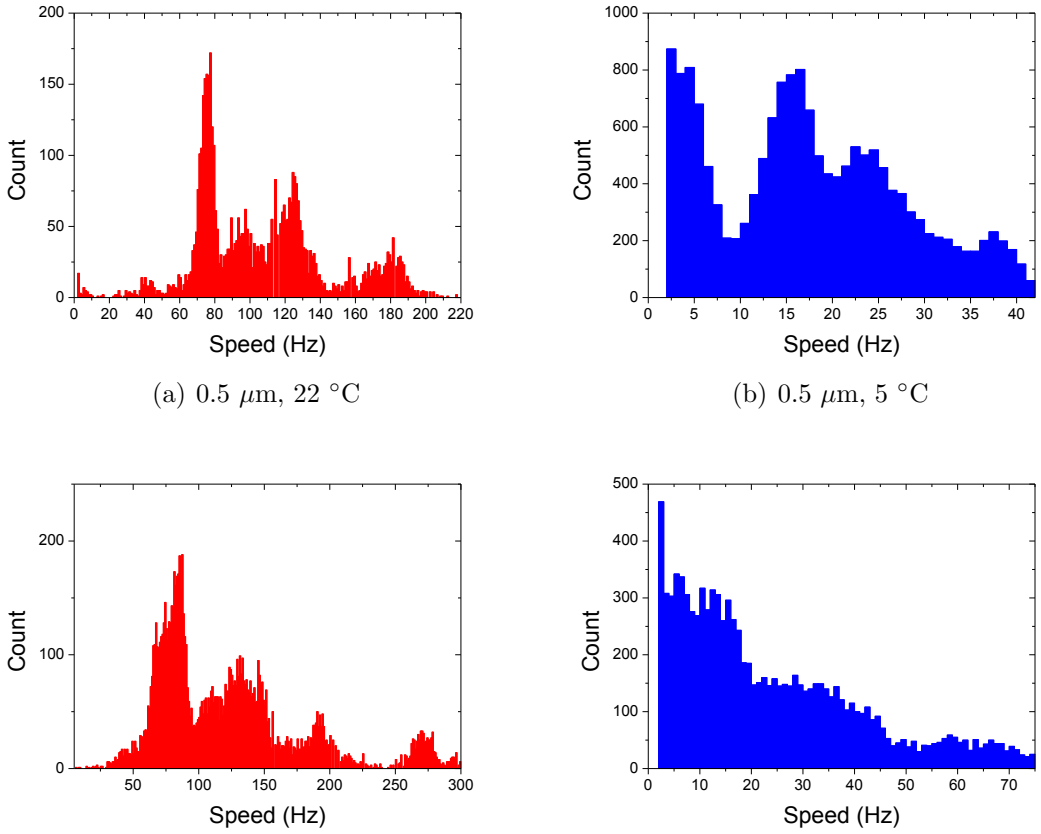

(a) 0.5 μm, 22 °C

(b) 0.5 μm, 5 °C

(c) 0.3 μm, 22 °C

(d) 0.3 μm, 5 °C

Figure 4.11: Histograms of speeds for 0.5 μm (top) and 0.3 μm beads (bottom) at 22 °C (left, red) and 5 °C (right, blue) at full energisation (85 mM [Na^+], pH 7). Each cell is recorded for ∼20 s. For the 0.5 μm beads, at room temperature (a, 30 cells) the peaks for double (75±2 Hz), triple (125±5 Hz) and four stators (179 ± 9) are visible and match with literature values (Table 4.1). There is also an erroneous peak at ∼100 Hz, putatively from a low speed triple stator motor with too long a filament. At low temperature (b, 22 cells) there are peaks at 4±5 Hz, 15±7 Hz, and 24±5 Hz. For the 0.3 μm beads, at room temperature (c, 32 cells) there are four visible peaks (79±21 Hz, 131±38 Hz, 191 ± 16 Hz and 271 ± 14 Hz) which correspond 1, 2, 3 and 4 stators, but at low temperature (d, 45 cells) it is difficult to identify and fit peaks. Peaks are fitted by estimating the number of peaks, and the centres and widths of these picks, and then fitting a sum of Gaussians to the overall histogram.

BFM stepping, for example, was using 1 mM [Na^+] at pH 7 to reduce the speed of steps below the resolution limit at that time (Sowa et al., 2005). In this thesis I examined histograms at 5 mM [Na^+] and pH 6, which reduces the SMF to ∼-80mV, and which results in approximately half the fully energised speed per stator[1]. One of the original aims of temperature control was to slow the motor to observe stepping at full energisation, and full induction, as mentioned in Section 1.5.5, and so it was necessary to investigate the combination of low temperature and low energy. Figure 4.12 shows histograms of under-energised BFM rotation at 5 °C and 22 °C.

In general the histograms of stator speed in this thesis are less clear than those published elsewhere (Reid et al., 2006; Lo et al., 2006). This may be due to more stringent user-imposed selection criteria when deciding which cells to measure in these other cases. Variation in filament stub length, from incomplete or varied truncation, will have an effect on the speed of motors as this stub length affects the drag and the radius of orbit of the bead. At low temperatures, it is more difficult to measure stable rotation for a 20 s interval due to frequent stopping and so there is less rotational time measured when calculating histograms. Ideally histograms would be measured with at least 50 cells in all cases, selecting only beads that are rotating directly over a cell fixed flat on the coverslip, with a perfectly circular trace recorded by the QPD, and with the diameter of this circle within a fixed tolerance. In practice the path of rotation can be a narrow ellipse in some cases, the orientation of the cell varies, in some cases angling up from the coverslip, and the filament stub length also varies. Ensuring consistency in any or all of these factors should lead to clearer peaks in these histograms.

4.4.2 Inducer Resurrections at Different Temperatures

An alternative method to calculate the speed per stator is to grow cells at low induction and subsequently flow a solution containing a high concentration of inducer through the sample. The cells respond to this resurrection solution by expressing stator protein in ∼30 minutes, and when this stator protein is available, the stators bind to the motor and increase the speed of rotation in discrete intervals. Only one cell can be monitored per resurrection attempt, since at the end of the measurements all cells are fully induced. It can require multiple samples to find a suitable candidate: a stable low-stator motor, prior to resurrection, that will continue to rotate over the course of the experiment. Full methods and materials for these IPTG

[1]Personal communication of unpublished data from Dr Chien-Jung Lo

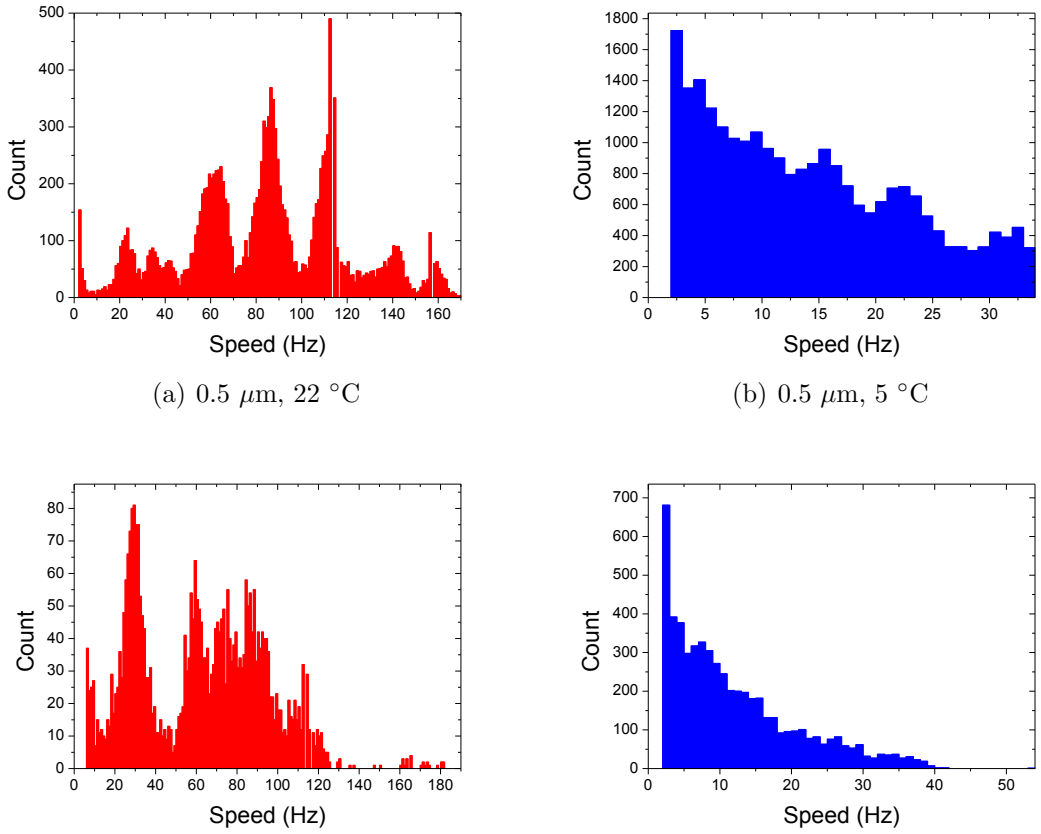

(a) 0.5 μm, 22 °C

(b) 0.5 μm, 5 °C

(c) 0.3 μm, 22 °C

(d) 0.3 μm, 5 °C

Figure 4.12: Histograms of speeds for 0.5 μm (top) and 0.3 μm beads (bottom) at 22 °C (left, red) and 5 °C (right, blue), at low energisation (5 mM [Na^+], pH 6). Each cell is recorded for ∼20 s. For the 0.5 μm beads, at 22 °C (a, 24 cells) the peaks for an estimated 1, 2, 3, 4 and 5 stators are visible (23 ± 5, 36 ± 8, 61 ± 11, 86 ± 10 and 111 ±6 Hz)with an average speed per stator, $\Delta\omega$, of 22 ± 3 Hz. At low temperature (b, 30 cells) the peaks are difficult to identify, but can be estimated at 4±1 Hz, 10±5 Hz, and 22±2 Hz. For the 0.3 μm beads, at 22 °C (c, 18 cells) peaks are visible for an estimated 1, and 2 stators (29 ± 10, 59 ± 6), with additional peaks difficult to allocate (71 ± 3 and 82 ± 34). These peaks are probably both for the 3rd stator level, but since the sample size is small in this measurement, the true mean of the fit cannot be resolved. At low temperature (d, 39 cells) it is difficult to identify peaks. Peaks are fitted by estimating the number of peaks, and the centres and widths of these picks, and then fitting a sum of Gaussians to the overall histogram.

inducer resurrection experiments are detailed in Section 2.4.3. Figure 4.13 shows successful IPTG inducer resurrections at 22 °C and 16 °C, and an unsuccessful resurrection at 5 °C.

Successful resurrection traces at 22 °C confirmed literature values of the speed per stator for 1.0 μm beads, and agreed with previous IPTG resurrections (Lo, 2007; Rowe, 2005). Resurrections were also successfully observed at 16 °C using air conditioning to control the entire room temperature. IPTG resurrections were attempted at 5 °C, and stable rotation was observed for an hour after the resurrection buffer was introduced to the sample. The longest continuous observation without resurrection was 90 minutes after the resurrection buffer was introduced. In this case, the sample was left at 5 °C for a further hour, and still no resurrection had occurred. In total, resurrection was observed in 12 out of 13 samples at 22 °C, 3 out of 3 samples at 16 °C and 0 out of 4 samples at 5 °C.

Gaussians were fitted to the peaks in the histogram (Figure 4.13(b,d,f)) to calculate the centres and widths associated with each speed level. Assuming approximately equal speed per stator (Reid et al., 2006), stator numbers were assigned by calculating the mean distance between peaks and using this as a divisor to determine the a speed/stator ratio. At 22 °C, the mean speed per stator $\Delta\overline{\omega}_{22°C}$, was 7.5 ± 0.9 Hz, which indicated that the peaks in the histogram corresponded to 2, 3, 4, 5, and 7 stators in order of increasing speed, with the peak size for the 6th level too small for successful Gaussian fitting. At 16 °C the mean speed per stator, $\Delta\overline{\omega}_{16°C}$, was 6.9 ± 1.2 Hz, which implied that the peaks in the histogram corresponded to 3, 4 5, and 6 stators in order of increasing speed. These results are summarised in Table 4.2.

4.4.3 Single Cell Tracking

At low temperatures, the instability of the motor makes it difficult to determine stator speeds from the distribution of speeds. Distributions of speed measured at 5 °C are blurred and it is difficult to make out the individual stator peaks. Similar difficulties affect IPTG resurrections; at 5 °C the machinery of the cell is slowed down, and no resurrections occur within 60 minutes, putatively because stator expression does not occur in this period.

A new technique was developed to estimate stator number and thus calculate speed per stator number at low temperature. This method involved tracking stably rotating individual cells from high temperatures to low temperatures, as detailed in Section 4.3.2. In this way a stably rotating motor can be located at room tempera-

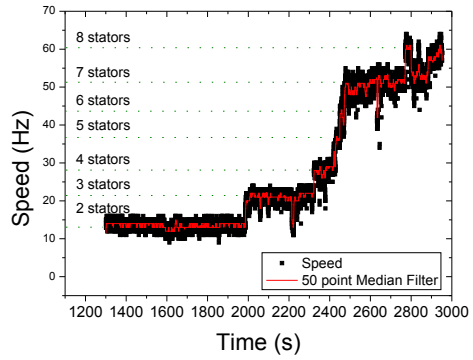

(a) 22 °C

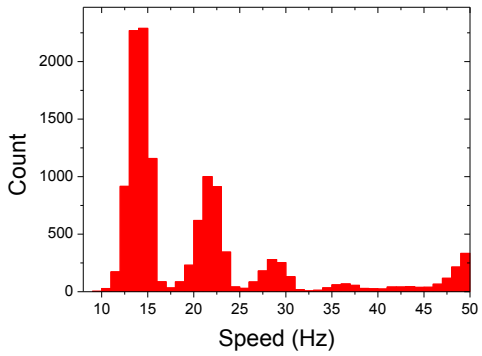

(b) 22 °C

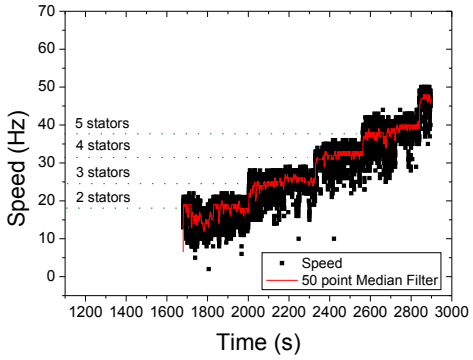

(c) 16 °C

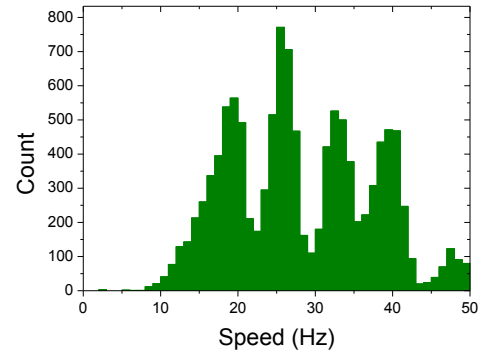

(d) 16 °C

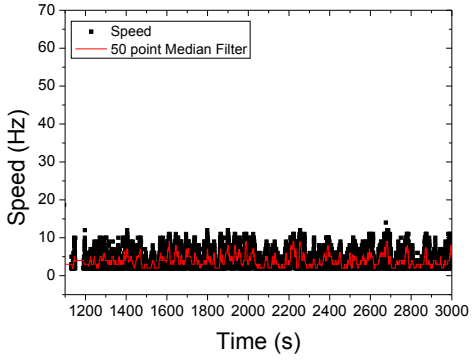

(e) 5 °C

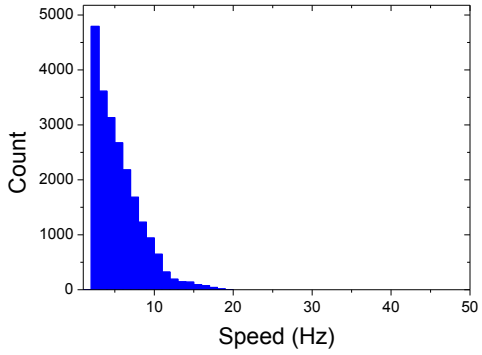

(f) 5 °C

Figure 4.13: Example IPTG inducer resurrections for a motor driving a 1.0 μm bead at 22 °C (a,b), 16 °C (c,d) and 5 °C (e,f), with raw data as black squares, and 50 point median filter shown as red line. IPTG resurrection buffer is flowed into each separate slide at time $t \approx 0$. a) Speed vs time at 22 °C. Stator units are expressed and bind to the motor at $t \approx 2000$ s, and maximum induction is reached at $t = 2800$ s. b) Histogram of unfiltered speeds showing discrete peaks for 2, 3, 4, 5 and 7 stators from left to right c) Speed vs time at 16 °C. Stator units are expressed and bind to the motor at $t = 2000$ s, with full induction reached at $t \approx 2800$ s, but with new levels reached more slowly than at 22 °C. d) Histogram of unfiltered speeds showing discrete peaks for 3, 4, 5 and 6 stators. e) Speed vs time at 5 °C. Even at $t = 3000$ s stator arrival is not indicated by an increase in speed, indicating that the expression of stator protein has not yet occurred. f) Histogram of unfiltered speeds showing no clear stator peak. Data for speed fitting and stator number allocation are shown in Table 4.2.

(a) 22 °C

Speed Level	Speed	Speed Interval	Ratio
1	14.1 ± 1.1	7.7 ± 1.6	1.87
2	21.7 ± 1.2	7.0 ± 1.7	2.89
3	28.8 ± 1.3	7.7 ± 1.8	3.83
4	36.5 ± 2.5	7.7 ± 2.3	4.86
5	-	7.7 ± 2.3	
6	51.9 ± 2.0	7.6 ± 2.7	6.92
7	59.5 ± 1.3		7.93

(b) 16 °C

Speed Level	Speed	Speed Interval	Ratio
1	18.7 ± 2.6	7.3 ± 2.9	2.70
2	25.9 ± 1.4	7.0 ± 2.1	3.76
3	32.9 ± 1.6	6.5 ± 2.3	4.77
4	39.3 ± 1.7		5.71

Table 4.2: Table showing calculations of average speed per stator and subsequent stator number allocation at 22 °C (a) and 16 °C (b). Gaussian fits are made to the peaks of the histograms shown in Figure 4.13, and the centre and width of these peaks are used to calculate the speed and SD shown in the 2nd column of these tables. The speed interval is then calculated between peaks, and these intervals are averaged to give an average speed per stator, $\Delta\omega$, which can be rounded to the nearest integral value to identify stator number. For 22 °C, $\Delta\overline{\omega}_{22°C} = 7.5 \pm 0.9$ Hz and for 16 °C $\Delta\overline{\omega}_{16°C} = 6.9 \pm 1.2$ Hz. The peak for the 5th speed level at 22 °C is not large enough to use for a Gaussian fit and so the interval between level 4 and level 6 (15.5 ± 1.2 Hz), is shown subdivided across both levels here.

ture, cooled to 5 °C while measuring the speed of the bead, noting any discrete speed jumps that indicate the arrival or departure of stators. Figure 4.14 shows a triple stator motor tracked during cooling and the steady state histograms calculated at stable temperature.

4.4.4 Torque Speed Relation at Low Temperature and Low Stator Number

As discussed in Section 4.2, the torque-speed curve is a measure of the torque, speed, and power of a motor across its operating range. Torque speed curves for the BFM have been measured between 15 °C and 23 °C (Berg and Turner, 1993), but never as cold as 5 °C. Additionally, torque speed curves are typically measured in fully induced proton-powered motors ($\sim 20\mu$M IPTG), with the maximum number of stators driving rotation, not in motors driven by a specific number of stators. Maximum induction yields more high speed stably spinning beads, that are easier to measure. Low induction ($\sim 5\mu$M IPTG), however, allows investigation of the effect of temperature on a single 'piston' of this bacterial engine. Figure 4.15 shows the torque speed curves of the Y34 sodium powered chimera at 22 °C for single, double and triple stators, calculated from the speeds per stator published in Lo (2007)

In this thesis I measured the torque-speed relation at 5 °C, 10 °C and 22 °C, in single, double, and triple stator chimeric sodium-powered motors. Figure 4.16 shows speed and torque measured for five loads at each temperature and for 1, 2, and 3 stators. Motors powered by single stators rotate less steadily, and have a greater variance in speed, as shown in Sections 4.4.1 and 4.4.2. This lack of stability, and also the frequent stopping of motors powered by few stators during cooling meant that it was not possible to measure every combination of speed and stator number for 1, 2 or 3 stators. Overall 49% (41/83) of traces were used to calculate the speed per stator, and traces were chosen as those that continuously rotated throughout the cooling process, with few stator jumps. Of the 41 cells chosen, the breakdown by bead size is as follows: 1.0 μm 61% (8/13), 0.75 μm 46% (13/28), 0.50 μm 52% (11/21), 0.35 μm 40% (4/10) and 0.20 μm 45% (5/11). Examples of selected and rejected traces for each load are shown in Appendix D.

The data points that were not measured were estimated from measurements at different stator number, for example the single stator speed (for the 0.50 μm,

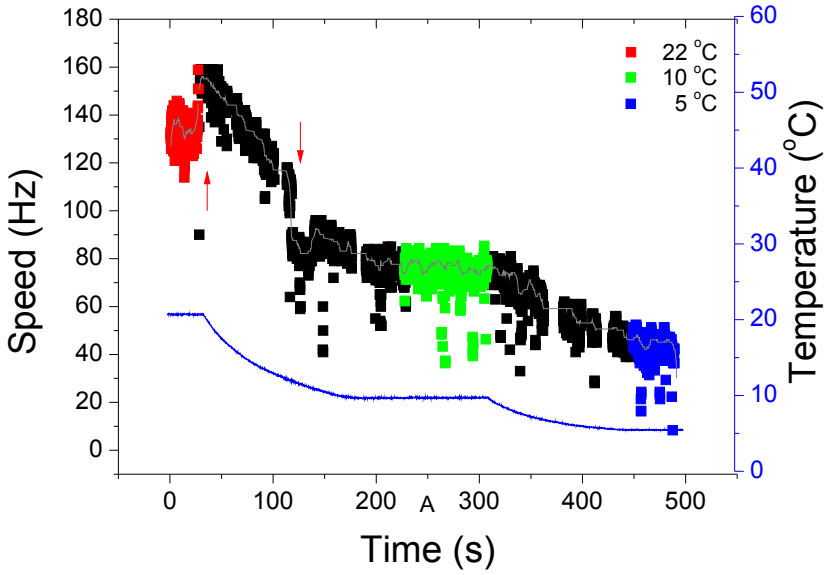

(a)

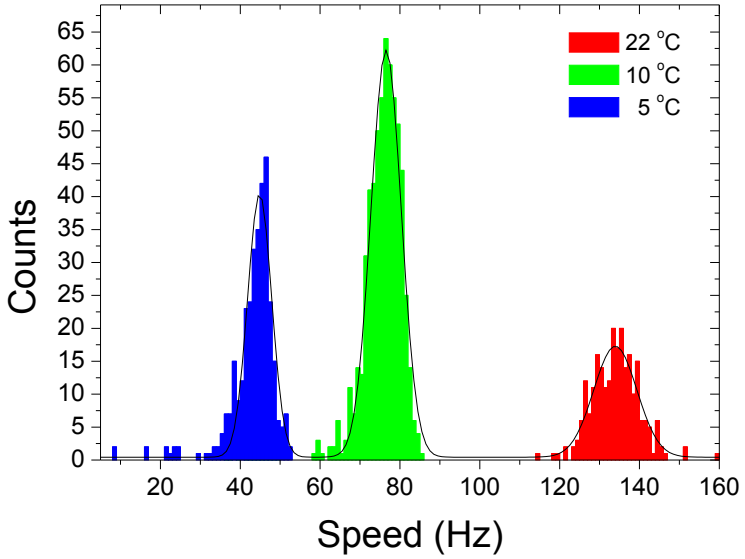

(b)

Figure 4.14: Tracking a single motor during cooling to determine motor speed (black) at a given temperature. (blue line) a) 0.50 μm bead attached to truncated BFM filament rotating at ∼130 Hz (3 stators) at 22 °C (red squares) was cooled first to 10 °C (green squares) and subsequently to 5.5 °C (blue squares). The arrival (red up arrow) and departure (red down arrow) of a stator are inferred from sharp discrete speed jumps that correspond to known single stator speeds at room temperature, resulting in a total speed that is 4/3 of the triple stator speed. The grey line overlaid shows a 50 point running window median filter on the speed data. b) Histograms for the three steady state regions indicated by colour in (a). Gaussian fits (black line) are calculated for each histogram to find the mean speed and SD for a three stator motor at each temperature. The steady state temperature fits are: $\omega_{5.5\ ^\circ C} = 45 \pm 6$ Hz, $\omega_{10\ ^\circ C} = 77 \pm 8$ Hz and $\omega_{22\ ^\circ C} = 134 \pm 10$ Hz.

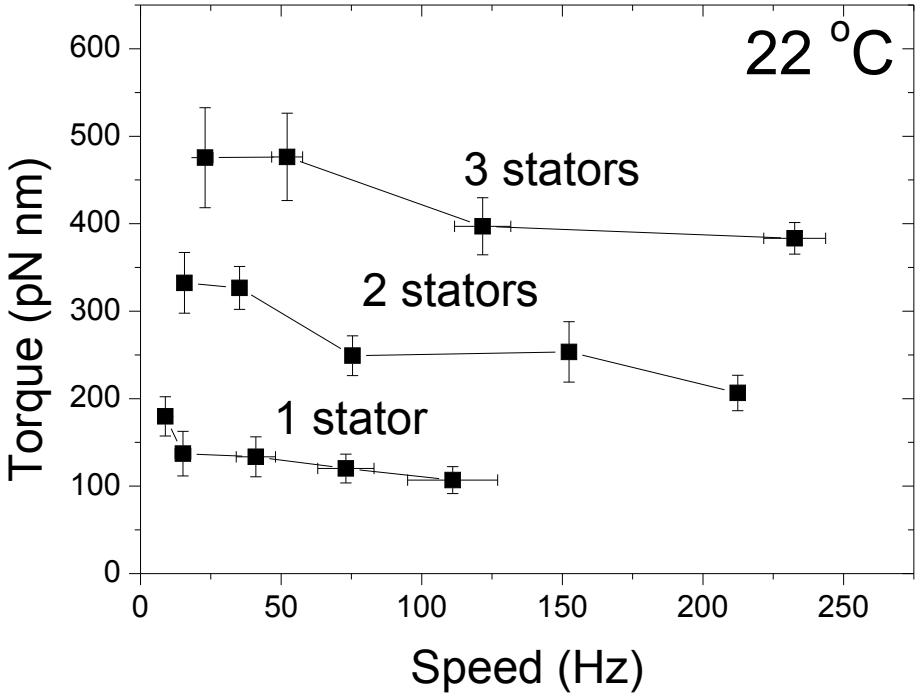

Figure 4.15: Torque-speed curves for single, double and triple stators using the mean stator speeds for the sodium chimera at 22 °C. Stator number increases from bottom (1 stator) to top (3 stators) and load decreases from left to right (slow to fast) using 1.0 μm, 0.75 μm, 0.5 μm, 0.35 μm, and 0.20 μm size beads respectively. The first data point for 1 stator is anomalously high due to difficulties resolving peak centres at high speed using the histogram method. Plateau-regime behaviour would be expected if further high load points were measured. Speed per stator values are from Lo (2007) and are also reproduced in Table 4.1. Drag and torques were calculated using the method in Section 4.3.3.

0.75 μm, and 1.0 μm beads) at 5 °C was estimated from:

$$\omega_{1s} = \frac{(1/2)\omega_{2s} + (1/3)\omega_{3s}}{2} \tag{4.10}$$

where ω_{is} is the mean speed for a BFM driven by i stators.

In total, 17 out of the 45 data points were estimated, 7 at 5 °C, 5 at 10 °C and 5 at 22 °C. Thirteen of these estimations were in cases where two out of the three speeds for a given load line were available (for example a single-stator and double stator speed was recorded, but not a triple stator speed), and four where only one of the three speeds for a given load line was available.

These torque-speed curves display the characteristic traits of the BFM: the plateau region at high loads (1.0 μm and 0.75 μm beads), the knee where the regime change occurs (near the 0.5 μm bead data point), and the linear regime where the torque decreases approximately linearly to the zero-torque speed. Torque speed curves at 5 °C and 22 °C were split into two segments by eye to estimate the knee (the 10 °C torque-speed curves were not segmented due to the lack of an apparent knee). For the 22 °C curves driven by one and two stators the curves were divided into segments of four point (across loads 1.0–0.35 μm bead sizes) and two points (0.35 and 0.20 μm bead sizes). For the curves at 5 °C driven by one, two and three stators, and the curve at 22 °C driven by one stator, the curves were divided into two segments of three points (1.0–0.50 μm and 0.50–0.20 μm beads respectively). The linear fits were then used to estimate the stall torque (abscissa intercept of high load linear fit), the maximum speed (ordinate intercept of low load linear fit) and the knee (intersection of both low load and high load linear fits). The stall torque, zero-speed torque, and approximate knee speed and torque are shown in Table 4.3. Errors were calculated by performing error analysis on the equations for the x,y-intercepts and the point of intersection using the values and errors for the slope and intercept of each linear fit. It should be noted that these properties were estimated by linear fits to two, three, and four, data points, and that the segmentation of the curves was arbitrary based upon curve appearance. This limited the predictive power of these calculations when determining knee properties. Further measurements across a greater range of loads would improve this.

The torque-speed relations at low temperature continue the trend indicated in Berg and Turner (1993), that is, temperature effects have a greater effect on the motor at low load than at high load. This is most noticeable at very low loads, using the 0.35 μm and 0.2 μm beads, where the speed decreases from 70 Hz to

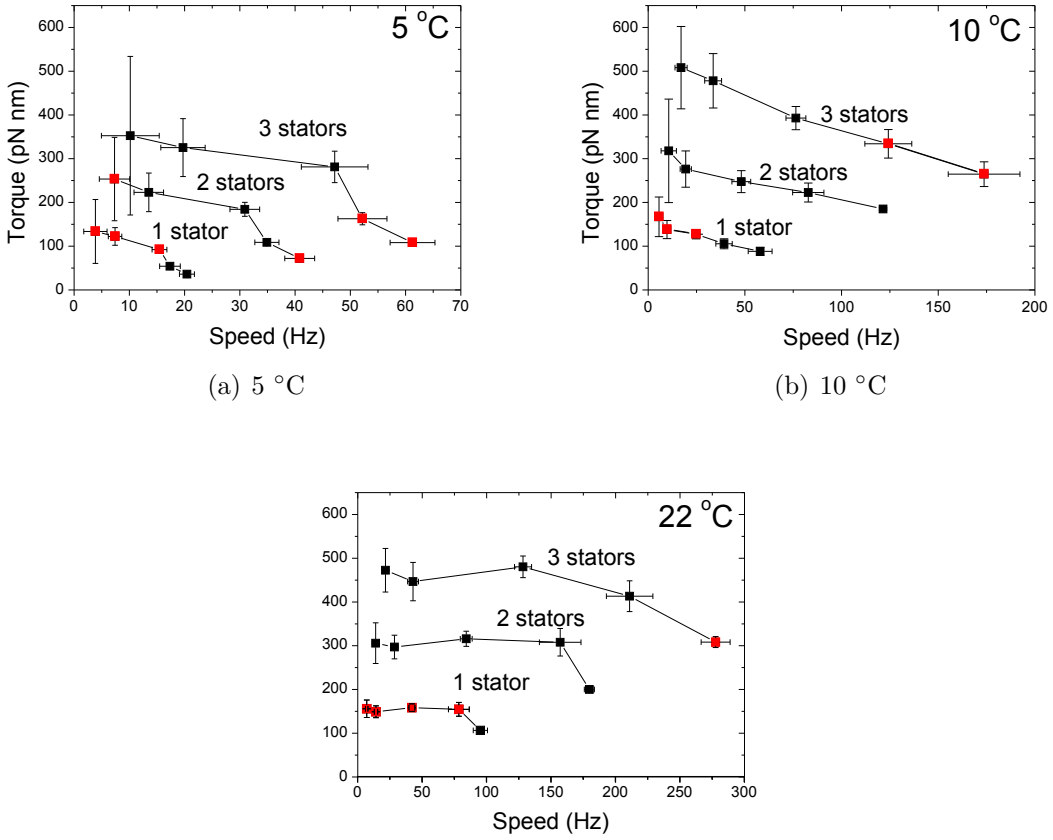

(a) 5 °C

(b) 10 °C

(c) 20 °C

Figure 4.16: Torque-speed relations for (a) 5C, (b) 10C, (c) and 22C. Speed was measured for 1, 2, and 3 stators driving BFM rotation on 5 different load sizes from left to right: 1.0 μm, 0.75 μm, 0.5 μm, 0.35 μm, and 0.20 μm beads. Stator number was estimated by tracking single motors from 22 °C to 5 °C while monitoring any change in stator number. Speed and error bars for a given bead size and temperature were calculated from the mean and width of a Gaussian fit to the histogram of the speed at given temperature. Due to instability and stopping at low temperature and stator number, few cells were stable over a temperature cycle (41/83 cells). Measured data (black squares) was augmented by estimated values (red squares) using information from different stator number. For example, the single stator speed for a 0.75 μm bead at 5 °C was calculated from the mean of half the two-stator speed and one-third the three-stator speed. Calculating the gradient from an Arrhenius plot of $1/RT$ vs $\ln(\omega)$ at low load gives an activation enthalpy ($\Delta H^{\ddagger}$) of 68 ± 30 kJ/mol and 69 ± 19 kJ/mol for 0.35 μm and 0.20 μm bead sizes respectively.

T	Stator No.	τ_{stall} (pNnm)	ω_{max} (Hz)	ω_{knee} (Hz)	τ_{knee} (pNnm)
22 °C	1	151.9 ±4.8	132.0	77.4 ±1.6	157.0 ±5.1
	2	302.1 ±9.8	221.6	155.5 ±2.0	314.8 ± 10.0
	3	451.4 ±20.9	540.3 ± 0.00	133.1 ± 28.9	479.3 ±35.7
5 °C	1	149.7 ±0.9	24.3 ± 0.01	13.4 ±10.7	99.8 ±10.8
	2	259.4 ±9.9	49.4 ± 0.01	25.1 ±19.9	198.1 ±22.2
	3	360.0 ±6.1	74.9 ± 0.01	36.7 ±30.1	298.6 ±30.7

Table 4.3: Table showing estimated fits for stall torque (τ_{stall}), maximum speed (ω_{max}), speed at knee (ω_{knee}) and torque at knee (τ_{knee}). Values are calculated by breaking the torque speed curve into two linear segments. The stall torque is estimated as the abscissa intercept of the high load linear fit, the maximum speed is the ordinate intercept of the low load linear fit, and the knee is estimated by the intersection of both linear fits. For 1, 2, and 3 stators at 5 °C and 3 stators at 22 °C the torque-speed curves are divided into two segments of three points (1.0–0.5 μm and 0.5–0.2 μm beads). For 1 and 2 stators at 22 °C the torque-speed curves are divided into one high load segment of 4 points (1.0–0.35 μm beads) and one low load segment of two points (0.35 – 0.20 μm beads). Linear fits were not used to estimate the knee for the torque-speed relation at 10 °C due to the difficulty in choosing a suitable segmentation of the line, and the lack of an apparent knee over the loads used to measure speed and torque. Errors for τ_{stall} and ω_{max} were calculated using the errors for intercept of each linear fit. Errors for the knee were calculated by using the errors for the slope of each fit and using error analysis to quantify the cumulative affect of this error on the calculation of the point of intersection. The mean slope error was 1.014 pN nm s and the mean intercept error 45.354 pN nm. Error is most significant for knee estimates at low temperature.

17 Hz and 100 Hz to 20 Hz respectively. The knee also becomes more pronounced at low temperatures (Figure 4.16a vs Figure 4.16b) because of this increased effect on low load.

4.4.5 Speed vs Temperature

An advantage of having temperature control in high numerical-aperture objectives is the ability to perform single molecule experiments during temperature transients. Thus, rather than observing the averaged behaviour of many molecules for a given temperature, it is possible to see the reversible and reproducible effects of temperature on the same molecule, and to investigate the response of a single molecule to temperature change. Figure 4.17 shows three traces of motors powered by different numbers of stators, and different loads, where speed is plotted against temperature.

The three traces indicate that speed is a continuous function of temperature in all three cases. When cells were measured at steady temperatures for longer periods, fluctuation in the motor speed was seen as many points at a single temperature. This can be seen at 5 °C and at 22 °C in Figure 4.17. In particular, at 5 °C the motor stability decreased and multiple speeds were measured for a single temperature, across a larger range. This is a symptom of greater instability at low temperature.

For the two traces for 1.0 μm loads there are two highly linear sections: for the single stator motor between 6 and 16 °C and for the two/three stator motor between 5 and 11 °C. Linear fits were chose for these regions as the data appeared linear, but the location and length of the fit was arbitrary based on the appearance of the data in an attempt to characterise any linear dependencies on temperature at high load. The fits for these sections, respectively, are:

$$v = (5.53 \pm 0.06) + (0.52 \pm 0.01)\ \mathrm{T} \tag{4.11}$$

$$v = (8.27 \pm 0.14) + (1.39 \pm 0.02)\ \mathrm{T} \tag{4.12}$$

where v is the speed in Hz and T is the temperature in °C. In each case $R^2 > 0.981$. At temperatures greater than these linear sections, the speed plateaus up to room temperature. For 0.5 μm bead it is not possible to fit linear estimates to 5 °C segments, however the overall speed vs temperature trace can be fitted accurately ($R^2 = 0.998$) by a quadratic. This is likely coincidental for this motor over this temperature range.

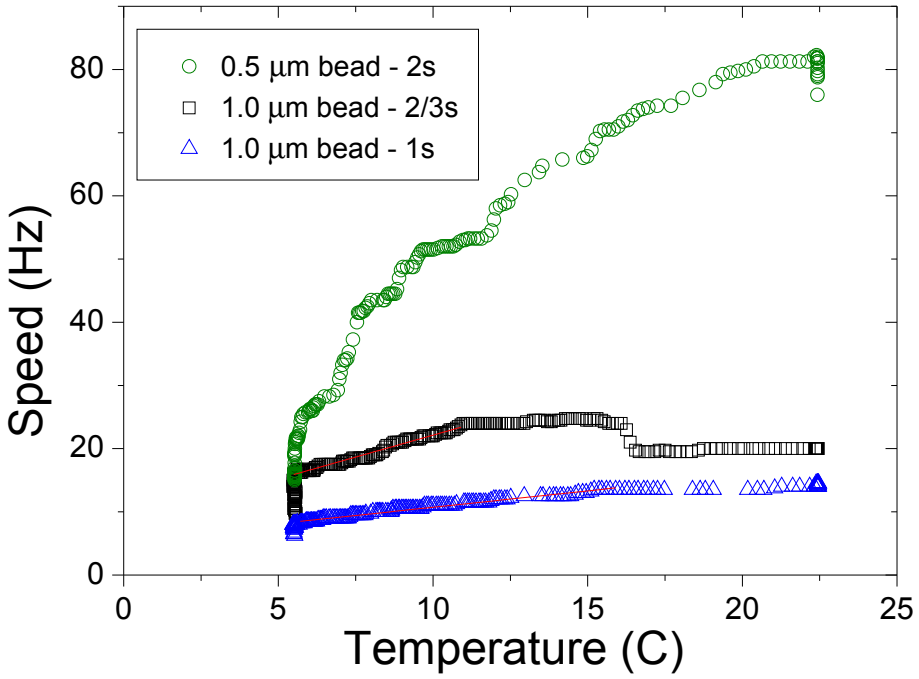

Figure 4.17: Speed vs temperature for a 1.0 μm bead powered by a single stator (blue triangles) and two/three stators (black squares), and a 0.5 μm bead powered by two stators (green circles). Speed data was filtered using a 50 point running window median filter. The red lines indicate linear fits to the linear sections of the 1.0 μm bead traces mentioned in the text ($(5.53 \pm 0.06) + (0.52 \pm 0.01)$ T and $(8.27 \pm 0.14) + (1.39 \pm 0.02)$ T for the single stator and double-triple stator motor respectively). In all cases the speed is a continuous function of temperature.

4.4.6 Single Motor Temperature Cycling

Hysteresis, or non-reversible behaviour over a temperature cycle, was observed at prolonged low temperatures. Reversibility of temperature effects, that is the reproducible change in speed with cooling and heating, is shown most clearly by speed vs temperature plots. Reversible behaviour is demonstrated when two cycles overlap each other, and hysteresis is demonstrated by patterns that do not overlap. Figures 4.18 and 4.19 show the speed against time and speed against temperature of a single molecule cycled through temperatures between 5 °C and 30 °C repeatedly.

These data show the advantages of temperature controlled single molecule measurements. Previously, to measure the dependence of temperature on speed, many measurements over many cells would have been taken at each fixed temperature, and the data aggregated into a plot similar to Figure 4.19(c). With a fast temperature controller on a high resolution microscope it is possible to measure the full temperature dependence of a single motor across multiple temperatures. This greatly reduces the number of samples necessary, and also allows investigation of transient behaviour. Figure 4.19(a) shows speed vs time for a single motor driving the rotation of a 0.75 μm bead, and from this record it is possible to identify stops at low temperature, stator jumps, and hysteretic behaviour. Taking the speed data at a steady temperature and calculating the average power spectrum in discrete 1 s windows, with a resolution of 1 Hz, is an alternative to the histogram measurement of speed. Rather than using the power spectrum to calculate the speed, and then making a histogram of the speed, the raw x,y signal is used to generate an averaged power spectrum. From the average power spectra of these long duration datasets we obtain sharp primary peaks (blue arrow in Figure 4.19(b)) when the motor is rotating stably, and broad secondary peaks where there is greater fluctuation in speed (red arrow in Figure 4.19(b)). Plotting the mean and width of a Gaussian fit to the broad peaks (Figure 4.19(d) gives an alternate speed-temperature relationship, showing transient behaviour, such as stopping or stator change, which can be exactly identified by returning to the raw data (Figure 4.19(a)). Temperature cycling of a single motor allows the measurement of general motor behaviour through averaged power spectra, but also the isolation of specific transient temperature related responses.

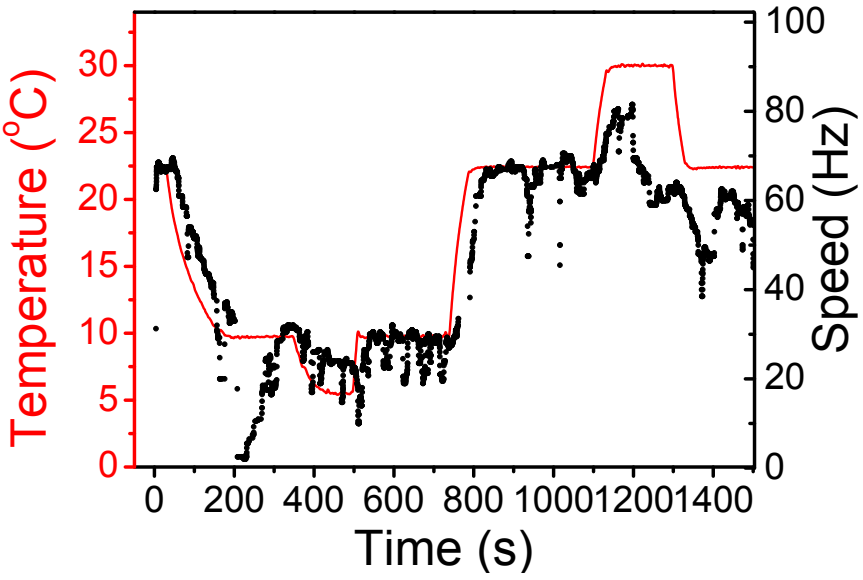

(a)

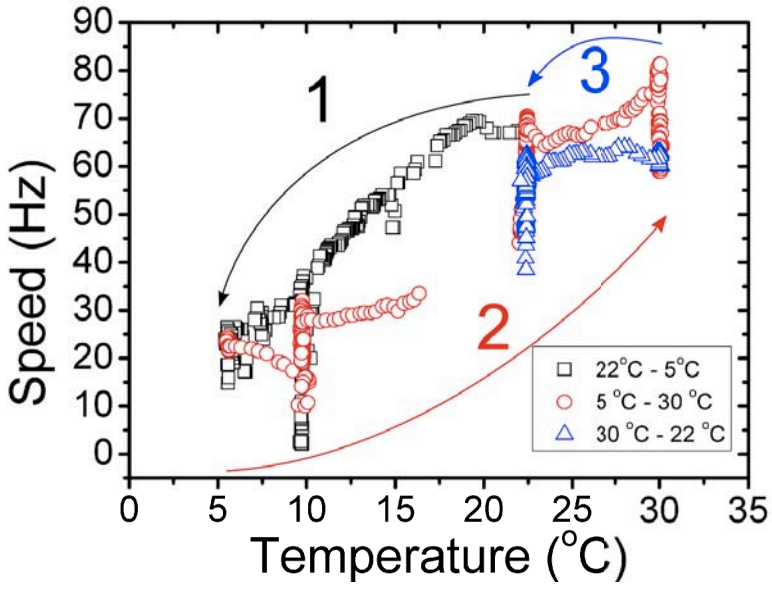

(b)

Figure 4.18: (a) Speed (black) and temperature (red) vs time for a 0.75 m bead attached to a single BFM. The initial temperature is 22 C, which is then cycled through 10 C, 5 C, 10 C, 22 C, 30 C and nally returned to 22 C. The delay in response between temperature and speed can be seen ($\gg$10 s) as can the response of the motor to transient temperature change.
(b) Speed vs temperature plot for the same cell as shown in (a). Three cycles are coloured and labelled with arrows: 1) 22 C 5 C black squares, 2) 5 C 30 C red circles, 3) 30 C 22 C blue triangles. Continuous reversible behaviour is observed along cycle 1), and 3), where the data points are overlaid (black squares and blue triangles), but along cycle 2) hysteresis at low temperature results in low speeds as the motor is returned to room temperature (red circles). Variations in speed due to local uctuations in noise, and stator arrival and departure, cause multiple speed measurements for a single temperatures (vertical clumps at 5, 10, 22, and 30 C).

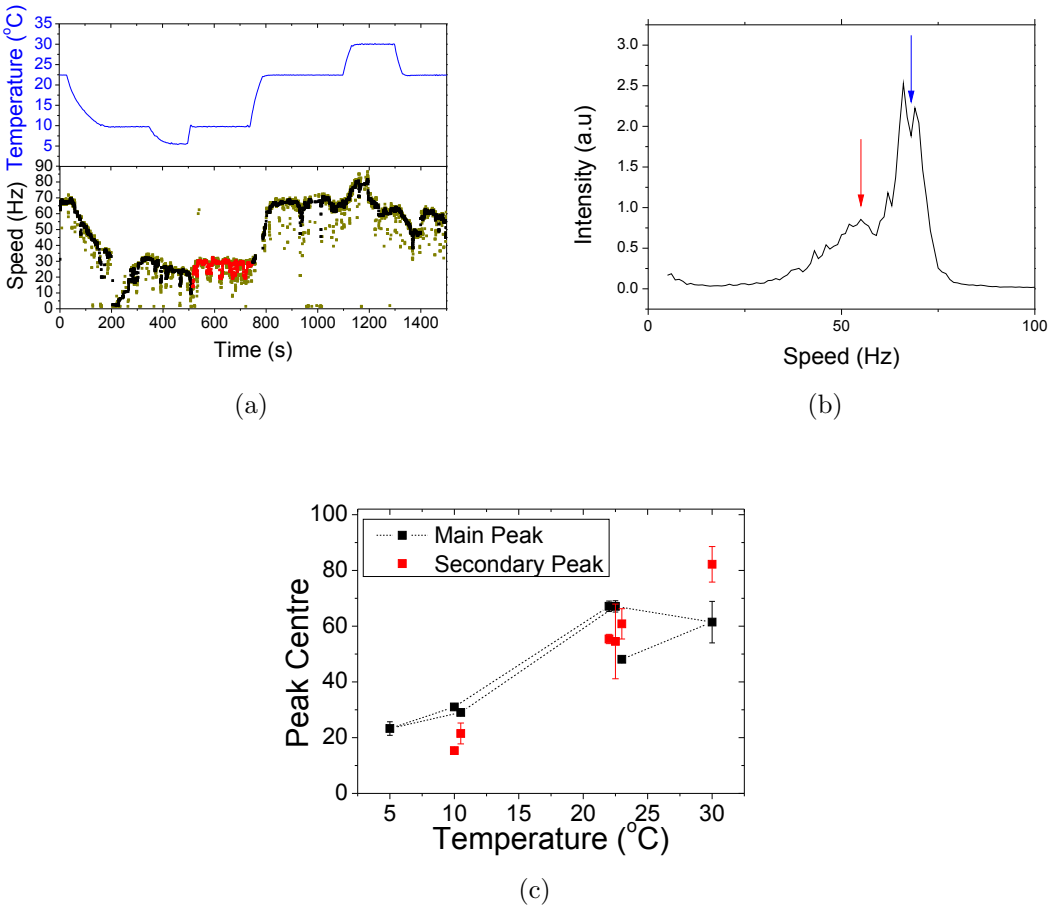

(a) (b)

(c)

Figure 4.19: (a) Speed vs time (bottom) and temperature vs time (top) for a 0.75 μm bead attached to a single BFM, with section at steady temperature of 10 °C highlighted in red. (b) Averaged 1 s power spectrum for the section indicated in red in (a). This smoothed power spectrum is produced by averaging the power spectrum of discrete 1 s windows over the entire period that the motor is at 10 °C for this point in the cycle (216 s). The narrow sharp bifurcated peak is the primary peak and is indicated with a blue arrow, and the broad peak is the secondary peak and indicated with a red arrow. Primary and secondary peaks are chosen based on intensity of the peak in the power spectrum. (c) Plots of Gaussian fit means and SD for the primary and secondary peaks of in the averaged power spectra at all steady state temperatures in (a) Fits are calculated using the sum of two Gaussians. Primary peaks correspond to stable rotation and these points show the reproducible speed vs temperature cycle for a single motor and secondary peaks show transient behaviour off-cycle, such as stopping ($\sim$ 230 s) and stator jumps ($\sim$ 800s , $\sim$ 900 s).

4.5 Discussion

Tracking the speed of a single BFM from room temperature to a target temperature is the most effective method of characterising temperature behaviour as it is possible to determine the initial conditions of the BFM and monitor it during a temperature change. This allows the accurate identification of stator number, and also matches the data taken at low temperature precisely with the same cell measured at room temperature. Histogram methods over large samples of cells at given temperatures do not have this precise accountability and ensemble averaged measurements can conceal information at low temperature.

Expression machinery is affected by temperature, as might be expected. Stator expression was induced using high concentration IPTG and the resulting increase in speed over multiple discrete steps indicated successful resurrection. At 5 °C this was not observed for any cells, indicating that the cellular expression was at least twice as slow in this case, which agrees with a Q_{10} of $\sim$3 for most biological processes. Transcription has been known to be affected by cold shock (Baneyx, 1999; Qing et al., 2004), and it is reasonable that cellular machinery would be affected by slow transcription rates at lower temperatures.

The torque-speed curves obtained at low temperature demonstrated a continuation of the trends previously measured (Berg and Turner, 1993), that is, a change in the slope of the linear region, and a large reduction in maximum speed. At high load, the mechanical relaxation limits the system, that is, the motor can advance multiple forwards and backwards steps before the load responds, as discussed in Section 1.5.2. At low loads however, the kinetic properties of the mechanochemical transition are rate-limiting. For example the rate of ion transit may be the rate limiting step, which would be expected to be highly dependent on temperature. The rate dependence of low load regimes was confirmed down to 5 °C, for loads as small as 0.2 μm diameter beads. The knee is more pronounced particularly at 5 °C due to the dependence of speed on temperature at low load. Typically in chimeric motors the low stator torque speed curves have a less sharp knee transition than for wild-type proton and sodium powered motors (Rowe, 2005). Less noticeable knees are shown in Figure 4.15, a torque speed curve at 22 °C using speed measurements by Lo (2007), and also in the higher temperature torque speed curves shown in Figure 4.16(b,c). The torque speed curve for 10 °C seems mostly linear, and it is unknown why the torque speed curve might change through an intermediate shape between 20 °C and 5 °C. Most likely the lack of a knee is an artifact that would be corrected with further low load measurements (using 100 nm and 200 nm gold

particles directly attached to the hook, for example as in Yuan and Berg (2008)). The trend in fully induced motors to shift the knee leftward upon reducing the temperature (Figure 4.6) is also observed at low stator number, and is one of the pronounced effects of cooling on the torque-speed relation.

Due to the instability when low temperature and low stator number are combined, finding a cell to track over a complete cycle from 22 °C to 5 °C and back can be a rare event. This forced the estimation of some points based on measurements at the same temperature but at a different stator number. In total 17 points were estimated, including 4 estimates based on a sole data point. In cases where two out of three points along a load line were known it was possible to compare a hypothetical estimate with a measured value. These calculations demonstrated that the mean error between an estimated speed and a measured speed was below 1 Hz.

Cooling slows the BFM, but introduces greater variation in speed, most probably by changing the rates of stator binding (k_{on}) and departure (k_{off}). A topic currently being investigated within our group is to examine how speed varies due to stator fluctuation as a function of different conditions. Tracking a single motor over multiple temperature cycles provides information about the different states of the motor, and explores temperature related hysteresis. By using high resolution microscopy with temperature control it is possible to measure the temperature dependence of a motor, such as the BFM, while still observing transient fluctuations in speed and motor function. This was something previously not possible with low resolution, ensemble averaged, temperature measurements.

Recently, after the submission of this thesis in May 2010, Yuan and Berg (2010) published interesting work detailing an analysis of temperature dependence on fully induced wild-type BFM using the temperature controller from Berg and Turner (1993) and gold beads attached directly onto the BFM hook. Yuan and Berg (2010) observed, as previously, that the high load dependence on temperature was not proton transit limited and displayed only ±10% variation across a temperature range of 9 °C to 37 °C. At low load they observed an exponential increase in speed with temperature, and calculated the activation enthalpy using a linear Arrhenius plot of $1/RT$ against $\ln(\omega)$ as 52 ± 4 kJ/mol. Additionally they tested the temperature effects on speed in H_2O and in D_2O and demonstrated that protonation of a single residue in the stator was not the rate limiting step[2]. This contrasted with the evidence from the strong Arrhenius rate dependence that there is a single rate limiting

[2]The rate would be expected to be $\sim 4.4\times$ slower in D_2O if a single protonation event is rate limiting, but rotation was only $1.5\times$ slower.

step driving rotation. Using the data in this thesis for low loads at 5 °C, 10 °C and 22 °C, the activation enthalpy was calculated as 68 ± 30 kJ/mol and 69 ± 19 kJ/mol for 0.20 μm and 0.35 μm beads respectively. These agree with the calculations of Yuan and Berg (2010), but have larger error since they are made using only data at 3 different temperatures, instead of 9 different temperatures.

Overall, the BFM is capable of rotating over the temperature range investigated, but there are significant reductions in the speed of rotation at low loads. The chimera, powered by the chimeric stators MotAPotB, was originally investigated to provide a sodium handle on the energetics across the BFM in *E. coli*. The characteristics of this motor under various energetics were then measured (Lo et al., 2006), and low energisation was used to slow the rotation and observe steps (Sowa et al., 2005). Likewise here the speed and torque have been characterised with cooling, and this provides another control to reduce speed, and potentially investigate stepping in fully energised and multiple stator motors.

4.6 Conclusion

To observe directly the kinetic response of the BFM to temperature, the speed was measured at transient and stable temperatures. Specifically, the properties of the torque generation and speed profile of the motor at low temperature were investigated. In this chapter the concept of torque-speed curves as a measure of motor performance was introduced, and the methods for measuring speed were outlined. The difficulties associated with measuring clear speeds at low temperature and identifying stator number have been listed, and a new technique involving tracking speed during temperature changes was detailed. This technique was used to measure single, double and triple stator speeds at three temperatures (5 °C, 10 °C and 22 °C). These measurements demonstrated the familiar plateau, knee, and linear regimes of the torque speed curve for the BFM, and the stall torque and maximum speed agreed with published data (Lo, 2007). Additionally measuring stator speed with IPTG resurrection at various temperatures was investigated. IPTG resurrections were possible at 22 °C and 16 °C, but stator expression was too slow at 5 °C to observe resurrection within a suitable timeframe. Temperature control provides a useful handle to vary the kinetics of the BFM, and at low load can cause a five-fold reduction in rotational speed. However the stability of the motor declines, and variance in speed increases. This slowed rotation could be used to study stepping in multiple stator motors, or other experiments that are currently operating at the

limit of resolution. In the next chapter, Chapter 5, the effect of cooling and heating on the energetics of the bacterial flagellar motor will be explored.

Chapter 5

The Dependency of Membrane Voltage on Temperature

5.1 Cellular Membrane Voltage

Membrane voltage constitutes the major component of ion motive force. By measuring it across a range of temperatures we can see how the energetics driving the bacterial flagellar motor change with temperature, and we can characterise the speed decrease associated with cooling. Is it mainly the kinetics that change with temperature, or is it also that there is less free energy available to drive the rotor?

Voltage measurements have always been of interest in biochemistry because maintaining the voltage across the membrane is one of the results of the metabolic cycle. The voltage is established through a balance between passive ion diffusion and pumping. The *resting potential* is the steady-state potential that arises from the balance between these pumped ions and ion pressure attempting to restore the equilibrium. In gram negative *E. coli*, the voltage is maintained across the inner lipid bilayer, or cytoplasmic membrane (Alberts et al., 2002; Lo et al., 2007). Membrane voltage is defined as the potential difference between the interior and the exterior of a cell, and so for a typical cell, the membrane voltage is negative, with negative charge accumulating inside the cell. The magnitude of this membrane voltage determines the major contribution to the ion motive force (IMF), or the free energy gain from a single ion transiting the membrane, with the minor contribution from the ion pressure (Lo et al., 2007). This voltage is also utilised to synthesise ATP by the rotary motor of bacterial F_1F_0ATPase (see Chapter 1). ATP in turn is used as

an energy carrier for all other ATPase functions in the cell, including motor function (such as myosins, kinesins and dyneins) (Alberts et al., 2002).

5.1.1 The Metabolic Cycle

The metabolic cycle is the process whereby carbohydrates and fats are broken down to produce energy that drives the cellular machinery. It consists of two parts, catabolism, the breaking down of large carbohydrates to produce energy, and anabolism, using this energy to create proteins and drive cellular function. Catabolism in *E. coli* is moderated depending on the environment surrounding the cell. *E. coli* does not produce catabolic enzymes to act on a specific substrate unless that substrate is present in its environment. The bacterium can produce energy from either fermentation or respiration, and can respire under aerobic or anaerobic conditions (using O_2 or NO_3 as the terminal electron acceptor respectively). *E. coli* can use glucose or lactose as a carbon source and has the metabolic activity to transform either sugar into the necessary amino acids and nucleotides that constitute cells. The overall end product of metabolism is to produce ATP which is used as a highly-transportable source of energy. The primary source of ATP in *E. coli* is from F_1-F_0-ATPase, which is powered by the free energy gain of proton transit across the membrane driving F_0 to counter-rotate F_1 and generate ATP. Cellular metabolism will not be discussed in detail here but for a further discussion see Todar (2010). Fig. 5.1 shows a cross section of a cell membrane and some of the machinery that maintains the membrane voltage, as well as some of the machinery that is powered by the free energy gain of ion transit.

5.2 Membrane Voltage and Temperature

The dependence of resting potential with temperature has been measured in a variety of different types of large cells previously, such as squid and lobster axons (Latorre and Hidalgo, 1969), barnacle muscle fibres (Dipolo and Latorre, 1972), frog muscle (Ling and Woodbury, 1949), rat diaphragm (Creese et al., 1958). In each the membrane voltage of these large cells was measured using microelectrodes, and the voltage did not differ by more than ∼20 mV across the temperature range 5 °C to 40 °C, although some local changes were noticeable, such as no temperature dependence on squid axon potential between 2 °C and 20 °C, but a 16 mV increase over the same temperature range for lobster axons.

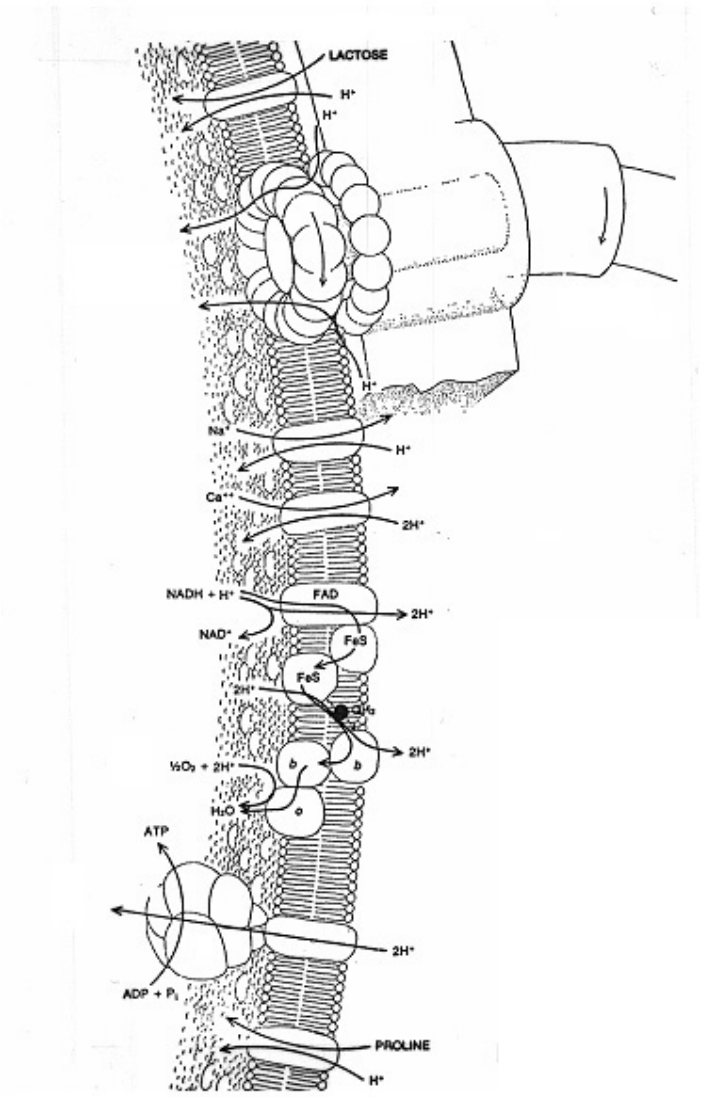

Figure 5.1: Cross section of cell membrane detailing some of the ion driven molecular motors operating across the membrane. The bacterial flagellar motor is shown, driven by proton flow (although the specific number of ions per step is not noted), as is F_0F_1, powered by the transit of two ions to synthesise ATP. Calcium and Sodium pumps are indicated schematically, as are lactose and proline channels. The reduction of NADH to NAD^- is also indicated. From Todar (2010).

There are previous observations showing that heating induces reversible effects on motility and swarming in bacteria with mutations in the rotor or stator. Fukuoka et al. (2004) studied motility in *S. enterica* with various neutral substitutions in PomA and found that the motility of certain mutants immediately ceased following a temperature shift from 20 °C to 42 °C and was then restored to the original level approximately ten minutes after the temperature was returned to 20 °C. Mashimo et al. (2007) discovered that three FliG mutants showed temperature sensitivity at 37 °C causing stops in BFM rotation, with function restored upon return to 20 °C. Possible links between temperature related stopping and membrane voltage are explored in Section 5.9.4.

5.3 Measuring the Membrane Voltage

5.3.1 Voltage Clamping

Kenneth Cole and George Marmount developed the first *voltage clamp* in the 1940s (Cole, 1949; Marmount, 1949). This is a two-electrode device that measures the voltage across the membrane by measuring the potential difference between an electrode placed inside the cell and one outside the cell. The voltage clamp was famously used by Hodgkin et al. (1952) to measure the action potential in squid axons. Hodgkin et. al. used electrodes made of a fine silver wire to make their voltage clamp. Later, when microelectrodes were available, Neher and Sakmann (1975) developed a single electrode voltage clamp, or *patch clamp*. The patch clamp is a modified voltage clamp where a single-electrode, inside a micropipette sealed around a removed section of the membrane, can measure the current to another electrode outside the cell while the voltage is kept constant. The patch clamp allowed a range of experiments on ion channels and further expanded the field of electrophysiology, particularly as applied in neurons and cardiomyocytes. Buechner et al. (1987) measured membrane voltage using patch clamps in giant conglomerated spheroplasts of *E. coli*, but at the current time individual *E. coli* cells have proven too small for patch clamps.

Micropipette experiments on *E. coli* have been accomplished by Fung and Berg (1995) to measure torque as a function of proton motive force (PMF). Fung and Berg found a linear relationship between torque and V_m up to applied voltages of -150 mV. Filamentous cells were sucked into micropipettes and the cell membrane permeabilized using gramicidin S. With permeabilisation of the membrane voltage,

the motor rotation ceased and was then restored by the application of a negative command voltage. Positive command voltages did not rotate stopped motors, however if a motor was running powered by a negative command voltage and the voltage was switched, reversals were noted. Fundamentally they showed that the torque generating elements of the bacterial flagellar motor (BFM) are disabled when the PMF is disrupted or of the reverse sign. Gauthier et al. (2008a,b) continued this work using a micropipette attached to filamentous bacteria across a 200 nm pore created using a high intensity pulsed laser. Using fluorescent filaments they were able to observe changes in direction of rotation as the applied voltage was reversed. Both these experiments, and the early Fung and Berg (1995) experiments, require long filamentous cells to be carefully inserted inside the tip of a micropipette, and are time-limited by the decay of the electrical seal around the cell, which typically occurs within 15 minutes.

5.3.2 Voltage Sensitive Dyes

Since voltage clamps and patch clamps are too large for common use in *E. coli*, other techniques, such as voltage sensitive dyes or radiolabelled cations, have been used to measure single cell membrane voltages. Voltage sensitive dyes have many different mechanisms, including the partitioning of the dye from the water to the membrane phase, reorientation of dyes within the membrane, aggregation of dyes in the membrane, and inherent voltage sensitivity (Lakowicz, 2006). Merocyanine was the first fluorescent dye to be used to measure transmembrane voltages (Cohen et al., 1968, 1974; Vergara and Bezanilla, 1976). Merocyanine responds to membrane potential both by partitioning and aggregating in the membrane and by responding to the electric field (Lakowicz, 2006). Another class of voltage sensitive dyes are the stryryl dyes, which change their absorbance directly in response to the electric field (Gross et al., 1994). These have fast responses, and can be used to measure the spatial and temporal variations in membrane potential along the surface of a cell (Loew, 1996). The type of voltage sensitive dye used in this thesis is a charged dye that equilibrates across the membrane dependent on the membrane voltage (Loew et al., 1993; Ehrenberg et al., 1988). Five common membrane potential probes were shown in Figure 1.25, and Figure 5.2 shows rhodamine and the tetramethylrhodaminemethyl ester (TMRM) dye used in this thesis. The effect of voltage on a probe is typically small hence intensity ratios of the fluorescence inside and outside the cell are used to provide stable measurements for the potential across the membrane.

Genetically encoded voltage sensitive dyes have been successfully produced in

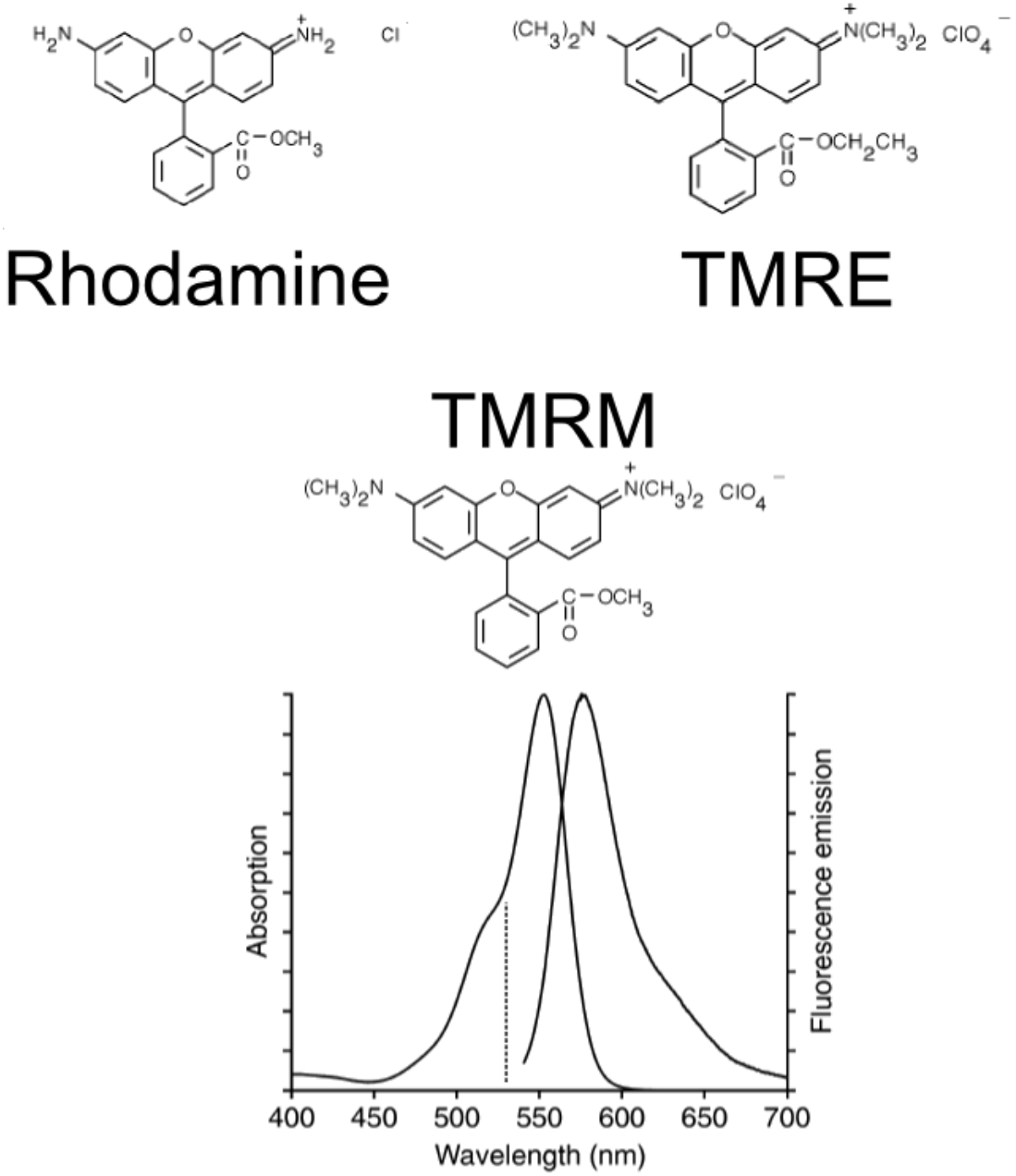

Figure 5.2: Chemical structure of rhodamine and derivatives. (top left) Rhodamine chemical structure. Note the highly aromatic structure typical in uorophores. (top right) Rhodamine derivative tetramethylrhodamineethyl ester (TMRE). (bottom) Rhodamine derivative tetramethylrhodaminemethyl ester (TMRM) and absorption/emission spectra. TMRM is the dye used for the experiments in Chapter 5 of this thesis. The dotted line shows the wavelength of the excitation light, in this case a 532 nm laser, which excites the uorophore TMRM but does not have signi cant cross over with the emission wavelengths. Spectra and structures from Invitrogen (2010).

neural cells. Siegel and Isacoff (1997) fused a GFP protein onto a K^+ channel to obtain a fluorophore that responded to rapid changes in membrane potential. The voltage dependent structural changes in the ion channel affected the fluorescence of the fused GFP and were detectable when voltage pulses were driven across the membrane using a voltage clamp. Currently no genetically encoded dye variant has been implemented in the study of *E. coli*.

Radiolabelled cations (^{31}P) and nuclear magnetic resonance (NMR) were used by Felle et al. (1980), in combination with microelectrodes, to measure the pH in giant *E. coli* cells. Castle et al. (1986a,b) used NMR to determine the intracellular sodium concentration (using ^{23}Na) and the intracellular pH (using ^{31}P), thus measuring the coupling between sodium and proton channels in *E. coli*. Minamino et al. (2003) also measured intracellular pH using a similar radiolabelled technique adapted from Slonczewski et al. (1981).

Recently a fluorescence-based single cell membrane voltage measurement technique was developed by our group by Lo et al. (2007). This technique involved incubating a cell with a rhodamine derivative voltage-sensitive fluorescent dye, TMRM (Figure 5.2), and measuring the fluorescence intensity resulting from the relative concentration of the dye inside and outside the cell. This is the method used in this thesis and discussed in Section 5.4.

None of these researchers have explored the dependence of membrane voltage on temperature using voltage sensitive dyes. This is probably due to the need to combine temperature control with high NA objectives, or NMR, for most of this work. As discussed in Chapter 3, the development of temperature control, in combination with nanometry and fluorescence measurements, is surprisingly recent.

5.4 Measuring Nernstian V_m Using Voltage Sensitive Dyes

The *Nernst Equation* dictates the reduction potential of a half cell in an electrochemical cell. In a biological context this equation determines the potential difference across a cell membrane as a function of ionic concentrations inside and outside the cell. It was developed by Walther Nernst, one of only two electrochemist nobel laureates, as an electrochemical form of the Van't Hoff equation (Nernst, 1904; Gabe, 2009). The equilibrium ratio of the concentration of a monovalent cationic dye inside and outside a cell will obey the Nernst relation for a given membrane voltage:

$$\frac{C_{\text{in}}}{C_{\text{out}}} = \exp(-eV_m/kT) \tag{5.1}$$

where k is the Boltzmann constant, T the absolute temperature, e the fundamental charge of an electron and C_{in} and C_{out} are the concentrations of the dye molecule inside and outside the cell respectively. This can be rearranged in terms of V_m to give:

$$V_m = -\frac{kT}{e}\ln(\frac{C_{\text{in}}}{C_{\text{out}}}). \tag{5.2}$$

Measurements taken using voltage sensitive dyes should have minimal binding to the membrane or other components inside or outside the cell so that the ratio $C_{\text{in}}/C_{\text{out}}$ can be accurately determined from the associated measured fluorescence. Also dyes should be bright, avoid aggregation, not self-quench and display low photobleaching (Lo, 2007). The dye used here, and by Lo et al. (2007), is tetramethylrhodamine methyl-ester (TMRM), a reversible cationic redistribution dye and a member of the rhodamine family. It is rapidly and reversibly equilibrated across membranes depending upon voltage as described by the Nernst equation. It is suitable because it has a high membrane permeability but is also not toxic to the cell. Lo et al. (2007) chose the TMRM dye based on the success of Loew et al. (1993) in using TMRM to make quantative measurements of V_m in mitochondria.

5.4.1 Convolution

Individual dye molecules are smaller than the diffraction limit of a light microscope and thus the intensity observed in any spot has contributions from the dye molecules in the nearby regions. Image restoration can be used to obtain an estimation of dye concentrations in objects smaller than the resolution limit of a light microscope. This is accomplished by determining the point spread function for an objective and assuming that the observed fluorescence is a convolution of the dye concentration and the point spread function. This approach was also developed by Loew et al. (1993) and further used in the study of *E. coli* by Lo et al. (2007).

In this work the method of Lo et al. (2007) is used measure the response in membrane voltage as a function of temperature. *E. coli* cells pre-treated with EDTA are immobilised on a coverslip and a high quantum efficiency EMCCD camera is used to image cells with an external concentration of 0.3 μM TMRM over exposure times of 10-30 ms. The correction factor data from the convolution model of Lo (2007) is used to provide a fit for the single parameter in an alternative linear model (Section 5.7.2), and this model is extended to remove the offset from membrane

bound dye (Section 5.7.3).

5.5 Methods and Materials

5.5.1 Cell Preparation

Cells are treated with EDTA to render the membrane porous to the voltage sensitive dye as described in Section 2.4.3. All membrane voltages were measured at pH 7 and $[Na^+] = 85$ mM which corresponds to a fully energised BFM (Reid et al., 2006).

5.5.2 Microscopy

The samples were observed using the fluorescent microscope described in Chapter 2, Section 2.2. A standard non-TIRF objective (Plan Fluor, 100x, N.A. = 1.40, Oil, Olympus) was used in epifluorescence mode with green 532nm laser illumination. The laser intensity entering the objective is measured ($\sim$12.5 W / cm^{-2}) and the illumination is centred.

After the TMR has infiltrated the cell ($\sim$20 mins at room temperature, longer at lower temperatures) cells are imaged at $\sim$50 nm per pixel using a 128 $\times$128-pixel, an EMCCD camera (iXon DV860-BI, Andor Technology). The sample was scanned under bright field until a suitable cell candidate was found and then the bright field illumination was shuttered closed, the laser illumination was shuttered open, and a fluorescent image was recorded.

After recording $\sim$50 cells in $\sim$15 minutes a solution of 100 μM CCCP was flowed into the sample in order to destroy the membrane voltage. During the next $\sim$15 minutes the fluorescence of $\sim$30 new cells was recorded. These images are later used to determine the amount of TMR that is bound to the membrane (C_{bound}), as a reference to calculate V_m.

5.5.3 Cell Plates and Growth and Fluorimetry

Cells were prepared for plate growth and imaged as detailed in Section 2.4.4. Fluorimetry of the TMRM dye with temperature was performed on a Cary Eclipse fluorimeter (Varian, Australia), as described in Section 2.2.2.

5.6 Measuring Fluorescent Intensity

Images are acquired as described above in Section 5.5.2 using a high sensitivity Andor camera and 532 nm laser illumination. The images are processed using MATLAB in three stages. The first stage takes the raw image file from the Andor camera and computes the fluorescent intensity, M_{live}, associated with the mean pixel intensity from the single cell (T_{cell}). The second stage calculates the external intensity, M_{absent}, from a series of background measurements, and the final stage calculates V_m from the linear model relating fluorescence ratio to dye concentrations (Equations 5.6 and 5.16).

5.6.1 Internal Fluorescent Intensity - M_{live}

For the first step a histogram is taken over the entire image and the mean and standard deviation of the pixel intensity are calculated. A mask is then taken to identify all of the pixels with an intensity greater than one standard deviation above the mean (T_{thresh}) as shown in Figure 5.3. Pixel intensities are referred as T, raw measurements by M, and subsequent concentrations by C. This mask is then filtered to find the largest continuous area (using the MATLAB function *bwlabel*), to discount single pixels of high intensity, and a subsequent visual check is done to see that this mask equates to the area of the cell. The median intensity in this masked region is calculated (T_{median}), and the mean of all points above the median is calculated as T_{cell}. The mean of the points above T_{median} is chosen, instead of the mean of all points above T_{thresh}, as this excludes values in the border region of the cell and makes the calculation of T_{cell} more resilient to changes in cell size (Lo, 2007). The mean of the inverted mask, ie, the background of the image excluding the cell is recorded as $T_{\text{background}}$. M_{live} is then defined as the difference between the two, that is:

$$M_{\text{live}} = T_{\text{cell}} - T_{\text{background}}. \tag{5.3}$$

This process is shown graphically in Figure 5.3. The MATLAB code used to calculate M_{live} is supplied in Appendix B

5.6.2 External Fluorescent Intensity - M_{absent}

The external fluorescent intensity, that is the fluorescent intensity corresponding to the dye outside the cell membrane, is a measure of the concentration of dye outside the cell. The external concentration, C_{out}, is measured separately for each slide and

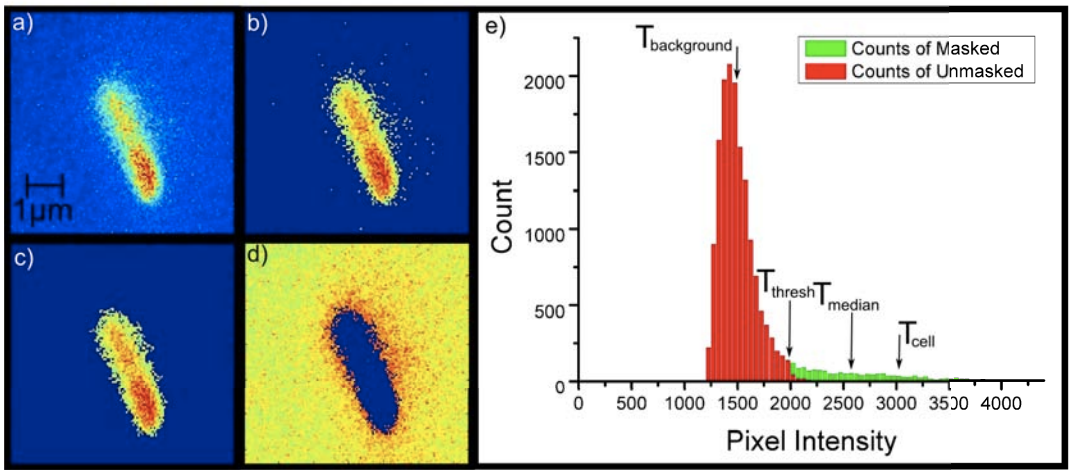

Figure 5.3: Method used to determine uorescent intensity of cell, M_{live}, from uorescent image. a) Full .sif image le recorded by camera including cell and background. b) All pixels in image that are more than one standard deviation above the mean in intensity. Note that there are occasionaly speckles far away from the cell representing uctuations in brightness not related to the cell. c) The masked image generated from taking the largest contiguous area with intensity greater than one standard deviation above the mean. d) The inverse of the mask. (a-d) shown with scaled false colour mapping which increases from blue through yellow to red. e) Histogram of total image, with histogram of masked area shown in green, and the histogram of the inverse section shown in red, in a stacked column plot. The median of the masked section, and the mean of all values greater than the median (T_{cell}), are indicated with arrows. The mean of the background is shown also ($T_{\text{background}}$). The intensity measurement, M_{live}, is calculated from T_{cell} $T_{\text{background}}$, and for this cell is 1692. The ratio of M_{live} to M_{absent} determines the voltage as shown in Section 5.7.

at each temperature at the end of the measurement. The background dye intensity is calculated from images of an empty area of the slide free from cells. Multiple images are taken with exposure times between 1 ms and 1 s, ~ 0.5 μm above the surface of the coverslip (corresponding to the depth of a cell). The gradient of the linear fit of intensity vs exposure time determines the contribution to the fluorescence from the external dye, and the y-intercept the background noise of the camera. This gradient is subsequently multiplied by the exposure time of the images taken to measure the internal fluorescent intensity. Thus for each image M_{live} is calculated, corresponding to the internal dye fluorescence, and M_{absent}, corresponding to the external dye fluorescence.

5.6.3 TMRM Dye Response with Temperature

To measure the V_m at different temperatures it is essential to ensure the dye behaviour is stable across the temperature range. This is accounted for by recording the background signal and measuring M_{absent} for slides at the temperature the sample will be measured. Thus our measurement of fluorescent intensity is calibrated for the temperature in question. Fig. 5.4 shows comparative linear fits for M_{absent} at three different temperatures. The background measurement can vary with preparation of the dye dilution and in practice it is measured for each slide to ensure the calibration of M_{absent} is accurate.

In order to test the response of TMRM dye across the temperature range, emission spectra from TMRM were recorded between 10 °C and 45 °C using a temperature controlled fluorimeter (see Section 2.2.2). Figure 5.5 shows the temperature response of a solution of 0.3 μM TMRM dye. Due to difficulties maintaining the spectrometer cuvette temperature below 10°C and condensation interfering with measurements, the measurements are taken in two sections: 10 °C - 45 °C and 5 °C - 10 °C. A linear decrease of intensity with temperature is observable between 10 °C and 45 °C with gradient of $-0.02A_{22}$ /°C where A_{22} is the mean absorbance measured at 22 °C. Cooling below 10 °C shows a peak in dye intensity at 7 °C and then a sharp drop in fluorescence at lower temperatures. Thus of the three temperatures used in this thesis, in general, the highest fluorescence signal for TMRM is at 22 °C, the second highest is at 5 °C, and the lowest intensity fluorescence signal is from TMRM at 45 °C.

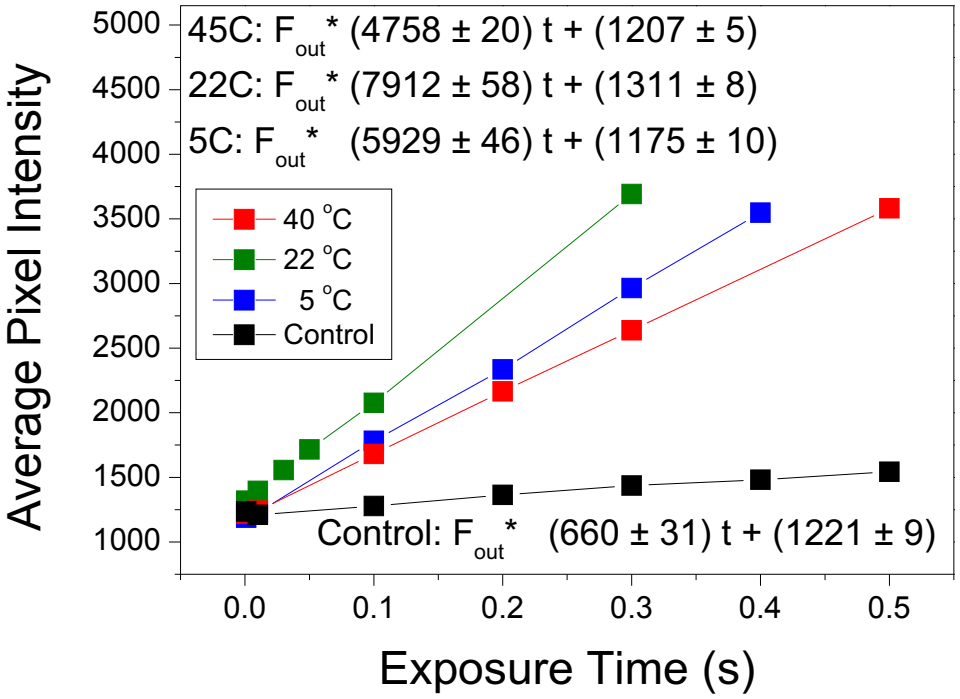

Figure 5.4: Linear relationships between mean fluorescent pixel intensity of 0.3 μM TMRM against exposure time for three individual measurements at 40 °C (red), 22 °C (green) and 5 °C (blue), with control (black) in absence of dye, at 22 °C. The gradient of the linear fits corresponds to the contribution from the dye in solution and the y-intercept corresponds to the offset of the camera. To calibrate M_{absent} the gradient of this fit is multiplied by the exposure time. In practice, background calibration curves are measured at the end of a set of cell measurements at all the temperatures involved in a measurement to minimize bleaching and to cross check for slide and temperature variation. The control is not subtracted from the background measurement since the variation in background from one slide to the next exceeds the background measurement by a factor of 3. It is included here to demonstrate that in the absence of dye there is only a weak relationship between exposure time and average pixel intensity. Standard error of the mean pixel intensity is 4 pixels at greatest and thus error bars are smaller than data points and not shown.

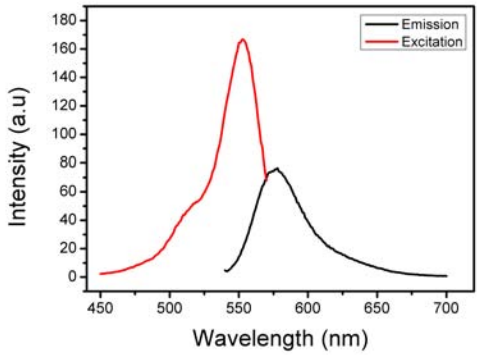

(a)

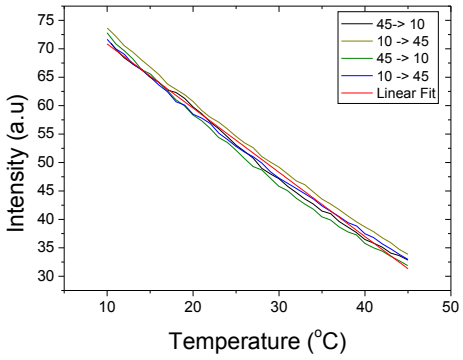

(b)

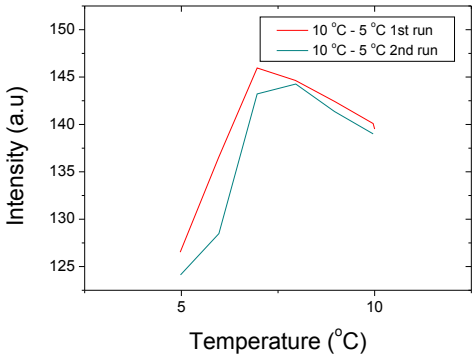

(c)

Figure 5.5: Plots of TMRM emission fluorescences fluctuation with temperature. a) 0.3 μM TMRM solution excitation and emission spectra. The maxima peak for the excitation spectra is at 553 nm, and for the emission spectra 578 nm. b) Plot of TMRM intensity vs temperature. The temperature is cycled twice, starting at 45 °C, the temperature is cycled first to 10 °C (black line), then back to 45 °C (yellow line), then down to 10 °C (green line), then finally back up to 45 °C (purple line). The red line shows a linear fit (Absorbance = $-0.02A_{22}$ /°C where A_{22} is the mean absorbance measured at 22 °C) over the average of all measurements. The discrepancy between individual ramps is due to lag in the system between the block temperature and the site of temperature measurement (a probe in an adjacent cuvette). c) TMRM intensity between 5 °C and 10 °C, from two attempts to slowly cool (0.01 °C / min) from 10 °C to 5 °C. TMRM intensity decays below 7 °C.

5.7 Measuring Voltage from Fluorescent Intensity

M_{live} and M_{absent} are used to calculate the concentration ratio across the membrane and thus the voltage. To measure the voltage it is necessary to cast a model to relate the relative fluorescent intensity into a measure of dye concentration. Lo (2007) described simulations for an optical convolution model for an ideal near-cylindrical cell filled with a known concentration of dye to create images which were subsequently analysed to measure M_{live}. In this thesis I show that a linear model is a suitable approximation to this model, and has the advantage that it can be extended to remove contributions from membrane bound dye. A full separation of membrane bound and cytoplasmic dye would require a further, more complicated convolution model, but it is not clear this would be a significant improvement over the linear model. The original convolution model is discussed initially, then the simple linear model, and finally the linear model accounting for membrane bound dye.

5.7.1 The Lo Convolution Model

Lo et al. (2007) created a three-dimensional model of a sample chamber, 14 μm $\times$12 μm $\times$ 3 μm in x, y, and z, filled with solution of known concentration (C_{out}). Inside this sample chamber an ideal cell was placed consisting of a cylinder 2 μm long and 0.9 μm in diameter, capped with 2 hemispheres 0.9 μm in diameter. The concentration of dye inside the cell was set to be C_{in}, and everywhere outside to C_{out}.

Lo et al. (2007) calculated the point spread function by taking snapshots at 50 nm intervals in the z-axis of 20 nm fluorescent beads. The point spread function, $P(x_i, y_i, z_i)$, was defined as the pixel intensity, $I(x_i, y_i)$ for these images. Since the image pixels were 50 nm square, this generated a cubic grid of intensity for voxels of size (50 nm)^3.

Lo et al. (2007) then calculated a simulated blurred fluorescent cell image (set at a distance $z_0 = 0.45$ μm from the coverslip) from the convolution of the point spread function and the dye distribution:

$$I_m(x_j, y_j, z_0) = \sum_i \left[C_i(x_i, y_i, z_i) \otimes P(x_j - x_i, y_j - y_i, z_0 - z_i) \right], \tag{5.4}$$

where $I_m(x_j, y_j, z_j)$ was the modeled intensity of image pixel j.

Lo et al. (2007) used these simulated images to calculate M_{live}[1] and calculated M_{absent} from a simulation in which $C_{\text{in}} = C_{\text{out}} = 0.1$ μM. Thus there was a set of fluorescent intensity measurements for cells of known concentration. This simulated data set could be used to relate fluorescent intensity to dye concentration using a correction function, $S(M_{\text{live}}/M_{\text{absent}})$, defined as:

$$S\left(\frac{M_{\text{live}}}{M_{\text{absent}}}\right) = \frac{\left(\frac{C_{\text{in}}}{C_{\text{out}}}\right)}{\left(\frac{M_{\text{live}}}{M_{\text{absent}}}\right)}. \tag{5.5}$$

In this thesis I use the data from this simulation from Lo (2007) to fit a hyperbola for the single free parameter for my equation for $S(M_{\text{live}}/M_{\text{absent}})$ derived from the linear model described in Section 5.7.2.

5.7.2 The Linear Model

To measure M_{live} a mask was chosen and T_{cell} was calculated within the area of this mask, as described in Section 5.6.1. M_{live} represents a pixel intensity within the area of the mask, however this value is calculated from an image which is generated from fluorescence inside a three dimensional volume. Consider a linear model in which the measurement of fluorescent intensity (M_{live}) is a linear sum of the internal dye concentration (C_{in}) and the external dye concentration (C_{out}) scaled by some factors a_1 and a_2. These factors have units that interconvert concentrations to pixel counts and they reflect the proportion of pixel intensity that is contributed from the volumes inside and outside the cell respectively. We have:

$$\begin{aligned}
M_{\text{live}} &= a_1 C_{\text{in}} + a_2 C_{\text{out}} \\
M_{\text{absent}} &= a_1 C_{\text{out}} + a_2 C_{\text{out}} = (a_1 + a_2) C_{\text{out}} \\
\Rightarrow \frac{M_{\text{live}}}{M_{\text{absent}}} &= \frac{a_1 C_{\text{in}}}{(a_1 + a_2) C_{\text{out}}} + \frac{a_2}{a_1 + a_2} \\
\Rightarrow \frac{C_{\text{in}}}{C_{\text{out}}} &= \frac{a_1 + a_2}{a_1}\left[\frac{M_{\text{live}}}{M_{\text{absent}}} - \frac{a_2}{a_1 + a_2}\right] \\
&= \frac{a_1 + a_2}{a_1}\left(\frac{M_{\text{live}}}{M_{\text{absent}}}\right) - \frac{a_2}{a_1}
\end{aligned}$$

[1]It should be noted that Lo (2007); Lo et al. (2007) used the notation F_{in} for M_{live} and F_{ex} for M_{absent}, but here I choose to use M notation for clarity in the subsequent linear model.

which using the substitution $\alpha = (\frac{a_1+a_2}{a_1})$ leaves:

$$\frac{C_{\text{in}}}{C_{\text{out}}} = \alpha \frac{M_{\text{live}}}{M_{\text{absent}}} + (1-\alpha). \tag{5.6}$$

Given Equation 5.5, this model naturally implies a hyperbolic fit for the correction factor. From Equation 5.6 we obtain:

$$\frac{\left(\frac{C_{\text{in}}}{C_{\text{out}}}\right)}{\left(\frac{M_{\text{live}}}{M_{\text{absent}}}\right)} = S\left(\frac{M_{\text{live}}}{M_{\text{absent}}}\right) = (1-\alpha)\frac{1}{\left(\frac{M_{\text{live}}}{M_{\text{absent}}}\right)} + \alpha. \tag{5.7}$$

Substituting $y = \frac{C_{\text{in}}}{C_{\text{out}}}$ and $x = \frac{M_{\text{live}}}{M_{\text{absent}}}$ gives:

$$S(x) = \frac{(1-\alpha)}{x} + \alpha, \tag{5.8}$$

which is the standard form for an hyperbola.

The value for α is calculated using the correction factor data calculated using Equation 5.4 (Lo, 2007). The data and fit are shown in Figure 5.6. An hyperbola was fitted to calculate $\alpha = 3.52899$ with reduced $\chi^2 = 2.2919 \times 10^{-4}$. By comparison, Lo (2007) used a linear combination of exponential fits to fit this data with reduced $\chi^2 = 102.8 \times 10^{-4}$, which is a less accurate estimation of this fit. The residuals (Figure 5.6(inset)) show that this is not a perfect fit for the data, especially at low V_m where $M_{\text{live}}/M_{\text{absent}} < 10$. This causes slight underestimation at very low fluorescence values. For example if $M_{\text{live}}/M_{\text{absent}} = 1.588$, the lowest non unity data point available, $C_{\text{in}}/C_{\text{out}} = 3$, while from the linear fit $C_{\text{in}}/C_{\text{out}}$ is estimated as 3.076, leading to an overestimation of V_m by 0.9 mV. This is well within the measurement error, discussed in Section 5.9.3.

This convolution model calculates $C_{\text{in}}/C_{\text{out}}$, the ratio of internal and external dye concentrations, from the fluorescence ratio $M_{\text{live}}/M_{\text{absent}}$. For conditions where the membrane bound dye (C_{bound}) is not significant then $C_{\text{in}}/C_{\text{out}}$ is calculated using Equation 5.6, and V_m is further calculated from this using Equation 5.2. In conditions where the membrane bound dye (C_{bound}) is significant, an additional measurement, M_{CCCP}, is needed. This measurement is then used with an extended linear model to remove the contribution from C_{bound} to get a more accurate estimate of C_{in}. This measurement and the extended linear model is discussed in Section 5.7.3.

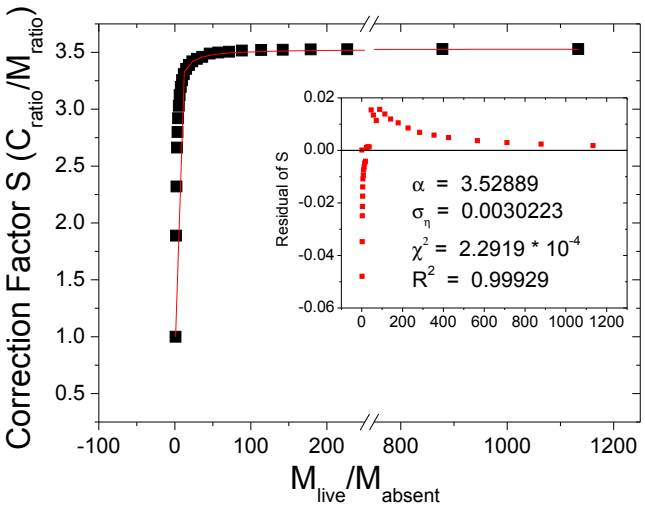

(a)

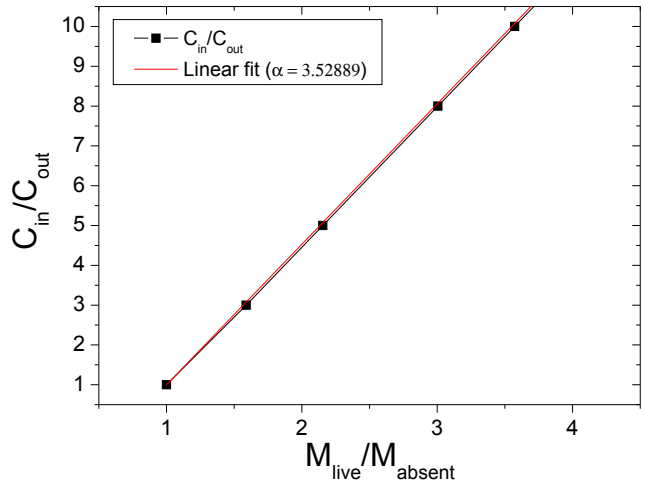

(b)

Figure 5.6: a) Plot of correction factor, S, against M_{ratio} ($M_{\text{live}}/M_{\text{absent}}$) where S is defined as per Equation 5.5. Data points taken from Lo (2007) but original fit using Origin to fit for α in Equation 5.6. The multiple exponential fit from Lo (2007) had a computational $\chi^2 = 0.01028$ and $R^2 = 0.97314$ while the fit here has a computational $\chi^2 = 2.2919 \times 10^{-4}$ and $R^2 = 0.99929$. Plot of the residual is shown inset and demonstrates that the hyperbola is not a perfect fit to the correction factor curve and deviates from the hyperbola particularly for low values, for example $F_{\text{ratio}} < 10$. The fit arises naturally from a consideration of the linear combination of the measured fluorescence intensities that make up a single image, as demonstrated in Equations 5.6–5.9. b) Plot of $C_{\text{in}}/C_{\text{out}}$ against $M_{\text{live}}/M_{\text{absent}}$ for low values of $M_{\text{live}}/M_{\text{absent}}$ with linear fit in red. The deviation between the fit and the actual data is very small, and the maximum associated voltage error is discussed in the text.

5.7.3 The Extended Linear Model and M_{CCCP}

The linear model was extended to be the linear sum of three cellular measurements: 1) M_{live}, associated with the fluorescence from the dye molecules bound inside the cell, 2) M_{absent}, taken with no cell in the field of the camera, as a measure of the background intensity of the dye, and 3) M_{CCCP}, the measurement of the cell after 100μM CCCP has been flowed in, which changes the internal concentration of the dye to match the external concentration of the dye. These three measurements are represented schematically in Figure 5.7.

The first measurement, M_{live}, taken inside the mask used to calculate T_{cell} (Section 5.6.1), consists of the linear sum of the fluorescence from dye inside the cell, outside the cell, and bound to the membrane itself.

$$M_{\mathrm{live}} = a_1 C_{\mathrm{in}} + a_2 C_{\mathrm{out}} + a_3 C_{\mathrm{bound}}, \tag{5.9}$$

where C_{in} is the concentration of dye molecules inside the cell, C_{out} is the concentration of dye molecules outside the cell, and C_{bound} is the amount of dye molecules bound to the membrane, and a_1, a_2, and a_3 reflect the linear biases. Similarly for M_{CCCP} we have:

$$M_{\mathrm{CCCP}} = a_1 C_{\mathrm{out}} + a_2 C_{\mathrm{out}} + a_3 C_{\mathrm{bound}}, \tag{5.10}$$

since CCCP makes ion concentration equal across the membrane and so the concentration of dye inside and outside the cell are equal. For M_{absent} we have:

$$M_{\mathrm{absent}} = a_1 C_{\mathrm{out}} + a_2 C_{\mathrm{out}} = (a_1 + a_2) C_{\mathrm{out}} \tag{5.11}$$

Subtracting M_{CCCP} from M_{live} we can remove C_{bound} and derive an equation to calculate C_{in}:

$$C_{\mathrm{in}} = \frac{M_{\mathrm{live}} - M_{\mathrm{CCCP}}}{a_1} + C_{\mathrm{out}} \tag{5.12}$$

$$= \frac{M_{\mathrm{live}} - M_{\mathrm{CCCP}}}{a_1} + \frac{M_{\mathrm{absent}}}{(a_1 + a_2)} \tag{5.13}$$

And thus it follows that we can calculate $C_{\mathrm{in}}/C_{\mathrm{out}}$ in terms of M_{live}, M_{CCCP} and

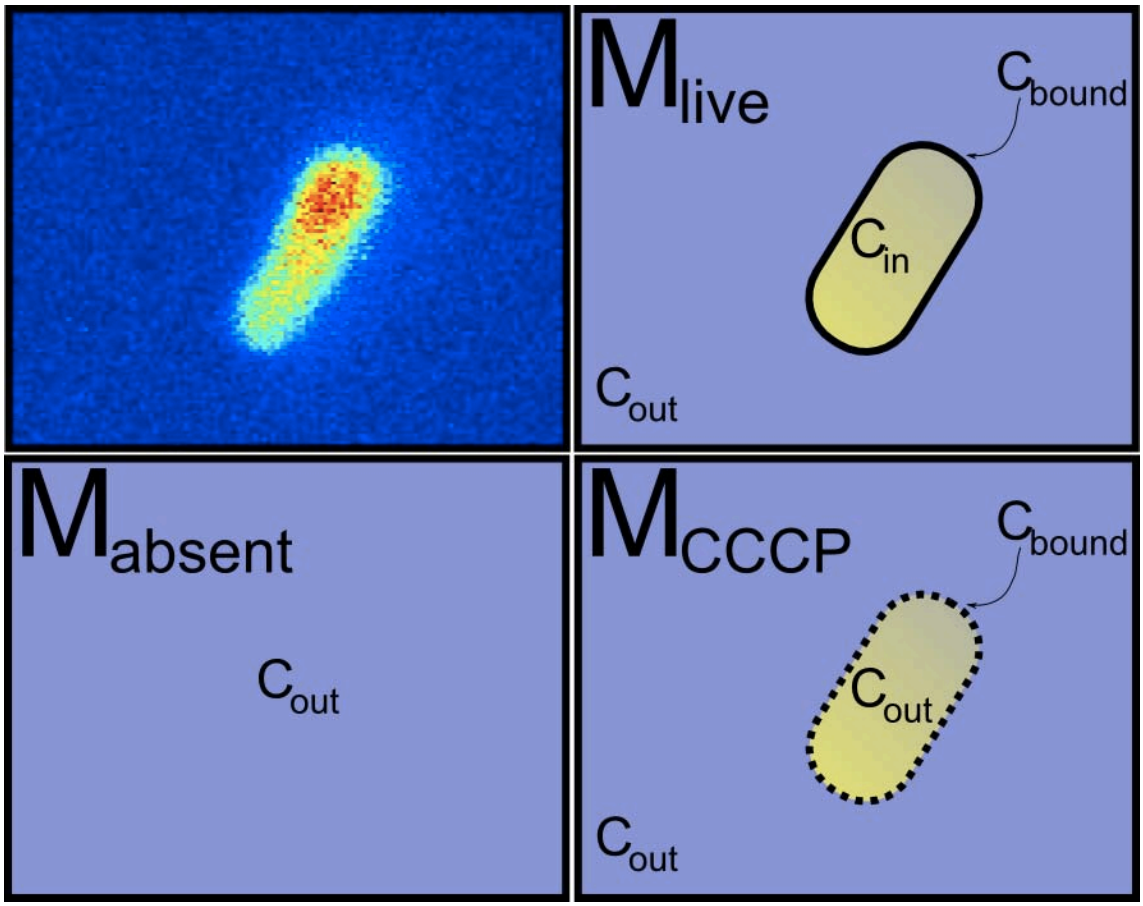

Figure 5.7: Figure showing uorescent image of a cell and a break down of the three measurements involved in the model. Clockwise from top left i) image of the dye TMR uorescing inside the cell when illuminated by 532 nm laser light in epi- uorescence. ii) The M_{live} measurement is calculated from this measurement, assuming the uorescent image consists of the linear sum of three populations of dye molecules, C_{in}, dye molecules from the volume inside the cell, C_{out}, dye molecules from the volume outside the cell and C_{bound}, dye molecules bound to the surface of the cell. iii) The M_{CCCP} measurement is identical to M_{live} except that the cell has been treated with CCCP and so the membrane is perforated and the concentration of dye inside and outside the cell are the same so the uorescence measured is the convolution of C_{out} and C_{bound}. iv) The nal measurement, M_{absent} is taken in the absence of any cell and is a measure of C_{out}. By combining these measurements C_{in} is determined in terms of M_{live}, M_{CCCP}, and M_{absent}.

M_{absent}.

$$\frac{C_{\text{in}}}{C_{\text{out}}} = \frac{(a_1 + a_2)(M_{\text{live}} - M_{\text{CCCP}})}{a_1 M_{\text{absent}}} + 1 \tag{5.14}$$

$$= \left(\frac{a_1 + a_2}{a_1}\right)\left(\frac{M_{\text{live}} - M_{\text{CCCP}}}{M_{\text{absent}}}\right) + 1 \tag{5.15}$$

$$= \alpha \frac{M_{\text{live}} - M_{\text{CCCP}}}{M_{\text{absent}}} + 1, \tag{5.16}$$

where the substitution $\alpha = (\frac{a_1+a_2}{a_1})$ is used, as in Section 5.7.2. The correction factor data from Lo (2007) (shown in Figure 5.6) is used to fit for α, and V_m is subsequently calculated using this value of α in Equation 5.16.

5.8 Mean Membrane Voltage as a Function of Temperature

The mean effect of temperature change on membrane voltage can be determined by measuring the V_m of multiple cells in identical conditions. The membrane voltage at 5 °C, 22 °C and 40 °C is shown in Figure 5.8.

The membrane voltage was -120 mV – -130 mV between 5°C - 40°C. An analysis of variance (ANOVA) one-way test was performed to determine for significant differences between the means. At the 0.05 level there was significant difference in the population means. Further analysis and mean comparison using a Scheffé test (Scheffé, 1959) indicated that the mean of the population of 5 °C measurements was significantly different from the mean of the population of 22 °C measurements, with no significant difference between 5 °C and 40 °C means, or between 22 °C and 40 °C population means. A Levene test for homogeneity of variance (Levene, 1960) demonstrated that the population variances were significantly different. (see Appendix C for full tabulated analysis). It should be noted that ANOVA tests assume normal distribution of populations, and that these populations were not significantly drawn from a normal distribution according to a Shapiro-Wilk normality test (see histograms in Figure 5.8(b,c)) (Shapiro and Wilk, 1965). However, ANOVA tests are robust to non-normality dependent on the skew and kurtosis of the distribution (Harwell et al., 1992), and the number of samples (Glass et al., 1972), and in these cases there are a large number of samples with low skew but high kurtosis. Use of ranked methods, such as the Kruskal-Wallis method (Kruskal and Wallis, 1952), may provide further information to help assess differences in mean and variance between

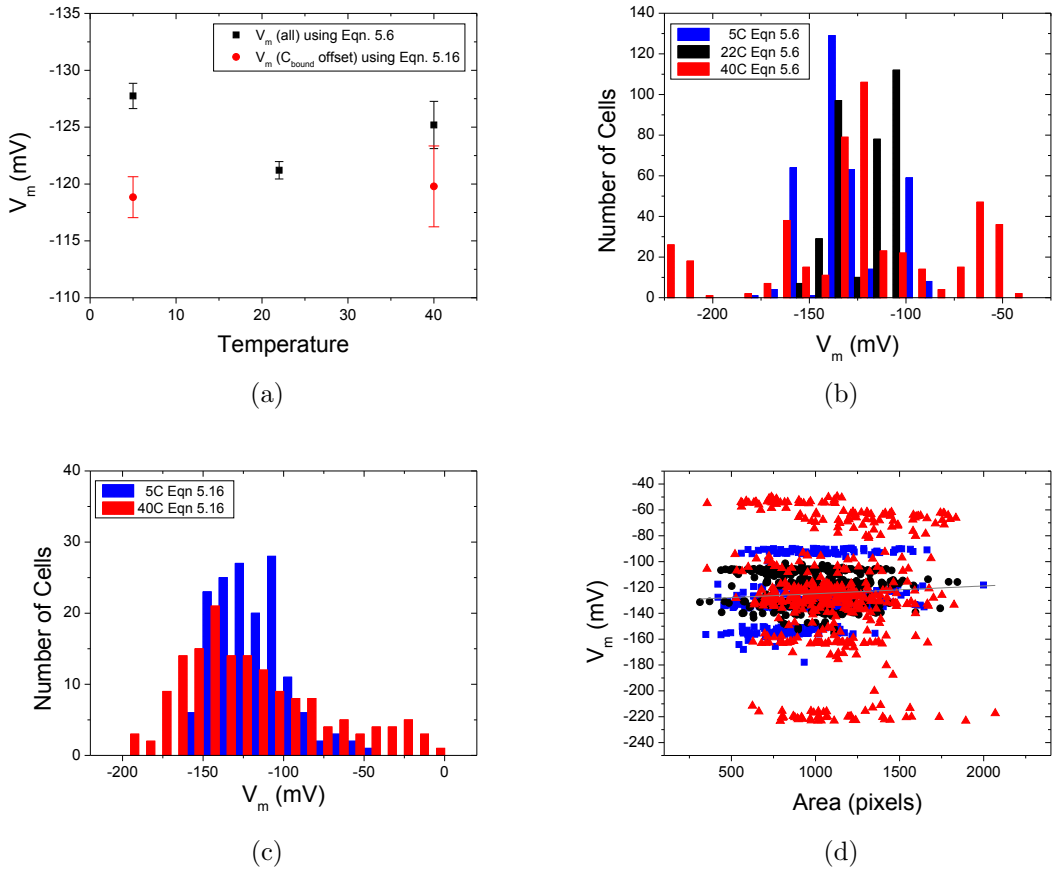

Figure 5.8: (a) Average membrane voltage against temperature for three temperatures: 5 °C (343 cells), 22 °C (333 cells), and 40 °C (467 cells) calculated using Equation 5.6, with standard error of the mean (SEM) indicated with error bars. The membrane voltage is nearly constant throughout the temperature range with a significant but small difference in mean between 20 °C and 5 °C as indicated by a Scheffé test (see text). Values offset for membrane bound dye (C_{bound}) indicated in red for 5 °C (151 cells) and 40 °C (158 cells), calculated using Equation 5.16. Membrane bound dye has a higher relative effect at 5 °C than at 40 °C as shown by the larger difference between offset and total V_m at low temperature, corresponding to a high value of M_{CCCP}. C_{bound} offset measurement not included for 22 °C as previously measured (Lo, 2007) (b) Histogram of total V_m at 5 °C, 22 °C and 40 °C demonstrating non-normality of distributions, as verified by Shapiro-Wilk test, and significant difference in variance at different temperature, as verified by Levene test. (c) Histogram of C_{bound} offset V_m at 5 °C and 40 °C. (d) Control showing V_m against cell area, measured as number of pixels in mask, to show that voltage is not dependent on cell size. Grey line is near horizontal linear fit to the concatenated data set of all temperatures ($V_m = 5.994 \times 10^{-3}$ mV / pixel · area + 130 mV), demonstrating independence of V_m on area.

the populations, but these were not considered here. Due to difficulties in discerning differences in population wide measurements a single cell tracking approach was developed, as discussed in Section 5.9.1. From these averaged measurements however, it can be noted that the membrane voltages stay constant within 5 mV across the temperature range.

In order to discount variation from cell size and orientation V_m was plotted against the mask area (in pixels). A linear fit for the concatenated measurements across all temperatures had a near horizontal gradient (5.994×10^{-3} mV / pixel) indicating there was little area dependent bias in the voltage measurement technique. This is shown in Figure 5.8(d).

It is of only marginal use to compare these measured values in *E. coli* to previous microelectrode measurements performed on large neuronal or mammalian cells (Latorre and Hidalgo, 1969; Dipolo and Latorre, 1972; Creese et al., 1958; Ling and Woodbury, 1949). However the variation in potential of axonal and mammalian cells with temperature is similar to my observations, that is, near-constant potential across a large temperature range.

5.9 Heating the Bacterial Flagellar Motor and the Energetic Response

5.9.1 Single Cell Tracking

The results in Section 5.8 suggest that temperature has little effect on membrane voltage. However, these measurements were complicated by taking an average over a population of cells. Due to high variance between cells, an alternative method for tracking the specific cellular membrane voltage response to temperature was tried. This method was to track a single cell across a temperature change. This allows for direct comparison of the values from a single cell at different temperatures, rather than a shift in the mean across many cells, and allows direct calibration of the quantity of bound dye for each cell.

To measure the response of a single cell to temperature TMRM is preincubated in the cells at room temperature for 20 minutes, as per Section 5.5.2, and the sample is then placed on a preheated microscope. A suitable cell is located quickly ($\sim$1 minute) and measurements of fluorescence are taken as the cell responds to the temperature change. The microscope is preheated to ensure that the immediate response of the cell to temperature change is recorded as the microscope is in a

steady state and drift is minimal. If the cell is measured at room temperature and then heated to a second temperature the drift associated with a system-wide temperature change prevents easy measurement of the immediate effects of heating (see Chapter 3). After a set of measurements over a period of ∼30 minutes, the ion gradient is uncoupled using CCCP (100 μM), and further fluorescent measurements are made to quantify the amount of bound dye. CCCP causes an exponential decay in the fluorescence. The limiting value of the exponential decay in fluorescence in response to CCCP was interpreted as due to membrane-bound dye.

5.9.2 Bleaching

Previous measurements (Lo et al., 2007) of membrane voltage took only a single measurement of each cell and calculated mean voltages over many cells in a single slide (as in Fig. 5.8). Single cell tracking requires multiple measurements of a single cell over a period of time. When tracking single cells up to 10 measurements of the same cell are taken and it is necessary to ensure that bleaching and recovery of a fluorophore do not cause an underestimation in the measurement of V_m. Specifically this involves ensuring that the TMRM dye does not bleach appreciably over typical aggregate exposures (∼0.75 J/cm^{-2}), or that if bleaching does occur, the turnover from dye in the reservoir of the sample to dye in the cell is sufficiently high that this bleaching will not interfere with the measurements. Figs. 5.9 and 5.10 show bleaching effects with 50 μW laser power entering the back of the objective for 60 ms and 20 ms exposure times respectively.

5.9.3 Error in Fluorescence Measurement

In Section 5.8, the error on V_m for ensemble measurements is calculated by taking the standard error across the sample. For single cell measurements, discussed in Section 5.9.1, standard errors cannot be calculated over a range of cell values and so error must be calculated by considering the variance in fluorescence measurement.

One approach is to calculate δM_{live} formulaically by looking at per-pixel variation in a single image, and considering the variance and standard deviation of pixel intensity across the image that generated the value of M_{live}. The primary sources of error here are the variance in the threshold, variance in the median (T_{median}), and in the points of intensity greater than the median, whose mean generates M_{live}. However by-pixel error estimation is most likely to be an underestimate and the theory is laborious. A simpler approach is to measure the variance in M_{live} across a

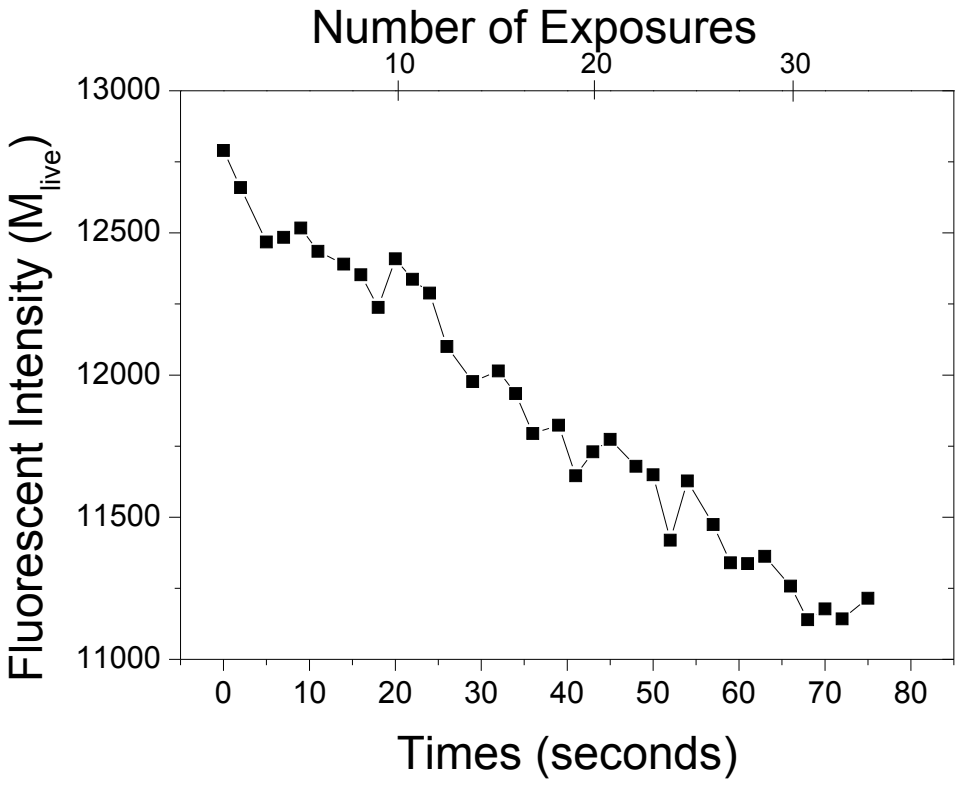

Figure 5.9: Bleaching trace of a single cell responding to 34 exposures of 60 ms 532nm laser at 7 W/cm^2 (40 μW laser entering back of objective). The total laser energy delivered is 14.28 J cm^{-2}. Over these exposures the M_{live} value of the cell decreases from 12790 to 11215, or 12%. In single cell tracking measurements typically less than 10 exposures are delivered, indicating that bleaching does not contribute significantly to measurements.

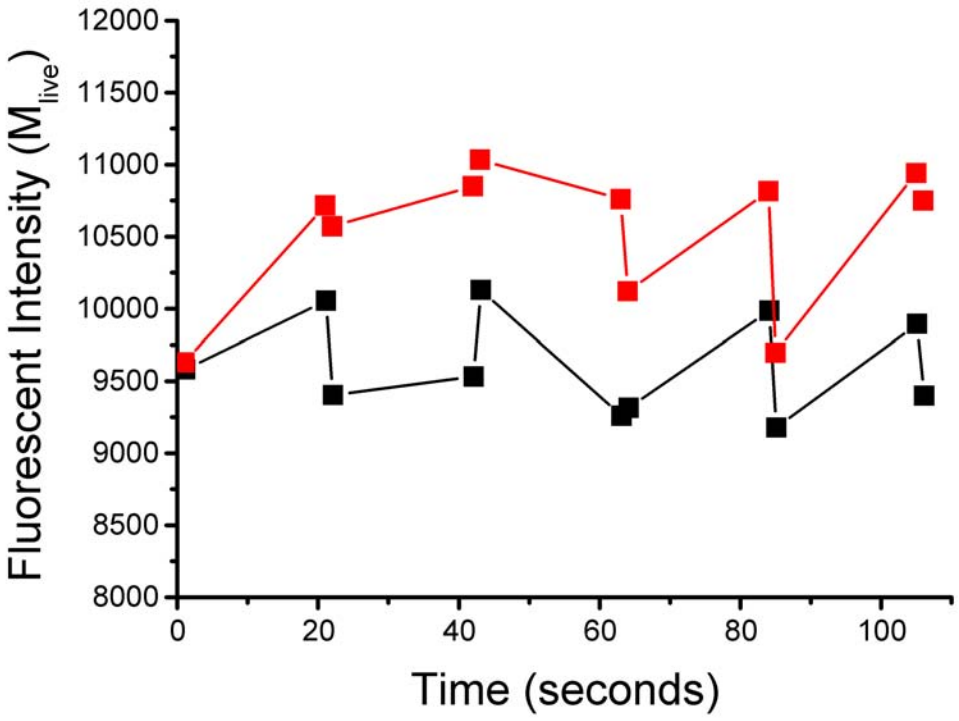

Figure 5.10: Two separate measurements of two single cells responding to 11 exposures of 20 ms 532nm laser at 40 μW power. The energy delivered is 1.54 J/cm^{-2}. M_{live}, stays approximately constant with a mean of 10535 $\pm$ 148 (red squares) and 9620 $\pm$ 104 (black squares) for the two cells. In typical single cell tracking measurements less than ten 20 ms shots of 50 μW exposure are delivered, or 1.4 J/cm^{-2}.

set of identical measurements on a single cell. From the mean variance in 5 sets of 11-shot measurements (identical to those in Figure 5.10) taken with a laser power of 200 μW and exposure time of 20 ms the standard error in M_{live}, δM_{live}, was calculated to be 125 counts. δM_{CCCP} was estimated from the standard error in the fit of the exponential decay to the data points from the cell fluorescence after CCCP is flowed in and similarly δM_{absent} was estimated from the standard error of the linear fit to the background data.

Standard error analysis was used with these values of δM_{live}, δM_{CCCP}, and δM_{absent} and Eqns 5.16 and 5.6 to calculate δC_{ratio} (where $C_{\text{ratio}} = C_{\text{in}}/C_{\text{out}}$). Since:

$$C_{\text{ratio}} = \frac{\alpha(M_{\text{live}} - M_{\text{CCCP}})}{M_{\text{absent}}} + 1 \tag{5.17}$$

we can calculate the root-mean-square error from:

$$\left(\frac{\delta C_{\text{ratio}}}{C_{\text{ratio}} - 1}\right)^2 = \left(\frac{\delta(M_{\text{live}} - M_{\text{CCCP}})}{M_{\text{live}} - M_{\text{CCCP}}}\right)^2 + \left(\frac{\delta M_{\text{absent}}}{M_{\text{absent}}}\right)^2 \tag{5.18}$$

$$\Rightarrow \left(\frac{\delta C_{\text{ratio}}}{C_{\text{ratio}} - 1}\right)^2 = \left(\frac{\delta M_{\text{live}}^2 + \delta M_{\text{CCCP}}^2}{(M_{\text{live}} - M_{\text{CCCP}})^2}\right) + \left(\frac{\delta M_{\text{absent}}}{M_{\text{absent}}}\right)^2 \tag{5.19}$$

$$\Rightarrow \delta C_{\text{ratio}}^2 = (C_{\text{ratio}} - 1)^2 \left[\frac{\delta M_{\text{live}}^2 + \delta M_{\text{CCCP}}^2}{(M_{\text{live}} - M_{\text{CCCP}})^2} + \frac{\delta M_{\text{absent}}^2}{M_{\text{absent}}^2}\right]. \tag{5.20}$$

Since $V_m = \frac{kT}{e}\ln(C_{\text{ratio}})$, the standard error in membrane voltage, δV_m, can be calculated from:

$$\delta V_m = \frac{\partial V_m}{\partial C_{\text{ratio}}}\delta C_{\text{ratio}} \tag{5.21}$$

$$\Rightarrow \delta V_m = \frac{kT}{e}\frac{1}{C_{\text{ratio}}}\delta C_{\text{ratio}}. \tag{5.22}$$

Excluding consideration of the bound dye and M_{CCCP}, the error is calculated from:

$$C_{\text{ratio}} = \frac{\alpha M_{\text{live}}}{M_{\text{absent}}} - (\alpha - 1) \tag{5.23}$$

$$\left(\frac{\delta C_{\text{ratio}}}{C_{\text{ratio}} + (\alpha - 1)}\right)^2 = \left(\frac{\delta M_{\text{live}}}{M_{\text{live}}}\right)^2 + \left(\frac{\delta M_{\text{absent}}}{M_{\text{absent}}}\right)^2 \tag{5.24}$$

$$\delta C_{\text{ratio}}^2 = (C_{\text{ratio}} + (\alpha - 1))^2 \left[\left(\frac{\delta M_{\text{live}}}{M_{\text{live}}}\right)^2 + \left(\frac{\delta M_{\text{absent}}}{M_{\text{absent}}}\right)^2\right] \tag{5.25}$$

$$\tag{5.26}$$

with the membrane voltage error calculated as before (Eqn. 5.22).

5.9.4 Membrane Voltage Decay above 40°C

Measuring the single cell response to temperature change provides the opportunity to calibrate the bound dye uniquely for each cell and gauge the cellular response to temperature change more closely. The presence of chimeric stator mutants has been shown to induce temperature sensitivity (Fukuoka et al., 2004; Mashimo et al., 2007), and so it is possible that the presence of PomAPotB induces temperature sensitivity in the motility of the BFM. In the case of the chimeric flagellar motor, long term exposure to temperatures above 40 $°C$ caused the fluorescence to decay, signifying a reduction in V_m. This decay in fluorescence was exponential and thus the decay in V_m was linear due to the logarithmic relation between V_m and fluorescence. This decay is shown in Figure 5.11.

The gradient of the linear decay in V_m corresponds to the time constant of the exponential decay of the fluorescence, and is quite rapid ($t_{1/2} \approx 500\ s$). Prolonged exposure to temperatures above 40 °C can irreversibly damage the membrane voltage of a cell. The resilience of cells to heat shows high variance, as demonstrated by the variance in gradient of the linear fit for decay in V_m. A total of 12 cells were observed with V_m decaying in response to high temperature. Of those, gradients were calculated for three, and these three had mean (± SEM) gradients 0.0327 ± 0.0025 mV/s (excluding C_{bound}) and 0.0397 ± 0.0035 mV/s (including C_{bound}).

In collaboration with the Ishijima group at Tohoku University, Sendai, Japan, the effects of high temperature on the motility and energetics of the chimeric BFM were measured. At high temperatures they have observed motor stoppage and stepwise recovery upon cooling. Figure 5.12 shows the torque and speed of a motor repeatedly heated above 40 °C. Most notably, the speed, and thus torque, falls to zero upon heating to 45 °C and then resurrects in stepwise fashion upon cooling. Removing and restoring the IMF exhibits an identical trend, that is stopping followed by stepwise resurrection. This has been demonstrated with sodium resurrection experiments, alternately flowing 0 mM [Na^+] and 85 mM [Na^+] through a sample, and by directly controlling the PMF with an electrode and micropipette (Fung and Berg, 1995). This cycles the IMF between 0 and ∼190 mV (Rowe, 2005; Baker and Berry, 2009). Lo et al. (2007) observed similar stoppages in alkaline conditions (pH = 8.0, V_m = 165 mV)) within 2 minutes, with voltage during the same period decaying over 10 minutes. Upon restoration of neutral pH, stopped cells resurrected in discrete steps, shown in Figure 5.13. Lo et al. (2007) proposed that these stops were a result of collapse in V_m, and resurrections a result of the restoration of the IMF. Similarly, the stoppages at high temperature could be a direct consequence of V_m and IMF

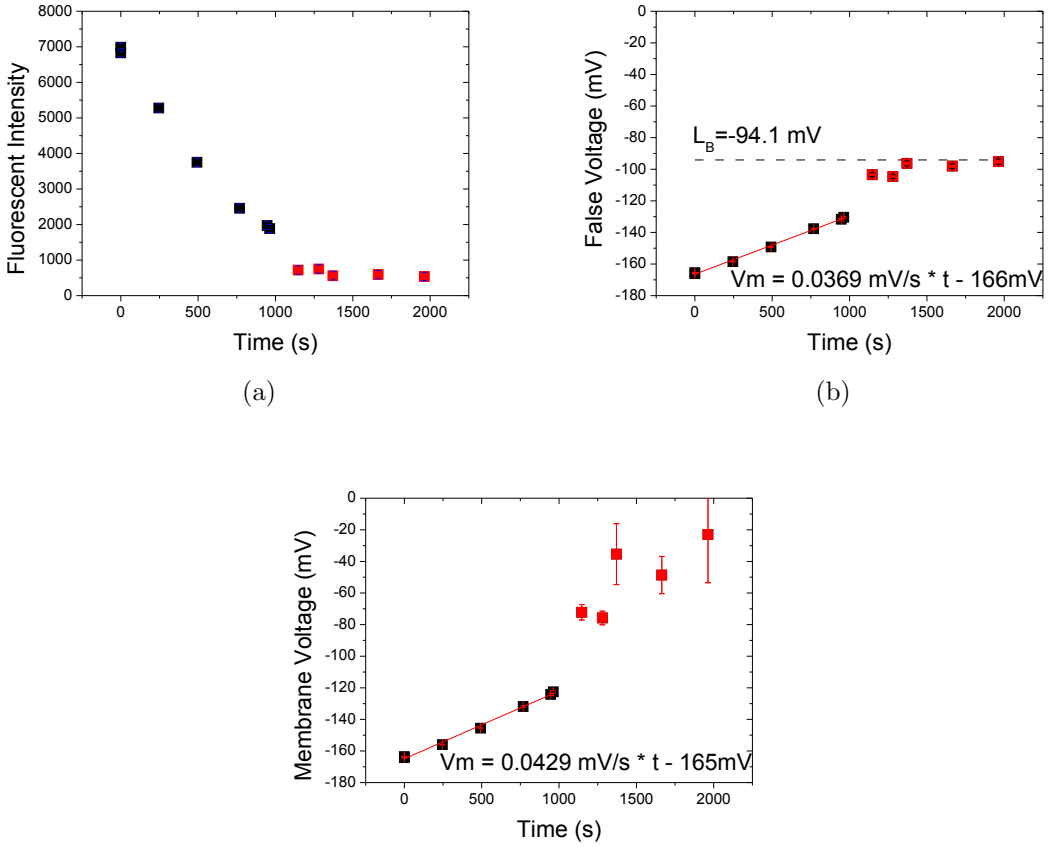

Figure 5.11: Decay in membrane voltage and associated fluorescence at 40°C. a) Fluorescent intensity, M_{live} against time for a single cell tracked at 40 °C (black squares). After ∼15 minutes 50 μM CCCP is flowed into the chamber to calculate the quantity of bound dye (M_{CCCP}, red squares). An exponential fit is taken for the measurements after CCCP is flowed in (red line) and the asymptote of this exponential decay is used as the value for M_{CCCP}, and the error in the fit as δM_{CCCP}. b) False membrane voltage against time for the same cell without including calculations for bound dye and M_{CCCP} (black squares pre-CCCP, red square post-CCCP). Voltage is calculated using Eqn. 5.6. A linear fit to the voltage for the pre-CCCP measurements shows the fluorescence decay is exponential with time constant 0.0369 mV/s. After CCCP is introduced this false membrane voltage approaches a limit corresponding to the equivalent fluorescence from the bound dye ($L_B = 94.1$ mV). This does not represent a voltage, as the voltage is destroyed by CCCP, but it instead represents the limit of resolution if C_{bound} is not measured and accounted for. c) Membrane voltage against time including considerations for bound dye and M_{CCCP}. Voltage is calculated using Equations 5.16 and 5.2. $V_m \to 0$ as $M_{\text{live}} \to M_{\text{CCCP}}$, which happens ∼15 minutes after CCCP is added to the solution. The error bars are calculated as detailed in Section 5.9.3. Note that the calculated voltages when $M_{\text{live}} \approx M_{\text{CCCP}}$ are small measurements based on the difference of two large numbers, and hence have large error bars.

decay upon heating, but further work is required to con rm this by, for example, investigating V_m decay and recovery upon heating and subsequent cooling. This is discussed in Section 5.9.5.

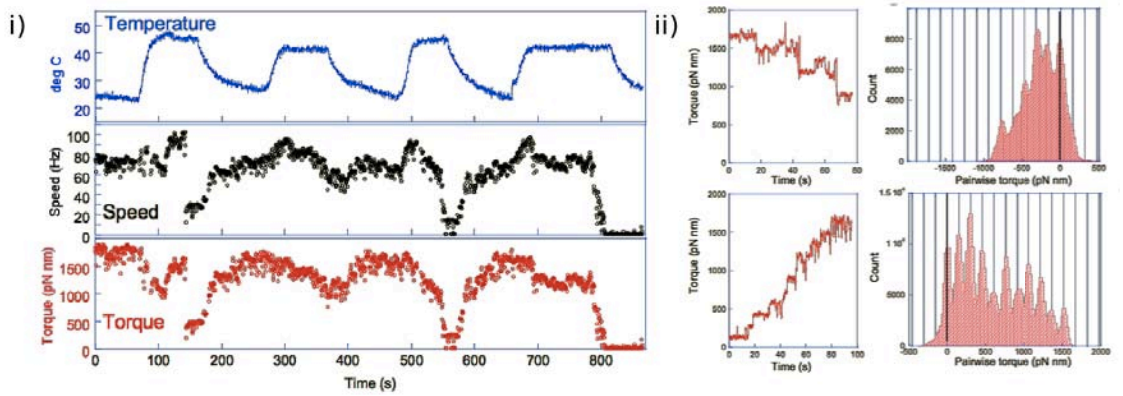

Figure 5.12: (a) Stopping and stepwise recovery of speed and torque on heating to 45 C. i) Traces showing transient heating and cooling and synchronous motor stopping during heating. Stops repeatedly occur when heated to 45 C and motility is restored upon cooling. ii) Close detail of recovery showing stepwise recovery of torque, putatively as stators return to the motor. Unpublished data from Dr Yuichi Inoue, Tohoku University, Sendai, Japan.

5.9.5 V_m Recovery with Transient Heating

If the stoppage and recovery of the chimeric motor at high temperature is caused by temperature driven voltage change, then it should be possible to observe not only V_m decay but also subsequent recovery. Figure 5.14 shows a cell with stable voltage (-112 mV) at 25 C heated to 45 C for 280 seconds. Upon heating to 45 C the V_m initially increased to -143 mV, and subsequently decayed to -87 mV, recovering to -120 mV when the cell was returned to room temperature. Decay commenced within 400 s of reaching 45 C. This was markedly slower than the stopping response upon heating shown in Fig. 5.12, which occurs within 50 s, however there is a time delay in the response of the uorescent dye to voltage. A $\gg$10 minute response in uorescence decay was observed when CCCP was introduced, reducing the V_m to zero (Figure 5.11). This decay response is similar to those observed by Lo et al. (2007), where voltage measurements in a motor at high pH lag motor stoppage by 5 minutes. It is likely therefore that stoppages are related to voltage decay.

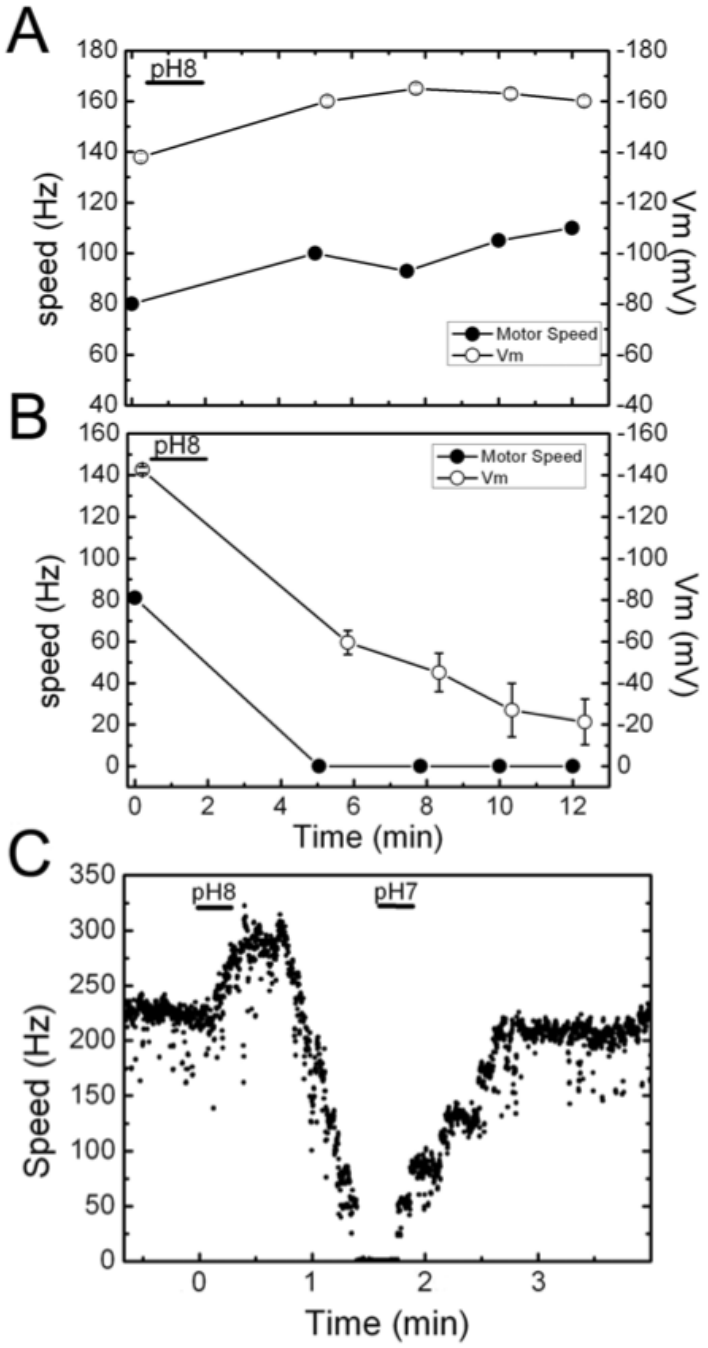

Figure 5.13: Drop in membrane voltage and motor speed in alkaline conditions. A) Voltage and speed measured in tandem for a cell that does not stop or suffer SMF collapse upon introduction of buffer at pH8. B) Voltage decay upon introduction of buffer at pH8 over 12 minutes (white circles) and speed decay (black circles). Speed in A) and B) measured using video analysis of rotating beads from method of Sowa et al. (2005), where speed and voltage are measured at intervals. C) Back focal plane measurements of the speed of a 0.5 μm bead in response to alkaline buffer. pH8 buffer and pH7 buffer introduced as marked by bars at top of figure. From Lo (2007).

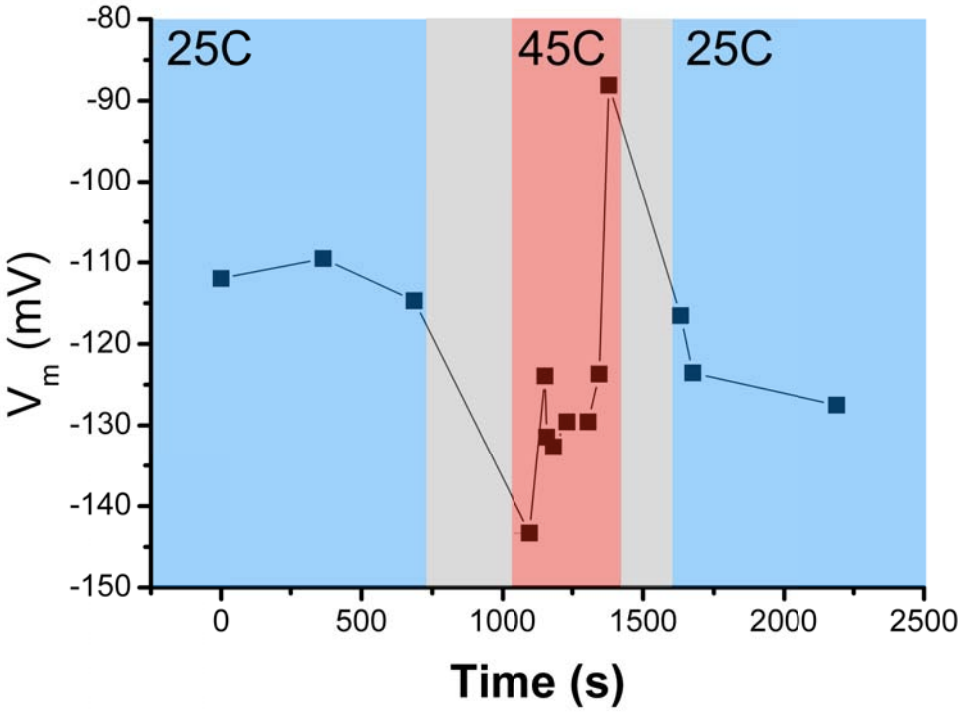

Figure 5.14: V_m decays at end of exposure to 45 C, but recovers during the transient temperature section marked in grey, shown by higher V_m measurement upon arrival at 25 C.

The strongest evidence for this is the stepwise resurrection of speed and torque, a signature of V_m removal and restoration, upon returning to room temperature. This is a signature of stator departure and return as observed in sodium resurrection experiments (Rowe, 2005), alkaline conditions (Lo et al., 2007), low voltage (Fung and Berg, 1995), and now at high temperature.

The membrane voltage is sensitive to the duration of exposure to 45 C heating, and there is also cellular variation in resistance to temperature and recovery, as shown by the change in voltage drop, and the speed of decay, for similar exposure. Putatively this corresponds to cellular variation in the quantity of heat-shock proteins (Bukau, 2006) expressed within the cell. Figure 5.15 shows two cells at a lower initial voltage responding to heat shock. Initially they decay very rapidly on arrival at 45 C, and then recover to their initial voltage more slowly. Figure 5.16 shows a cell that maintains V_m throughout the heating period ($\gg$8 minutes) and then decays during the cooling to room temperature, upon which point it rapidly recovers to

its initial V_m. Lastly Fig. 5.17 shows a cell that decays rapidly upon heating, even before arrival at 45 °C, is kept at 45 °C for 10 minutes and does not recover upon cooling to 25 °C. The range of effects are difficult to fully characterise due to the rarity of observing recovery (roughly 1 cell in 5 recovers). Here individual traces displaying decay and recovery behaviour are shown to demonstrate that recovery can occur after transient heating of various durations. To conclusively identify the link between voltage decay and high temperature stops in the chimera simultaneous measurements of voltage and speed at high time resolution are needed, as discussed further in Section 5.12.

5.10 Temperature Effects on Plated Cell Growth

Heat has been shown to affect motility and V_m in the chimera. If function, in particular motility, is reduced at high temperature, then this may also be reflected in growth assays. To test this cells were plated out after being incubated in eppendorf tubes in a water bath at 45 °C for 1, 5, 10 and 20 minutes respectively, as detailed in Section 2.4.4. Cells were then diluted to 2×10^{-6} of their original concentration and spread over plates and incubated at 30 °C. A comparative image of the plates is shown in Figure 5.18(a) and a plot of colony count vs incubation time is shown in Figure 5.18(b).

As Figure 5.18 shows, there is an exponential decrease in colony growth with increased incubation time at 45 °C. This implies that cellular function is affected by prolonged heat exposure, and is further evidence of cellular metabolic failing at high temperature which may first be observed as stops and subsequently voltage decay.

5.11 Discussion

In this thesis a linear model was developed to measure dye concentration and subsequently voltage. This model was used to establish that the membrane voltage remains between 120 – 130 mV between 5 °C and 40 °C, which agrees with the very recent high-load measurements from Yuan and Berg (2010) that PMF does not change by more than ±10% between 9 °C and 37 °C. This linear model has the advantage that it can be extended to subtract and remove the offset from the membrane bound dye. The single parameter in this model is fitted using the correction factor data from Lo (2007) however it is possible to postulate methods by which this constant could be independently measured. When $C_{\text{in}} = C_{\text{out}}$, then $M_{\text{live}} = M_{\text{absent}}$,

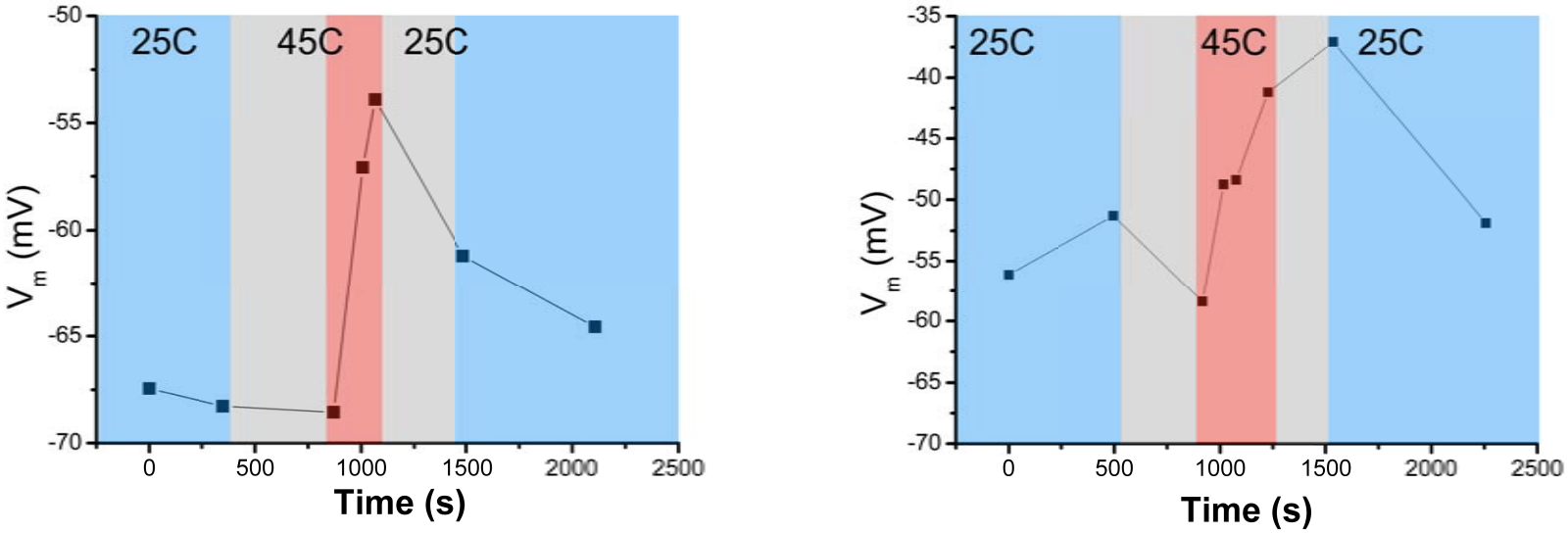

(a) (b)

Figure 5.15: Two single cell traces showing immediate decrease in V_m upon heating to 45 C and subsequent recovery. 25 C is shown with blue background, 45 C shown with pink background, and transient sections where temperature is increasing or decreasing respectively are shown with a grey background. In both V_m increases slightly at 45 C, but starts to decay immediately afterwards. Upon cooling to 25 C the V_m recovers, and continues to recover while held at room temperature.

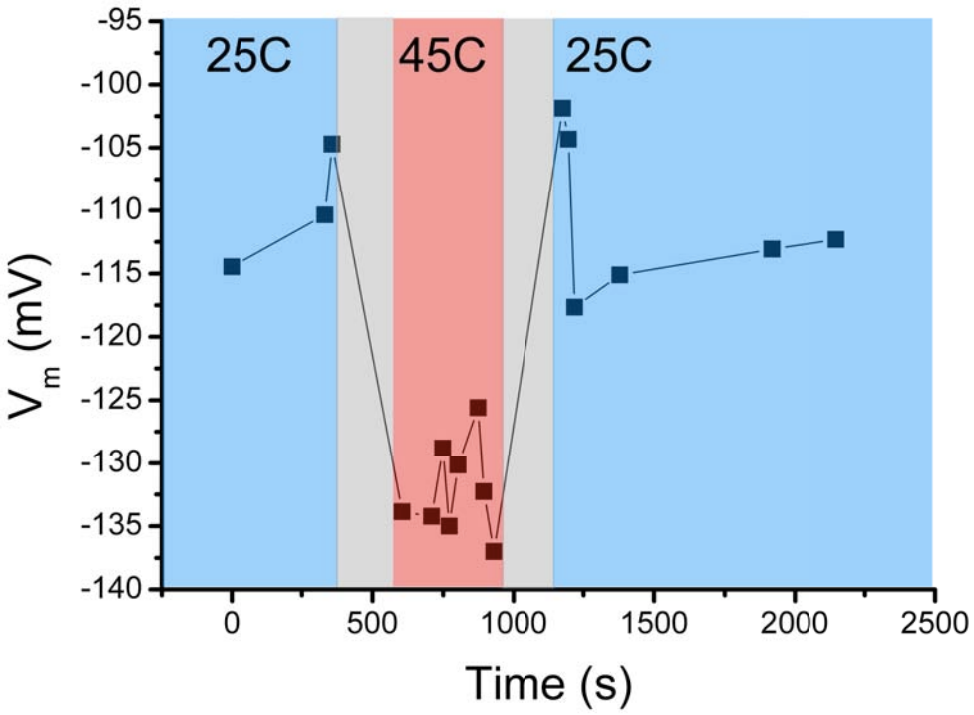

Figure 5.16: Immediate increase in V_m upon heating a single cell to 45 C, followed by decay and subsequent recovery. 25 C is shown with blue background, 45 C shown with pink background, and transient sections where temperature is increasing or decreasing are shown with a grey background. V_m decays at the end of the 5 minutes the cell is maintained at 45 C and during cooling to room temperature the V_m recovers beyond its initial value.

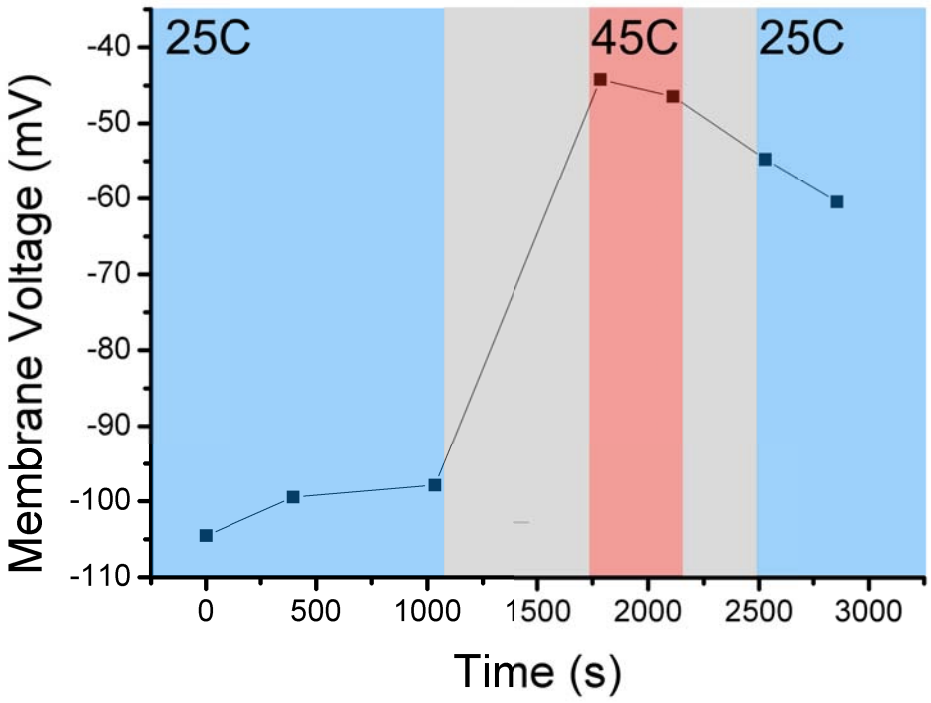

Figure 5.17: Decrease of V_m upon heating and failure to recover upon cooling. This cell starts decaying before the cell has completely arrived at 45 C and remains at 45 C for 10 minutes before being cooled, whereupon the cell is damaged and V_m does not recover.

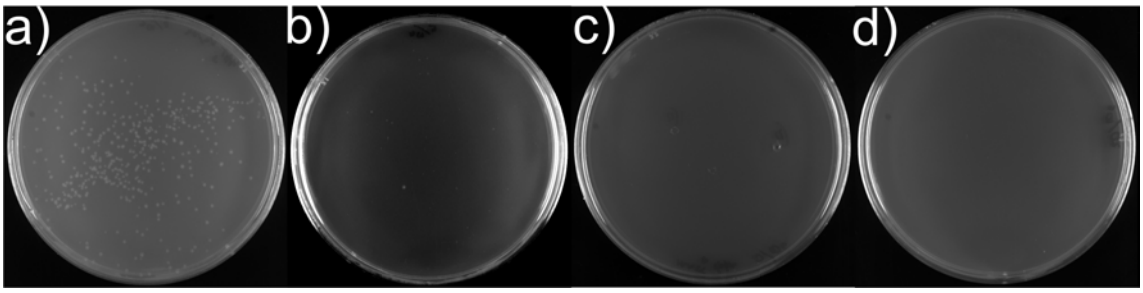

(a)

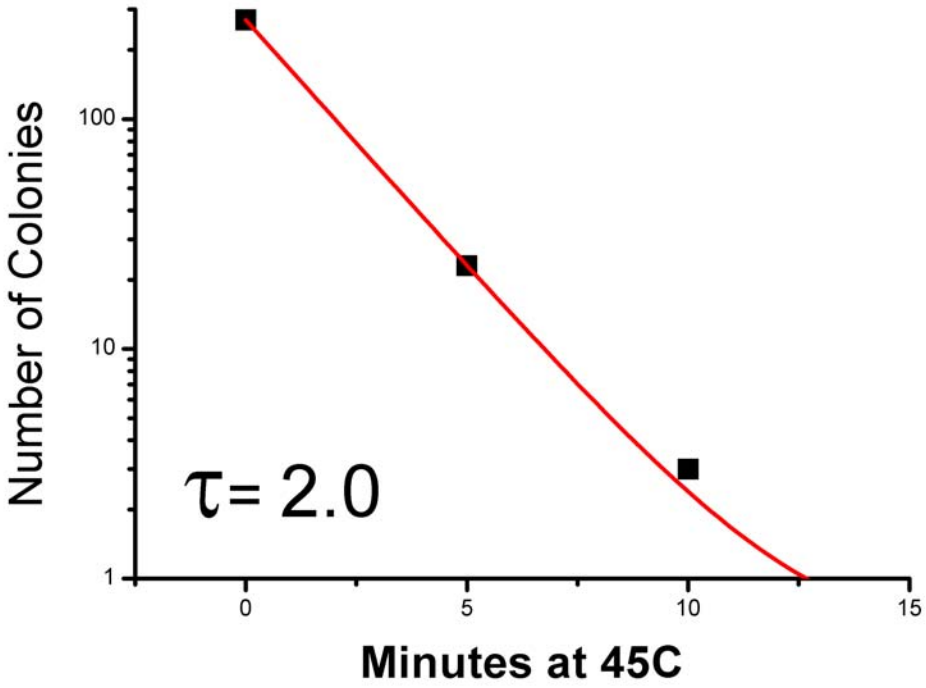

(b)

Figure 5.18: Figure showing cell response to incubation at 45 C prior to plating. (a) Photographs of cell culture plates where the seed cells were incubated for a) 0, b) 5, c) 10, and d) 20 minutes respectively. Colony count decreases exponentially with length of time incubated at 45 C. (b) log plot showing colony count vs temperature. Exponential t is shown in red with time constant $\rho = 2$ min ^{1}.

and $S = 1$. Thus to fit a line, and determine α, what is needed are additional points where the concentration inside and outside the cell is known. One possible technique to measure this would be to look at cells that have been treated with CCCP, effectively acting only as a container of dye, and use step changes in the external concentration of dye, in combination with rapid measurements of M_{live}. For example, if $C_{\text{out,A}}$ was exchanged with $C_{\text{out,B}}$, and M_{live} was measured rapidly, $C_{\text{in}} \approx C_{\text{out,A}}$ and $C_{\text{out}} = C_{\text{out,B}}$. In practice this would be limited by the ability to measure M_{CCCP} rapidly, and the rate of leakage of dye.

A more accurate method to relate dye concentration to observed fluorescence, while accounting for membrane bound dye, may involve using better masks on a bright field image of a cell. This would enable clear identification of the border of the cell and allow a more accurate measurement for the fluorescent intensity inside the cell. Mask techniques have been successfully used by Leake et al. (2006) on bright-field images to identify cells. Also, the simulation that produced the convolution model of Lo (2007) could be extended to include membrane bound dye, generating images that correspond to known concentrations of C_{in}, C_{out}, and C_{bound}, or a deconvolution could be performed to calculate local dye concentrations inside the cell. This was not pursued in this thesis due to the sufficiency of the linear model, but it could be useful to further model the optical properties of cells.

To characterise the energetics of the BFM with temperature completely it is necessary also to measure the ion pressure component of the IMF, that is, the relative internal and external sodium concentration of the cell. This has been done previously at room temperature (Lo et al., 2007) but measuring the internal sodium concentration as a function of temperature has not been done. This would require calibration of the Sodium Green dye for each individual cell and also controls to ensure Sodium Green can permeate the cell membrane over the desired temperature range. To complete the energetic description of the BFM as a function of temperature this is required, however the membrane voltage is known to make up the primary component of IMF (Lo et al., 2007) and is likely to be a good indicator of trends in the total IMF.

Observing impeded cellular function at high temperatures allows the probing of what is a comfortable environment for a cell and the assessing of the boundary between life and death. Section 5.9.4 showed that when heated a cell has a reduced membrane voltage and is non-motile, but can recover from this state to function normally when room temperature is restored (Section 5.9.5). This recovery is dependent on the length of exposure to high temperature, and the variation in the resilience

of the cell to heating. Future work at a higher time resolution may expand upon these results to quantify the exposure or voltage-decay limit which causes a cell to lose membrane potential, and also to examine whether voltage recovery also occurs in discrete steps correlated to stator return.

Stepwise resurrection of motor speed is inherent to the BFM. When the motor is stressed either due to low energisation or high temperature the motor will stop. Upon cooling to room temperature, or in the presence of an energised buffer solution, the motor will recover in discrete steps of torque and speed as the stators return to the motor (Leake et al., 2006). Temperature provides yet another handle to probe stator dynamics, not only by altering the kinetics of stator turnover, but also by driving chimeric stators away through temperature induced de-energisations. Some of these temperature induced destabilisations were shown already in Chapter 4.1, but in this chapter I have quantified the energy available to stators at different temperatures and observed the response of voltage to heating in cells with the chimeric BFM.

5.12 Conclusions and Future Work

Membrane voltage is essential to cell function and is one of the end products of the metabolic cycle, providing the energy source that drives bacterial motility and ATP synthesis. Measuring V_m in *E. coli* is difficult due to the small size of the cell and the unsuitability of patch clamping for this task. A voltage sensitive dye was used that can equilibrate rapidly across an EDTA treated cell membrane to determine the membrane voltage of averaged and individual cells of *E. coli* across a range of temperatures. The membrane voltage did not change appreciably across the temperature range, but V_m decreased when chimeric cells were exposed to heat at 45 °C, and recovered when the sample was restored to room temperature. This agrees with observed pauses and resurrections in speed and torque in samples with the same temperature history. The timescales over which a stop occurs, and over which voltage is observed to decay, however, are different, due to a delayed response in the voltage sensitive dye to the membrane potential.

Future work involving simultaneous measurement of voltage and speed, using a combined fluorescence and back-focal-plane interferometry microscope could conclusively demonstrate the link between voltage, stall and recovery at high temperature extremes, and quantify the response time and link between the three. Studies correlating energetics and performance of the BFM could also be performed on such

an apparatus, and in the near future the fluorescent microscope used in this thesis will be upgraded to include back focal plane speed measurement. Combining simultaneously both the techniques of fluorescence and force measurement will allow a twinned attack on the mysteries of the flagellar motor.

In the final chapter, Chapter 6, the overall conclusions of this thesis, and suggestions for future work are presented, which will detail some proposals for temperature control in combination with high resolution step experiments for the BFM.

Chapter 6

Conclusions and Future Work

6.1 Conclusions

6.1.1 Temperature Control

Over the last decade and a half, single molecule techniques have transformed our understanding of biology (Hinterdorfer and van Oijen, 2009; Knight, 2009). Molecular processes that were previously experimentally accessible only as averaged measurements over huge numbers of molecules can now be observed at the level of single substrate turnovers in single protein complexes, revealing static and dynamic heterogeneity and the details of mechanical and chemical cycles. Single molecule methods are now transitioning from highly specialized experiments in a small number of laboratories around the world into standard lab techniques that are a required element in any effort to demonstrate bio-molecular mechanisms.

To that end this thesis has introduced a temperature controller that can control the temperature rapidly, over temperatures of biological interest, while retaining the nanometry that is essential to single molecule measurements. This should be of interest to single-molecule researchers seeking to use the extra dimension of temperature to probe and control the kinetics and energetics of a system, and also to biologists and biochemists considering the potential of single-molecule methods in their own fields.

Temperature control is a logical 'next-step' in any biophysical research and measuring the dependence of biochemical rates on temperature has long been an important tool to test kinetics. Single molecule experiments usually require high-numerical-aperture optical microscopes and recent examples have controlled sample

temperature by heating or cooling microscope objectives using water flow (Mao et al., 2005; Furuike et al., 2008). This thesis has demonstrated rapid (±20 °C in 2 minutes) temperature control using a Peltier heat pump located on an objective collar, integrating electronic bidirectional temperature control with high-resolution microscopy.

6.1.2 Torque and Speed Response to Cooling

The torque-speed relation is the canonical characteristic of any rotary motor as it conveys the relationship between speed and power across the operating range. For the BFM, the single, double and triple stator speeds were measured or estimated at 5 °C, 10 °C and 22 °C. From these, torque-speed relations were calculated and were found to display similar traits to room temperature torque-speed relations in the chimera, that is, there was a plateau region at high load, and a linear region at low loads. These low-stator low-temperature torque-speed curves characterized the properties of the chimeric BFM at low temperature. These curves can be used as benchmarks for any future measurements of speed, stepping or energetics in any type of bacterial flagellar motor at low temperature, as they can be used to estimate the reduction of speed with cooling in other bacterial flagellar motors. This is of particular use for any future low temperature measurements performed on the chimeric flagellar motor as these data provide information on the operating range and expected performance of the motor during and after cooling.

Cooling can reduce the speed of rotation of the flagellar motor by up to 5× in the smallest loads measured in this thesis. Cooling to 5 °C affects other cellular function however, such as protein expression, which was partially demonstrated through incomplete IPTG resurrections. This effect was not noticeable when the sample was only moderately cooled (to 16 °C).

6.1.3 Membrane Voltage and the Response to Temperature Change

Membrane voltage is a measure of the energy available to the BFM, and its relationship with temperature determines the amount of energy available to the BFM across a range of temperatures. This thesis has shown that the mean membrane voltage is 120–130 mV between 5 °C and 40 °C, with the variance differing significantly across this temperature range, most noticeably for the measurements at 40 °C. The lack of a large change in membrane voltage with temperature implies that the speed changes

observed in the BFM are primarily kinetic, however the effect of temperature on the sodium concentration gradient needs to be measured to confirm this.

This thesis has also demonstrated that the membrane voltage decays upon prolonged exposure to heat (∼45 °C for ∼5 minutes). This decay in membrane voltage occurred after varying lengths of exposure to 45 °C heat, in some cases near instantaneously, in others after 5 minutes. The decay occured in ∼ 2 minutes, but high time resolution measurements during cooling were not possible, and so it is difficult to make estimates on the timescales of the decay.

This decay in membrane voltage at high temperature relates closely to stoppages at high temperature observed by the Ishijima group at Sendai University, Japan. The speed response to heat is faster, but since the lag for voltage response is ∼10 minutes, it is again difficult to make timescale based inferences. Motor stoppage is a widespread phenomenon when the motor ion-motive force (IMF) is reduced. This is observed when the external sodium concentration is dropped to zero (Rowe, 2005; Sowa and Berry, 2008), when the proton concentration is reduced ten-fold (Lo, 2007), when the voltage is removed or reversed (Fung and Berg, 1995), and has now been shown to occur when the membrane voltage is reduced in response to heat shock.

6.2 Outlook and Future Work

Objective based temperature control has been successfully implemented in this thesis. However, for greater stability, some additional measures could be implemented, for example, using a temperature controlled low magnification objective in thermal contact on top of the slide as a condenser. Two water cooled objectives were used by Mao et al. (2005) who observed greater stability as a result. Ideal temperature control would consist of all components of a system at the same temperature to ensure zero drift. This might be achievable using co-ordinated Peltier control of both the stage and objective. Additionally, it should be possible to measure sample temperature with specialist microscopic thermocouples directly at the focus for the most direct feedback control. These would, however, be optically opaque, and so a calibration method as used in this thesis with wax droplets may be preferable.

Membrane voltage was measured as a function of temperature but the entire component of IMF, the sodium pressure gradient, has not been measured. This is required for a full characterisation of the energetics with temperature. Additionally, since the stoppages at high temperature are only observed in chimeric sodium pow-

ered motors, not in proton powered wild type motors, the properties of the sodium gradient with temperature may provide additional insight into ion based differences between the two stator types. The sodium measurement is necessary to completely characterise the temperature response, however in this work the membrane voltage was targeted first as it is the major component of IMF.

The original motivation for considering temperature control was to slow the motor to help resolve stepping of the flagellar motor. Stepping provides insight into one of the central questions of molecular motor research: how is torque generated? Steps were measured previously in under-energised motors (Sowa et al., 2005), but have not been measured in fully energised motors. Recently our group has successfully measured stepping in fully energised motors at speeds of up to 100 Hz. Temperature control still has a role to play in stepping, for example to study stepping in motors powered by multiple stators, or to look at stepping in combination with switching. The temperature controller developed in this thesis has low levels of noise, and so it should be possible to combine it with our group's current high resolution dark field microscopes, not discussed here, to investigate stepping at high speeds and at high stator number. Temperature control not only offers a method to observe steps in conditions that were previously beyond our resolution, but it also allows the investigation of how stepping responds to temperature change. How the step size, duration, and dwell time change with temperature all provide essential information about the energetics and kinetics of the step mechanism and bring us closer to understanding the process of torque-generation in the bacterial flagellar motor.

References

Aathavan, K., Politzer, A. T., Kaplan, A., Moffitt, J. R., Chemla, Y. R., Grimes, S., Jardine, P., Anderson, D., and Bustamante, C. (2009). Substrate interactions and promiscuity in a viral DNA packaging motor. *Nature*, 461:669–673.

Abrahams, J., Leslie, A., Lutter, R., and Walker, J. (1994). Structure at 2.8 $\mathring{A}$ resolution of F_1-ATPase from bovine heart mitochondria. *Nature*, 370:621–628.

Aikens, R., Agard, D., and Sedat, J. (1989). Solid-state imagers for microscopy. *Methods Cell Biology*, 29:291–313.

Alberts, B., Johnson, A., Lewis, J., Raff, M., Roberts, K., and Walter, P. (2002). *Molecular Biology of the Cell*. Garland Science, USA.

Amblard, F., Yurke, B., Pargellis, A., and Leibler, S. (1996). A magnetic manipulator for studying local rheology and micromechanical properties of biological systems. *Review of Scientific Instruments*, 67:818–827.

Amos, W. B. and White, J. G. (2003). How the confocal laser scanning microscope entered biological research. *Biology of the Cell*, 95:335–342.

Asai, Y., Yakushi, T., Kawagishi, I., and Homma, M. (2003). Ion-coupling determinants of Na^+-driven and H^+-driven flagellar motors. *Journal of Molecular Biology*, 327:453–463.

Ashkin, A., Dziedzic, J. M., Bjorkholm, J. E., and Chu, S. (1986). Observation of a single-beam gradient force optical trap for dielectric particles. *Optics Letters*, 11(5):288.

Astrom, K. J. and Murray, R. M. (2008). *Feedback Systems: An Introduction for Scientists and Engineers*. Princeton University Press, USA, illustrated edition.

Atkins, P. W. and de Paula, J. (2002). *Atkins' Physical Chemistry*. Oxford University Press, 7th ed. edition.

Bai, F., Branch, R. W., Nicolau, D. V., Pilizota, T., Steel, B. C., Maini, P. K., and Berry, R. M. (2010). Conformational spread as a mechanism for cooperativity in the bacterial flagellar switch. *Science*, 327:685–689.

Bai, F., Lo, C.-J., Berry, R. M., and Xing, J. (2009). Model studies of the dynamics of bacterial flagellar motors. *Biophysical Journal*, 96:3154–3167.

Baker, M. A. B. and Berry, R. M. (2009). An introduction to the physics of the bacterial flagellar motor: a nanoscale rotary electric motor. *Contemporary Physics*, 50:617–632.

Baneyx, F. (1999). Recombinant protein expression in escherichia coli. *Current Opinion in Biotechnology*, 10(5):411–21.

Berg, H. (2003). The rotary motor of bacterial flagella. *Annual Reviews of Biochemistry*, 72:19–54.

Berg, H. and Turner, L. (1993). Torque generated by the flagellar motor of *Escherichia coli*. *Biophysical Journal*, 65:2201–2216.

Berry, R. and Berg, H. (1996). Torque generated by the bacterial flagellar motor close to stall. *Biophysical Journal*, 71:3501–3510.

Berry, R. and Berg, H. (1999). Torque generated by the flagellar motor of *Escherichia coli* while driven backwards. *Biophysical Journal*, 76:580–587.

Berry, R. M. and Berg, H. C. (1997). Absence of a barrier to backwards rotation of the bacterial flagellar motor demonstrated with optical tweezers. *Proceedings of the National Academy of Sciences of the USA*, 94:14433–14437.

Block, S. M. (1996). Fifty ways to love your lever: myosin motors. *Cell*, 87:151–7.

Block, S. M., Blair, D. F., and Berg, H. C. (1989). Compliance of bacterial flagella measured with optical tweezers. *Nature*, 338:514–518.

Bridgman, P. (1924). The connections between the four transverse galvanomagnetic and thermomagnetic phenomena. *Physical Review*, 24(6):644–651.

Buechner, M., Delcour, A., Adler, J., and Kung, C. (1987). Pressure-sensitive ion channel in *Escherichia coli*. *Proceedings of the National Academy of Sciences of the USA*, 84:2297–2301.

Bukau, B. (2006). Regulation of the *Escherichia coli* heat-shock response. *Molecular Microbiology*, 9:671–680.

Bustamante, C., Keller, D., and Oster, G. (2001). The physics of molecular motors. *Accounts of Chemical Research*, 34:412—420.

Callen, H. B. (1948). The application of onsager's reciprocal relations to thermo-electical, thermomagnetic, and galvanomagnetic effects. *Physics Review Letters*, 73:1350–1358.

Capitanio, M., Canepari, M., Cacciafesta, P., Lombardi, V., Cicchi, R., Maffei, M., Pavone, F. S., and Bottinelli, R. (2006). Two independent mechanical events in the interaction cycle of skeletal muscle myosin with actin. *Proceedings of the National Academy of Sciences of the United States of America*, 103:87–92.

Carter, N. J. and Cross, R. A. (2005). Mechanics of the kinesin step. *Nature*, 435:308–312.

Case, R. B., Rice, S., Hart, C. L., Ly, B., and Vale, R. D. (2000). Role of the kinesin neck linker and catalytic core in microtubule-based motility. *Current Biology*, 10:157–160.

Castle, A., Macnab, R., and Shulman, R. (1986a). Measurement of intracellular sodium concentration and sodium transport in *Escherichia coli* by ^{23}na nuclear magnetic resonance. *Journal of Biological Chemistry*, 261:3288–3294.

Castle, A. M., Macnab, R. M., and Shulman, R. G. (1986b). Coupling between the sodium and proton gradients in respiring escherichia coli cells measured by 23na and 31p nuclear magnetic resonance. *Journal of Biological Chemistry*, 261:7797–806.

Chabala, L., Sheridan, R., and Hodge, D. (1985). A microscope stage temperature controller for the study of whole-cell or single-channel currents. *Pflügers Archiv*, 404:374–377.

Chapman, C., Liu, Y., Sonek, G., and Tromberg, B. (1995). The use of exogenous fluorescent probes for temperature measurements in single living cells. *Photochemistry and Photobiology*, 62:416–425.

Chattopadhyay, Moldovan, R., Yeung, C., and Wu, X. (2006). Swimming efficiency of bacterium *Escherichia coli*. *Proceedings of the National Academy of Sciences*, 103(37):13712–13717.

Chen, X. and Berg, H. (2000a). Solvent-isotope and pH effects on flagellar rotation in escherichia coli. *Biophysical Journal*, 78:2280–2284.

Chen, X. and Berg, H. C. (2000b). Torque-speed relationship of the flagellar rotary motor of *Escherichia coli*. *Biophysical Journal*, 78:1036–1041.

Cohen, L., Salzburg, B., Davila, H., Ross, W., Landowne, D., Waggoner, A., and Wange, C. (1974). Changes in axon fluorescence during activity: molecular probes of membrane potential. *Journal of Membrane Biology*, 19:1–36.

Cohen, L. B., Keynes, R. D., and Hille, B. (1968). Light scattering and birefringence changes during nerve activity. *Nature*, 218(5140):438–41.

Cole, K. (1949). Some physical aspects of bioelectric phenomena. *Proceedings of the National Academy of Sciences of the USA*, 35:558–566.

Collins, C. and Vallee, R. (1987). Temperature-dependent reversible assembly of taxol-treated microtubules. *Journal of Cell Biology*, 105:2847–2854.

Cowern, E. (2004). Understanding Induction Motor Nameplate Information. *Electrical Construction and Maintenance*. `http://ecmweb.com/mag/electric_understanding_induction_motor/` [accessed 1-May-2010].

Cox, G. (2002). Biological confocal microscopy. *Materials Today*, 5:34–41.

Creese, R., Scholes, N. W., Taylor, D. B., and Zinn, D. (1958). Temperature and resting potential of diaphragm muscle in a CO_2-bicarbonate medium. *Journal of Pharmacology*, 124:47–52.

Crick, F. and Hughes, A. (1950). The physical properties of cytoplasm: A study by means of the magnetic particle methods. *Experimental Cell Research*, 1:37–80.

Croarkin, M. C., Guthrie, W. F., Burns, G. W., Kaeser, M., and Strouse, G. F. (1993). Temperature-electromotive force reference functions and tables for the letter-designated thermocouple types based on the ITS-90. *National Institute of Standards and Technology Monograph*, 175:630.

Cyranoski, D. (2000). Swimming against the tide. *Nature*, 408(6814):764–766.

Dao, D. N., Kessin, R. H., and Ennis, H. L. (2000). Developmental cheating and the evolutionary biology of dictyostelium and myxococcus. *Microbiology*, 146:1505–1512.

Decostre, V., Bianco, P., and Lombardi, V. (2005). Effect of temperature on the working stroke of muscle myosin. *Proceedings of the National Academy of Sciences of the USA*, 102:13927–13932.

Dipolo, R. and Latorre, R. (1972). Effect of temperature on membrane potential and ionic fluxes in intact and dialysed barnacle muscle fibres. *The Journal of Physiology*, 225:255–273.

Doering, C., Ermentrout, B., and Oster, G. (1995). Rotary DNA motors. *Biophysical Journal*, 69:2256–2267.

Dox, A. W. and Roark Jr, G. W. (1917). The determination of gelatinization temperatures of starches by means of an electrically heated chamber on the microscope stage. *Journal of the American Chemical Society*, 39:742–745.

Eckburg, P. B., Bik, E. M., Bernstein, C. N., Purdom, E., Dethlefsen, L., Sargent, M., Gill, S. R., Nelson, K. E., and Relman, D. A. (2005). Diversity of the human intestinal microbial flora. *Science*, 308:1635–1638.

Ehrenberg, B., Montana, V., and Wei, M. (1988). Membrane potential can be determined in individual cells from the nernstian distribution of cationic dyes. *Biophysical Journal*, 53:785–794.

Eyring, H. (1935). The activated complex in chemical reactions. *Journal of Chemical Physics*, 3(2):107.

Felle, H., Porter, J. S., Slayman, C. L., and Kaback, H. R. (1980). Quantitative measurements of membrane potential in *Escherichia coli*. *Biochemistry*, 19:3585–3590.

Finer, J., Simmons, R., and Spudich, J. (1994). Single myosin molecule mechanics: piconewton forces and nanometre steps. *Nature*, 368:114–119.

Francis, C. K. and Smith, O. C. (1916). The determination of the gelatinizing temperature of the starches from the grain sorghums by means of a thermo-slide. *Journal of Industrial and Engineering Chemistry*, 8:509–511.

Fukuoka, H., Yakushi, T., and Homma, M. (2004). Concerted effects of amino acid substitutions in conserved charged residues and other residues in the cytoplasmic domain of PomA, a stator component of Na^+-driven flagella. *Journal of Bacteriology*, 186:6749–6758.

Fung, D. and Berg, H. (1995). Powering the flagellar motor of *Escherichia coli* with an external voltage source. *Nature*, 375:809–812.

Furuike, S., Adachi, K., Sakaki, N., Shimo-Kon, R., Itoh, H., Muneyuki, E., Yoshida, M., and Kinosita, K. (2008). Temperature dependence of the rotation and hydrolysis activities of F_1-ATPase. *Biophysical Journal*, 95:761–70.

Gabe, D. (2009). Walther Nernst. *Transactions of the Institute of Metal Finishing*, 87:60.

Gabel, C. and Berg, H. (2003). The speed of the flagellar rotary motor of *escherichia coli* varies linearly with protonmotive forces. *Proceedings of the National Academy of Sciences of the USA*, 100:8748–8751.

Gammell, C. (2009). E-coli cases nearly double at godstone farm. The Telegraph. September 20th.

Gauthier, M., Truchon, D., and Rainville, S. (2008a). Taking control of the flagellar motor. *Proceedings of SPIE*, 7099(70990F).

Gauthier, M., Truchon, D., and Rainville, S. (2008b). Taking control of the flagellar motor. *Physics in Canada*, 64:135–137.

Gauthier-Manuel, B. and Garnier, L. (1997). Design for a 10 picometer magnetic actuator. *Review of Scientific Instruments*, 68(6):2486–2489.

Geeves, M. A. and Holmes, K. C. (1999). Structural mechanism of muscle contraction. *Annual Review of Biochemistry*, 68:687–728.

Gibbons, I. R. (1963). Studies on the protein components of cilia from *Tetrahymena pyriformis*. *Proceedings of the National Academy of Sciences of the USA*, 50:1002–1010.

Gittes, F. and Schmidt, C. F. (1998). Interference model for back-focal-plane displacement detection in optical tweezers. *Optics Letters*, 23:7–9.

Glass, G. V., Peckham, P. D., and Sanders, J. R. (1972). Consequences of failure to meet assumptions underlying the fixed effects analyses of variance and covariance. *Review of Educational Research*, 42(3):237–288.

Gmehling, J. (2010). Dortmund data bank software and separation technology. `http://www.ddbst.com` [Accessed 1-May-2010].

Gosse, C. and Croquette, V. (2002). Magnetic tweezers: Micromanipulation and force measurement at the molecular level. *Biophysical Journal*, 82:3314–3329.

Gross, E., Bedlack, R., and Loew, L. (1994). Dual-wavelength ratiometric fluorescence measurement of the membrane dipole potential. *Biophysical Journal*, 67:208—216.

Guilford, W. H., Dupuis, D. E., Kennedy, G., Wu, J., Patlak, J. B., and Warshaw, D. M. (1997). Smooth muscle and skeletal muscle myosins produce similar unitary forces and displacements in the laser trap. *Biophysical Journal*, 72(3):1006–1021.

Gurevich, Y. and Logvinov, G. (2005). Physics of thermoelectric cooling. *Semiconductor Science and Technology*, 20:R57–R64.

Harwell, M., Rubinstein, E., and Hayes, W. (1992). Summarizing monte carlo results in methodological research: The one-and two-factor fixed effects ANOVA cases. *Journal of Educational Statistics*, 17(4):315–339.

Haselgrove, J. C., Stewart, M., and Huxley, H. E. (1976). Cross-bridge movement during muscle contraction. *Nature*, 261:606–608.

Hazelbauer, G. L., Falke, J. J., and Parkinson, J. S. (2008). Bacterial chemoreceptors: high-performance signaling in networked arrays. *Trends in Biochemical Sciences*, 33:9–19.

Hegarty, T. W. (1973). Temperature coefficient (q10), seed germination and other biological processes. *Nature*, 243:305–306.

Hinterdorfer, P. and van Oijen, A. (2009). *Handbook of Single-molecule Biophysics*. Springer, US.

Hirakawa, E., Higuchi, H., and Toyoshima, Y. Y. (2000). Processive movement of single 22S dynein molecules occurs only at low ATP concentrations. *Proceedings of the National Academy of Sciences of the United States of America*, 97(6):2533–7.

Hodgkin, A., Huxley, A., and Katz, B. (1952). Measurement of current-voltage relations in the membrane of the giant axon of loligo. *The Journal of Physiology*, 116:424–448.

Homma, K., Yoshimura, M., Saito, J., Ikebe, R., and Ikebe, M. (2001). The core of the motor domain determines the direction of myosin movement. *Nature*.

Houdusse, A. and Carter, A. P. (2009). Dynein swings into action. *Cell*, 136:395–396.

Houdusse, A., Szent-Györgyi, A. G., and Cohen, C. (2000). Three conformational states of scallop myosin S1. *Proceedings of the National Academy of Sciences of the USA*, 97(21):11238–11243.

Howard, J. (2001). *Mechanics of Motor Proteins and the Cytoskeleton*. Sinauer Associates, Sunderland Mass. USA.

Huxley, A. F. and Simmons, R. M. (1971). Proposed mechanism of force generation in striated muscle. *Nature*, 233:533–538.

Hwang, G. C., Watabe, S., and Hashimoto, K. (1990). Changes in carp myosin ATPase induced by temperature acclimation. *Journal of Comparative Physiology B*, 160:233–239.

Inoue, Y., Lo, C.-J., Fukuoka, H., Takahashi, H., Sowa, Y., Pilizota, T., Wadhams, G. H., Homma, M., Berry, R. M., and Ishijima, A. (2008). Torque-speed relationships of Na^+-driven chimeric flagellar motors in *Escherichia coli*. *Journal of Molecular Biology*, 376:1251–1259.

Invitrogen (2010). Invitrogen Product Information - TMRM. `http://products.invitrogen.com/ivgn/product/T668?ICID==Search-Product` [Online; accessed 10-Apr-2010].

Itoh, H., Takahashi, A., Adachi, K., Noji, H., Yasuda, R., Yoshida, M., and Kinosita, K. (2004). Mechanically driven ATP synthesis by F_1-ATPase. *Nature*, 427:465.

Johnston, I. A., Walesby, N. J., Davison, W., and Goldspink, G. (1975). Temperature adaptation in myosin of antarctic fish. *Nature*, 254:74.

Kapitein, L., Kwok, B., Weinger, J., Schmidt, C. F., Kapoor, T. M., and Peterman, E. J. G. (2008). Microtubule cross-linking triggers the directional motility of kinesin-5. *Journal of Cell Biology*, 182:421–428.

Kapitein, L., Peterman, E., Kwok, B., Kim, J., Kapoor, T. M., and Schmidt, C. F. (2005). The bipolar mitotic kinesin Eg5 moves on both microtubules that it crosslinks. *Nature*, 435:114–118.

Kasha, M. (1950). Characterization of electronic transitions in complex molecules. *Discussions of the Faraday Society*, 9:14–19.

Kashina, A. S., Baskin, R. J., Cole, D. G., Wedaman, K. P., Saxton, W. M., and Scholey, J. M. (1996). A bipolar kinesin. *Nature*, 379:270–2.

Kawaguchi, K. and Ishiwata, S. (2000). Temperature dependence of force, velocity, and processivity of single kinesin molecules. *Biochemical and Biophysical Research Communications*, 272:895–899.

Khan, S. and Berg, H. (1983). Isotope and thermal effects in chemiosmotic coupling to the membrane atpase of *Streptococcus*. *Journal of Biological Chemistry*, 258:6709–6712.

Kim, M. J., Kim, M. J., Bird, J. C., Park, J., Powers, T. R., and Breuer, K. S. (2004). Particle image velocimetry experiments on a macro-scale model for bacterial flagellar bundling. *Experiments in Fluids*, 37:782–788.

King, S. M., Marchese-Ragona, S. P., Parker, S. K., and Detrich, III, H. W. (1997). Inner and outer arm axonemal dyneins from the antarctic rockcod *Notothenia coriiceps*. *Biochemistry*, 36(6):1306–1314.

Klionsky, D., Brusilow, W., and Simoni, R. (1984). In vivo evidence for the role of the ϵ subunit as an inhibitor of the proton-translocating ATPase of *Escherichia coli*. *Journal of Bacteriology*, 160:1055–1060.

Knight, A. E., editor (2009). *Single Molecule Biology*. Associated Press, London.

Kojima, S. and Blair, D. (2004). The bacterial flagellar motor: structure and function of a complex molecular machine. In Jeon, K. W., editor, *International Review of Cytology - A Survey of Cell Biology*, volume 232, pages 93–110. Elsevier.

Komarova, Y., Groot, C. O. D., Grigoriev, I., Gouveia, S. M., Munteanu, E. L., Schober, J. M., Honappa, S., Buey, R., Hoogenraad, C., and Dogterom, M. (2009). Mammalian end binding proteins control persistent microtubule growth. *Journal of Cell Biology*, 184(5):691–706.

Krog, J. and Simmet, R. (1954). An attachment for the low-power binocular microscope facilitating observations at controlled temperatures. *Transactions of the American Microscopical Society*, 73(4):407–409.

Kruskal, W. and Wallis, W. (1952). Use of ranks in one-criterion variance analysis. *Journal of the American Statistical Association*, 47(260):583–621.

Kuwajima, G. (1988). Construction of a minimum-size functional flagellin of escherichia coli. *Journal of Bacteriology*, 170(7):3305–9.

Lakowicz, J. R. (2006). *Principles of Fluorescence Spectroscopy*. Springer, USA.

Lambert, A. M. and Bajer, A. S. (1977). Microtubules distribution and reversible arrest of chromosome movements induced by tow temperature. *Cytobiologie*, 15:1–23.

Landgraf, S. (2004). Use of ultrabright LEDs for the determination of static and time-resolved florescence information of liquid and solid crude oil samples. *Journal of Biochemical and Biophysical Methods*, 61:125–134.

Langevin, M. (1905). Recombination and diffusion of gaseous ions (Recombinaison et diffusion des ions gazeux). *Journal de Physique Théorique et Applique*, 4:322–333.

Latorre, R. and Hidalgo, M. C. (1969). Effect of temperature on resting potential in giant axons of squid. *Nature*, 221:962–3.

Leake, M. C. (2001). *Investigation of the extensile properties of the giant sarcomeric protein titin by single-molecule manipulation using a laser- tweezers technique.* PhD thesis, Randall Institute, King's College London, UK.

Leake, M. C., Chandler, J. H., Wadhams, G. H., Bai, F., Berry, R. M., and Armitage, J. P. (2006). Stoichiometry and turnover in single, functioning membrane protein complexes. *Nature*, 443:355–358.

Leduc, C., Ruhnow, F., Howard, J., and Diez, S. (2007). Detection of fractional steps in cargo movement by the collective operation of kinesin-1 motors. *Proceedings of the National Academy of Sciences of the USA*, 104:1084710852.

Lee, T. J., Schwartz, C., and Guo, P. (2009). Construction of bacteriophage phi29 DNA packaging motor and its applications in nanotechnology and therapy. *Annals of Biomedical Engineering*, 37:2064–2081.

Levene, H. (1960). Robust tests for equality of variances. In Olkin, I., editor, *Contributions to probability and statistics*, Stanford Studies in Mathematics and Statistics. Stanford University Press (Stanford, CA, USA).

Lichtman, J. W. and Conchello, J.-A. (2005). Fluorescence microscopy. *Nature Methods*, 2:910.

Ling, G. and Woodbury, J. W. (1949). Effect of temperature on the membrane potential of frog muscle fibers. *Journal of Cellular and Comparative Physiology*, 34(3):407–412.

Lipták, B. G. (1995). *Instrument engineers' handbook: process control*. CRC Press LLC, USA.

Lo, C., Leake, M., and Berry, R. (2006). Fluorescence measurement of intracellular sodium concentration in single *Escherichia coli* cells. *Biophysical Journal*, 90:357–365.

Lo, C.-J. (2007). *Sodium Energetics of Chimeric Flagellar Motors in* Escherichia coli. PhD thesis, Unversity of Oxford.

Lo, C.-J., Leake, M. C., Pilizota, T., and Berry, R. M. (2007). Nonequivalence of membrane voltage and ion-gradient as driving forces for the bacterial flagellar motor at low load. *Biophysical Journal*, 93:294–302.

Loew, L., Tuft, R., Carrington, W., and Fay, F. (1993). Imaging in five dimensions: time-dependent membrane potentials in individual mitochondria. *Biophysical Journal*, 65:2396–2407.

Loew, L. M. (1996). Potentiometric dyes: Imaging electrical activity of cell membranes. *Pure and Applied Chemistry*, 7:1405–1409.

Lymn, R. and Taylor, E. (1971). Mechanism of adenosine triphosphate hydrolysis by actomyosin. *Biochemistry*, 10:4617–4624.

Macnab, R. M. (2003). How bacteria assemble flagella. *Annual Review of Microbiology*, 57:77–100.

Mao, H., Arias-Gonzalez, J. R., Smith, S. B., Jr, I. T., and Bustamante, C. (2005). Temperature control methods in a laser tweezers system. *Biophysical Journal*, 89:1308–1316.

Marmount, G. (1949). Electrode clamp for squid axon: Studies on the axon membrane. *Journal of Cellular and Comparative Physiology*, 34:351–382.

Marshall, B. (2000). How electric motors work. In *How Stuff Works*. HowStuffWorks.com. `http://www.howstuffworks.com` [Online; accessed 29-Apr-2010].

Mashimo, T., Hashimoto, M., Yamaguchi, S., and Aizawa, S.-I. (2007). Temperature-hypersensitive sites of the flagellar switch component FliG in *Salmonella enterica* Serovar Typhimurium. *Journal of Bacteriology*, 189:5153–5160.

Mast, S. (1903). Reactions to temperature changes in spirillum, hydra, and fresh-water planarians. *Journal of the American Chemical Society*, 10:165–190.

McGee, T. D. (1988). *Principles and Methods of Temperature Measurement*. John Wiley & Sons, USA.

McNaught, A. D. and Wilkinson, A. (1997). *IUPAC. Compendium of Chemical Terminology*. Blackwell Scientific Publications, UK.

Melkle, J. (2009). Three-year-old recovering from E coli but woman still in coma. The Guardian. August 5.

Michalet, X., Kapanidis, A. N., Laurence, T., Pinaud, F., Doose, S., Pflughoefft, M., and Weiss, S. (2003). The power and prospects of fluorescence microscopies and spectroscopies. *Annual Review of Biophysics*, 32:161–182.

Min, T., Mears, P., Chubiz, L., Rao, C., and Golding, I. (2009). High-resolution, long-term characterization of bacterial motility using optical tweezers. *Nature Methods*, 6(11):831–838.

Minamino, T., Imae, Y., Oosawa, F., Kobayashi, Y., and Oosawa, K. (2003). Effect of intracellular pH on rotational speed of bacterial flagellar motors. *Journal of Bacteriology*, 185:1190–1194.

Molloy, J., Burns, J., Kendrick-Jones, J., and Tregear, R. (1995). Movement and force produced by a single myosin head. *Nature*, 378:209–212.

Namba, K. and Vonderviszt, F. (1997). Molecular architecture of bacterial flagellum. *Quarterly Review of Biophysics*, 30:1–65.

Neher, E. and Sakmann, B. (1975). Voltage-dependence of drug-induced conductance in frog neuromuscular junction. *Proceedings of the National Academy of Sciences of the USA*, 72:2140–2144.

Nelson, P. C. (2004). *Biological Physics: Energy, Information, Life*. W. H. Freeman, USA.

Nernst, W. (1904). *Theoretical chemistry from the stand point of Avogadro's rule and thermodynamics*. Macmillan & Co, London, 2nd edition.

Neter, J., Kutner, M., Wasserman, W., Nachtsheim, C., and Neter, J. (1996). *Applied Linear Statistical Models*. McGraw-Hill/Irwin, 4 edition.

Nikon (2010). Nikon MicroscopyU. `http://www.microscopyu.com/` [Online; accessed 29-Apr-2010].

Noji, H., Yasuda, R., Yoshida, M., and Kinosita, K. (1997). Direct observation of the rotation of F_1-ATPase. *Nature*, 386:299–302.

Noumi, T., Moriyama, Y., Maeda, M., and Futai, M. (1992). *Escherichia coli* H^+-ATPase: Role of the δ subunit in binding F_1 to the F_0 sector. *Archives of Biochemistry and Biophysics*, 292:376–381.

Oiwa, K. and Kojima, H. (2009). Force-generating mechanisms of dynein revealed through single molecule studies. In Knight, A. E., editor, *Single Molecule Biology*, pages 61–104. Academic Press, USA.

Osioptoelectronics (2007). *Osioptoelectronic Product Catalog*. OSI Systems.

Petsko, G. and Ringe, D. (2004). *Protein Structure and Function*. Sinauer Associates, USA.

PHYWE (2008). *Laboratory Experiments Physics - Peltier Heat Pump*. PHYWE Systeme.

Piazzesi, G., Reconditi, M., and Koubassova, N. (2003). Temperature dependence of the force-generating process in single fibres from frog skeletal muscle. *The Journal of Physiology*, 549:93–106.

Pijper, A. (1955). Heating and cooling the microscope stage. *American Journal of Clinical Pathology*, 8:980–982.

Pijper, A., Neser, M., and Abraham, G. (1956). The wavelengths of helical bacterial flagella. *Microbiology*, 14:371–380.

Pilizota, T., Bilyard, T., Bai, F., Futai, M., Hosokawa, H., and Berry, R. M. (2007). A programmable optical angle clamp for rotary molecular motors. *Biophysical Journal*, 93:264–275.

Plank, M., Wadhams, G. H., and Leake, M. C. (2009). Millisecond timescale slim-field imaging and automated quantification of single fluorescent protein molecules for use in probing complex biological processes. *Journal of Integrative Biology*, 1(10):602–12.

Purcell, E. (1977). Life at low Reynolds number. *American Journal of Physics*, 45:3–11.

Qing, G., Ma, L., Khorchid, A., Swapna, G., Mal, T. K., Takayama, M. M., Xia, B., Phadtare, S., Ke, H., Acton, T., Montelione, G. T., Ikura, M., and Inouye, M. (2004). Cold-shock induced high-yield protein production in *Escherichia coli*. *Nature Biotechnology*, 22(7):877–882.

Rabin, Y. and Podbilewicz, B. (2000). Temperature-controlled microscopy for imaging living cells: apparatus, thermal analysis and temperature dependency of embryonic elongation in *C. elegans*. *Journal of Microscopy*, 199:214–223.

Reid, S. W., Leake, M. C., Chandler, J. H., Lo, C.-J., Armitage, J. P., and Berry, R. M. (2006). The maximum number of torque-generating units in the flagellar motor of *Escherichia coli* is at least 11. *Proceedings of the National Academy of Sciences of the USA*, 103:8066–8071.

Reynolds, O. (1883). An experimental investigation of the circumstances which determine whether the motion of water shall be direct of sinuous, and of the law of resistance in parallel channels. *Philosophical Transactions of the Royal Society of London*, 174:935–982.

Riedel-Kruse, I. H., Hilfinger, A., Howard, J., and Julicher, F. (2007). How molecular motors shape the flagellar beat. *HFSP Journal*, 1:192–208.

Rief, M., Rock, R., Mehta, A., and Mooseker, M. (2000). Myosin-V stepping kinetics: a molecular model for processivity. *Proceedings of the National Academy of Sciences*, 97:94829486.

Rosenberger, C. M. and Finlay, B. B. (2003). Phagocyte sabotage: disruption of macrophage signalling by bacterial pathogens. *Nature Reviews of Molecular Cell Biology*, 4:385–396.

Ross, D., Locascio, L. E., and Gaitan, M. (2001). Temperature measurement in microfluidic systems using a temperature-dependent fluorescent dye. *Analytical Chemistry*, 73:4117–4123.

Rowe, A. D. (2005). *Rotation of the Sodium Driven Bacterial Flagellar Motors*. PhD thesis, University of Oxford.

Ruff, C., Furch, M., Brenner, B., and Manstein, D. (2001). Single-molecule tracking of myosins with genetically engineered amplifier domains. *Nature Structural Biology*, 8:226–229.

Ryu, W., Berry, R., and Berg, H. (2000). Torque-generating units of the flagellar motor of *Escherichia coli* have a high duty ratio. *Nature*, 403:444–447.

Samatey, F., Imada, K., Nagashima, S., and Vonderviszt, F. (2001). Structure of the bacterial flagellar protofilament and implications for a switch for supercoiling. *Nature*, 410:331–337.

Samatey, F. A., Matsunami, H., Imada, K., Nagashima, S., Shaikh, T. R., Thomas, D. R., Chen, J. Z., DeRosier, D. J., Kitao, A., and Namba, K. (2004). Structure of the bacterial flagellar hook and implication for the molecular universal joint mechanism. *Nature*, 431:1062–1068.

Samuel, A. and Berg, H. (1995). Fluctuation analysis of rotational speeds of the bacterial flagellar motor. *Proceedings of the National Academy of Sciences of the USA*, 92:3502–3506.

Samuel, A. D. and Berg, H. C. (1996). Torque-generating units of the bacterial flagellar motor step independently. *Biophysical Journal*, 71(2):918–923.

Saxl, T. E. (2007). *Electrorotation of the Bacterial Flagellar Motor*. PhD thesis, University of Oxford.

Say, M. G. (1958). *The performance and design of alternating current machines; transformers, three-phase induction motors and synchronous machines*. Pittman paperbacks, London, 3rd edition.

Scharf, B., Fahrner, K., Turner, L., and Berg, H. (1998). Control of direction of flagellar rotation in bacterial chemotaxis. *Proceedings of the National Academy of Sciences of the USA*, 95:201–206.

Scheffé, H. (1959). *The Analysis of Variance*. Wiley-IEEE.

Schnitzer, M. J., Visscher, K., and Block, S. M. (2000). Force production by single kinesin motors. *Nature Cell Biology*, 2:718–23.

Sevick, E., Prabhakar, R., and Williams, S. (2008). Fluctuation theorems. *Annuals Review of Physical Chemistry*, 59:603–33.

Shapiro, S. and Wilk, M. (1965). An analysis of variance test for normality (complete samples). *Biometrika*, 52(3-4):591.

Siegel, M. S. and Isacoff, E. Y. (1997). A genetically encoded optical probe of membrane voltage. *Neuron*, 19:735–741.

Silverman, M. and Simon, M. (1974). Flagellar rotation and the mechanism of bacterial motility. *Nature*, 249(5452):73–74.

Slonczewski, J. L., Rosen, B. P., Alger, J. R., and Macnab, R. M. (1981). pH homeostasis in *Escherichia coli*: measurement by ^{31}P nuclear magnetic resonance of methylphosphonate and phosphate. *Proceedings of the National Academy of Sciences*, 78(10):6271–5.

Smith, D., Steffen, W., Simmons, R., and Sleep, J. (2001a). Hidden-markov methods for the analysis of single-molecule actomyosin displacement data: The variance-hidden-markov method. *Biophysical Journal*, 81:2795–2816.

Smith, D. E., Tans, S. J., Smith, S., Grimes, S., Anderson, D., and Bustamante, C. (2001b). The bacteriophage ϕ29 portal motor can package DNA against a large forces. *Nature*, 413(748-752):748–752.

Sourjik, V. (2004). Receptor clustering and signal processing in *E. coli* chemotaxis. *Trends in Microbiology*, 12(12):569–76.

Sowa, Y. and Berry, R. M. (2008). Bacterial flagellar motor. *Quarterly Review of Biophysics*, 41(02):1–30.

Sowa, Y., Rowe, A. D., Leake, M. C., Yakushi, T., Homma, M., Ishijima, A., and Berry, R. M. (2005). Direct observation of steps in rotation of the bacterial flagellar motor. *Nature*, 437(7060):916–919.

Steffen, W., Smith, D., and Simmons, R. (2001). Mapping the actin filament with myosin. *Proceedings of the National Academy of Sciences*, 98(26):14949–14954.

Stokes, G. (1842). On the steady motion of incompressible fluids. *Transactions of the Cambridge Philosophical Society*, 7:439–453.

Stokes, G. (1847). On the theory of oscillatory waves. *Transactions of the Cambridge Philosophical Society*, pages 441–445.

Stokes, G. (1852). On the change of refrangibility of light. *Philosophical Transactions of the Royal Society*, 142:463–562.

Svoboda, K., Schmidt, C. F., Schnapp, B. J., and Block, S. M. (1993). Direct observation of kinesin stepping by optical trapping interferometry. *Nature*, 365(6448):721–727.

Tauber, A. I. (2003). Metchnikoff and the phagocytosis theory. *Nature Reviews of Molecular Cell Biology*, 4:897–901.

Thomas, D. R., Francis, N. R., Xu, C., and DeRosier, D. J. (2006). The three-dimensional structure of the flagellar rotor from a clockwise-locked mutant of *Salmonella enterica* serovar typhimurium. *Journal of Bacteriology*, 188:7039–7048.

Thomson, W. (1854). On account of researches in thermo-electricity. *Proceedings of the Royal Society of London*, 7:49–58.

Tilney, L. and Porter, K. (1967). Studies on the microtubules in heliozoa: II. the effect of low temperature on these structures in the formation and maintenance of the axopodia. *Journal of Cell Biology*, 34:327–343.

Todar, K. (2010). Online Encyclopedia of Bacteriology. `http://www.textbookofbacteriology.net/` [Online; accessed 29-Apr-2010].

Trautz, M. (1916). Das Gesetz der Reaktionsgeschwindigkeit und der Gleichgewichte in Gasen. Bestätigung der Additivität von c_v-3/2r. Neue Bestimmung der Integrationskonstanten und der Molekül durchmesser. *Zeitschrift für Anorganische und Allgemeine Chemie*, 96(1):1–28.

Turner, L., Caplan, S., and Berg, H. (1996). Temperature-induced switching of the bacterial flagellar motor. *Biophysical Journal*, 71:2227–2233.

Vale, R. D. (2003). The molecular motor toolbox for intracellular transport. *Cell*, 112:467–80.

Vale, R. D. and Milligan, R. A. (2000). The way things move: Looking under the hood of molecular motor proteins. *Science*, 288:88–95.

Vale, R. D., Reese, T. S., and Sheetz, M. P. (1985). Identification of a novel force-generating protein, kinesin, involved in microtubule-based motility. *Cell*, 42(1):39–50.

Vallee, R. B., Williams, J. C., Varma, D., and Barnhart, L. E. (2004). Dynein: An ancient motor protein involved in multiple modes of transport. *Journal of Neurobiology*, 58:189–200.

Veigel, Wang, F., Bartoo, M., Sellers, J., and Molloy, J. (2001). The gated gait of the processive molecular motor, myosin V. *Nature Cell Biology*, 4:59–65.

Veigel, C., Coluccio, L. M., Jontes, J. D., Sparrow, J. C., Milligan, R. A., and Molloy, J. E. (1999). The motor protein myosin-I produces its working stroke in two steps. *Nature*, 398:530–3.

Vergara, J. and Bezanilla, F. (1976). Fluorescence changes during electrical activity in frog muscle stained with merocyanine. *Nature*, 259:684–686.

Walnut, D. F. (2004). *An Introduction to Wavelet Analysis*. Birkhuser, Boston, USA, 1st edition.

Wang, H. and Oster, G. (2002). The stokes efficiency for molecular motors and its applications. *Europhysics Letters*, 57:134–140.

Wikipedia (2010a). Dynamometer — wikipedia, the free encyclopedia. `http://en.wikipedia.org/wiki/Dynamometer` [Online; accessed 4-May-2010].

Wikipedia (2010b). Induction motor — wikipedia, the free encyclopedia. `http://en.wikipedia.org/wiki/Induction_motor` [Online; accessed 4-May-2010].

Winstanley, C. and Hart, C. (2001). Type III secretion systems and pathogenicity islands. *Journal of Medical Microbiology*, 50:116–126.

Woledge, Barclay, C., and Curtin, N. (2009). Temperature change as a probe of muscle crossbridge kinetics: a review and discussion. *Proceedings of the Royal Society B*, 276:2685–2695.

Xing, J., Bai, F., Berry, R., and Oster, G. (2006). Torque-speed relationship of the bacterial flagellar motor. *Proceedings of the National Academy of Sciences*, 103(5):1260–1265.

Yasuda, R., Noji, H., Yoshida, M., and Kinosita, K. (2001). Resolution of distinct rotational substeps by submillisecond kinetic analysis of F_1-ATPase. *Nature*, 410:898–904.

Yonekura, K., Maki-Yonekura, S., and Namba, K. (2003). Complete atomic model of the bacterial flagellar filament by electron cryomicroscopy. *Nature*, 424:643–650.

Yorimitsu, T. and Homma, M. (2001). Na-driven flagellar motor of *Vibrio*. *Biochimica et Biophysica Acta*, 1505:82–93.

Yoshida, M., Muneyuki, E., and Hisabori, T. (2001). ATP synthase? a marvellous rotary engine of the cells. *Nature Reviews Molecular Cell Biology*, 2:669–677.

Young, M. and Edis, T. (2004). *Why Intelligent Design Fails: A Scientific Critique of the New Creationism*. Rutgers University Press.

Yuan, J. and Berg, H. C. (2008). Resurrection of the flagellar rotary motor near zero load. *Proceedings of the National Academy of Sciences of the USA*, 105:1182–1185.

Yuan, J. and Berg, H. C. (2010). Thermal and solvent-isotope effects on the flagellar rotary motor near zero load. *Biophysical Journal*, 98:2121–6.

Zhou, J., Lloyd, S., and Blair, D. (1998). Electrostatic interactions between rotor and stator in the bacterial flagellar motor. *Proceedings of the National Academy of Sciences of the USA*, 95:6436–6441.

Ziegler, J. and Nichols, N. (1993). Optimum settings for automatic controllers. *Journal of Dynamic Systems*, 115:220–222.

Appendix A

Temperature Controller Schematic

The temperature control collar itself consists of 3 circular plates assembled together in a sandwich. The two base parts are soldered together to form a hollowed out chamber (the bottom plate) through which the water flows, and then the sandwich is assembled consisting of the top plate, the Peltier, and the bottom plate. This is held together with nylon screws to avoid creating a thermal short circuit. The top piece fits directly over the nose of the objective (21 mm in diameter) and is fastened onto the nose using a 3 mm hex screw binding around the nose. The Peltier plate and the bottom plate hang below this top plate, not in contact with the objective. Heat is pumped by the Peltier from the top to the bottom when the Peltier is driven in cooling mode. Figure A.1 shows a 1:1 scale full schematic of the Peltier collar.

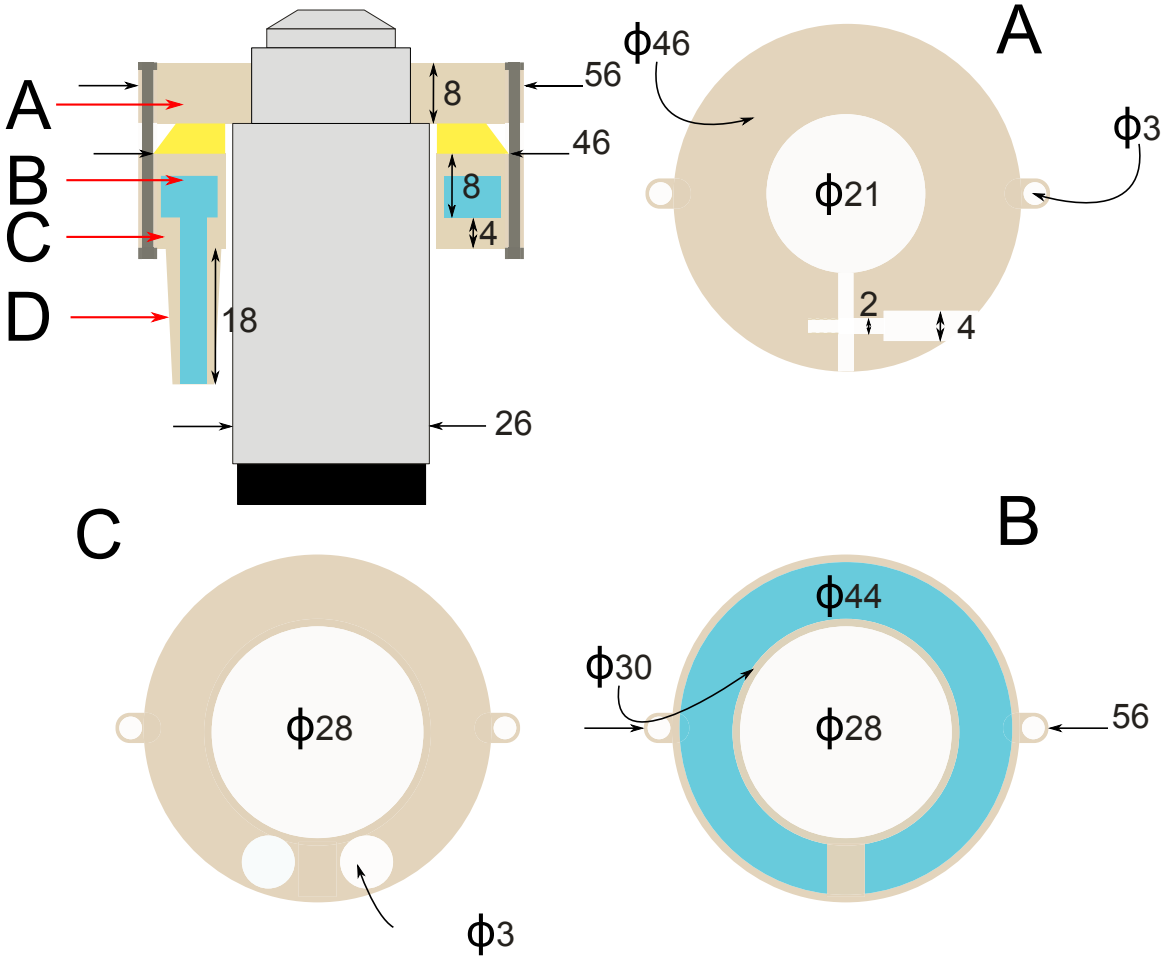

Figure A.1: Schematic for the Peltier Collar. Scale is 1:1 and all measurements are in mm. Diameters indicated by π. The collar is constructed from 3 copper (brown) segments, A) the top section that fastens around the nose of the objective (21 mm diameter), B) the middle section through which most of the water (blue) ows, and C) the bottom section with two holes for water inlet and outlet. When the three sections are ready, sections B and C are soldered together to form a water tight seal around the chamber that will be lled with water, which ts around the objectve shaft with 1 mm space (28 mm diameter). Finally an outlet (D) (17 mm length) is soldered into the holes in plate C. The collar is held together using nylon screws to prevent any thermal short circuit.

Appendix B

MATLAB code used for Analysis

This Appendix includes the three MATLAB m-files that are used to calculate the membrane voltage from .sif image files from the iXon camera (see Section 2.2. The first file, Tcell.m, is used to calculate the brightness of a single cell, that is the value T_{cell} discussed in Section 5.6.1. The second file listed here, Vm2.m, is used to calculate the membrane voltage without flowing carbonyl cyanide m-chlorophenylhydrazone (CCCP) into the slide or calculating M_{CCCP} (using Equation 5.6). It uses as input the value for T_{cell} calculated by Tcell.m, and the value for M_{absent}, calculated from the gradient of the linear fit of intensity vs exposure time in the absence of any cells, as detailed in Section 5.6.2. The third file, vmcp.m, is used to calculate the membrane voltage using a series of measurements after CCCP has been flowed over the cell to measure M_{CCCP} and offset the V_m (using Equation 5.16). The model used as the basis for the code shown in this appendix is discussed in detail in Sections 5.6–5.7.

B.1 Tcell.m

```
%%%%%%%%%%%%%%%%%%%%%%%%%%%%%%%%%%%%%%%%%%%%%%%%%%%%%%%%%%%%%%%%%%%%%%%%%%%%%%%%
% Tcell.m - last saved by Matt Baker 4/5/2010
% This MATLAB programme reads and analyses raw .sif image files taken by
% the Andor iXon camera on the Fluorescence microscope.
% The programme has 5 steps
% 1) Load file
% 2) Define threshold, thresh
```

```
% 3) Find largest contiguous area where pixel intensity is greater than
%    thresh
% 4) Calculate the mean of the inverse of the mask (background)
% 5) Calculate the median intensity over this mask (mediancell)
% 6) Calculate the mean of the pixels with greater intensity than the
%    median (cell)
% 7) Calculate the difference between Step 5 (cell) and Step 4 (background)
% 8) Save an ascii file out with time (s), F, exposure time, and mask size
%%%%%%%%%%%%%%%%%%%%%%%%%%%%%%%%%%%%%%%%%%%%%%%%%%%%%%%%%%%%%%%%%%%%%%%%%%%

%% load files
dirname = uigetdir
filelist = dir(fullfile(dirname,'*.sif'));
numfiles = length(filelist);
files = struct2cell(filelist);
dates = files(2,:)' %calculates times from image timestamp
T = zeros(numfiles,3)
std_bias = 1; %the number of standard deviations above mean for thresh
keeper = 0;
% resize screen for better image
scrsz = get(0,'ScreenSize');
figure('Position',[1 scrsz(4)/2 scrsz(3)/2 scrsz(4)/2])

%% Calculate thresh, background, cell for each image file
for i = 1:numfiles
    A = sifread(fullfile(dirname,filelist(i).name));
    image = A.imageData;
    figure('Position',[1 1 scrsz(3) scrsz(4)])
    imagesc(image);
    % Offer the user opportunity to investigate cell for image cropping or
    % rejection (if image not correct)
    if keeper == 1
        % if multiple crops wanted in same place, fiddle with this.
        image3 = imcrop(image,[0, size(image,1) - cropsize(1), ...
        cropsize(2), cropsize(1)]);
        copyfile(fullfile(dirname,filelist(i).name), ...
         fullfile(dirname,strcat('good_image',num2str(i))))
    elseif keeper == 0
    keep = questdlg('keep?', 'title', 'Yes', 'No', 'Crop', 'All on crop1')
    end
    if strcmpi(keep,'No')
        close
        continue
    end
```

```
if strcmpi(keep,'Yes')
   copyfile(fullfile(dirname,filelist(i).name), ...
     fullfile(dirname,strcat('good_image',num2str(i))))
end
if strcmpi(keep,'Crop')
    image = imcrop;
    cropsize = size(image);
    copyfile(fullfile(dirname,filelist(i).name), ...
     fullfile(dirname,strcat('needscrop_image',num2str(i))))
end

close
%% Calculate thresh
%% Method one - take one std dev away from the mean and chop
thresh = mean(image(:)) + std_bias*std(image(:));
imagesc((image>thresh).*image)
%%
%% Method 2 - take the max count (mode), *2, then chop
%% commented this out as it proved a bogus method upon check
%% thresh_mode = 2 * mode(image(:));
%% imagesc((image>thresh_mode).*image)
%% above_thresh = image(image>thresh)
%%

%% Find largest contiguous area (bwlabel), of pixels brighter than
%% thresh
try
selection = bwlabel(image>thresh);
histcount = histc(selection(:),1:max(selection(:)));
index = find(histcount == max(histcount));
mask = (selection == index);
catch
end
%% define mask and inverse of mask
masked_image = image.*(mask);
unmasked_image = image.*(1-mask); %the inverse of mask = everything else
%% find median intensity of pixels in mask
mediancell = median(image(mask));
%% old method used midpoint calculation
% T_cell = thresh + (((max(masked_image(:)) - thresh)) / 2);
%% calculate cell, the brightness measurement for the cell
% cell = mean(masked_image(masked_image>T_cell));
cell = mean(masked_image(masked_image>mediancell));
%% calculate background from mean of inverse of mask
```

```
    background = mean(unmasked_image(:));
    cell - background % this is the F_in value for the cell
    T(i,2) = cell - background;
    %% record exposure time and time
    T(i,3) = A.exposureTime;
    T(i,1) = datenum(dates(i));
    %optional line to record cell area as 4th column.
    T(i,4) = sum(mask(:));
end
%% Save ascii data out
% save data so far in case of crash
save(fullfile(dirname,'T-draft.out'), 'T', '-ascii', '-double', '-tabs')
% Sort data in order of time
sortT = sortrows(T);
[Ti, Tj] = find(sortT);
sortT = sortT(min(Ti):max(Ti),:);  % reorder sortT in time order
time = sortT(:,1);
% turn timestamp into seconds, where first file is t = 0
timeshift = [time(1) ; time(1:(length(time) - 1))]
time = time - timeshift;
time = cumsum(time);
timestr = datestr(time - 7);
hrs = timestr(:,14);
mins10 = timestr(:,16);
mins1 = timestr(:,17);
seconds10 = timestr(:,19);
seconds1 = timestr(:,20);
minutes = (str2num(hrs) * 60) + str2num(mins10) * 10 + str2num(mins1);
seconds = minutes * 60 + str2num(seconds10)*10 + str2num(seconds1);
sortT(:,1) = seconds;
% save sorted, time in seconds data, out to file named after the name of
% the image file with -T.out appended
fileout = [filelist(2).name '-T.out']
save(fullfile(dirname,fileout), 'sortT', '-ascii', '-double', '-tabs');
%% END
```

B.2 Vm2.m

```
%%%%%%%%%%%%%%%%%%%%%%%%%%%%%%%%%%%%%%%%%%%%%%%%%%%%%%%%%%%%%%%%%%%%%%%%%%%%
% Vm2.m - last saved by Matt Baker 4/5/2010
% This MATLAB programme reads ascii data containing the output from Tcell.m
% and calculates the membrane voltage (V_m) (with no CCCP subtraction).
```

```
% The programme has 5 steps
% 1) Load background information (M_absent)
% 2) Load T file information
% 3) Find largest contiguous area where pixel intensity is greater than
%    thresh
% 4) Calculate M_live, M_absent and C_ratio for every cell
% 5) Write ascii output.
%%%%%%%%%%%%%%%%%%%%%%%%%%%%%%%%%%%%%%%%%%%%%%%%%%%%%%%%%%%%%%%%%%%%%%%%%%%%%%%
clear
%% Load Files
% Load background file
[backfile, backpath] = uigetfile({'*.out'}, 'Pick background calibration file');
background = load(fullfile(backpath, backfile))
% Load background data: p(1) = slope, p(2) = const
p = polyfit(background(:,1),background(:,2),1);
% Load Tfile (data from Tcell)
temp = input('What T, 5, 10 or 20?')
[Tfile, Tpath] = uigetfile({'*.out'}, 'Pick T file')
T = load(fullfile(Tpath, Tfile))
% [T_cccp_file, T_cccp_path] = uigetfile({'*.out'}, 'Pick CCCP T file')
% T_CCCP = load(fullfile(T_cccp_path, T_cccp_file))
% F_CCCP = mean(T_CCCP(:,2))
sums = 0
%% Calculate M and C_ratio for every row of T, ie every cell

for i=1:length(T(:,1))
    %% Calculate M_live, M_absent
    alpha = 3.52899;
    M_live(i) = (T(i,2)/T(i,3)) * 0.02; %% normalised exp time is 0.02 / T(i,3)
    M_absent(i) = 0.02 * p(1);
    F_ratioB(i) = M_live(i)/M_absent(i);
    C_ratioB(i) = alpha * F_ratioB(i) - (alpha - 1);
    %% calculate voltage - function of temperature and C_ratio, from Nernst
    V_mB(i) = voltage(C_ratioB(i),temp);
    %function C_ratio = C_ratio(F_ratio)
end
V_m_mean = mean(V_mB);
M_live_mean = mean(M_live);
M_end_mean = mean(M_live((end-2):end));
Vm_end_mean = mean(V_mB((end-2):end));
%% arrange output in one cell structure, and write to .csv file
out = [T(:,1) M_live' M_absent' F_ratioB' C_ratioB' V_mB'];
size_out = size(out);
cell_out = cell((size_out(1)+1),size_out(2));
```

```
cell_out(1,1) = cellstr('Time');
cell_out(1,2) = cellstr('M_live');
cell_out(1,3) = cellstr('M_absent');
cell_out(1,4) = cellstr('F ratio');
cell_out(1,5) = cellstr('C ratio');
cell_out(1,6) = cellstr('Vm');
cell_out(2:(size_out(1)+1),:) = num2cell(out);
fileoutput = input('outputfile name?','s');
fileoutput_out = [fileoutput '.out'];
cell2csv(fullfile(Tpath,fileoutput), cell_out);
%% Statistics on Vm
%takes the unique clumps, records mean and std dev and writes out to
%file labelled stats_vm. etc based on the input from user before the Vm
%write.
Un = unique(out(:,1));
for i=1:length(Un)
    rows = find(out == Un(i));
    keeps = out(min(rows):max(rows),:);
    stats(i,1) = Un(i);
    stats(i,2) = mean(keeps(:,6));
    stats(i,3) = std(keeps(:,6));
end

%% plot figures of Vm and Stats and save as .png files
% stats
figure
%plots means of clumps, with errorbars
errorbar(stats(:,1),stats(:,2),stats(:,3),'+')
axis_vals = axis;
axis_vals(4) = -0.02;
axis_vals(3) = -0.22;
axis(axis_vals);
title(fileoutput);
png_out = [fileoutput '.png']
% print('-dpng', '-zbuffer', png_out) %saves fig as .png in T file directory
save(fullfile(Tpath,strcat('stats_',fileoutput_out)),  ...
    'stats', '-ascii', '-double', '-tabs');
% Plot of M_live, F_ratio and Vm
figure
subplot(2,2,1), plot(out(:,1),out(:,6), '.')
axis_vals = axis;
axis_vals(4) = -0.05;
axis_vals(3) = -0.15;
axis(axis_vals);
```

```
title(fileoutput);
subplot(2,2,2), plot(out(:,1), out(:,2),'.')
title('Raw F')
subplot(2,2,3), plot(out(:,1), out(:,4),'.')
title('raw F ratio')
subplot(2,2,4), plot(out(:,1), out(:,5),'.')
title('raw C ratio')
Vm_mean_str = ['Vm mean = ' num2str(V_m_mean)];
F_mean_str = ['F mean = ' num2str(M_live
_mean)];
Vm_end_mean_str = ['Vm last3 mean = ' num2str(Vm_end_mean)];
gtext(Vm_mean_str);
gtext(F_mean_str)
gtext(Vm_end_mean_str);
print('-dpng', '-zbuffer', png_out) %saves fig as .png in T file directory
%% END
```

B.3 vmcp.m

```
%%%%%%%%%%%%%%%%%%%%%%%%%%%%%%%%%%%%%%%%%%%%%%%%%%%%%%%%%%%%%%%%%%%%%%%%%%%%
% vm_cp.m - last saved Matt Baker 4/5/2010
% This MATLAB programme reads T file data for cells before CCCP exposure
% and after CCCP exposure and calculates M_CCCP, M_live, and M_absent..
% The programme has 5 steps
% 1) Load files (Background, T_CCCP, T).
% 2) Calculate M_CCCP.
% 3) Calculate M_absent, and M_live from M_absent and M_CCCP.
% 4) Perform error analysis.
% 5) Write ascii data out.
%%%%%%%%%%%%%%%%%%%%%%%%%%%%%%%%%%%%%%%%%%%%%%%%%%%%%%%%%%%%%%%%%%%%%%%%%%%%

%% Initial variables
% determine type of fit to CCCP curve
tails = 0;
expfut = 0;
%%%%%%%%%%%%%%%%%%%%%%%%%%%%%%%%%%%%%%%%%%%%%%%%%%%%%%%%%%%%%%%%%%%%%%%%%%%%
%% Load files
%%%%%%%%%%%%%%%%%%%%%%%%%%%%%%%%%%%%%%%%%%%%%%%%%%%%%%%%%%%%%%%%%%%%%%%%%%%%

% load background
[backfile, backpath] = uigetfile({'*.out'}, 'Pick background calibration file');
background = load(fullfile(backpath, backfile))
```

```
p = polyfit(background(:,1),background(:,2),1); %now p(1) = slope, p(2) = const
% load T file
[Tfile, Tpath] = uigetfile({'*.out'}, 'Pick T file')
T = load(fullfile(Tpath, Tfile));
% load T_CCCP file - the cells after CCCP flowed in
[T_cccp_file, T_cccp_path] = uigetfile({'*.out'}, 'Pick CCCP T file')
T_CCCP = load(fullfile(T_cccp_path, T_cccp_file))
sums = 0
F_in_mean = mean(T(:,2));
temp = input('What T, 5, 10 or 20?')

% Which part of T_CCCP are we looking at? Just the tails? if so, tails == 1
% and we count all T that are after 600 s
if tails == 1
    ind1 = 1 %min(find(T(:,1) > 0));
    ind2 = min(find(T_CCCP(:,1) > 600));
    %we are choosing the last 10 above now, so don't need to restrict on time
else % otherwise, we look at all of T_CCCP
    ind1 = 1;
    ind2 = 1;
end

%% Calculate M_CCCP

% Calculate F_CP (M_CCCP)
for i=ind2:length(T_CCCP(:,1)) %for cells after CCCP flowed in
    F_CP(i) = (T_CCCP(i,2) / T_CCCP(i,3)) * 0.02;
    F_CP_ratio(i) = F_CP(i)/ (0.02*p(1));
end

F_CCCP = mean(F_CP(ind2:end)); %M_CCCP measurement from mean of tails

alpha = 3.52899; %constant for convolution fit

% Exponential Fit for F_CP (M_CCCP)
if expfut == 1
    % fit using exponential fit:
    coeffs = expoffsetfit(T_CCCP(:,1), T_CCCP(:,2))
    %   cf_(x) = a*exp(-b*x)+c
    % coeffs(1) = a, coeffs(2) = b, coeffs(3) = c
    F_CCCP = coeffs{3}
end
% alternatively, if fitting in a separate program (eg Origin)
% can just set M_CCCP here:
```

```
% F_CCCP = 100


%%%%%%%%%%%%%%%%%%%%%%%%%%%%%%%%%%%%%%%%%%%%%%%%%%%%%%%%
%% Calculate M_live and M_absent
%%%%%%%%%%%%%%%%%%%%%%%%%%%%%%%%%%%%%%%%%%%%%%%%%%%%%%%%
for i=ind1:length(T(:,1))  %for F no CCCP, subtracting average F_CCCP background

    M_live(i) = (T(i,2)/T(i,3)) * 0.02;
    M_absent(i) = 0.02 * p(1);
    M_CCCP(i) = F_CCCP;
    F_ratioB(i) = M_live(i) / M_absent(i);
    C_ratioB(i) = (M_live(i) - M_CCCP(i))/((1/alpha)*M_absent(i))+1;
    V_mB(i) = voltage(C_ratioB(i),temp);

%% error analysis

    %this line sets M_CCCP error as std error over F_CP measurements (form
    %T_CCCP)
    M_CCCP_err = std(F_CP(ind2:end)) / sqrt(size(F_CP(ind2:end),2));
    M_live_err =    115.27; %from variance and std error for non bleached
    p_err =   22.39; %from fit error to line for M_absent calibration

    live_error(i) = (M_live_err^2 + M_CCCP_err^2)/((M_live(i) - M_CCCP(i))^2);
    Δ_C_rat_squared(i) = (C_ratioB(i) - 1)^2 * ( (M_live_err^2 + M_CCCP_err^2) ...
    /((M_live(i) - M_CCCP(i))^2) + (p_err/p(1))^2 );
    V_mB_error(i) = voltage(sqrt(Δ_C_rat_squared(i)),temp) / C_ratioB(i);

    % take the mean over all non-imaginary V_mB (ie, where C_ratio > 0)
    index = find(imag(V_mB) == 0);
    V_mB_mean = mean(V_mB(index));

end
%%%%%%%%%%%%%%%%%%%%%%%%%%%%%%%%%%%%%%%%%%%%%%%%%%%%%%%%%%%
%% Write files out
%%%%%%%%%%%%%%%%%%%%%%%%%%%%%%%%%%%%%%%%%%%%%%%%%%%%%%%%%%%

out = [T(:,1) M_live' T(:,3) F_ratioB' V_mB'*1000 1000*V_mB_error'];
%currently this will run if T file and TCCCP are same file only!
%set up out with T and T_CCCP values, with zero spacefillers under Vm
size_out = size(out);
cell_out = cell((size_out(1)+1),size_out(2));
cell_out(1,1) = cellstr('Time');
cell_out(1,2) = cellstr('F');
```

```
cell_out(1,3) = cellstr('exposure Time');
cell_out(1,4) = cellstr('F ratio');
cell_out(1,5) = cellstr('VmB');
cell_out(1,6) = cellstr('VmB Error');
cell_out(2:(size_out(1)+1),:) = num2cell(out);

fileoutput = input('Name of output file','s');
fileoutput_out = [fileoutput '.out'];

cell2csv(fullfile(Tpath,fileoutput_out), cell_out);


%% Plot Vm and raw F
close all
subplot(2,2,1), plot(out(1:length(T),1),out(1:length(T),5), '.')
axis_vals = axis;
axis_vals(4) = -0.02;
axis_vals(3) = -0.22;
axis(axis_vals);
title(fileoutput);
subplot(2,2,1), plot(out(1:size(T,1),1),V_mB, '.')
title('V_mB - offset for CCCP')
subplot(2,2,2), plot(out(1:size(T,1),1),M_live, '.')
title('raw M_{live}')
subplot(2,2,3), plot(T_CCCP(:,1),F_CP, '.')
title('raw F_CCCP')

png_out = [fileoutput '.png']
% label graph
labelstr2 = ['V_mB mean = ' num2str(V_mB_mean)];
gtext(labelstr2)
labelstr3 = ['F_CCCP = ' num2str(F_CCCP)];
gtext(labelstr3)

print('-dpng', '-zbuffer', png_out)
```

Appendix C

Analysis of Variance (ANOVA) for V_m Measurements

This appendix includes the tabulated data for the statistical tests performed in Section 5.8 to test for significant difference in the mean and variance of the membrane voltage at different temperatures. The tests performed were an ANOVA one-way test to test for the presence of significant differences (at the 0.05 level) in the means, a Scheffé test to compare the means between each level specifically, a Levene test to determine if the population variances were significantly different (at the 0.05 level), and a Shapiro-Wilk test on the data at each temperature to determine if the data was significantly drawn from a normal distribution (at the 0.05 level). Note the Shapiro-Wilk normality test failed for all populations, limiting the usefulness of the other parametric tests, but ANOVA tests are robust to non-normality in certain conditions described in Section 5.8 (Glass et al., 1972; Harwell et al., 1992). The tests are described briefly in Section 5.8, and the original references for the tests are given (Scheffé, 1959; Levene, 1960; Shapiro and Wilk, 1965). These ANOVA tests are parametric tests that test the hypothesis that two populations have the same mean, and calculate the probability of obtaining a test-statistic at least as extreme as the one that was actually observed, in this case, to the 0.05 level. For further information on these tests a good text is Neter et al. (1996). All tests were performed using the built-in parametric test functions of the Origin data analysis and plotting programme.

In Table C.1 the analysis of the data without added CCCP is presented, using voltages calculated from Equation 5.6. In Table C.2 the analysis of the data after

CCCP was added is presented, considering the offset from C_{bound} and using voltages calculated from Equation 5.16.

(a) Descriptive Statistics

	Sample Size	Mean	Standard Deviation	SE of Mean
5 °C V_m	343	-0.12775	0.0206	0.00111
22 °C V_m	333	-0.12121	0.01398	7.66E-04
40 °C V_m	467	-0.12519	0.04487	0.00208

(b) Shapiro-Wilk Normality Test

	Degrees of Freedom	Statistic	Prob $< W$
5 °C Vm	343	0.89054	5.77E-15
22 °C Vm	333	0.89238	1.39E-14
40 °C Vm	466	0.92959	5.36E-14

(c) Overall ANOVA Test

	DF	Sum of Squares	Mean Square	F	Prob $> F$
Model	2	0.00734	0.00367	3.64449	0.02644
Error	1140	1.14814	0.00101		
Total	1142	1.15548			

(d) Scheffé Test

	MeanDiff	SEM	F	P	α	Sig	LCL	UCL
22 °C 5 °C	0.00654	0.00244	3.58414	0.02807	0.05	1	5.53E-04	0.01252
40 °C 5 °C	0.00256	0.00226	0.64169	0.52659	0.05	0	-0.00297	0.00809
40 °C 22 °C	-0.00398	0.00228	1.52876	0.21725	0.05	0	-0.00956	0.0016

(e) Levene Test

	Degrees of Freedom	Sum of Squares	Mean Square	F	Prob $> F$
Model	2	0.09669	0.04834	107.6694	0
Error	1140	0.51186	4.49E-04		

Table C.1: Table showing analysis of variance data for the voltages calculated using Equation 5.6 in the absence of CCCP. a) Descriptive statistics showing mean, standard deviation and standard error of the mean for the voltages at all three temperatures. b) Shapiro-Wilk Normality Tests. Since in all cases the P value is less than the α value (0.05) none of the populations are significantly drawn from a normal distribution. c) Overall ANOVA test. Since the P value is less than the significance level ($0.026 < 0.05$) the means are significantly different here. c) Scheffé test to compare all means with each other in a single step. Since the P value is less than α for the comparison between the V_m at 22 °C and the V_m at 5 °C, there is a significant difference at the 0.05 level between these two means, but not between the other means. d) Levene Test. Since the P value is less than 0.05 (F is very large here so $P \sim 0$) there is significant difference in the variances of the three populations.

(a) Descriptive Statistics

	Sample Size	Mean	Standard Deviation	SE of Mean
40C	158	-119.796	44.67824	3.55441
5C	154	-118.842	22.31727	1.79838

(b) Shapiro-Wilk Normality Test

	DF	Statistic	Prob $< W$
40C	158	0.94151	4.08E-06
5C	154	0.96228	3.26E-04

(c) Overall ANOVA

	Degrees of Freedom	Sum of Squares	Mean Square	F	Prob $> F$
Model	1	70.90771	70.90771	0.05642	0.8124
Error	310	389598	1256.768		
Total	311	389669			

(d) Scheffé Test

	MeanDiff	SEM	F	P	α	Sig	LCL	UCL
Level2 Level1	0.95353	4.01436	0.05642	0.8124	0.05	0	-6.94531	8.85237

(e) Levene Test

	Degres of Freedom	Sum of Squares	Mean Square	F	Prob $> F$
Model	1	24243.53	24243.53	54.65543	1.35E-12
Error	310	137506.8	443.5703		

Table C.2: Table showing analysis of variance data for the voltages calculated using Equation 5.6 in the absence of CCCP. a) Descriptive statistics showing mean, standard deviation and standard error of the mean for the voltages at all three temperatures. b) Shapiro-Wilk Normality Tests. Since in both cases the P value is less than the α value (0.05) neither of the populations are significantly drawn from a normal distribution. c) Overall ANOVA test. Since the P value is greater than the significance level ($0.8124 > 0.05$) the means are significantly different here. Since there are only two populations, the ANOVA test here is the same as a t-test. d) Scheffé test to compare means with each other in a single step. Again, this shows the means are not significantly different. e) Levene Test. Since the P value is less than 0.05 there is significant difference in the variances of the two populations.

Appendix D

Single Cell Tracking During Cooling

This Appendix shows example raw speed vs time traces for the single cells with varying loads (1.0 μm – 0.20 μm diameter beads) tracked from 22 °C down to 5 °C. The traces shown in this Appendix (Figures D.1–D.6) were were used to calculate points shown in the torque speed curves shown in Figure 4.16 and discussed in Section 4.4.4. Speeds are calculated using running window power spectrums, as described in Section 4.3.1. For the larger bead sizes (1.0 and 0.75 μm beads) windows lengths were 3 s, for all other beads the window size was 1 s, to increase the resolution of slow speeds. For the smallest beads (0.20 μm) the position of the bead was measured using the 638 nm HeNe laser, and for all other beads the position was measured using the 1064 nm IR laser, as described in Section 2.3. Speeds are then filtered with a running window 50 point median filter, speeds at constant temperature are isolated, and histograms are calculated.

For each size load, an example of a good trace (one used to produce a data point in Figure 4.4.4) and a bad trace (one not used for calculation) are shown, and the reasons for selection and rejection are listed in each case. The histograms of the speeds at each steady state temperature are shown in both cases, showing three clear peaks, or overlapping unclear peaks in the case of a good or bad trace respectively. Stator allocation for each trace is done by comparison with literature values from Lo (2007) and Reid et al. (2006) (shown in Table 4.1, Section 4.3.2).

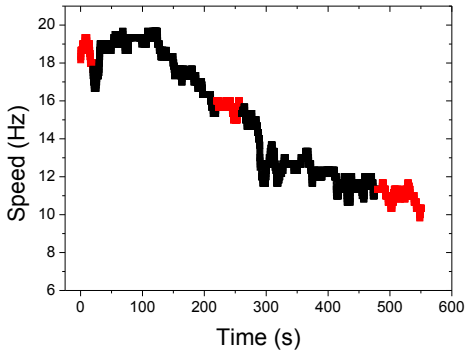

(a) Good 1.0 μm bead

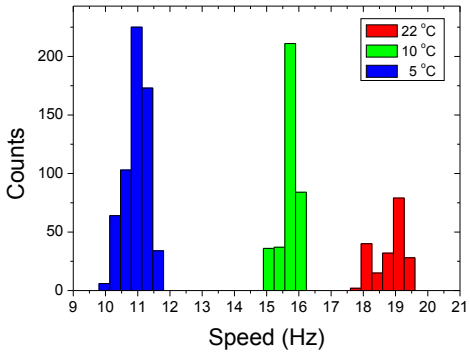

(b) Good 1.0 μm bead

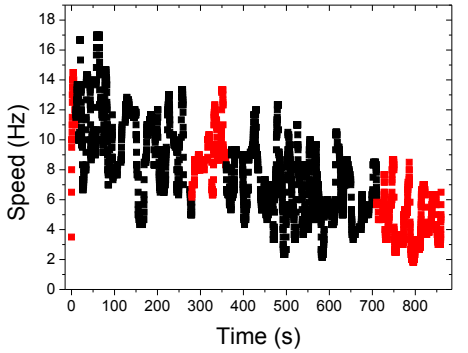

(c) Bad 1.0 μm bead

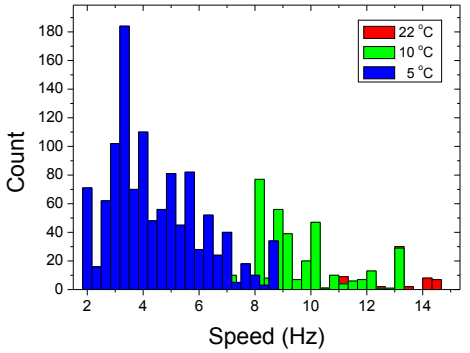

(d) Bad 1.0 μm bead

Figure D.1: Example traces for stator motors driving a 1.0 μm bead load. Speeds are calculated using a 3 s running window complex power spectrum and taking the maximum peak. All speed traces are filtered using a 50 point running window median filter. Black squares show speed, and red squares show speed at constant temperatures of 22 °C (red bars on histogram), 10 °C (green bars on histogram) and 5 °C (blue bars on histogram) from left to right respectively. Histograms are calculated with bin sizes corresponding to the minimum resolution (1/3 Hz). (a) Good trace for triple stator motor (literature speed at 22 °C is 23.3± 2.8 Hz) as indicated by tight band of speeds, little fluctuation, and continuous speed during cooling sections. (b) Histogram shows clear peaks at constant temperature which can be used to fit Gaussians. (c) Bad trace for $\sim$ 2 stator motor showing large fluctuation and non continuous speed during cooling. (d) Overlapping histograms with multiple peaks make it hard to identify clear stator peaks.

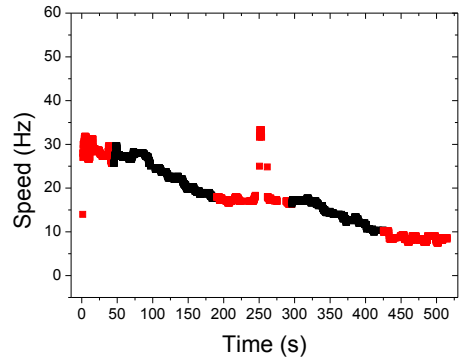

(a) Good 0.75 μm bead

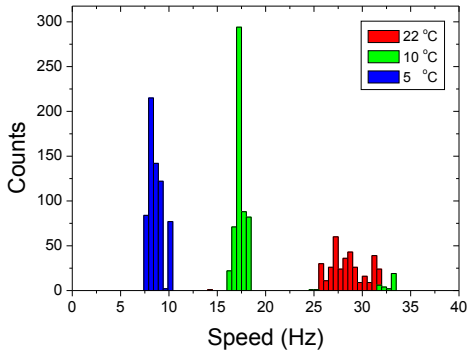

(b) Good 0.75 μm bead

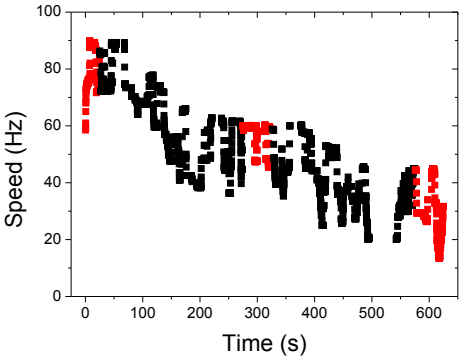

(c) Bad 0.75 μm bead

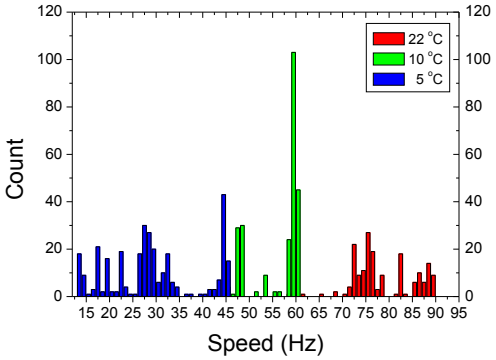

(d) Bad 0.75 μm bead

Figure D.2: Example traces for stator motors driving a 0.75 μm bead load. Speeds are calculated using a 3 s running window complex power spectrum and taking the maximum peak. All speed traces are filtered using a 50 point running window median filter. Black squares show speed, and red squares show speed at constant temperatures of 22 °C (red bars on histogram), 10 °C (green bars on histogram) and 5 °C (blue bars on histogram) from left to right respectively. Histograms are calculated with bin sizes corresponding to the minimum resolution (1/3 Hz). (a) Good trace for double stator motor (literature speed at 22 °C is 35.8 $\pm$ 2.7 Hz) as indicated by tight band of speeds, little fluctuation, and continuous speed during cooling sections. (b) Histogram shows clear peaks at constant temperature which can be used to fit Gaussians. (c) Bad trace for $\sim$ 4 stator motor (literature average speed per stator is 17 Hz) showing large fluctuation during cooling. (d) Overlapping histograms with multiple peaks make it hard to identify clear stator peaks.

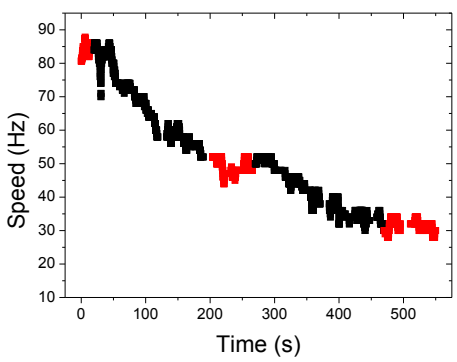

(a) Good 0.50 μm bead

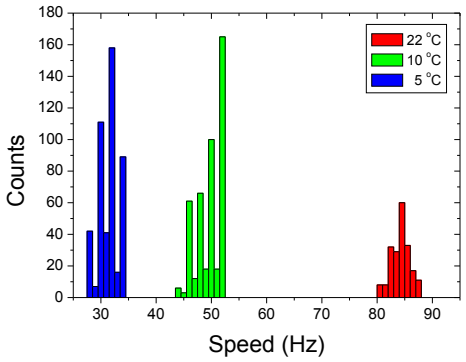

(b) Good 0.50 μm bead

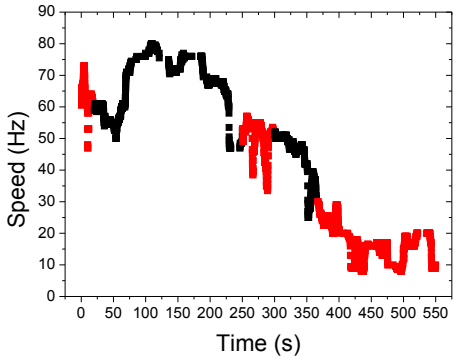

(c) Bad 0.50 μm bead

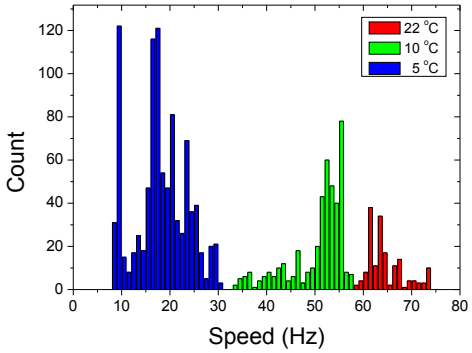

(d) Bad 0.50 μm bead

Figure D.3: Example traces for stator motors driving a 0.50 μm bead load. Speeds are calculated using a 1 s running window complex power spectrum and taking the maximum peak. All speed traces are filtered using a 50 point running window median filter. Black squares show speed, and red squares show speed at constant temperatures of 22 °C (red bars on histogram), 10 °C (green bars on histogram) and 5 °C (blue bars on histogram) from left to right respectively. Histograms are calculated with bin sizes corresponding to the minimum resolution (1 Hz). (a) Good trace for double stator motor (literature speed at 22 °C is 76 $\pm$ 7 Hz) as indicated by tight band of speeds, little fluctuation, and continuous speed during cooling sections. (b) Histogram shows clear peaks at constant temperature which can be used to fit Gaussians. (c) Bad trace for $\sim$ 4 stator motor (literature speed is 76 $\pm$ 7 Hz) showing large fluctuation during cooling. (d) Overlapping histograms with multiple peaks make it hard to identify clear stator peaks.

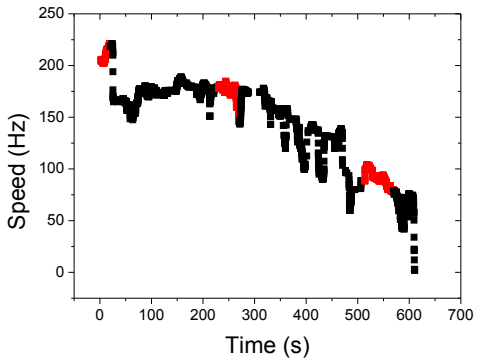

(a) Good 0.35 μm bead

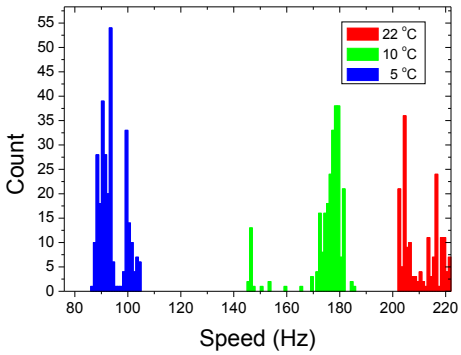

(b) Good 0.35 μm bead

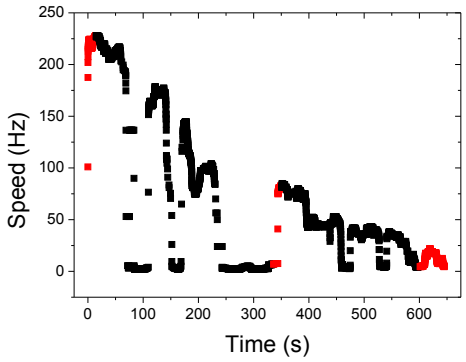

(c) Bad 0.35 μm bead

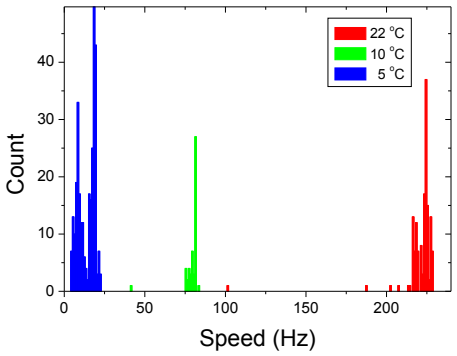

(d) Bad 0.35 μm bead

Figure D.4: Example traces for stator motors driving a 0.35 μm bead load. Speeds are calculated using a 1 s running window complex power spectrum and taking the maximum peak. All speed traces are filtered using a 50 point running window median filter. Black squares show speed, and red squares show speed at constant temperatures of 22 °C (red bars on histogram), 10 °C (green bars on histogram) and 5 °C (blue bars on histogram) from left to right respectively. Histograms are calculated with bin sizes corresponding to the minimum resolution (1 Hz). (a) Good trace for triple stator motor (literature speed at 22 °C is 233 $\pm$ 11 Hz) as indicated by tight band of speeds, little fluctuation, and continuous speed during cooling sections. (b) Histogram shows clear peaks at constant temperature which can be used to fit Gaussians. (c) Bad trace for $\sim$ 4 stator motor showing many stops and erratic speeds. (d) Stopping and speed changes during cooling cause doubt for stator allocation and overlapping histograms with multiple peaks make it hard to identify clear stator peaks.

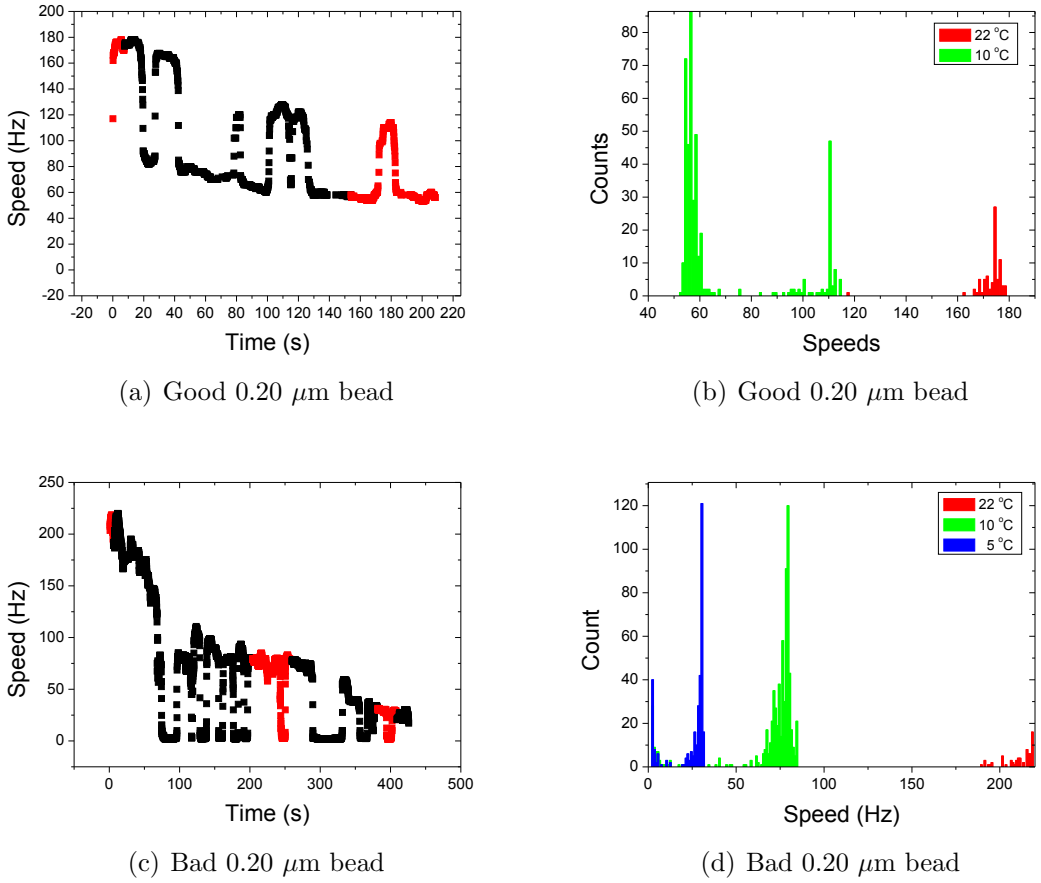

(a) Good 0.20 μm bead

(b) Good 0.20 μm bead

(c) Bad 0.20 μm bead

(d) Bad 0.20 μm bead

Figure D.5: Example traces for stator motors driving a 0.20 μm bead load. Position signal is taken using a 638 nm laser and back focal interferometry as described in Section 2.3, since the 0.20 μm beads are at the limit of resolution for the 1064 nm wavelength IR laser and laser damage becomes relevant over cooling timescales (Rowe, 2005). Speeds are calculated using a 1 s running window complex power spectrum and taking the maximum peak. All speed traces are filtered using a 50 point running window median filter. Black squares show speed, and red squares show speed at constant temperatures of 22 °C (red bars on histogram), 10 °C (green bars on histogram) and 5 °C (blue bars on histogram) from left to right respectively. Histograms are calculated with bin sizes corresponding to the minimum resolution (1 Hz). (a) Good tracked trace for a motor jumping between one and two stators (literature speeds at 22 °C are 111 $\pm$ 16 Hz and 213 $\pm$ 21 Hz respectively). Trace shows clear jumps that halve the speed, indicating transition from two to one stators. (b) Histogram shows clear peaks at constant temperature which can be used to fit Gaussians for one and two stators at 22 °C and 10 °C. (c) Bad trace for $\sim$ 2 stator motor (literature speed at 22 °C is 213 $\pm$ 21 Hz) showing many stops and possible stator jump at t $\approx$ 60 s. (d) Histograms show broad peaks, and a significant peak near zero speed, making it hard to allocate stators accurately.

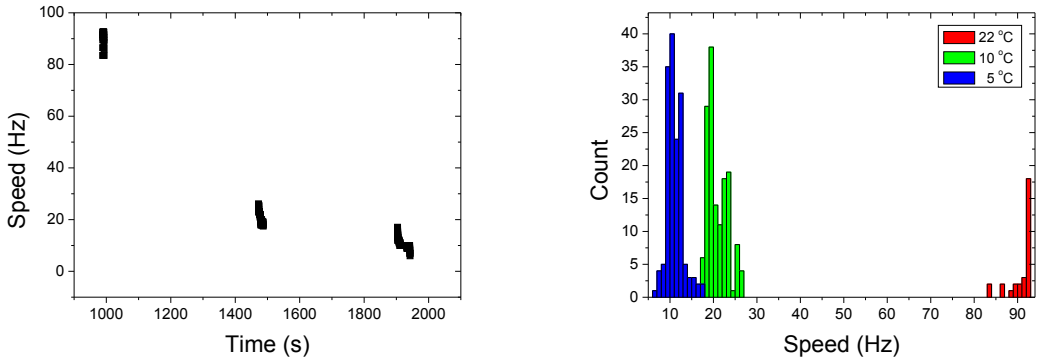

(a) Untracked 0.20 μm bead

(b) Untracked 0.20 μm bead

Figure D.6: Example traces for stator motors driving a 0.20 μm bead load. Position signal is taken using a 638 nm laser and back focal interferometry as described in Section 2.3. Speeds are calculated using a 1 s running window complex power spectrum and taking the maximum peak. All speed traces are filtered using a 50 point running window median filter. Black squares show speed, and red squares show speed at constant temperatures of 22 °C (red bars on histogram), 10 °C (green bars on histogram) and 5 °C (blue bars on histogram) from left to right respectively. Here the motor is not tracked with temperature as laser damage will affect the cell speed over 15 mins (Rowe, 2005). Due to the high speed of 0.20 μm bead rotation it is possible, but not ideal, to measure speed without tracking, since extra stator arrival should affect the speed significantly. Single stator motors that stably rotate 0.20 μm beads are rare (2 / 11 stable cells were single stator) (a) Good untracked trace for single stator motor (literature speed is 111 $\pm$ 16 Hz). (b) Speed is stable at each temperature and Gaussians can be fitted to peaks to identify stator speed at 10 °C and 5 °C. Histograms are calculated with bin sizes corresponding to the minimum resolution (1 Hz).